RADIATION DAMAGE IN FERRITIC STEELS PRODUCED BY VARIOUS PROCESSING METHODS

A Dissertation

by

EDA AYDOGAN

Submitted to the Office of Graduate and Professional Studies of
Texas A&M University
in partial fulfillment of the requirements for the degree of

DOCTOR OF PHILOSOPHY

Chair of Committee,	Lin Shao
Committee Members,	Ibrahim Karaman
	Haiyan Wang
	Karl T. Hartwig
Head of Department,	Ibrahim Karaman

August 2016

Major Subject: Materials Science and Engineering

Copyright 2016 Eda Aydogan

ABSTRACT

Next generation fast spectrum reactors require structural materials that can tolerate higher temperature and radiation damage compared to the currently used metal alloys. It has been discovered that the ferritic steels having bcc structure have higher swelling and creep resistance than the fcc austenitic steels. However, once the ferritic steels reach the steady state swelling regime, they can end up with considerable swelling. Radiation damage resistance in metals is directly correlated with the microstructure. In terms of microstructure tailoring to reduce radiation damage, the density of sinks (dislocations, grain boundaries, phase boundaries, twin boundaries etc.) can be increased. In this research, engineering alloys were produced with increased sink densities by various processing methods in order to improve swelling resistance. Various alloys of EK-181, HT-9 and 14YWT were processed by high pressure torsion (HPT), high rate shock deformation and hydrostatic extrusion, respectively. The effects of the resultant microstructures on the irradiation response of the materials were investigated with special interest paid to the influence of grain boundaries, phase boundaries and dislocations on swelling. In this study, we reported that initial stable and homogenous microstructure is the key to determine swelling resistance. Homogenously distributed nano-sized oxide dispersoids act as sinks for defects and help to stabilize microstructures through pinning dislocations and grain boundaries. The stability of oxide dispersoids is determined by irradiation conditions and key parameters influencing dispersoids' stability are identified. The study is important for development of accident tolerant components for fast reactors.

DEDICATION

To my husband, Gokhan Gungor

To my mom, Inci Aydogan

To my dad, Necati Aydogan

ACKNOWLEDGEMENTS

Firstly, I would like to thank my advisors Dr. Lin Shao and Dr. Stuart A. Maloy for their invaluable advice, endless encouragement and financial support for this Ph.D. dissertation. I also thank other committee members, Dr. Karl Ted Hartwig, Dr. Haiyan Wang and Dr. Ibrahim Karaman for their guidance and suggestions throughout the course of entire research.

Thanks also go to my mentor at Los Alamos National Laboratory, Dr. O. Anderoglu for his guidance and endless support. A sincere “thank you” to Dr. F.A. Garner who was always helpful for the interpretation of the data with his constructive discussions. I would like to give my appreciation to Dr. G.R. Odette for his fruitful discussions on atom probe tomography studies. I am grateful to Dr. K.G. Field for his aid in high resolution transmission electron microscopy experiments at Oak Ridge National Laboratory. I also want to extend my gratitude to Dr. S.C. Vogel for providing the opportunity of using HIPPO instrument for neutron diffraction experiments.

I am also grateful to my teammates at Texas A&M University, T. Chen, J.G. Gigax, L. Price, D. Chen, X. Wang, W. Kinnison. I appreciate their help on continuous days-long overnight irradiations. I would like to give my special thanks to MST-8 family at Los Alamos National Laboratory for their helps, advice and support.

Finally, thanks to my mother and father for their encouragement and to my husband for his patience, support and love.

NOMENCLATURE

APT	Atom probe tomography
BCC	Body centered cubic
BF	Bright field
BSE	Back scattered electrons
CSLB	Coincidence site lattice boundary
DBH	Dispersed barrier hardening
DPA	Displacements per atom
EBSD	Electron back scatter diffraction
ECAP	Equal channel angular pressure
EDS	Energy dispersive spectroscopy
EFTEM	Energy filtered transmission electron microscopy
F/M	Ferritic/martensitic
FCC	Face centered cubic
FIB	Focused ion beam
FWHM	Full width at half maximum
GB	Grain boundary
HAADF	High annular angular dark field
HAB	High angle boundary
HE	Hot extrusion
HIP	Hot isostatic pressing

HPT	High pressure torsion
HRTEM	High resolution transmission electron microscopy
HVOF	High velocity oxy-fuel
LAB	Low angle boundary
LANL	Los Alamos National Laboratory
NF	Nanofeature
NFA	Nanostructured ferritic alloy
ODF	Orientation distribution function
OIM	Orientation imaging microscopy
OR	Orientation relationship
ORNL	Oak Ridge National Laboratory
PKA	Primary knock-on atom
RAGB	Random grain boundary
RED	Radiation enhanced diffusion
REP	Radiation enhanced precipitation
RID	Radiation induced depletion
RIP	Radiation induced precipitation
RIS	Radiation induced segregation
RMS	Root mean square
Rp	Projected ion range
SE	Secondary electrons
SEM	Scanning electron microscopy

SIA	Self-interstitial atoms
SPD	Severe plastic deformation
STEM	Scanning transmission electron microscopy
TEM	Transmission electron microscopy
TMS	Tempered martensitic steel
UCSB	University of California Santa Barbara
VAR	Vacuum arc remelting
VIM	Vacuum induction melting
XRD	X-ray diffraction

TABLE OF CONTENTS

Page

LIST OF FIGURES

Page

LIST OF TABLES

Page

1. INTRODUCTION AND LITERATURE REVIEW

1.1 Motivation

There is a worldwide need of nuclear energy due to the increase in the world's population and the desire to reduce greenhouse gasses from burning of fossil fuels. Therefore, the fission and fusion reactors are important to meet the need for clean sources of energy [1]. However, nuclear energy systems operate under high temperatures and stresses, chemically corrosive environments, and high neutron fluxes which can produce displacement damage levels up to 400 displacements per atom (dpa) for the next generation reactors. Thus, the operation of nuclear energy systems under above stated hostile conditions requires the development of high performance structural materials [2-5].

In the United States, 316L austenitic stainless steel was initially chosen to be used for fast reactor structural components. However, because of extensive volume expansion as a result of extreme void swelling under irradiation, research shifted towards ferritic and later ferritic/martensitic steels for high dose fast reactor applications [6]. Today, the research on the ferritic/martensitic (F/M) steels is focused mainly on the 9–12Cr steels. While 12Cr F/M steels show high corrosion and void swelling resistance, 9Cr steels are more resistant to irradiation hardening at 350 °C [6]. Even though F/M steels have better corrosion and void swelling resistance compared to austenitic steels, their creep resistance above 600 °C is quite poor [7]. Therefore, in order to improve high-temperature strength,

stability, and creep resistance together with irradiation resistance, nanostructured ferritic alloys (NFAs) having nanoscale Y-Ti-O particles have been developed [8-10].

In this study, the effect of the initial processing methods on the irradiation response of conventional F/M steels together with NFAs has been investigated. A literature review on radiation effects in materials, nuclear materials and their radiation resistance as well as ferritic steel production methods is provided in the first chapter. The second chapter provides information about materials and experimental procedures. Results and discussion on the irradiation response of ferritic steels after various processing methods are given followed by experimental methods. In the last chapter, conclusive remarks are presented.

1.2 Radiation effects in materials

1.2.1 Radiation damage

Radiation damage occurs as a result of energy transfer from a projectile to a solid. First, an incident particle interacts with a lattice atom leading to a displacement of lattice atom from its original position if the transferred energy is higher than a critical value. The struck and displaced atom is credited as the primary knock-on atom (PKA) which can create additional knock-on atoms if its energy is high enough. Those secondary knock-on atoms are called recoils and generate a displacement cascade. When the energy of the atoms is not enough to create additional knock-on atoms, the damage event ends. The displacement cascade occurs in ~10^{-11} picoseconds and the displacement cascade created defects lead to mechanical and thermal property changes [11]. Fig. 1.1 summarizes the radiation damage in the materials.

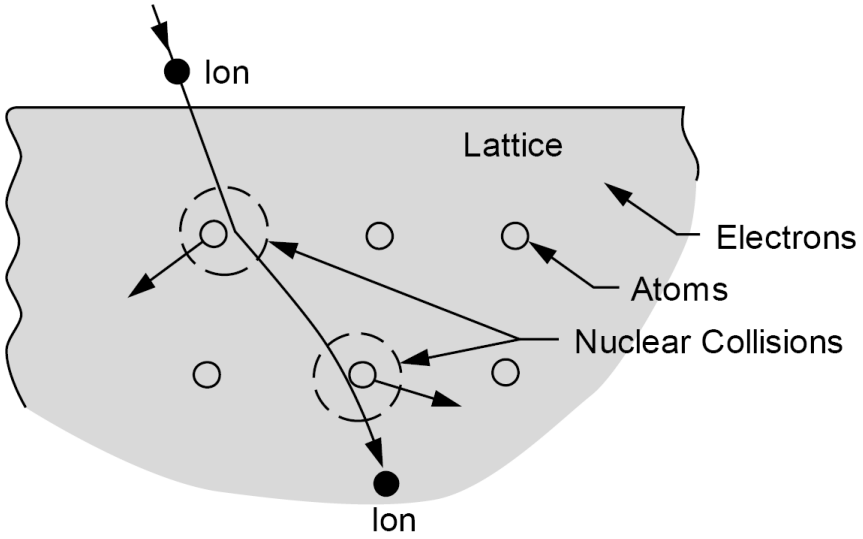

Figure 1.1 Schematic illustration of ion-mater interaction [12].

The damage created in the material can be quantified as in the following damage rate equation:

$$R_d = N\int_{\check{E}}^{\hat{E}} \phi(E_i)\sigma_D(\mathrm{E}_i)dE_i \tag{1.1}$$

where N, $\phi(E_i)$, $\sigma_D(\mathrm{E}_i)$ are denoted as the lattice atom density, particle flux and displacement cross section which is the displacement probability, respectively [13]. $\sigma_D(\mathrm{E}_i)$ can be given as:

$$\sigma_d(E_i) = \int_{\check{T}}^{\hat{T}} \sigma(E_i, T)\nu(T)dT \tag{1.2}$$

where $\sigma(E_i, T)$ is the probability of transmission of recoil energy T from incident particle having energy E_i to target lattice atom; $\nu(T)$ is the number of resultant displaced atoms

[13]. Energy transfer cross section can be determined based on the energy and type of the ion, however, it is quite complex. Assuming the collisions are purely ballistic and ignoring the Coulombic and electronic interactions, the energy transferred, *T*, can be defined as in the following equation:

$$T = \frac{4E \cdot m_1 \cdot m_2}{(m_1 + m_2)^2} \sin^2 \frac{\theta_c}{2} \tag{1.3}$$

where E is the incident particle's energy, m_1 and m_2 are mass of the incident and the target atom, respectively. θ_c is defined as the deflection angle of the target particle in the center of mass coordinate and it is given as:

$$\theta_c = \pi - 2\int_{r_{\min}}^{\infty} \frac{b \cdot dr}{r^2 \left[1 - \frac{V(r)}{E_C} - \frac{b^2}{r^2}\right]^{1/2}} \tag{1.4}$$

where b is the collision parameter, r_{min} is the closest distance between the two particles and $V(r)$ is the interatomic potential. E_c is the kinetic energy of the system in center of mass coordinate.

1.2.1.1 Primary knock-on atom (PKA) displacements and displacement energies

In order to calculate the average number of atom displacements in the target lattice during collisions, Kinchin and Pease developed a model [14]. The Kinchin-Pease model ignores the periodicity in the metals and assumes the hard sphere approximation where all the collisions are elastic. As mentioned in the previous section, it is assumed that the incident atom having energy E_i, transfers its energy T to the initial PKA. The displacement energy of the target, E_d, can be defined as the minimum energy to displace an atom from

its original lattice position. If $T > E_d$, the target atom is moved from its original lattice position and turns into a PKA; however, if $T < E_d$, it keeps its original position. If the transferred energy is between $E_d < T < 2E_d$, the collision process can move only one atom. At the energies lying between $2E_d < T < E_c$ (where E_c is the cut-off value of transferred energy above which no displacements take place), the average number of displacements becomes $T/(2E_d)$. Above the energies of E_c, there are no further displacements and the average number of displacement is defined as $E_c/(2E_d)$. Graphical representation of the average number of displacements with respect to the transferred energy is shown in Fig. 1.2 [13,14].

The number of displacements per atom (dpa) can be defined as in the following formula:

$$dpa(x) = 0.8\frac{F_d(x)}{N \cdot 2E_d}\Phi \tag{1.5}$$

where $F_d(x)$ is the energy distribution function, N is the number of displaced atom and Φ is the fluence.

In the periodic crystals as in metals, displacement energy is dependent on the crystallographic directions. In other words, displacement energy is strongly correlated with the number of barrier atoms, the distance to the nearest atoms and the distance of the struck atom in its original lattice point to the barrier atoms [13,15]. The displacement energy of the struck atom is minimum along the direction of high lattice symmetry. However, recoil direction which is determined by the collision kinetics is random. Thus, the displacement energy is the average along all directions [16,17].

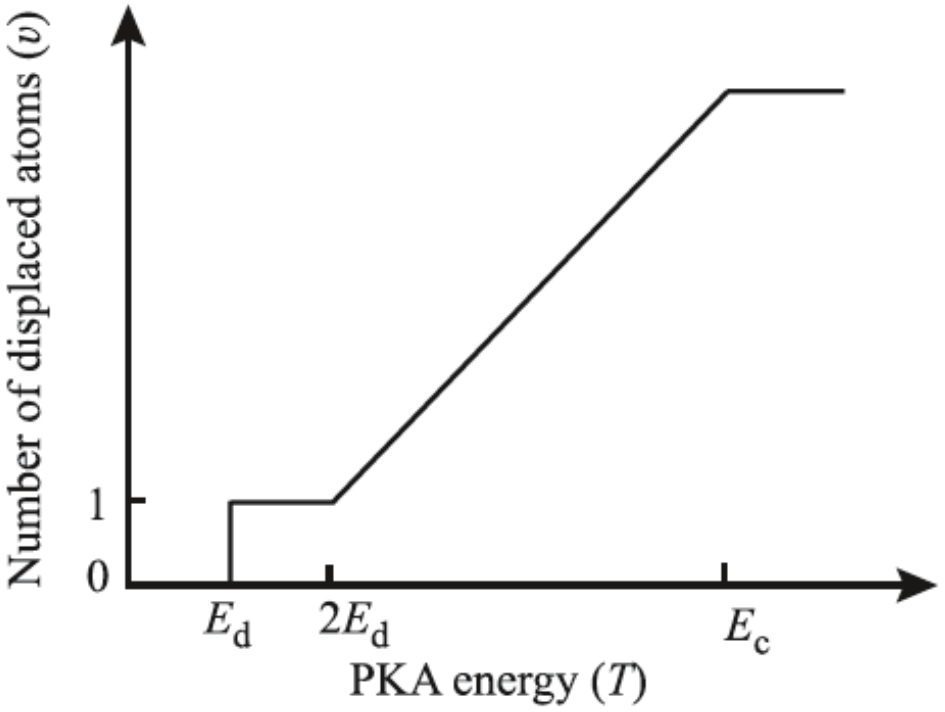

Figure 1.2 Graphical representation of Kinchin-Pease model [13].

1.2.2 Radiation effects on the microstructure and mechanical properties

Irradiation damage can introduce various defects. Table 1.1 shows the defect evolution at different irradiation temperatures. At low temperatures, mobility of atoms is limited, thus point defects can form small defect clusters. With the increase in the temperature, those defects evolve into planar vacancy loops and clusters. At the temperatures of $0.1T_m$-$0.3T_m$ (where T_m is the melting point of the alloy), interstitials are highly mobile while the mobility of vacancies is still limited. At this temperature range, interstitials can form clusters and loops, and vacancies can form small vacancy clusters. Further increase in temperature results in the annihilation of defects either by recombination within the grains or at the sinks. At this temperature range of $0.3T_m$-$0.5T_m$,

while interstitial atoms form interstitial dislocation loops, high vacancy concentration can lead to the formation of voids [18].

Table 1.1 Irradiation induced defect evolution at different temperatures [18].

Temperature (T/Tm)	Defect type
0-0.1	Generation of point defects (vacancies and interstitials)
0.1-0.3	Point defect clusters Vacancy loops, clusters and depleted zones Interstitial loops
0.3-0.5	Rafts (agglomerates of clusters and small loops) Voids

Fig. 1.3 summarizes the radiation damage in metals. Fig. 1.3a shows the displacement cascade event and the production of vacancies and self-interstitial atoms (SIAs). Fig. 1.3b through 1.3g show the annihilation of irradiation induced defects (either by recombination or at sinks), effect of irradiation on the diffusion and formation of radiation induced segregation (RIS) and radiation induced precipitation (RIP) together with void formation and irradiation induced creep [19].

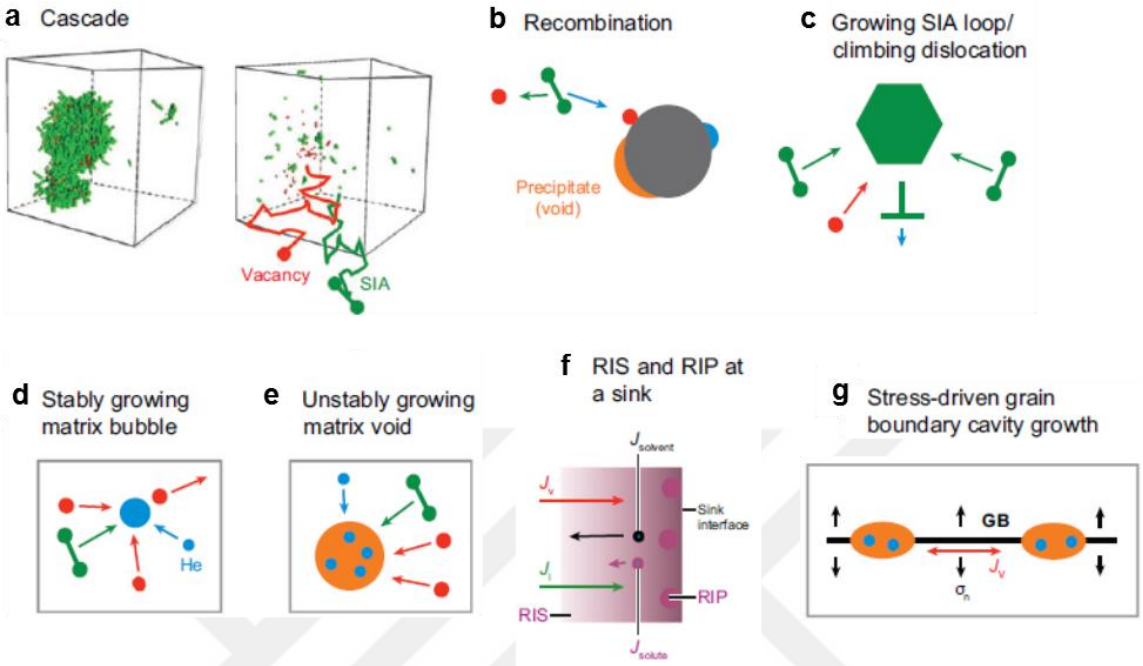

Figure 1.3 (a) Displacement cascade and generation of vacancies and self-interstitial atoms (SIAs) (b-e) Annihilation of defects either by recombination or at sinks (f) Radiation-induced segregation (RIS) and radiation-induced precipitation (RIP) at sinks. J_v: flux of vacancies, J_i: flux of SIAs, J_{solute}: flux of solutes and $J_{solvent}$: flux of solvents (g) Growth of the bubbles at the grain boundaries under stress-driven creep conditions [19].

1.2.2.1 Radiation induced segregation (RIS)

Irradiation at elevated temperatures results in redistribution of solutes by an imbalance of point defect migration to sinks such as dislocations, grain boundaries, voids, etc. This phenomenon is known as RIS [20]. RIS occurs at intermediate temperatures at which both vacancies and interstitials are generated and diffuse [18]. It has been reported that RIS occurs as a result of flux and size difference between the elements and binding energy difference between elements and point defects [18]. For engineering alloys, each alloying elements can diffuse through interactions with interstitials and vacancies, depending on atom size. An oversized atom prefers to interact with vacancies and an

undersized atom prefers to interact with interstitials. If one alloying element is dominated through interaction with interstitials, it will have the same flux direction as interstitials, hence resulting in sink enrichment. If one element prefers to interact with vacancies, it will have the opposite flux direction leading to depletion of the atom at the sink. Fig. 1.4 shows the flux direction of A and B atoms when they couple with interstitials and vacancies. Fig. 1.5 shows an example of RIS in austenitic stainless steels [22].

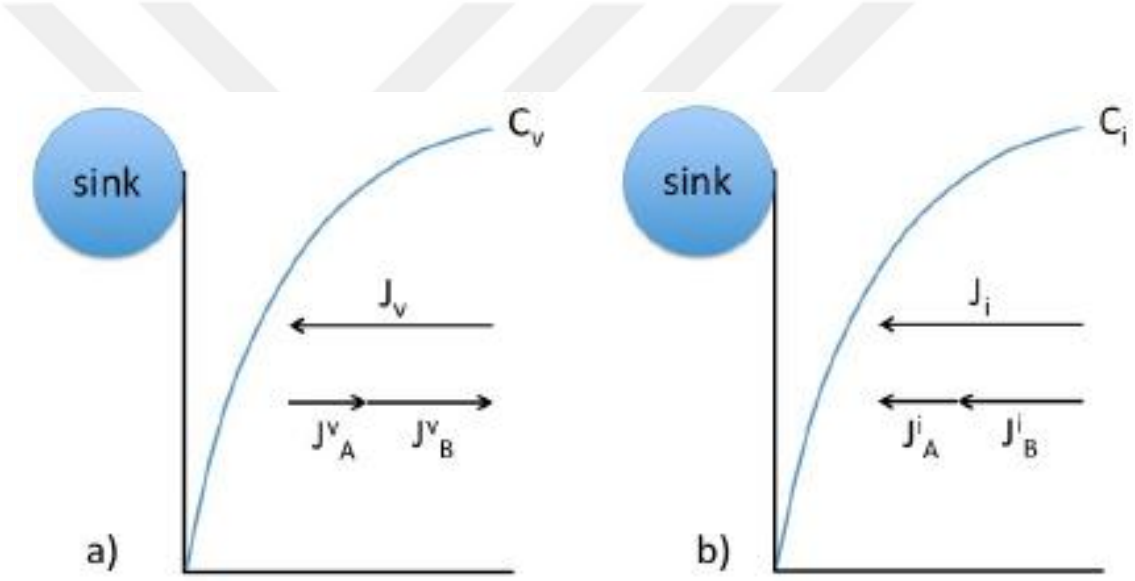

Figure 1.4 RIS by (a) vacancy mechanism and (b) interstitial mechanism. The length of the arrows represent the magnitude of the fluxes for A and B atoms [21].

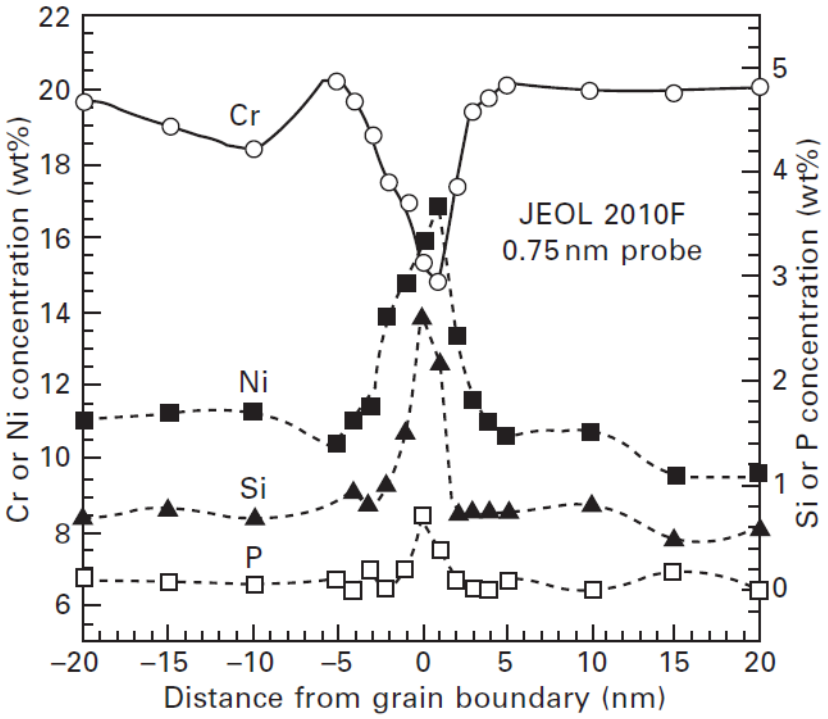

Figure 1.5 Radiation-induced segregation of Ni, Si, P; depletion of Cr at the grain boundary of a 300 series stainless steel neutron irradiated to several dpa at ~300 °C [22].

1.2.2.2 Radiation induced precipitation (RIP)

Radiation might cause chemical mixing leading to the dissolution of precipitates depending on the radiation conditions. On the other hand, point defects resulted from radiation damage can favour precipitation by reducing the resultant strain. Therefore, during an irradiation, there might be radiation induced, radiation enhanced and radiation modified phase formation. Radiation induced phases are the ones that do not form under equilibrium annealing condition but form only under irradiation. Ni_3Si (γ') and G-phase (Mn-Ni-Si) precipitation in stainless steels are two examples which have been reported to affect hardening of alloys as well as the swelling behaviour [18].

Radiation enhanced precipitates normally form under thermal annealing conditions; however, their formation is accelerated under irradiation. M_6C formation is an example of irradiation enhanced precipitation [18].

α' is a Cr-rich precipitate which forms as a result of spinodal decomposition by both irradiation enhanced and irradiation induced mechanisms [6,35]. Irradiation induced depletion of Cr atoms at the sinks as a result of RIS might result in local enrichment of Cr atoms which results in the formation of α' by irradiation induced mechanism. Moreover, excess point defect formation under irradiation results in increased diffusivity of Cr atoms which accelerates the α' formation by irradiation enhanced mechanism [23].

1.2.2.3 Dislocation loops

Nucleation of dislocation loops occurs by clustering of point defects and net arrival of the defects determine the growth or shrinkage of the loops. Under cascade damage conditions, SIAs are emitted and transported in 1-D diffusional motion and the amount of freely migrating interstitials and vacancies is different. The reason of the bias is basically the energy release difference between absorbing an interstitial and a vacancy [24].

At the temperatures of 0.1Tm-0.3Tm, the microstructure is characterized by dislocation loops and point defect clusters. At relatively high temperatures (still within $0.1T_m$ -$0.3T_m$), the dislocation density has been reported to decrease slightly while their size increases [20]. Fig. 1.6 shows the dislocation size and density with increasing irradiation dose at 300 °C. The loop size and density reach saturation within a few dpa as the formation rate of loops becomes equal to the destruction rate.

At the temperatures below 300 °C in iron-based alloys, dislocation loops are replaced by a high density of black dots, Frank loops, stacking fault tetrahedra and dislocation networks. On the other hand, at the temperatures above 300 °C, the microstructure is characterized by a high density dislocation networks and dislocation loops [20].

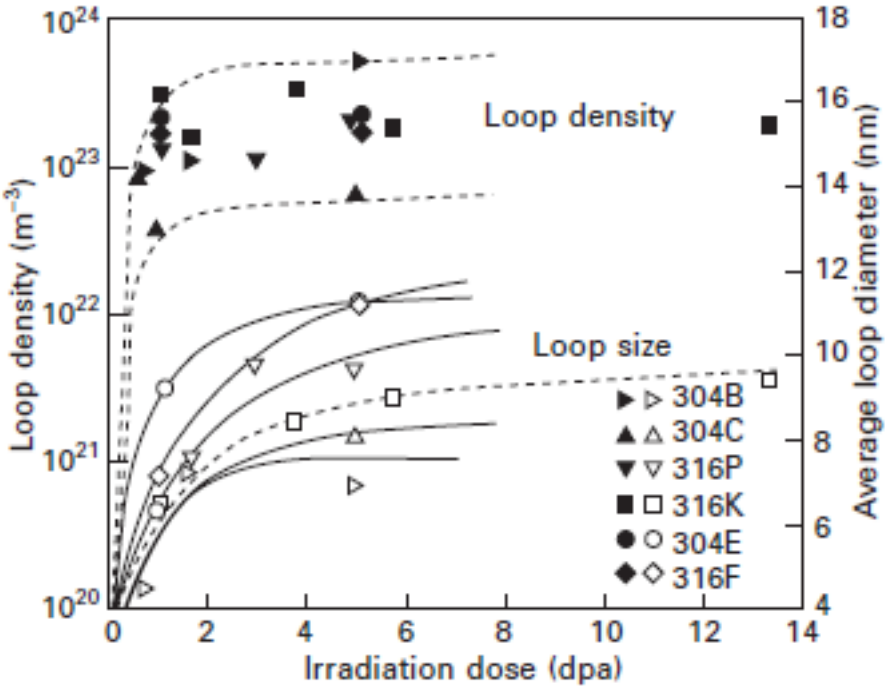

Figure 1.6 Dislocation loop size and density with increasing irradiation dose up to 13 dpa at 300 °C in various austenitic steels [25].

Fig. 1.7 shows the microstructure of a F/M steel (HT-9) neutron irradiated in FFTF at various temperature and damage levels. Microstructures consist of dislocation networks and loops. As mentioned above, dislocation loop size increases at higher temperatures [26].

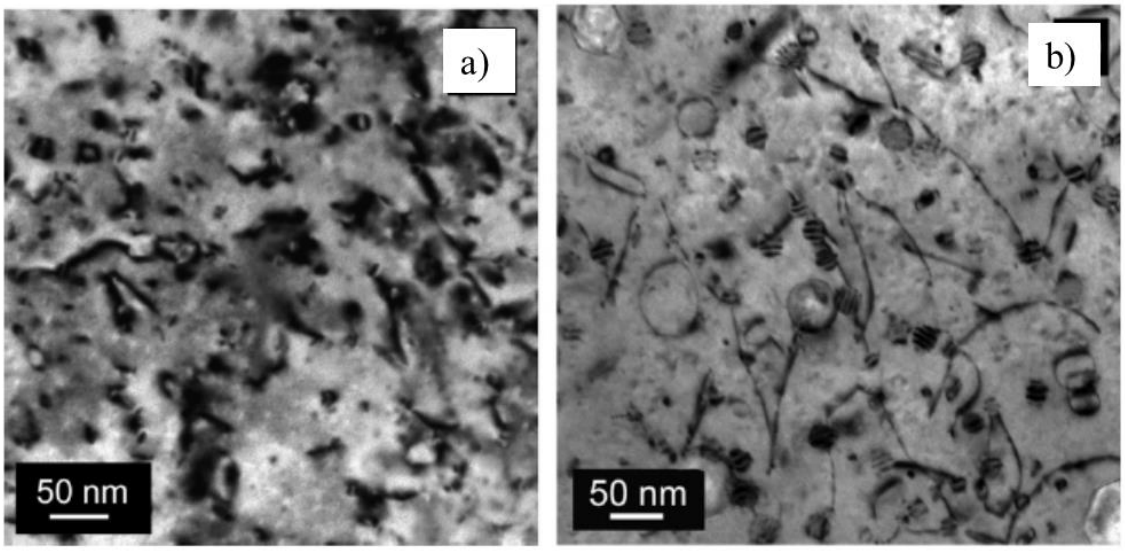

Figure 1.7 TEM image showing dislocation loops and networks in HT-9 neutron irradiated (a) at 28 dpa, 384 °C (along g=200) (b) at 443 °C and 155 dpa (along g=110) [26].

1.2.2.4 Void swelling

The formation of voids under irradiation results in a volumetric expansion which is also denoted as 'swelling'. Fig. 1.8 shows the formation of voids at 500 °C to a dose of 10 dpa and dimensional changes after irradiation at 533 °C in austenitic stainless steels [27,28].

Higher affinity of interstitials to dislocations results in excess vacancies leading to the void formation and swelling [18,29]. Swelling occurs in three stages. After the first stage of void nucleation, a transient swelling region appears where the swelling increases with increasing dose at an increasing rate. At the final stage, the steady state swelling regime, the swelling rate becomes constant [20].

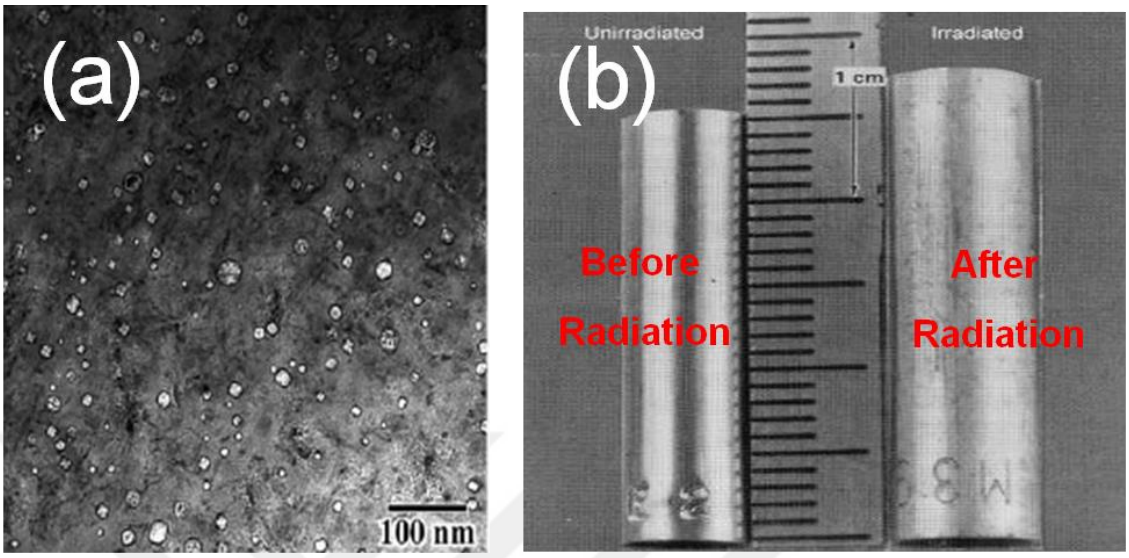

Figure 1.8 (a) Void formation in 304 austenitic stainless steel after neutron irradiation at 500 °C up to 10 dpa [27]. (b) Volume change in 316 stainless steel rods irradiated at 533 °C to a fluence of 1.5 $\times 10^{23}/m^2$ in the EBR-11 reactor [28].

Void formation kinetics are strongly correlated with alloy composition, dose, dose rate, temperature and helium from transmutation reactions. Swelling is maximized at an intermediate temperature (0.3Tm-0.5Tm) resulting in a bell-shape curve of volume percent increase vs. temperature. This bell-shape is caused by low vacancy mobility at low temperature (hence less vacancy clustering) and vacancy loss to defect sinks at high temperature. Fig. 1.9 shows the bell-shaped swelling distribution with respect to temperature in nickel after a neutron fluence of $5x10^{23}$ n/m^2 [20].

Swelling is sensitive to stress and dpa rate. A higher dpa rate results in a shift of the swelling peak to higher temperatures [20].

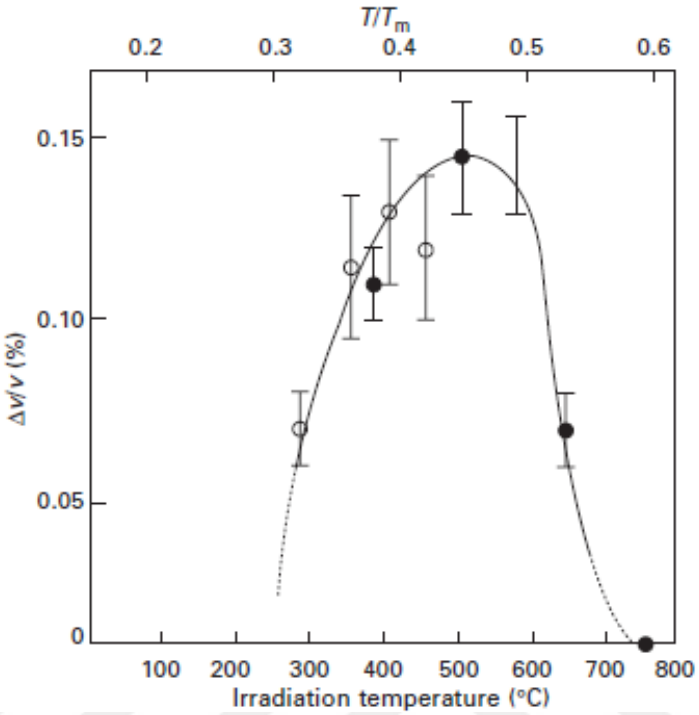

Figure 1.9 Swelling vs. irradiation temperature curve in nickel for a neutron fluence of $5x10^{23}$ n/m^2 [30].

1.2.2.5 Radiation hardening

For over 20 years, there have been extensive studies to investigate the hardness increase in metals as a result of irradiation. It is believed that irradiation induced hardening is resulted from defect production during irradiation. Those defects are defect clusters, impurity-defect cluster complexes, dislocation loops, dislocation networks, voids and bubbles, and precipitates [20].

The effect of irradiation hardening on body centered cubic (bcc) and face centered cubic (fcc) metals is different at different temperatures. Fig. 1.10 shows the behaviour of fcc and bcc metals under irradiation. At low temperatures (below 0.3Tm), radiation hardening results in an increase in yield strength and a decrease in ductility for both

austenitic and ferritic steels. At high irradiation temperatures (above 0.3Tm-0.5Tm), the yield strength of austenitic steels remains the same while ductility decreases as shown in Fig 1.10a. On the other hand, ferritic steels show small amount of hardening at those temperatures [17].

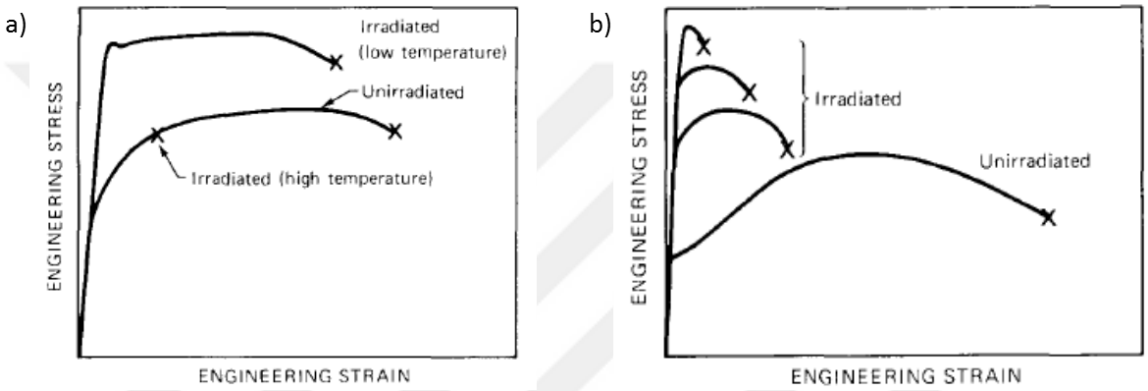

Figure 1.10 Effect of neutron irradiation on stress-strain curves of (a) fcc structure (austenitic steels) (b) bcc structure (ferritic steels) [17].

Radiation strengthening occurs in two ways [17]: (1) 'Source hardening' is a result of starting of dislocation motion; (2) 'Friction hardening' is a result of dislocation-irradiation induced defects interactions.

For radiation induced hardening studies, the dispersed barrier model has been widely used [31]. In this model, interactions between obstacles and dislocations are based on the geometrical considerations. The yield strength increase resulting from radiation can be represented as:

$$\Delta\sigma_y = \alpha M \mu b \sqrt{Nd} \qquad (1.7)$$

where α is a barrier strength coefficient of the defects to restrict dislocation motion; M is Taylor factor; μ is the shear modulus; b is the length of the Burgers vector; N and d are the density and size of the obstacles, respectively [32].

1.3 Radiation resistance of materials: Effect of phase content, initial dislocation density, grain size, orientation and precipitate stability

Next generation fast spectrum reactors require structural materials that can tolerate higher temperature and radiation damage compared to the currently used austenitic steels. Initially, in order to increase the swelling and creep resistance of austenitic steels, cold-worked austenitic stainless steels containing fine precipitates were developed [33-37]. However, it has been shown that even though these modifications increase the transient regime up to ~150 dpa, they swell considerably (at a rate of 1% per dpa) once they reach steady state swelling regime [38-40]. Therefore, irradiation induced swelling becomes a serious problem and it limits the burn-up of the fuel [41-43].

It has been discovered that the ferritic steels have higher swelling and creep resistance than the austenitic steels [44]. Thus, tempered martensitic steels with bcc structure were determined to be one of the best candidates for next generation reactors because of their high defect sinks of submicron size lath structure, smaller dislocation bias and higher self-diffusion coefficient in the bcc structure [45-47]. Their creep strength has been increased considerably by the addition of alloying elements such as N, C, B, Ti, Ta, V, Nb to form fine size MX precipitates [19]. Recently, nanostructured alloys having a uniform microstructure with 1-2 nm Y-Ti-O rich nanofeatures (NFs) have been developed

by Oak Ridge National Laboratory (ORNL) and University of California Santa Barbara (UCSB) [48]. They have a ferritic matrix with a bcc structure having the above stated advantages over the fcc matrix. Those very small NFs provide higher strength and better thermal stability to the NFAs. Moreover, they serve as sinks for point defects and He gas, and trap the He gas in extremely small bubbles during neutron irradiation, resulting in a reduction in void swelling [9,19,49-51].

Radiation damage resistance in metals is directly correlated with the microstructure. In terms of microstructure tailoring to reduce radiation damage, there is little one can change in the primary defect generation stage to reduce the defect number. On the other hand, the eventual fate of defects in the next stage can be manipulated by microstructural designs. One way is to increase the sink strength by providing high density stable dislocations to reduce the diffusion coefficient and number of the vacancies and interstitials. By this way, RED, RIS and defect pile up at the cavities, voids and dislocations can be reduced [19]. Fig. 1.11 shows that high dislocation densities result in a lower amount of defects due to higher sink densities. Furthermore, higher displacement rates produce a larger amount of defects as the defect production rate is higher than the loss rate to sinks [17].

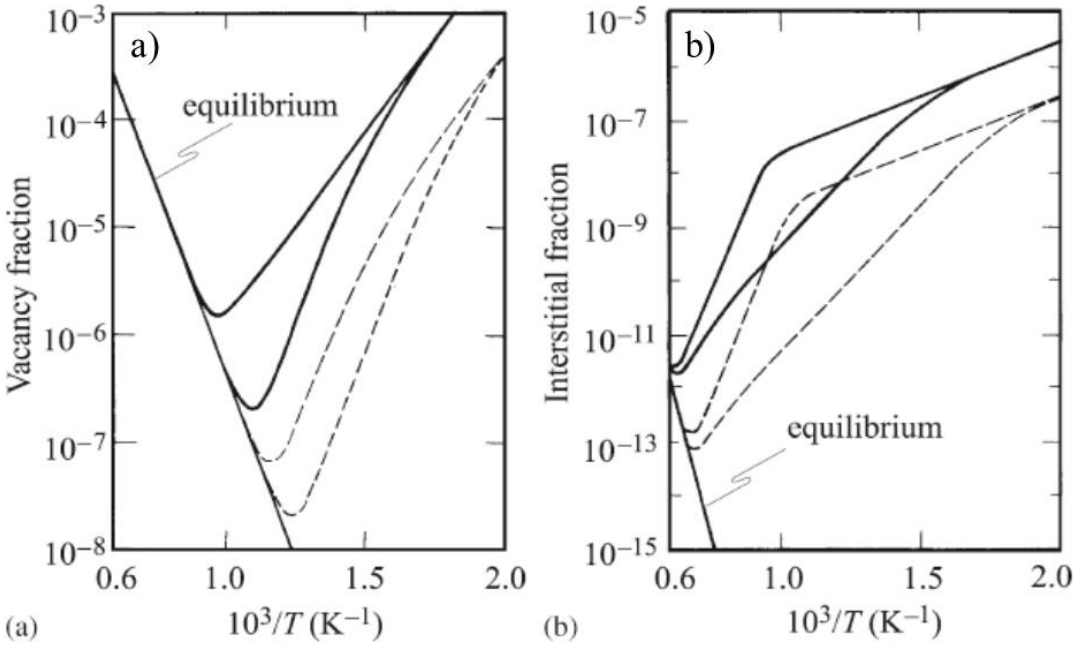

Figure 1.11 (a) vacancy and (b) interstitial concentrations in an irradiated metal as a function of temperature. Solid and dashed lines represent high and low defect production rates, respectively. Upper curves of the solid and dashed lines represent higher dislocation density [17].

High dislocation densities generally result in reduced swelling due to the sink imbalances [52-55]. Formation of small bubbles below a critical size is also beneficial for improving the void swelling resistance. High dislocation density results in the nucleation of small bubbles on dislocations [19]. In general, this results in a longer incubation period before void nucleation can occur resulting in less void swelling. Fig. 1.12 shows that a high dislocation density introduced by plastic strain decreases the swelling of austenitic stainless steels considerably [55].

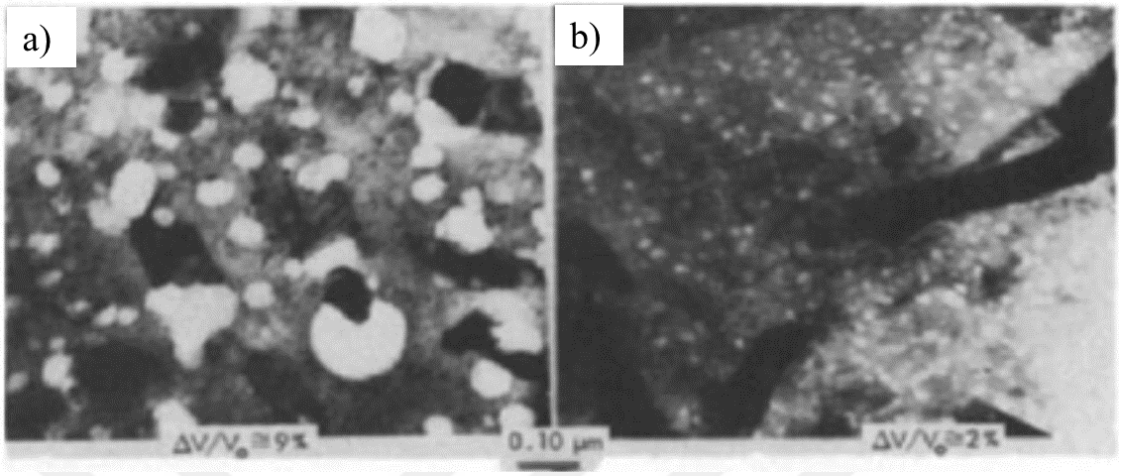

Figure 1.12 Micrographs illustrating the microstructures of (a) solution annealed austenitic stainless steel irradiated to 36 dpa at 520 °C and (b) 20% cold worked stainless steel irradiated to 54 dpa at 550 °C in HFIR [55].

A second way of microstructural tailoring to improve radiation resistance is to create large incoherent interface areas by grain size refinement. It has been shown that void swelling of the stainless steels is strongly related to the grain size [56-58]. Bai et al. studied the mechanism of grain boundary (GB) enhancement of radiation resistance in copper [59]. They found that grain boundaries have a “loading-unloading” effect in such a way that interstitials are loaded into the boundary during irradiation and then they are emitted by grain boundaries to annihilate vacancies within the grain, as shown in Fig. 1.13 [59]. Chen et al. studied the defect annihilation mechanisms at the grain boundaries of alpha-iron [60]. They reported that chain like defects consisting of alternately positioned interstitials and vacancies form and annihilate at the grain boundaries showing the high sink efficiency of the grain boundaries [60]. Moreover, Sun et al. observed the annihilation

of dislocation loops at the grain boundaries in nano-grained Ni by in-situ Kr ion irradiation [61].

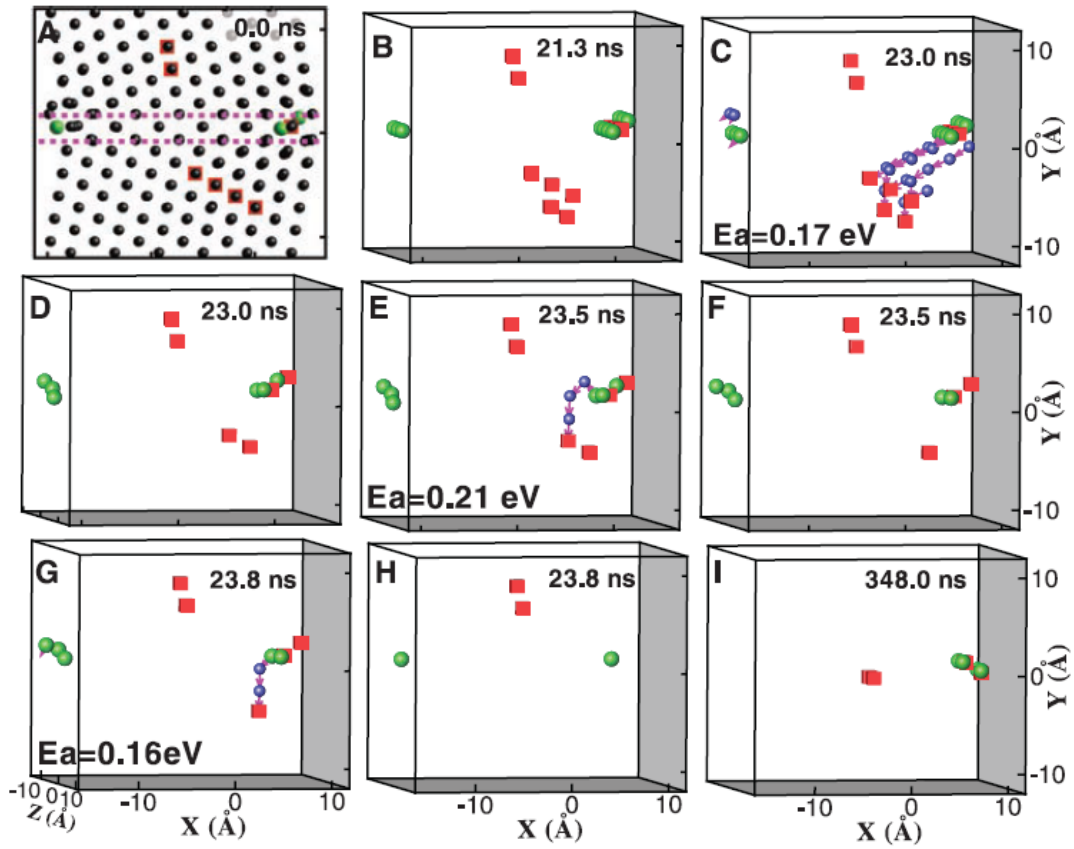

Figure 1.13 Temperature accelerated dynamics simulations of damage self-healing near the GB (within 10 Å of the GB). Smaller black spheres in A: nondefective atoms; larger green spheres: interstitials; red cubes: vacancies; smaller blue spheres: atoms that move more than 1 Å during an event; purple vectors: the moving directions and distances of moving atoms [59].

Geometrically, a grain boundary has a 3D structure consisting of a boundary plane and a misorientation between two adjacent crystals. Sink efficiency of GBs is directly related with the grain boundary plane i.e. local habit plane and surface curvature of the

plane as well as the misorientation angle. Even though high angle grain boundaries (HABs) provide a larger sink strength for defect annihilation due to their large free volume, it has been shown that the RIS and REP occur mostly at those boundaries [62]. Moreover, Sekio et al. reported that while random grain boundaries serve as annihilation sites for defects leading to the formation of void denuded zones, coincidence site lattice boundaries (CSLBs) have no effect on the void distribution [63]. Fig. 1.14 shows the void distribution near a high angle random boundary having high sink strength and a CSLB having low sink strength.

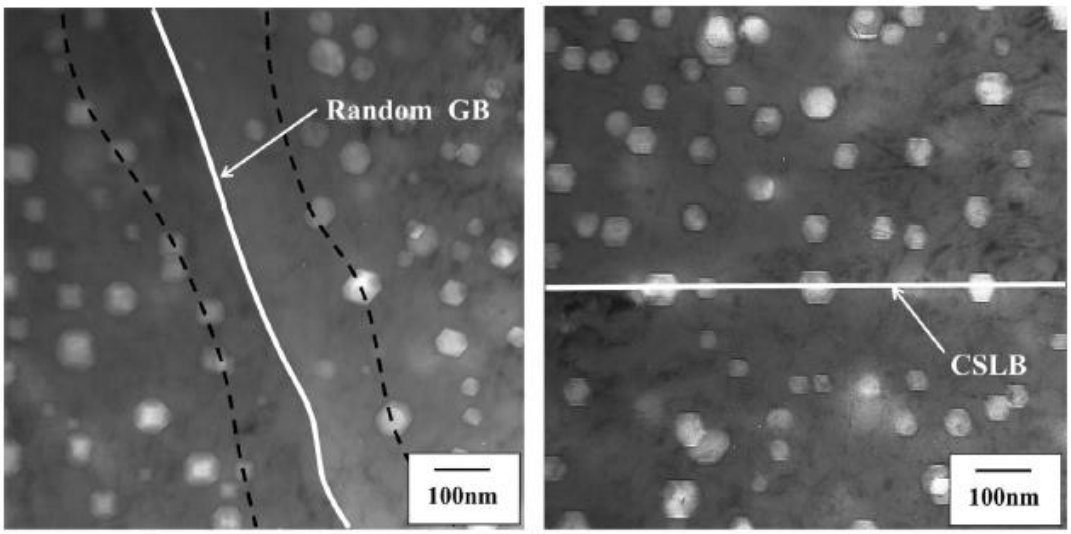

Figure 1.14 Void distributions in the Fe–15Cr–15Ni steel neutron-irradiated at 749 K to 18 dpa near the (a) random GB (b) CSLB. The black dashed lines represent the region of void denuded zone [63].

The third method of microstructural manipulation to enhance materials' radiation resistance is the introduction of dispersoids in the matrix. This can have two benefits. At

low temperatures (below 0.3 Tm) a fine distribution of dispersoids can serve as sinks for defects resulting in a reduced defect density and a reduction in hardening. At intermediate temperatures (0.3Tm-0.5Tm) a fine distribution of dispersoids can delay void nucleation by trapping helium and point defects, and reducing void swelling. Therefore, it is critical to have high density of precipitates homogenously distributed in the matrix. Fig. 1.15 shows the irradiation response of two types of alloys. One contains a large population oxide dispersoids (MA957) while the other does not (F82H). It is obvious that the oxide dispersion results in a considerable improvement in the swelling resistance [64].

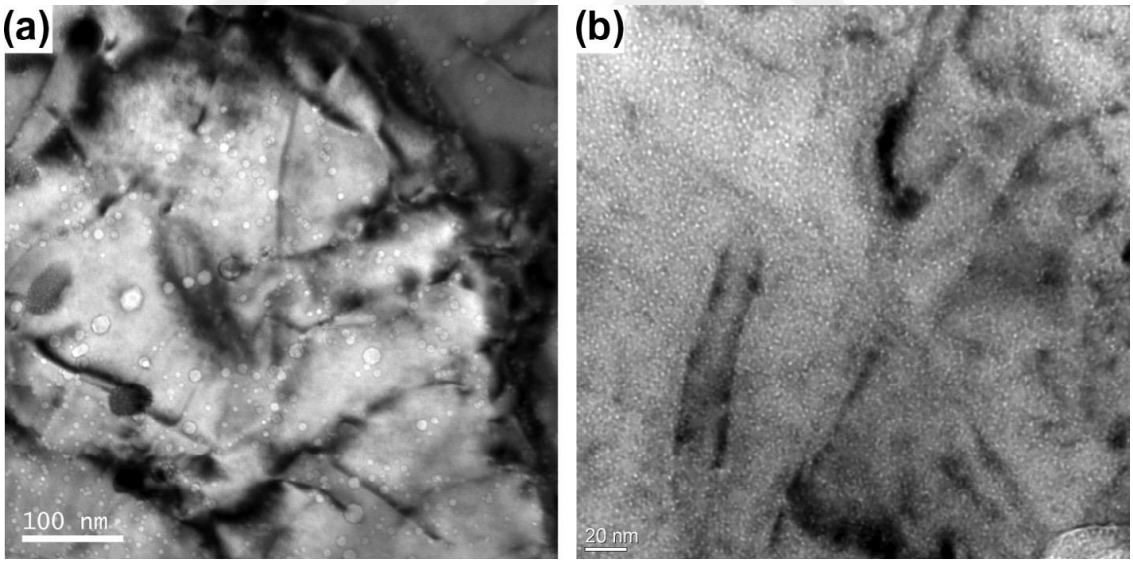

Figure 1.15 Under-focused bright field TEM images of the dual ion beam irradiated cavity structures in (a) F82H and (b) MA957 irradiated to 42 dpa and 2100 appm He at 500 °C (at 1000 nm from the surface) [64].

1.4 Materials for nuclear applications and radiation resistance of ferritic steels

Ferritic and F/M steels having the bcc structure have higher swelling resistance compared to fcc austenitic stainless steels as their dislocation bias, *B*, is lower, reducing their steady state swelling rate and increasing the incubation periods for void nucleation. The lower *B* in bcc metals is resulted from their defect relaxation volumes [65]. Together with their high swelling resistance, ferritic steels show low RED and RIS compared to fcc austenitic steels since their self-diffusion coefficient is higher [45].

Fig. 1.16 shows schematics explaining the irradiation damage resistance in NFAs versus 9Cr normalized and tempered martensitic steels (TMS). Fig.1.16a shows how the irradiation resistance of NFAs is a result of a high density of NFs and dislocations. NFs can trap the He gas into small bubbles. Further, they can pin the dislocations and grain boundaries resulting in the conservation of the high sink densities for defect annihilation, high strength and creep resistance. Moreover, high dislocation density keeps the He bubbles away from the grain boundaries leading to high creep resistance [19]. Fig. 16b indicates that coarser scale microstructures together with lower sink strengths result in lower irradiation damage resistance in TMS compared to NFAs [19]. Therefore, it leads to more swelling, a large number of dislocation loops, REP and a high amount of He accumulation at the grain boundaries in TMS [12]. When the concentration of He is ~1700 appm, TMS shows intergranular brittle fracture while NFA shows ductile fracture [66].

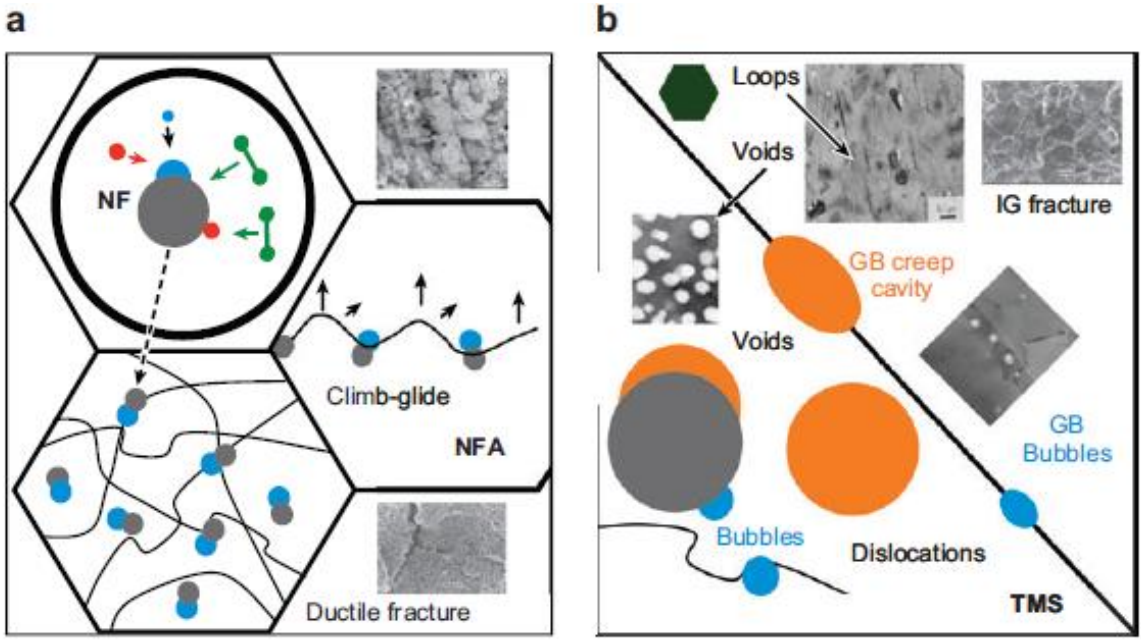

Figure 1.16 Schematic of irradiation effects in (a) nanostructured ferritic alloys (NFAs) (b) 9Cr normalized and tempered martensitic steels (TMSs) [19].

In conclusion, high precipitate, dislocation, grain boundary and bubble concentrations reduce RED, RIS, and vacancy flux as well as void swelling. Unfortunately, high temperature recovery processes make the conservation of the high dislocation density difficult. However, NFs hinder the recovery by pinning the dislocation motion. Therefore, a high density of dislocations and NFs supply the high radiation damage resistance in NFAs. This also provides higher creep strength at high temperature as the NFs are thermodynamically stable above 1000 °C even though there is a probability of recoil dissolution and amorphization under irradiation [67].

1.5 Production methods of ferritic steels

1.5.1 Production methods of precursor slab

The chemistry of structural materials for nuclear applications should be tightly controlled during their production. Therefore, either casting methods by vacuum induction melting (VIM) followed by vacuum arc refining (VAR) or powder metallurgy routes are used.

1.5.1.1 Casting by vacuum induction melting (VIM) and vacuum arc remelting (VAR)

VIM is a refining process that is used to reduce the impurity levels in the alloy steels. During remelting process, the elements that are difficult to dissolve should be added at the early stages when the stirring rates are high. On the other hand, alloying elements that are easy to oxidize or evaporate should be added later. The remelting process can be conducted with a controlled gas composition at pressures as low as 5 mmHg. Thus, oxygen, hydrogen, nitrogen and carbon content can be decreased to quite low levels. Moreover, the loss of volatile elements can be prevented by using an inert gas atmosphere instead of vacuum over the melt. By using VIM, it is possible to produce very clean steels. VIM can also be used as the first step for VAR for further refinement. VAR can be conducted using either a low pressure vacuum induction melter or a stream degasser [68]. The process can produce very clean steels with low hydrogen and oxygen contents with minimum inclusion and segregation [69].

1.5.1.2 Powder metallurgy methods: Mechanical alloying

High temperature alloys can be produced by mechanical alloying which is a powder metallurgical process for the introduction of stable refractory oxides. This method has been developed by the International Nickel Company using high-energy ball milling of dry powder mixtures of raw materials [70]. The mixture is consolidated by canning under vacuum followed by hot-isostatic pressing or extrusion. Further thermo-mechanical treatments such as annealing or hot rolling can be applied for microstructure tailoring [71]. ODS nickel and iron-based superalloys are produced by mechanical alloying method [72]. Fig. 1.17 shows the typical steps taken in ODS alloy production by mechanical alloying method.

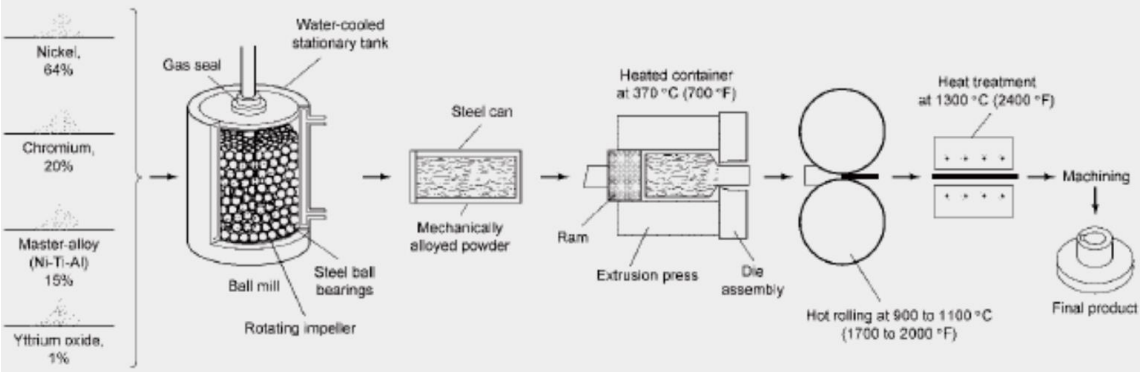

Figure 1.17 Typical mechanical alloying process for the production of ODS alloys [72].

1.5.2 Further processing methods

1.5.2.1 Tube production methods

1.5.2.1.1 Hydrostatic extrusion

Hydrostatic extrusion is a process where the billet is extruded through the action of a liquid pressure medium instead of direct application of the load through a ram. The advantages of hydrostatic extrusion are that (1) since the friction between billet and die is zero, the length of the billet is not a factor affecting the extrusion pressure; (2) since the pressure is hydrostatic in nature, buckling of the billets is also not a problem making the extrusion of skewed billets possible [73].

Many different materials have been hydrostatically extruded successfully [74-76]. Hydrostatic extrusion can be applied at the temperatures below the recrystallization temperature of the materials where it is not possible with conventional extrusion. Also, it creates a beneficial stress state resulting in materials with better strength and ductility [77-79].

1.5.2.1.2 Pilger processing

Pilger processing is one of the methods to produce seamless tubes using both hot and cold working methods. Hot pilgering is executed by steady forward and backward motion of cylindrical rotary mandrel. After each pass, the tube-mandrel assembly is turned 90°. To obtain final thin walled tubes, up to six passes can be applied. However, further thinning with well controlled dimensional accuracy requires cold pilgering. Cold pilgering

uses tapered grooved rolls which rotate forward and backward with 180°. In cold pilgering, the sample is fixed and rolls propagate while it is the reverse in hot pilgering [80].

Generally, cold pilgering is a well controlled process and used for the tubes having the wall thickness tolerances less than 10%. The final product can be used either directly or as an intermediate product before a final drawing process [80].

1.5.2.1.3 Spray forming

Spray forming is a process consisting of spraying of gas atomized powders on a substrate for the production of near-net shape parts [81-83]. By directly spraying of the powders, powder metallurgical steps can be eliminated. During spray forming process, high energy gas jets break apart the liquid metal melted in the atomization zone which results in metal flowing rates of 0.2-2.0 kg/s [82,83]. Modelling studies have shown that 0.5-0.8 fraction of the metal droplets can be solidified by high velocity gas flow during spraying in a few milliseconds [84]. The rest of the metal droplets solidify at a slower rates ~10 to 100 s or more [84,85]. The resulting deposit takes the shape of the billet and has very low porosity with fine microstructure. This preform can be used either as its sprayed form or as a substrate for further processing. Fig. 1.18 shows a typical spray forming principle and a preform in tubular shape.

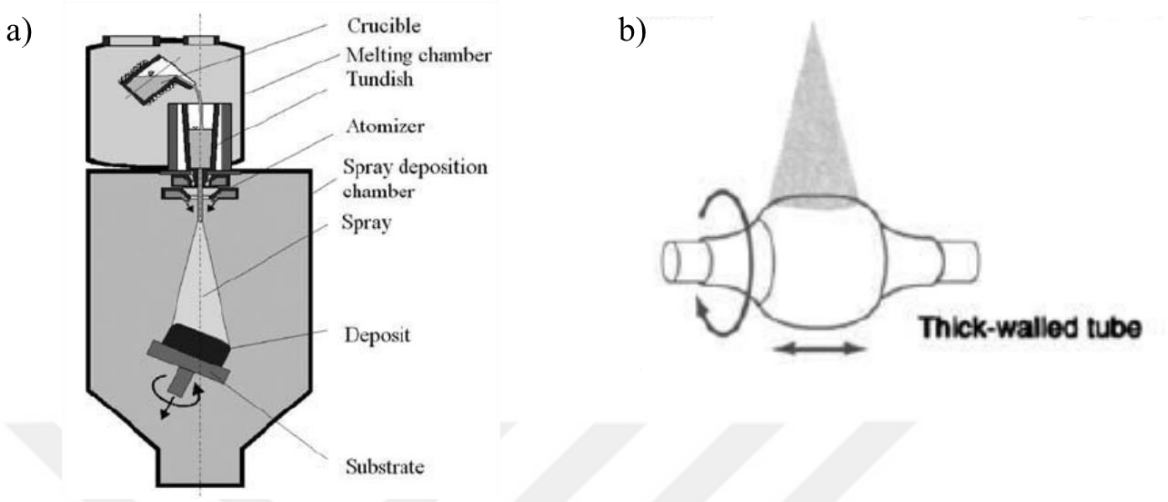

Figure 1.18 (a) A typical spray forming set up and principle [81] (b) tubular preform produced by spray forming [83].

Advantages of the spray forming include [83]:

- high densities >98%,
- fine grained microstructure with equiaxed grains,
- no prior particle boundaries,
- no macroscopic segregation,
- improved mechanical properties,
- flexibility in alloying components,
- high rate deposition and reduction in overall production time.

In spite of a large number of advantages, low overall yield and poor shape and composition control are the main limitations of this method [83].

1.5.2.2 Severe plastic deformation (SPD)

Previous studies have shown that nano-grained metals often exhibit improved swelling resistance due to defect sink properties of high density nano-grain boundaries [86]. For microstructure refinement, SPD which is the combination of shear deformation and pressure is one of the most promising methods. Cracking is prevented by the application of pressure allowing the application of large deformations. High pressure torsion (HPT) [87] and equal channel angular pressing (ECAP) [88] are the two most commonly used methods of SPD that have been utilized to produce nanostructured metals for a few decades.

HPT is the simplest method and it consists of the deformation of the sample between the two Bridgman anvils as shown in Fig. 1.19a. The upper anvil is fixed and the lower one is rotatable which provides various strains. The imposed shear strain at half-radius was estimated by $\gamma=2\pi rn/h$ (where r is the distance from a disk center, h is the thickness of the disk and n is the number of rotations). Fig. 1.19b explains the geometry of shear deformation in HPT process. By this method, large strains up to 15 GPa can be applied at low temperatures [89].

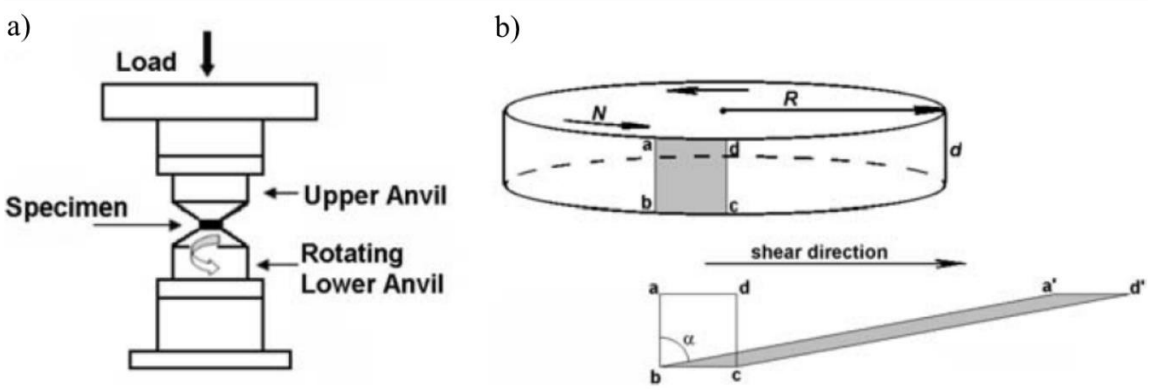

Figure 1.19 Schematic diagram of (a) HPT process; (b) shear geometry in HPT process [89].

1.5.2.3 High rate shock loading

Shock loading is a one-dimensional plane strain deformation similar to the uniaxial loading if the loading is enough and the sample is thin enough [90]. Shock loading of samples is applied either under laboratory conditions or under controlled firing-point conditions. These experiments can be conducted by high-exposure explosives, gun-launched impactors such as flyer or driver plates, exploding foils, or direct radiation impingement such as lasers and electron beams [91-93].

Shock loading creates defects, basically edge dislocations, and those defects move in the direction of shock wave propagation in the case of a planar shock wave. Moreover, the density of defects increases with the increase in the peak shock pressure. However, depending on the crystal structure and stacking fault energy of the materials, shock loading can create deformation twins and stacking faults above certain pressures or at lower temperatures. If the stacking fault energy is low, which is the case especially for fcc metals, dislocations dissociate into partial dislocations which makes the cross-slip of

dislocations more difficult. Fig. 1.20 shows the dislocation cell formation together with twin and stacking fault formation with increasing shock pressure in fcc metals. The stacking fault energy of nickel is 128 mJ/m^2 while it is 20 mJ/m^2 for 304 stainless steel [94]. Thus, their resultant microstructures as a result of shock loading is very different [95].

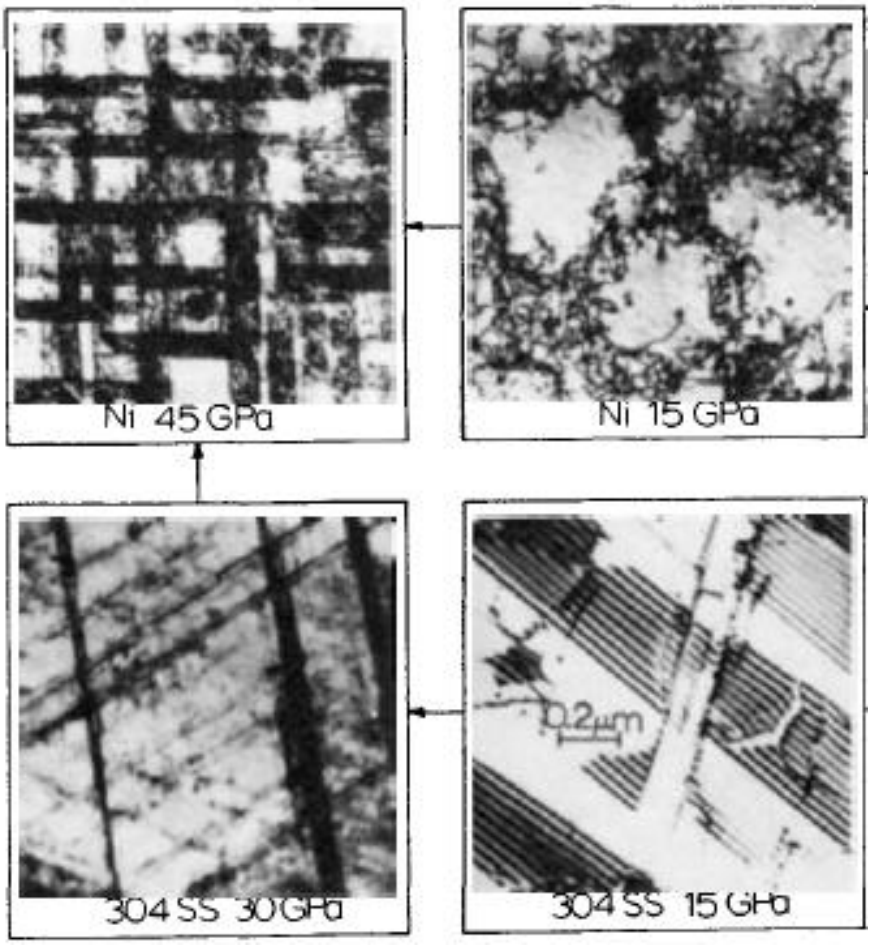

Figure 1.20 Micrographs showing the evolution of microstructure with increasing shock loading pressures in Nickel and 304 stainless steel [95].

2. EXPERIMENTAL METHODS

2.1 Specimen materials

Ferritic and F/M steels are two of the most promising materials as structural components for next generation fast spectrum reactors. In this study, three types of materials have been investigated after different heat treatment and processing conditions. The first material is an EK-181 alloy having both fine and coarse grain ferritic structure. The second material is an HT-9 alloy in the tempered martensitic condition. The third material is 14YWT which has a ferritic matrix with homogenously distributed small nano-oxide particles. Tables 2.1 to Table 2.3 show the compositions of EK-181, HT-9 and 14YWT alloys, respectively. Furthermore, Table 2.4 summarizes the methods used for processing the materials. The principles of the methods were explained in the previous chapter.

Table 2.1 Composition of supplied EK-181 samples (wt %).

C	Cr	Ni	Mo	Nb	W	V	Ta	B	Si	N	Mn	Zr
0.14	11.2	0.03	0.04	0.01	1.17	0.29	0.17	0.004	0.37	0.044	0.94	0.05

Table 2.2 Composition of the HT-9 samples (wt %).

C	Cr	Mo	Si	Mn	Ni	V	W
0.21	12.5	1.10	0.29	0.41	0.60	0.30	0.51

Table 2.3 Composition of the 14YWT samples (wt %).

Cr	W	Ti	Y
12.8	2.95	0.38	0.22

Table 2.4 Summary of the processing methods of the materials.

Material	EK-181	HT-9	14YWT
Deformation type	HPT deformation	High strain shock deformation	(1) HVOF spray forming + hydrostatic extrusion (2) Hot extrusion + hot rolling + hydrostatic extrusion

2.2 Heavy ion irradiations

In this study, iron ions were used to simulate radiation damage, due to their low experimental cost and it being the primary element in the alloys, a much shorter experimental duration and the ease of handling compared to neutron irradiations. To irradiate these materials, an ion source is used to produce incident ions which are accelerated through the acceleration column. The accelerator system includes at least two magnets to purify ion mass at the low energy end and to purify ion charge/energy at high energy end. The acceleration column consists of magnets to separate the ion species according to their charge to mass ratio and to guide them towards the target chamber by creating a magnetic field. The ion beam is focused to a well-defined shape using

electrostatic and magnetic lenses to produce a sufficiently large and uniform irradiation area. The whole system operates at high vacuum conditions to prevent ion energy loss and contamination of the energy spectrum of the ions [96].

Samples were irradiated at the Ions and Materials Facility at Texas A&M University using 3.5 MeV Fe^{2+} to different dose levels and temperatures. A SNICS source was used to produce Fe ions and ions were accelerated through the 1.7 MV Ionex Tandetron Accelerator. Fig. 2.1 shows the calculated dose and implanted Fe distributions in pure iron material for a peak dose of 100 dpa as a function of depth using Monte Carlo simulation code SRIM [97]. Due to the recent finding that the full damage cascade option in SRIM overestimates the damage creation by a factor of two, calculations were obtained using the recommended Kinchin-Pease option with displacement energy of 40 eV for consistency with the neutron damage code SPECTER [98,99]. For 3.5 MeV Fe ions, the peak projected ion range (Rp) is ~1.2 μm. The resultant dpa peak is located at a depth of ~1.0 μm.

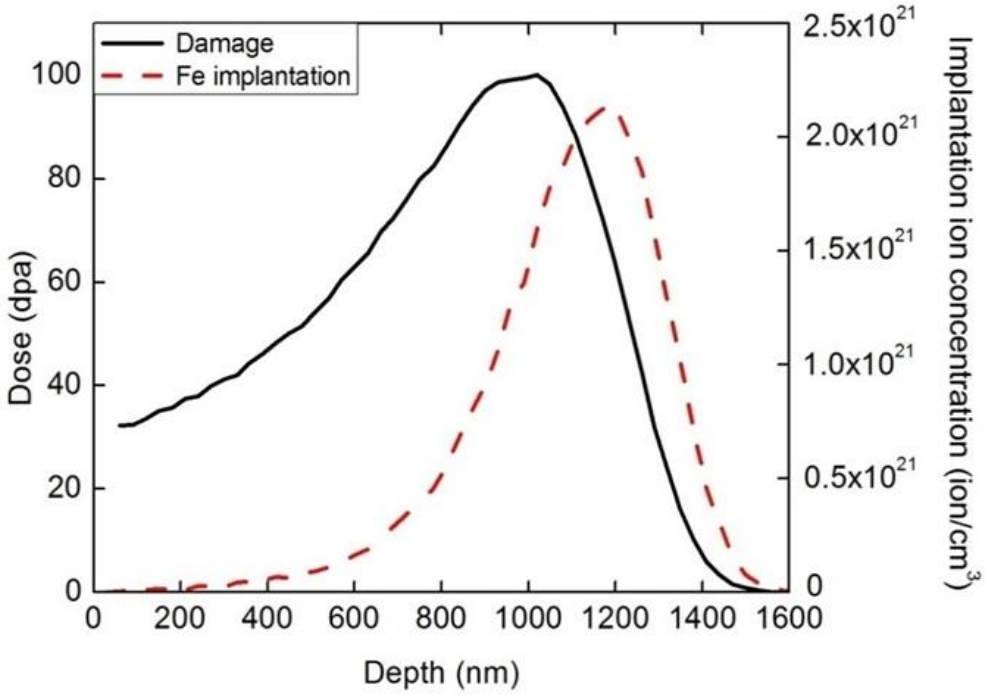

Figure 2.1 SRIM-calculated depth profiles of dpa and implanted atoms in pure Fe irradiated with 3.5 MeV Fe^{2+} ions for 100 peak dpa.

2.3 Microstructure characterization

2.3.1 Scanning electron microscopy (SEM)

SEM gives microstructural information by using a focused electron beam to scan the samples. Interaction of the electron beam with the materials results in the production of secondary electrons (SE), back-scattered electrons (BSE), and characteristic X-rays. SE come from a small layer on the surface, which can be used to study the topography of the samples. BSE are reflected from regions under the surface of the material. BSE provide compositional contrast since a higher atomic number of material gives brighter signals. The chemical composition of the sample can be determined from the excitation of inner

shell electrons that produce characteristic X-rays. In this research, SEM was used to obtain the chemical analysis by energy dispersive spectroscopy (EDS) as well as grain size, crystallography and grain orientation determinations by electron back scatter diffraction (EBSD) methods.

A FEI Inspect F FEG SEM having Schottky-based field-emission electron source was used for EDS and EBSD studies. EDS mapping analysis was conducted using EDAX Apollo 40 SDD detector at 30 keV electron energy. EBSD has been used as a useful technique to study the microstructure quantitatively, local texture as well as interface characteristics. However, as the technique requires 70° of sample tilting, diffraction data is very sensitive to the surface quality. Moreover, the resolution of EBSD is limited to mesoscale studies of grain sizes down to 60 nm [100,101]. It is employed by using TSL/EDAX EBSD equipment.

2.3.2 Neutron diffraction*

Neutrons are proven characterization tools especially for nuclear materials [102]. Bulk texture measurements probing the grain orientation distribution function over the complete volume of the NFA tubes were collected on the HIPPO instrument at the pulsed neutron spallation source at LANSCE [103]. HIPPO is a general purpose TOF

* Reprinted, in part, from "Effect of tube processing methods on the texture and grain boundary characteristics of 14YWT nanostructured ferritic alloys" by E. Aydogan, S. Pal, O. Anderoglu, S.A. Maloy, S.C. Vogel, et al., 2016, Materials Science and Engineering A, 661, 222-232, Copyright 2016 by Elsevier.

diffractometer described in detail by Wenk et al. [104]. Fig. 2.2 shows the schematic of HIPPO diffractometer.

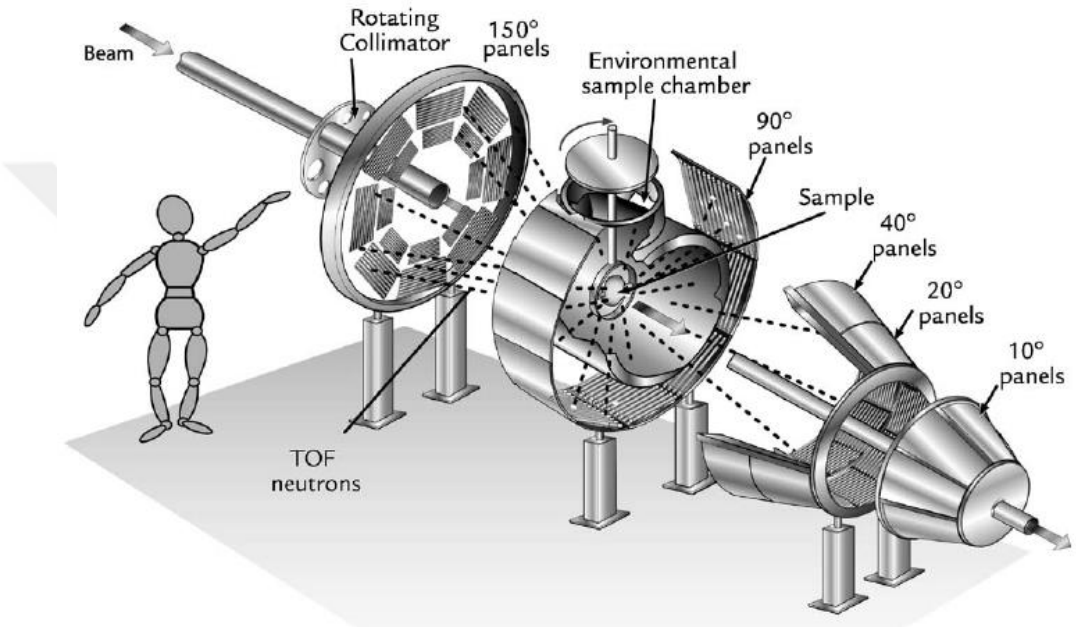

Figure 2.2 Schematic view of the HIPPO diffractometer showing the structure of the instrument and arrangement of detectors panels. A person is used for a scale. The distance between 10° and 150° panel is 3 m [104].

The samples are located ~9 m from the neutron moderator and diffracted neutrons are detected by 1240 ^{3}He tubes arranged on panels distributed over five conical rings with scattering angles ranging from 2θ=40° to 150°. A large sample chamber can accommodate an automatic sample changer, furnaces, cryo-equipment, a load frame, high pressure cells or a magnet. Samples are glued on standard HIPPO sample holders and loaded into the robotic samples changer [105]. They are rotated around the vertical axis (i.e. the tube axis) and data is collected at different angles per orientation.

2.3.3 X-ray diffraction (XRD)

XRD is a diffraction technique that is used to obtain phase and crystallographic information about the materials. Together with crystallographic information, it can be useful for texture and residual stress measurements.

High energy electron bombardment of a metal target results in the ionization of electrons from the K-shell of the target metal. This results in x-rays having Kα and Kβ energies. Thus, X-ray beam is collimated and monochromated by filtering before targeting the sample. Diffraction occurs when the Bragg's condition ($n\lambda=2d\sin\theta$, where λ is the wavelength of X-rays, d is interplanar spacing of the target material and θ is diffraction angle) is satisfied and constructive interference takes place. Since the X-rays are monochromatic (having single wavelength), different scanning angles reveal different d-spacing and diffraction planes.

Ideally, diffraction occurs at certain diffraction angles. However, in reality, there is peak broadening caused by the instrument together with the crystallite size and/or residual stresses which can be calculated by line profile analysis.

2.3.4 Transmission electron microscopy (TEM)

TEM was utilized to characterize the initial and post irradiation microstructures of the materials. It is a destructive method where a high energy electron beam transmitting through a thin specimen interacts with the atoms of the specimen and creates an image on the fluorescent screen or CCD camera [106]. A typical TEM incorporates an electron source and electron column in which there is a set of electromagnetic lenses. The electron

source emits electrons when high voltage is passed through and the potential difference between anode and cathode accelerates the electrons. Pre-focusing is applied in the source gun by Wehnelt cylinder and upper lenses and a set of apertures and electromagnetic lenses are used to generate well-focused, collimated and monochromatic electron beam. Fig. 2.3 shows a schematic of a TEM [107].

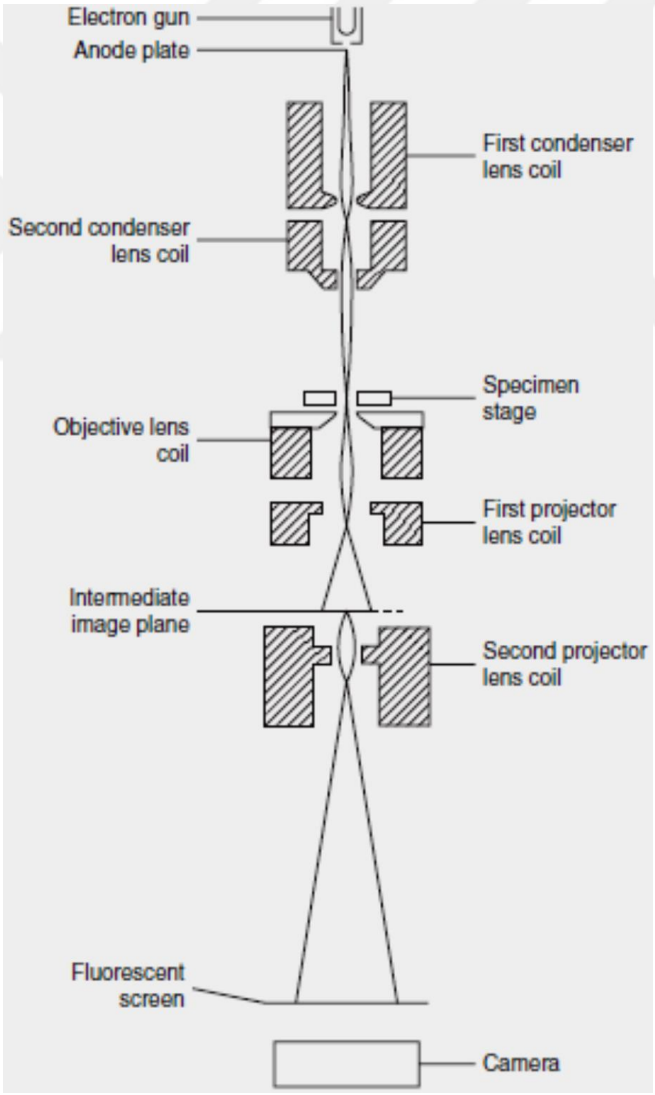

Figure 2.3 Schematic illustration of optics of transmission electron microscopy [107].

In this study, bright field (BF) TEM in two beam kinematical conditions, scanning TEM (STEM) and energy filtered TEM (EFTEM) are utilized. The techniques are explained briefly in the following section:

(1) BF TEM in two-beam dynamical imaging conditions: A two-beam dynamical imaging condition is ideal for investigation of dislocations. Diffraction contrast in crystalline materials result from coherent elastic scattering of electrons at certain Bragg angles. Under two-beam conditions, the sample is tilted in such a way that only one diffraction plane is excited.

(2) STEM imaging and composition analysis: When a focused beam is scanned across the sample, complementary information can be obtained by detecting the variety of scattering electrons. In order to construct high resolution, atomic number contrast (z-contrast) images, transmitted electrons scattered at high angles are collected. Moreover, by collecting the generated x-rays, high spatial resolution maps can be obtained.

(3) EFTEM composition and thickness maps: EFTEM is a technique which is used to form images by the electrons having specific kinetic energies. High energy images can be obtained by using zero-loss beam in which there is no inelastically scattered electrons. Moreover, elemental distribution maps can be generated by using those inelastically scattered electrons having well-defined energy loss. Thickness maps can be produced by acquiring zero-loss and unfiltered images using the $t/\lambda=-ln(I_0/I_t)$ where t is the thickness, λ is the average inelastic scattering mean free path length, I_t is unfiltered intensity and I_0 is zero-loss (filtered) intensity. λ is defined as;

$$\lambda = \frac{106F(E_0 / E_M)}{\ln(2\beta E_0 / E_M)} \quad (2.1)$$

where F is a relativistic correction factor; β is the collection semi-angle (mrad); E_0 is the electron beam accelerating voltage (keV); E_M is the average energy loss (eV) which can be denoted as $E_M = 7.6Z^{0.36}$ where Z is atomic number [106].

TEM studies were conducted on both FEI Tecnai F30 Analytical TEM/STEM operating at 300 kV at Los Alamos National Laboratory and FEI Tecnai F20 ST operating at 200 kV at Texas A&M University. Some of the high resolution TEM (HRTEM) studies were performed on JEOL 2100F TEM operating at 200kV at Oak Ridge National Laboratory. The resolution of the microscopes are better than 0.2 nm.

2.3.5 Atom probe tomography (APT)

APT is a destructive 3D technique that can resolve the atom types and positions in a sharp needle having the diameter <100 nm. Specimens are prepared either by electropolishing or focused ion beam (FIB) to obtain sharp needles. Atoms are extracted either by applying high voltage to exceed the field barrier in voltage pulse mode or by applying laser pulses to decrease field barrier as a result of temperature increase in laser pulse mode. By applying either high voltage pulse or laser pulse, a high electric field is created on sharp tip and atoms are evaporated and accelerated towards the imaging detector. The chemical composition is determined by pulsing the evaporation and measuring the time-of-flight to find the mass-to-charge ratio. The position of the atoms on

the tip can be detected from the position where atoms hit to the detectors and the depth information is obtained by the sequence of evaporation [108].

Even though laser pulsing has the advantage of long tip life by preventing the early tip cracking, voltage pulsing is mostly used for steels. It has been shown that laser pulsing creates nonuniform evaporation because of low heat diffusivity of steels [109].

In this study, NFs in 14YWT NFAs were analyzed using the APT method. The APT measurements were conducted using a Cameca Local Electrode Atom Probe (LEAP) 3000xHR in voltage pulsing mode.

2.4 Mechanical property testing by hardness tests

Microhardness testing is employed to determine the hardness of the materials before irradiation using Vickers indenter which uses a diamond indenter having square based pyramidal shape. In this test, force is applied to the polished sample surface and held in contact for 10-15 seconds. Hardness Vickers (HV) is calculated using the following formula after measuring and averaging the two diagonals.

$$HV = \frac{2000P\sin(\alpha/2)}{d^2} \tag{2.2}$$

where P is the load α is the face angle which is 136° and d is the average diagonal length [110]. In this study, Struers DuraScan-70 hardness tester with 1 kg load was used for microhardness measurements.

Nanohardness testing was performed to study the irradiation-induced hardening. The indentation hardness, H_{IT}, is determined by the maximum applied force, F_{max}, and cross-sectional area, A_c, of the contact between the indenter and the sample [111]:

$$H_{IT} = F_{\max} / A_c \tag{2.3}$$

To calculate the indentation cross-section, first the load-displacement curve shown in Fig. 2.4 should be fitted. The intercept depth, h_i, and maximum depth, h_{max}, at maximum load is acquired to calculate the contact depth, h_c, as $h_c=h_{max}-\varepsilon(h_{max}-h_i)$. ε is the correction factor of tip shape which is 0.75 for Berkovich indenter [112]. Therefore, indentation cross-section for Berkovich tip is calculated using the formula of $A_c=23.96\times h_c^2$ and indentation hardness can be found by inserting the values to equation 2.3.

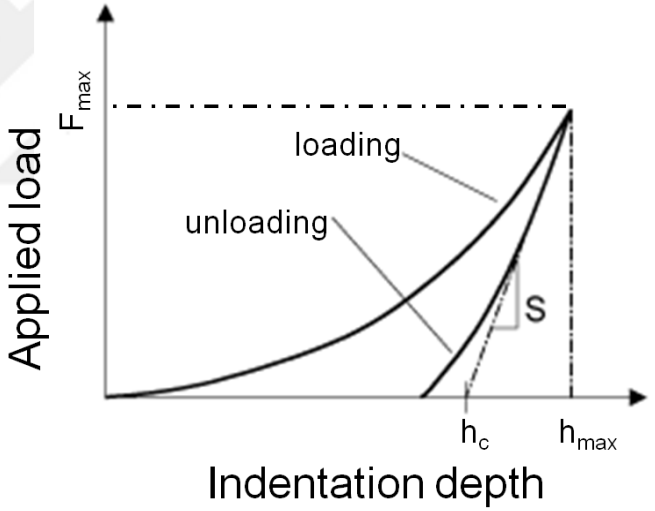

Figure 2.4 Schematic of a typical loading-unloading curve during indentation [113].

In this study, nanoindentation hardness measurements were performed on the irradiated samples using a MTS Nano Indenter XP™ using Berkovich tip.

3. EFFECTS OF HIGH DOSE IRRADIATION ON MICROSTRUCTURE DEVELOPMENT IN EK-181

3.1 Overview

EK-181 is a low-activation ferritic/martensitic steel that is an attractive candidate for in-core component materials for both fast reactors and fusion reactors. To assess the effect of structural engineering on radiation responses, two variants of EK-181 were studied: one in an annealed condition and the other subject to severe plastic deformation. These specimens were irradiated with 3.5 MeV Fe self-ions up to 400 peak dpa at temperatures ranging from 400 °C to 500 °C. The deformation did not suppress swelling over the whole irradiated region. Instead, deformed samples showed higher swelling in the near surface region. Void swelling was found to be correlated with grain boundary instability. Significant grain growth occurred when steady-state void growth stages started. It was believed that stable void nuclei and growing grain boundaries act as biased trapping centers for vacancies and interstitials, respectively.

3.2 Introduction

In-core structural materials for next-generation nuclear reactors require good radiation resistance to embrittlement and void swelling, but also require a rapid reduction of neutron induced activity to meet low-activation goals [44,114-116]. Among various high-chromium reduced activation F/M alloys [114,117,118], the Russian alloy EK-181, often designated as "Rusfer", has been intensively studied as one promising candidate for

in-core components for both fast reactors and fusion reactors [119]. Its popularity arises from the potentially lower swelling, low activation, and high strength, especially at higher irradiation temperatures [119,120]. The alloy is normally used in quenched and tempered conditions, yielding a dual phase tempered F/M structure [119,121]. Furthermore, extensive research efforts have been and continue to be made to improve this alloy and its variants through the optimization of heat treatments and surface modification to produce better corrosion resistance and mechanical properties [114,119,121-127].

Previous studies have shown that nano-grained metals often exhibit improved swelling resistance due to defect sink properties of the high density of nano-grain boundaries [86]. Void swelling studies on nano-grained EK-181 have not yet been performed and are critical to evaluating the impact of this processing technique for further increasing its radiation tolerance. Severe plastic deformation (SPD) techniques which allow nano-structuring of a wide range of bulk metallic materials appear to be promising tools for producing high strength and radiation-resistant materials.

Early studies on the ion irradiation of alloys treated by SPD suggest that they often develop significantly enhanced radiation tolerance [128-131]. ECAP, one SPD technique, has been used to introduce ultrafine grains in both austenitic and F/M alloys [132,133]. Studies on austenitic Fe-14Cr-16Ni and F/M T91 have shown that ECAP can improve swelling resistance due to increased defect sink densities arising from very high interface-to-volume ratios introduced by SPD [134-136]. In addition to increases in grain boundary densities, large shear stresses involved in the ECAP process result in fragmentation and redistribution of second phase particles [137,138]. Several studies have shown that ion

irradiation results in compositional and size changes of nanostructured precipitates occurring together with grain boundary segregation [129,139]. The overall structural stability of SPD-introduced features depends strongly on material composition and fabrication. The first neutron irradiation experiments on ECAPed low carbon steel [140,141] and ECAPed 321 stainless austenitic steel [142] demonstrated the potential to produce more radiation-tolerant materials for fission reactor environments. Since the EK-181 alloy has a substantial and growing database for both unirradiated and neutron-irradiated conditions, it is ideal to use high dose self-ion irradiation as a surrogate to neutron irradiation for accelerated screening of different processing techniques. Comparison of the microstructural evolution of ion irradiated specimens with neutron irradiation data can validate behaviours observed in ion irradiated specimens and further refines ion irradiation testing. The present study is part of a larger effort where EK-181 is being irradiated in an annealed ferritic condition, an F/M condition, and in several severely plastically deformed conditions. In this report we focus only on two conditions, namely annealed ferritic EK-181 and one severely deformed variant starting from the annealed condition.

3.3 Experimental procedure

In order to study the effect of nano-structuring on the irradiation response, EK-181 was produced in two variants. The first variant was hot rolled and annealed at 800 °C for 1 hour, slowly cooled in a furnace down to 600 °C, and then air cooled. This variant is

referred as the "annealed" condition in the following discussion. The annealed samples were received in the form of 10 mm diameter rods.

The second variant was produced starting from the annealed condition. The samples were subjected to HPT, a method of severe plastic deformation that introduces extremely high strain into processed materials [143]. This variant is referred as 'severely deformed' condition in the present study. HPT was performed with an applied pressure of 6 GPa at 400 °C, and at 0.5 rotations per minute. In this study, 10 rotations of the die-set were performed. As a result, nano-structured specimens of EK-181 steel were produced in the form of disks, 10 mm in diameter and 0.9 mm in thickness. The imposed shear strain at half-radius was estimated by $\gamma=2\pi rn/h$ (where r is the distance from a disk center, h is the thickness of the disk and n is the number of rotations), leading to $\gamma\approx175$.

EK-181 samples of both variants were cut into thin disks of ~1 mm thickness. The specimen thickness was further reduced down to about 600 μm by applying mechanical polishing starting from SiC paper grit of 800 up to 4000. The mechanically polished samples were then chemically polished in a solution of sulfuric acid (50%) and phosphoric acid at 20 °C with an applied voltage of 5 V for 20-30 seconds to remove surface damage introduced by mechanical polishing.

Samples were irradiated by using 3.5 MeV Fe^{2+} to 100 peak dpa at 400, 425, 450, 475 and 500 °C, to determine the temperature range of swelling under these ion irradiation conditions. In another set of experiments, samples were irradiated at the peak swelling temperature of 475 °C to higher doses of 200, 300 and 400 peak dpa. Damage range was calculated using Kinchin-Peace option of SRIM with displacement energy of 40 eV.

The vacuum during ion irradiations was better than 1×10^{-6} Torr. A 6mm×6mm defocused ion beam was used, rather than a rastering or beam-sweeping mode, due to the fact that rastering suppresses void swelling [16,144]. Swelling suppression by rastering has been experimentally demonstrated in two recent studies [145,146]. The dose uniformity within a 6mm×6mm irradiated region is tested by Fe ion irradiation on a monocrystalline Si sample, following by channeling Rutherford backscattering spectrometry analysis by using a 2 MeV He analysis beam of 1mm beam spot size. The Fe irradiation induced damage on different testing spots varies within about 5%.

The beam current was controlled to be ~200 nA to minimize localized beam heating, with the temperature rise estimated to be at most 5 °C. The sample temperature was monitored by using a thermocouple mounted on the side of the face that the specimens were mounted on. The temperature reading provided feedback to the power supply controlling the heating filament within the hot stage positioned beneath the target holder. The temperature fluctuation recorded during the irradiation was less than ±5 °C. The displacement rate at the peak displacement depth was 1.7×10^{-3} dpa per second.

The original microstructure was characterized in Russia using a Zeiss EVO 50 XVP SEM, followed by additional transmission electron microscopy at Texas A&M University using an FEI Tecnai F20 ST TEM operating at 200 kV. STEM and BF TEM imaging at an under-focus condition of ~500 nm were used for the swelling studies. Grain size measurements were performed by using BF imaging as well. The specimens for cross-sectional TEM were prepared by using a FIB lift-out technique. Prior to FIB cutting, a thin Pt layer was deposited on the sample surface to protect the features beneath the surface.

The FIB specimen thickness was determined by using electron energy loss spectroscopy for each specimen. Typical thicknesses ranged from 50 nm to 100 nm.

The present study focuses on the swelling resistance and grain stability during irradiation of the two EK-181 variants. Therefore, a comparison was always made for the irradiated region ≤Rp and the region far beyond Rp, in order to differentiate irradiation and thermal annealing effects on grain growth.

3.4 Results and discussion

Fig. 3.1a and Fig. 3.1b compare the SEM surface imaging of annealed EK-181 and severely deformed EK-181, respectively, prior to ion irradiation. The grain sizes of the annealed sample ranged from ~1 to 10 μm. Furthermore, carbides, shown by arrows, were found to form along grain boundaries. For the severely deformed sample, grains were observed to be homogenous and equiaxed. This suggests that there was no large strain gradient across the deformed samples. Grain size measurements, for the severely deformed samples, is challenging for SEM due to its resolution limit. TEM characterization, averaged over more than 100 grains, showed that the grain size is reduced to ~135 nm after HPT deformation.

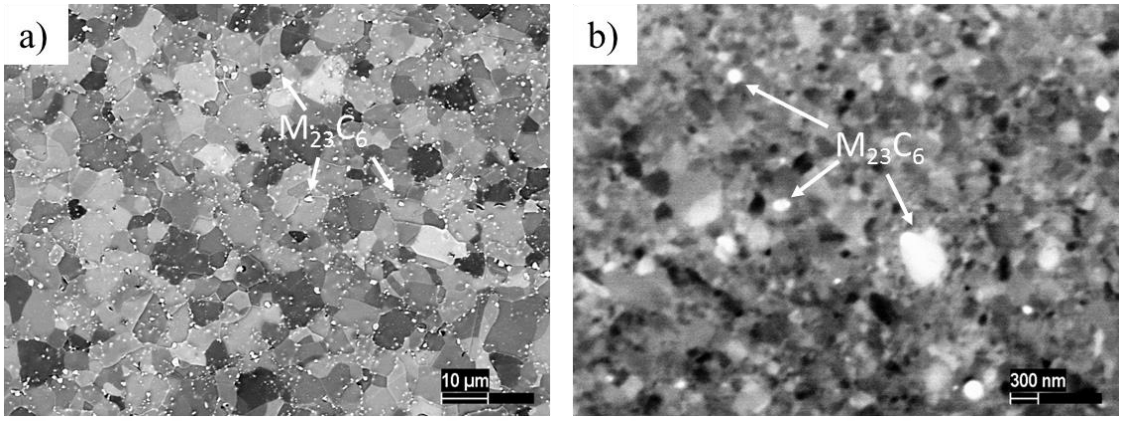

Figure 3.1 SEM images of (a) annealed EK-181 (b) HPT processed, severely deformed EK-181, showing the non-homogenous distribution of carbides along the grain boundaries on both variants. Typical $M_{23}C_6$ type carbides in bright contrast along the grain boundaries are shown by arrows. Note difference in scale of the two micrographs.

Figure 3.1 SEM images of (a) annealed EK-181 (b) HPT processed, severely deformed EK-181, showing the non-homogenous distribution of carbides along the grain boundaries on both variants. Typical $M_{23}C_6$ type carbides in bright contrast along the grain boundaries are shown by arrows. Note difference in scale of the two micrographs.

3.4.1 Swelling

3.4.1.1 Temperature dependent swelling

Fig. 3.2a and Fig. 3.2b show typical TEM micrographs obtained from the annealed and severely deformed samples, respectively, after irradiation to 100 peak dpa at 400, 425, 450, 475 and 500 °C. With increasing temperature, the void size increased and the void density decreased. In all samples, voids formed only within a shallow region near the front portion of the ion range, less than 300 nm from the surface. No voids were observed

at deeper regions, similar to the behavior observed in earlier studies in pure iron arising from the spatial difference in interstitial and vacancy concentrations, and excess interstitial concentration close to the projected range of implanted Fe [147]. Comparison between the temperature dependence of swelling of the annealed and severely deformed samples shows that severely deformed samples exhibited higher swelling than annealed samples. Furthermore, maximum swelling occurred at 475 °C for both conditions, a temperature that is in agreement with results of earlier studies on similar alloys [44,148,149]. Due to this reason, our studies on swelling dependence on dpa selected 475 °C as the irradiation temperature.

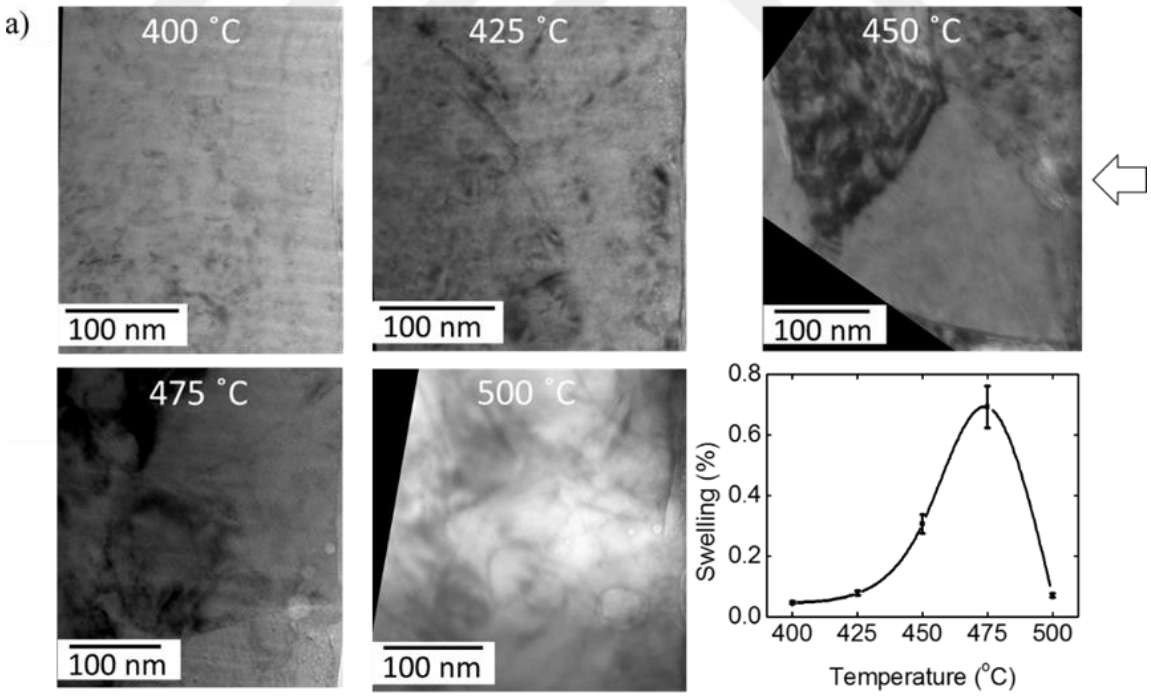

Figure 3.2 TEM micrographs of (a) annealed EK-181 samples and (b) severely deformed EK-181 samples, irradiated to 100 peak dpa at 400 °C, 425 °C, 450 °C, 475 °C, 500 °C, and their corresponding summary plot of swelling as a function of dpa values. Arrows refer to the beam bombardment direction.

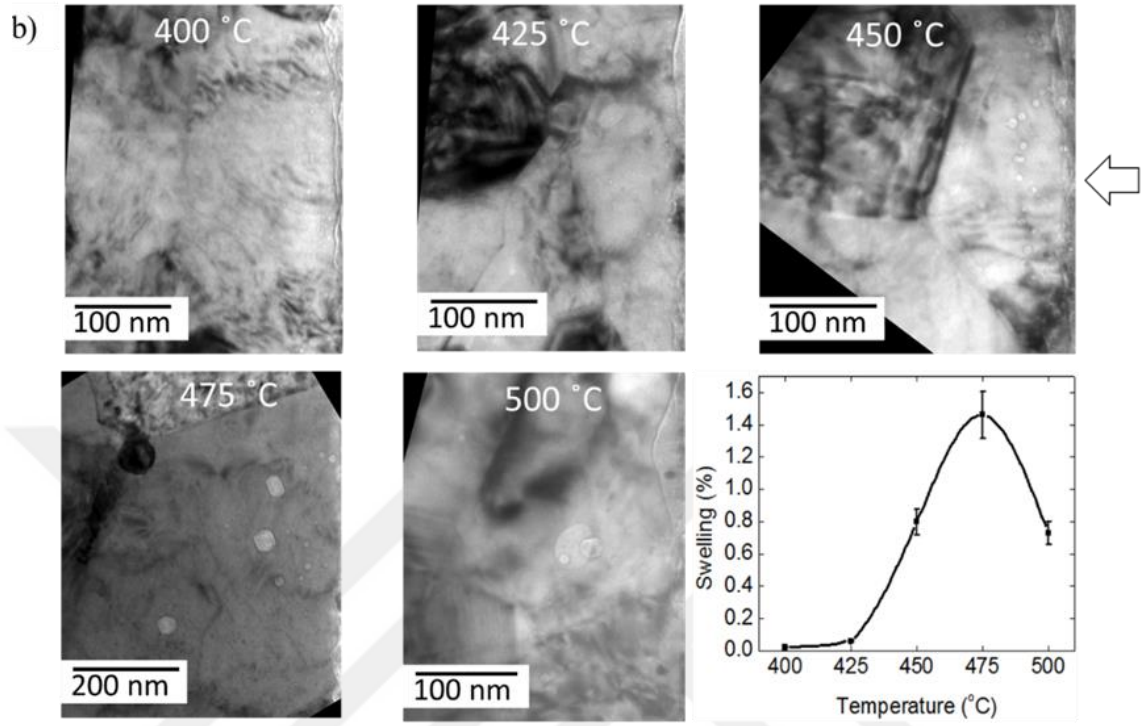

Figure 3.2 Continued.

3.4.1.2 Dose dependent swelling

Fig. 3.3a to Fig. 3.3d show TEM micrographs of void distributions in annealed EK-181 samples irradiated at 475 °C to 100, 200, 300 and 400 peak dpa, respectively. Both void density and size increased with increasing dpa. For the sample at 100 peak dpa, the mean void size was determined to be ~7 nm, and increased to ~85 nm in the 400 peak dpa sample. Fig. 3.3e shows the depth-dependent swelling curves for the four dpa levels, superimposed on the SRIM-calculated dpa and injected Fe ion profiles. With increasing dpa, void swelling pushed into deeper regions and the swelling profile began to more closely resemble the dpa curve. However, the defect imbalance effect strongly suppressed void swelling throughout much of the ion-deposited range. This suppression is a well-

known phenomenon where void nucleation is strongly suppressed by orders of magnitude, and the post-transient swelling rate is often suppressed by a factor of 3 to 5 [150].

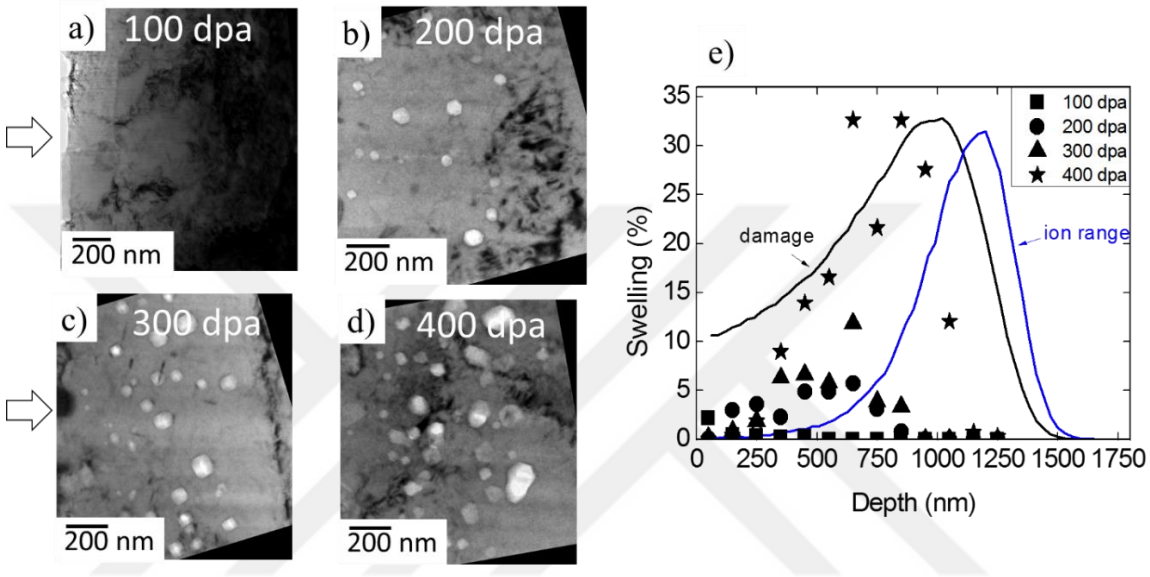

Figure 3.3 TEM images of annealed EK-181 samples irradiated to (a) 100 peak dpa, (b) 200 peak dpa, (c) 300 peak dpa, and (d) 400 peak dpa at 475 °C; and (e) swelling vs. depth profiles. Arrows refer to the beam bombardment direction.

Void characteristics measured over a depth range of 400 to 700 nm are shown in Fig. 3.4. This depth interval is ideal to minimize both the injected interstitial and surface sink effects. With increasing dpa, voids grew and began to approach saturation to a size of ~70 nm.

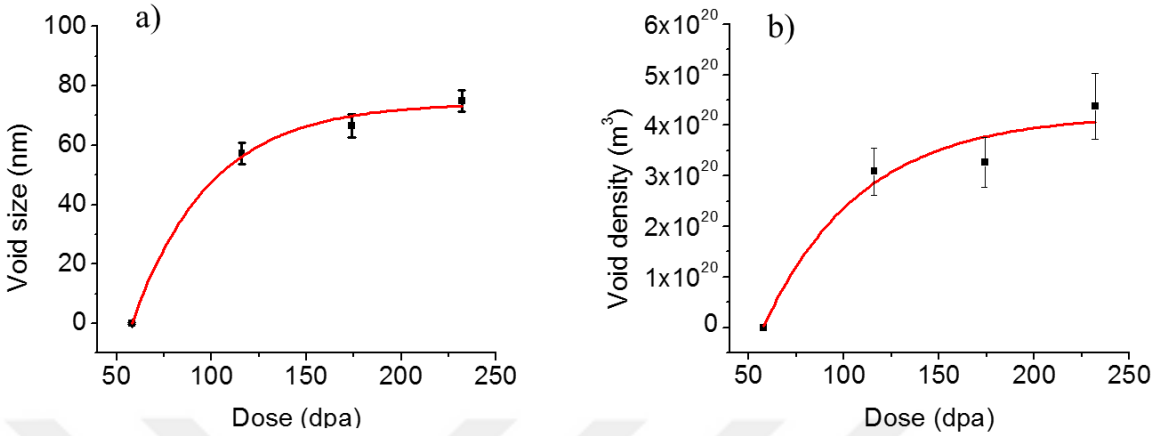

Figure 3.4 Plots of (a) void size and (b) void density as a function of local dpa for annealed EK-181. Measurements were performed at the depth region between 400 to 700 nm.

Fig. 3.5a to Fig. 3.5d show typical micrographs of void distributions in severely deformed EK-181 samples irradiated at 475 °C to 100, 200, 300 and 400 peak dpa, respectively. Fig. 3.5e shows the depth dependent swelling curves for different dpa levels. Similar to the annealed samples, defect imbalance effects are still dominant even for the highest dpa and voids are suppressed in most of the injected ion range. Compared to the annealed specimens, however, void distributions in the deformed samples peak closer to the front surface with the maximum swelling in the region of 100 nm to 400 nm depth for all peak dpa levels.

Fig. 3.6a and Fig. 3.6b show the void size and density changes as a function of dpa at the depth range of 400 nm to 700 nm. The void size increased with dpa and appeared to saturate at ~21 nm while the void density remained almost constant. In contrast with the annealed samples, the observed voids are smaller but present at higher concentration in the deformed samples.

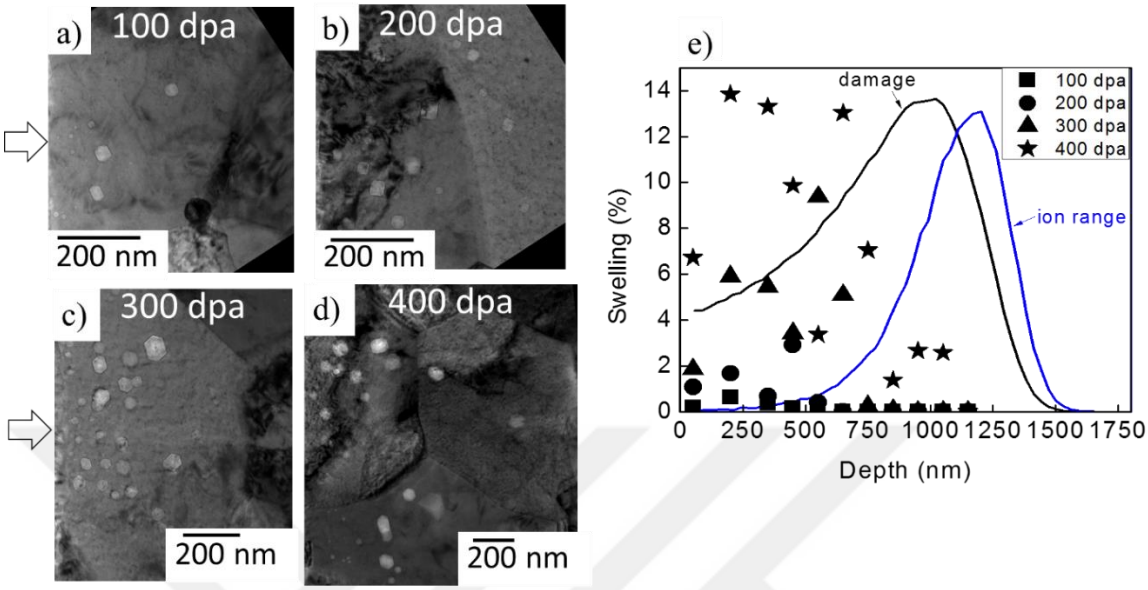

Figure 3.5 TEM micrographs of severely deformed EK-181 after irradiation to (a) 100 peak dpa, (b) 200 peak dpa, (c) 300 peak dpa, and (d) 400 peak dpa at 475 °C, and (e) corresponding depth profiles of swelling. Arrows refer to the beam bombardment direction.

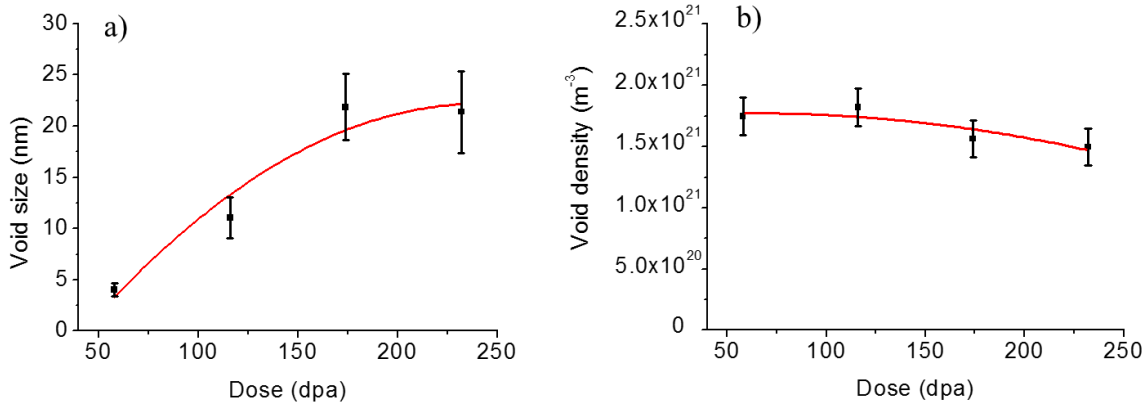

Figure 3.6 Plots of (a) void size and (b) void density as a function of local dpa for severely deformed EK-181. Measurements were performed at a depth region between 400 to 700 nm.

3.4.1.3 Swelling comparison

If deformation or grain engineering increases swelling resistance, it is expected that swelling should be lower within the irradiated regions. However, it is difficult to conclude from the present study on whether severe deformation reduces swelling in a systematic and obvious manner. The complexity comes from the observation that, while swelling peaked at about half of Fe projected range for the annealed sample, the maximum swelling depth shifted to a much shallower depth region for the deformed samples. At this shallow region (100 to 400 nm), deformed samples swelled more than annealed sample. However, if the comparison is made at the half of Fe projected range, the annealed sample swelled more than the deformed samples. In order to alleviate this issue, we compare the swelling as a function of local dpa for the two sets of samples, with more focus on the swelling incubation period difference, rather than the absolute swelling value. As to be discussed, the study suggests that the near surface region of the deformed samples have the shortest swelling incubation periods.

Due to the combined influence of the gradients in dpa and injected interstitials, the resultant depth distribution of swelling can be challenging to analyze. It is not surprising that the results might be sensitive to the depth range chosen for void counting. When searching for void characteristics, we chose reasonably wide depth intervals.

To demonstrate the sensitivity of void swelling to both local dpa and local depth, Fig. 3.7a and Fig. 3.7b plot the swelling curves at different depth regions for annealed and severely deformed samples, respectively. For the annealed samples, their void swelling incubation periods varied at different depths. The deeper the depth, the longer the

incubation periods, due to a strong injected interstitial effect which influences the most when the depth approaches the peak dpa location. An early paper by Garner and Guthrie assessed the possible impact of such "internal gradients" in dpa rate on the resultant swelling vs. depth profile [151]. Of most importance, they showed that higher dpa rates frequently extended the transient regime of swelling in neutron irradiations of austenitic steels [7,34]. It was also shown in the previous studies that ion-induced swelling of simple model austenitic alloys exhibited an incubation period that increased with increasing dpa rate [152]. Variation of incubation periods in the severely deformed samples are much less since swelling occurs in a relatively narrower and shallower region with less dpa rate effect and weaker injected interstitial effect.

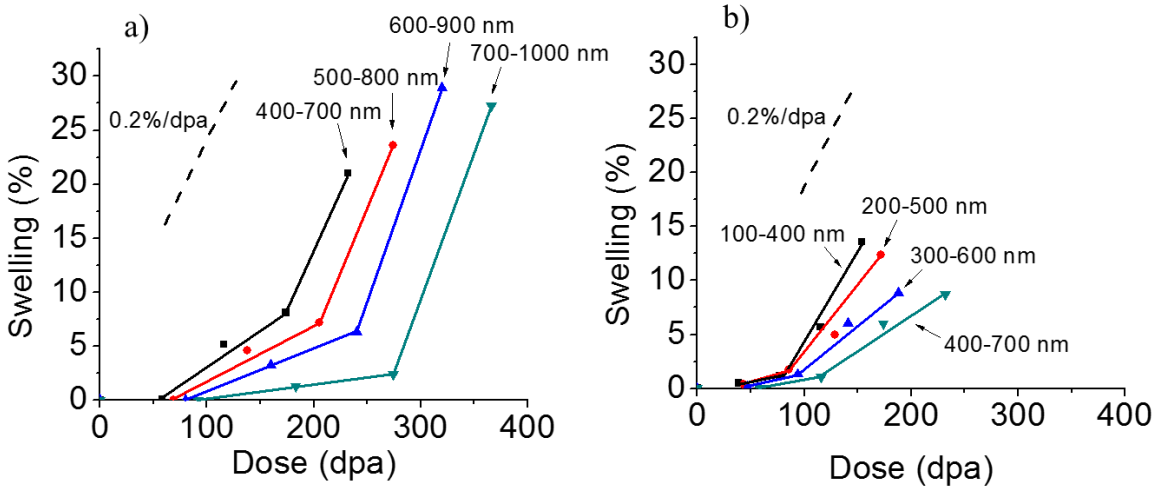

Figure 3.7 Swelling curves of (a) annealed and (b) severely deformed EK-181 samples as a function of dpa, extracted from different depth regions.

Since the maximum swelling in the deformed samples occurs at shallow depths which correspond to low local dpa region, the final swelling is not as significant as that in annealed samples. This leads to the difference that, while the annealed samples reach steady-state swelling of 0.2%/dpa at all depths sampled, it is more difficult to see this effect in the severely deformed sample. Only the depth region of 100 to 400 nm of the deformed sample reach the steady-state swelling of 0.2%/dpa, and its swelling incubation period is only about 75 local dpa. In a comparison with Fig. 3.7a, this swelling incubation period represents the lowest, regardless of the analysis depth in all samples.

If the swelling regions are not affected by the injected interstitial effect, the swelling dependence on depth can be converted to swelling dependence on local dpa values, thus obtaining useful information on swelling/dpa rate. Fig. 3.8a plots swelling depth profile obtained from the annealed sample after 400 peak dpa irradiation. The solid circles refer to the region unaffected by injected interstitials and the hollow circles refer to the regions where injected interstitials (blue colored curve) begin to suppress swelling, judged by comparing with SRIM calculated dpa profile. Fig. 3.8b plots the swelling values as a function of local dpa values, extracted from Fig. 3.8a. We once again see a swelling rate in the injected-interstitial-free zone that is comparable to the 0.2%/dpa.

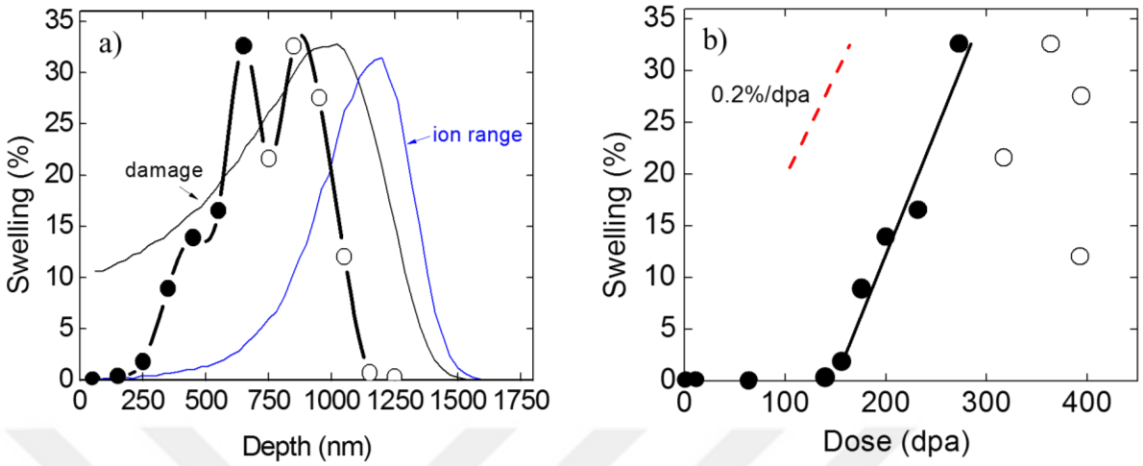

Figure 3.8 (a) Depth dependent swelling of annealed specimen after 400 peak dpa irradiation and (b) swelling of the same sample as a function of its local dpa values.

3.4.2 Grain growth in severely deformed EK-181

Fig. 3.9a shows cross-sectional TEM images obtained from severely deformed samples irradiated to 100 peak dpa at different temperatures. Fig. 3.9b shows micrographs of the severely deformed samples irradiated to doses of 100 to 400 peak dpa at 475 °C. Irradiated regions are marked by the dashed boxes. Comparisons between irradiated and unirradiated regions show that there is a significant grain growth in the irradiated regions. It is clear that the grain size increased with both increasing temperature and dpa level.

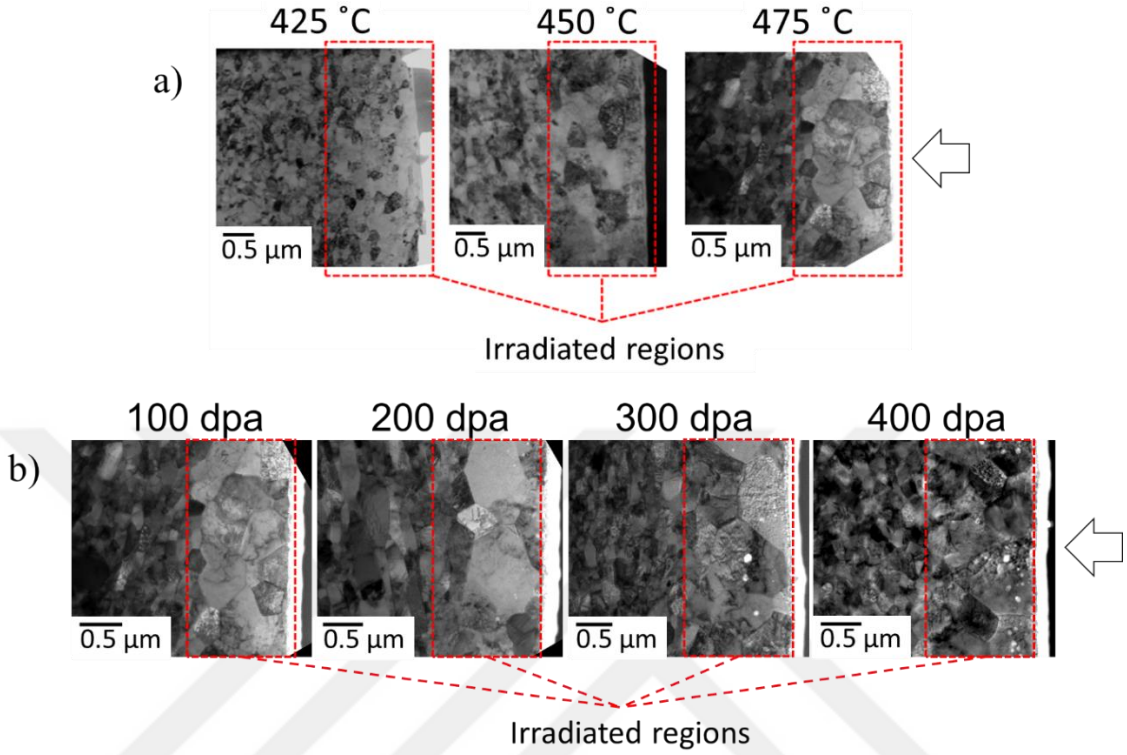

Figure 3.9 TEM micrographs showing extensive grain growth in the irradiated regions (a) for 100 peak dpa irradiation at different temperatures, and (b) for different dose levels at 475 °C. Arrows refer to the beam bombardment direction.

Fig. 3.10a compares the grain sizes of irradiated and unirradiated regions as a function of irradiation temperatures under the same dose (100 peak dpa). Statistics were obtained by performing 20 to 120 measurements to calculate the average grain size in both irradiated and unirradiated regions. The dashed lines represent the grain size before irradiation. The triangular symbols refer to the grain sizes in the unirradiated region influenced by thermal annealing only. The square symbols refer to the grain sizes within the irradiated region which has both an irradiation effect and thermal annealing effect. While thermal annealing slightly increased grain sizes, additional size growth was

noticeable even for the lowest irradiation temperature and irradiation-induced growth became significant at temperatures higher than 700 K. Fig. 3.10b shows grain sizes where all samples were irradiated to different dpa values at 475 °C. Systematically, ion irradiation increased grain sizes at all dpa values. Significant irradiation-driven grain growth was observed even at the lowest dpa (100 peak dpa). Both irradiated and unirradiated regions reached saturation at high dpa values. Beyond 200 peak dpa, the average grain size in irradiated region approached ~1000 nm and the size in the unirradiated region approached ~370 nm.

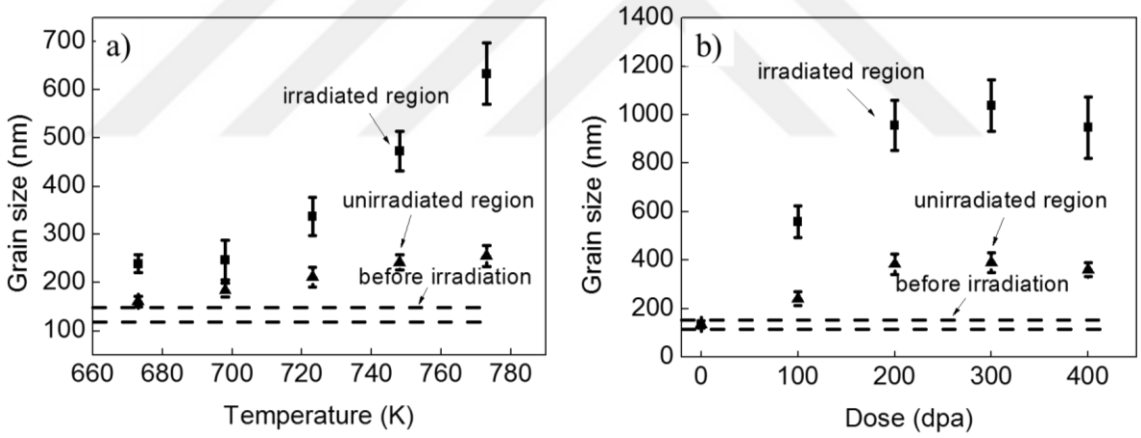

Figure 3.10 (a) Temperature dependence of mean grain size at 100 peak dpa (b) dose dependence of mean grain size at 475 °C in irradiated and unirradiated regions of severely deformed EK-181 samples.

Grain growth mechanisms are complicated. Previous studies suggested that if the damage cascade and thermal spike volume are comparable to grain sizes, grain growth is promoted [153]. Molecular dynamics simulations also observed such grain growth [154]. However, the initial grain size of the severely deformed sample is about 135 nm, which is

much larger than the typical cascade volume (a few nanometers from an ion track). Hence direct damage cascade interactions with grain boundaries are possible but may not play a significant role in the present study, considering relatively large grain sizes in the deformed samples. Furthermore, the damage cascade effect should be most dominant in the peak dpa region where nuclear stopping powers reach the maximum. This effect is less dominant in the near surface region where electronic stopping powers are significant. In a contrast, there is no such depth dependent grain growth observed from the TEM cross sectional characterization.

If a grain boundary acts as an equally efficient trapping/absorption center for both interstitials and vacancies, the defect absorption by boundaries should not lead to significant boundary reconfiguration. However, if boundaries become a biased trapping center for interstitials, grain boundary growth may occur. We suspect that grain coarsening is driven by net absorption of interstitials, although the detail mechanism is unclear at this point. Once stable void nuclei form within grains, these voids act as biased vacancy absorption centers and growing grain boundaries may act as biased interstitial absorption centers. This biased point defect trapping accelerates swelling. In other words, grain growth is correlated to swelling.

Note that significant grain growth occurs even for the low dose of 100 peak dpa. If we believe that void swelling is correlated with grain growth, two observations are expected: one is that after 100 peak dpa irradiation, the deformed sample may already exhibit noticeable swelling. The other is that the void swelling incubation period for the deformed samples may be less than 100 dpa. As shown in Fig. 3.5e, for the 100 peak dpa,

swelling is noticeable in the shallow depth region of 100 to 400 nm. Furthermore, the shortest swelling incubation period for the depth region of 100 to 400 nm, as suggested by Fig. 3.7b, is about 75 local dpa. While these observations cannot serve as direct evidence that grain instability causes void swelling, they support a correlation between these two. That is, grain instability reduces the incubation period for void swelling.

Grain coarsening reduces the benefit of introducing high density grain boundaries as defect sinks. In comparison with the effects from the changes of boundary densities, the effect from coarsening itself plays a significant role in swelling. Hence, even after grain coarsening with grain sizes smaller than the annealed samples, noticeable swelling occurred in deformed samples. The present studies suggest that grain boundary engineering needs to consider boundary stability. As for the technological development, using oxide particles or carbide precipitates to immobilize grain boundaries may be a realistic approach.

3.5 Conclusions

Self-ion irradiations of two variants of ferritic-martensitic alloy EK-181 have been examined with special interest paid to the neutron-atypical factors of injected interstitial and internal gradients in dpa rate. While severe plastic deformation changes the depth distribution of swelling in EK-181, it does not confer any significant improvement in swelling resistance and appears to actually accelerate the onset of swelling in the shallow depth region. This result is attributed to the instability of nano-grains in the severely deformed samples arising from the combined effects of thermal annealing and ion

irradiation. It appears that once steady-state swelling is attained in any alloy variant or depth position in that variant the swelling rate is on the order of ~0.2% per dpa, but that the incubation period preceding this rate is dependent on the dpa rate associated with the depth range where the data were extracted.

4. EFFECT OF SHOCK LOADING ON THE MICROSTRUCTURE, MECHANICAL PROPERTIES AND GRAIN BOUNDARY CHARACTERISTICS OF HT-9 FERRITIC/MARTENSITIC STEELS[†]

4.1 Overview

The microstructural changes and mechanical response of an HT-9 sample shock loaded to a peak pressure of 11 GPa have been investigated by TEM, XRD, microhardness and EBSD techniques. Dislocation densities obtained by both direct measurements (via TEM) and indirect calculations (by XRD and hardness) indicate that shock loading results in ~2-3 fold increase in dislocation density. TEM analyses show that the shape, and density of the dislocations change after shock loading. In addition, shock loading causes local plastic deformation of the continuous parallel lath structure in some regions, together with an overall decrease in the aspect ratio of laths due to local plastic deformation and lath fragmentation. As a result of XRD analyses, the fraction of edge dislocations is determined to increase by ~24% after shock loading. Furthermore, hardness increases by ~40 HV after shock loading due to the increased dislocation density. EBSD analyses show that the fraction of CSL boundaries decreases by ~5-10 % as a result of shock loading.

[*] Reprinted with permission from "Effect of shock loading on microstructure, mechanical properties and grain boundary characteristics of HT-9 ferritic/martensitic steels" by E. Aydogan, O. Anderoglu, S.A. Maloy, V. Livescu, G.T. Gray III, et al., 2016, Materials Science and Engineering A, 651, 75-82, Copyright 2016 by Elsevier.

4.2 Introduction

The effect of shock-loading on the microstructural evolution and mechanical response of metals has been studied for over 50 years. By studying the capability of materials to withstand a shockwave created plastic wave, new knowledge can be obtained on defect generation and mobility mechanisms. The first response of materials to shock loading is elastic deformation within 100 picoseconds [155,156]. At the same time, if the pressure is high enough, second phase particles can precipitate due to instantaneous heating and activation of thermal processes [157]. If the pressure is not high enough for phase transformations, existing defects can be activated or new ones can be nucleated as slip continues along preferred planes. Following defect activation and slip processes, either twinning occurs if it is favorable, or strain hardening occurs owing to the interaction and entangling of dislocations which promotes the formation of new dislocations. Since bcc crystals lack the number of close packed planes compared to fcc crystals, in addition to having fewer slip planes, the interaction and entanglement of dislocations are more severe in bcc crystals [158]. On the other hand, shock generated deformation twinning in fcc metals is much more sensitive than bcc metals [159] to both material properties (e.g. grain size [160], crystallographic orientation with respect to the deviatoric stress state [161]) and experimental parameters (e.g. peak pressure [162] and pulse duration [163]).

In the literature, there are many studies on the shock response of iron-based materials. Together with the fully reversible phase transformation from alpha-iron (α) to epsilon-iron (ε) at 13 GPa [164-167], shock loading creates a number of defects [168]. Shock deformation in bcc iron alloys occurs by the competition between deformation

twinning and slip mechanisms [169]. A critical twinning stress is postulated to be directly proportional to the stacking fault energy [170,171]. Therefore, under normal deformation conditions, pure bcc iron deforms by dislocation glide since it has a relatively high stacking fault energy [172,173]. On the other hand, low temperatures and high deformation rates facilitate twin formation in most crystal structures by retarding thermally-activated dislocation processes [169]. Recently, Gregory et al. [174] studied the effect of high strain rate explosive loading on the microstructure of plain carbon steels. It was discovered that shock loading leads to elongated grains in ferrite and pearlite phases and the formation of slip bands along with mechanical twins. Similarly, De Resseguier and Hallouin [175] observed a considerable amount of twin formation at high peak loading pressures up to 60 GPa in polycrystalline iron. They reported that twin volume fraction decreases with decreasing shock loading and predicted the elastic-plastic response of the materials and twin volume fractions as a function of pressure using a constitutive twinning model proposed by Johnson and Rohde [176].

F/M HT-9 steel is a promising material with extensive irradiation experience for use in the nuclear materials community. Although the effect of shock loading on plain carbon steels, pure iron and FCC stainless steels has been extensively studied, there are no detailed studies on the effect of shock loading on microstructural and mechanical properties of bcc stainless steels. Therefore, in this study, the effect of shock loading on microstructure, dislocation density and mechanical properties, together with (sub)grain boundary characteristics has been investigated below the α-iron to ε-iron transformation

pressure. As-received and shock deformed microstructures and mechanical properties were investigated using TEM, XRD, microhardness and EBSD techniques.

4.3 Experimental procedure

The HT-9 alloy was normalized at 1040 °C for 30 minutes and air cooled followed by tempering at 760 °C for 1 hour and air cooling. During tempering, carbon released from martensite precipitated as carbides on the lath boundaries and primary austenite grain boundaries.

The present shock recovery experiments were performed using an 80-mm single-stage launcher. The shock recovery technique was presented previously elsewhere [177,178]. A 5.08-mm-thick, 25.4-mm-diameter sample was stacked behind a 38-mm-diameter, 1-mm-thick cover plate and slip fit into a precisely bored recess on top of a 7 degree tapered, 12.7-mm-thick, inner momentum disk. Sample spallation was suppressed by backing the sample assembly with a 3.8-mm-thick spall plate, which also served as a longitudinal momentum trap. The central disk and spall plate were further surrounded by two concentric rings with outside diameters of 69.8 and 82.5 mm which protected the center of the sample from large amplitude release tensions. All assembly components were fabricated from AISI 4340 steel to ensure good impedance matching with the HT-9 steel sample during shock loading. The sample assembly was placed inside a steel impact cylinder that permitted passage of the sample inner momentum trapping ring through a central hole but stopped the projectile. Samples were shock loaded to an ~11 GPa peak pressure and "soft" recovered and cooled by decelerating the sample and inner

momentum trapping ring in a water catch chamber positioned immediately behind the impact area [178].

Standard metallographic techniques were used to prepare the samples for characterization. Jet electropolishing was performed using a solution of perchloric acid (5%) and methanol at -40 °C with an applied voltage of 20 V. Samples were investigated using both TEM and SEM. The microstructure and dislocation morphology were characterized using an FEI Tecnai F30 TEM operating at 300kV. Dislocation densities from TEM images were calculated by using two different methods. A line-intercept method defined in Ref [179] was used for the TEM images taken at the same kinematic conditions, whereby six randomly placed lines of different angular orientation were drawn over the TEM images. The dislocation density ρ is simply the number of points N divided by the total line length of the random lines L_t, multiplied by foil thickness t [180]:

$$\rho = \frac{N}{L_t t} \tag{4.1}$$

A second technique was used to check the reliability of the dislocation density results obtained from the line-intercept method. This technique was employed simply by measuring the total length (L_t) of the dislocations divided by the volume of the investigated region (V). The thickness of the region of interest was measured by the energy filtered TEM technique which introduces ~10% error to the measurements. The total dislocation density ρ was calculated using the following relationship [181]:

$$\rho = \frac{L_t}{V} \tag{4.2}$$

In addition to the TEM investigations, dislocation densities were also calculated using XRD and hardness methods. X-ray analysis of the specimens was conducted with Rigaku Ultima III. The wavelength of the source was Cu K_α containing both $K_{\alpha1}$=1.54056 Å and $K_{\alpha2}$=1.5444 Å. Instrumental broadening was determined by using NIST calibrated LaB_6 powders. Scans were operated from 10° to 140° with the rate of 0.02°/min using a constant slit to reveal the diffraction planes of (110), (200), (211), (220), (310) and (222). Moreover, the effect of shock loading on the mechanical properties was tested by measuring microhardness using a Struers DuraScan-70 hardness tester with 1 kg load.

The grain boundary characteristics of the as-received and shock pre-strained specimens were examined with EBSD using an FEI Inspect FEG SEM equipped with TSL EBSD equipment. Since the sample was tilted 70° from the horizontal, diffraction data were obtained from a very thin surface layer, meaning that the results were surface sensitive. During scans, an acceleration voltage of 20 kV and aperture size of 50 µm were used. The size of the scan region was determined according to the grain and substructure size as 50µm x 145µm. The step size showing the scan rate of the selected region was kept at 140 nm for all scans.

4.4 Results and discussion

4.4.1 Effect of shock loading on the microstructure and mechanical properties

The effect of shock loading on the microstructure was investigated by TEM and XRD methods while microhardness and compression tests were utilized to assess the shock loading effect on the mechanical properties. Dislocation densities of the as-received

and as-shocked samples were obtained by using TEM, XRD and hardness methods. Details of those methods are explained in the following sections.

4.4.1.1 Effect of shock loading on the microstructure

Fig. 4.1 shows the TEM bright field images of the HT-9 samples in the as-received and as-shocked conditions. In the as-received condition, carbides precipitate along primary austenite grain boundaries together with parallel lath boundaries as a result of tempering. After shock loading, carbides remain at the lath and prior austenite boundaries; however, the dislocation density increases considerably (~2-3 fold). The dislocation density of the as-received sample is calculated as $3.3\pm0.7x10^{14}$ m^{-2} while it is calculated as $7.8\pm1.6x10^{14}$ m^{-2} for the as-shocked sample. The calculated errors occur during thickness and dislocation counting measurements.

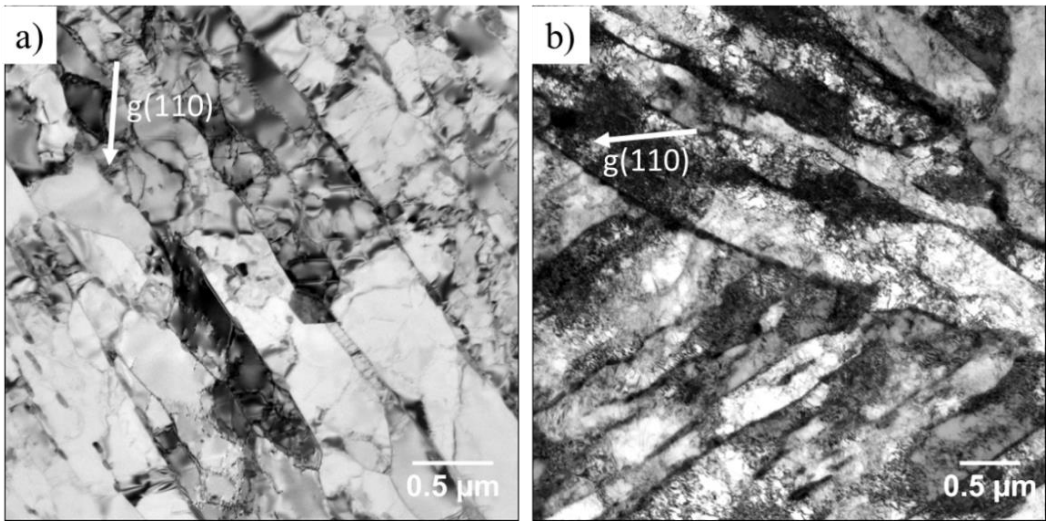

Figure 4.1 TEM bright field images of the (a) as-received sample (b) shocked loaded sample with the peak pressure of 11 GPa at room temperature.

Detailed investigations performed under the same kinematic conditions (g-vector of (110)) indicate that the dislocation structures in both cases are quite different. Initially, dislocations are continuous and distributed homogenously within the laths (Fig. 4.2a). On the other hand, dislocations are observed to become entangled as a result of shock loading. Moreover, the dislocation density at the lath boundaries is considerably higher compared to the inner parts of the laths (Fig. 4.2b). As a result of the high dislocation density at the lath boundaries, contrast of the carbide particles increases leading to a coarsened shape.

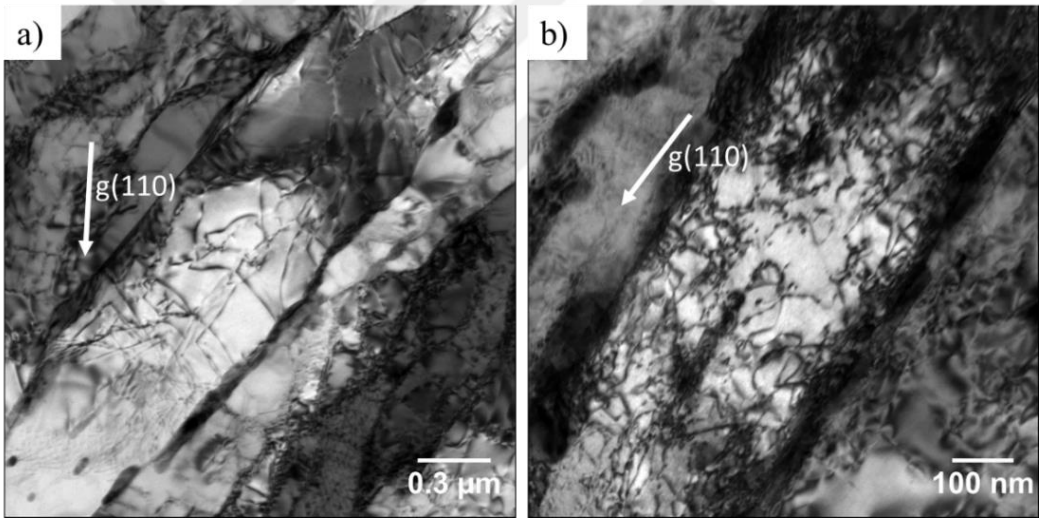

Figure 4.2 TEM bright field images of (a) as-received (b) as-shocked conditions along (110) direction showing the structure of dislocations.

Yasunaga et al. observed that at high strain rates exceeding ~10^3 s^{-1}, dislocation cell structures do not tend to form and small dislocation loop formation occurs in bcc metals of V, Nb and Mo [182]. Similarly, HT-9 F/M steel shows dislocation loops without

dislocation cell formation after high rate shock loading as shown in Fig. 4.3. As an example, some of the dislocation loops are circled with red dashed lines.

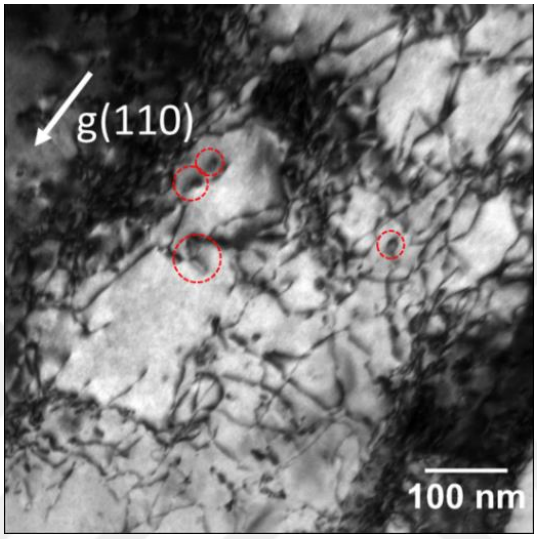

Figure 4.3 TEM bright field image of the as-shocked sample showing the dislocation structure and dislocation loops (red dashed circles) on g=(110).

Together with subtle changes in the dislocation structure, shock loading is observed to reflect local plastic deformation of the continuous parallel lath structure in some regions, as well as an overall decrease in the aspect ratio of laths due to local plastic deformation and lath fragmentation. Fig. 4.4a and Fig. 4.4b show bright field images of different regions where several of the continuous laths are observed to be deformed and fragmented. Lath boundaries are denoted by the dashed red lines for better visualization in Fig. 4.4b. Fragmentation of the lath structure is consistent with previous observations in the literature. Zel'dovich et al. [183] studied the effect of shock loading on the cementite laths in a pearlite structure and observed that depending on the macroscopic

orientation of the pearlite structure relative to the shock-wave propagation direction, the cementite laths were observed to be either deformed or locally fragmented. In addition, Fig. 4.4c shows that the overall aspect ratio of the laths is reduced in some regions. This decrease in the aspect ratio of the laths is attributed to the local plastic deformation of the laths compared to the surrounding microstructure during the plastic compression and rarefaction portions of the shock pulse. Since shock loading subjects a sample to principally 1-D uniaxial strain compression [184], plastic flow predominantly occurs in the loading direction. Accordingly, if the lath structure lies parallel with the direction of shock loading, plastic flow is mostly along the laths resulting in preservation in the parallel structure. Conversely, if the packets are oriented at an angle to the loading direction, plastic deformation and localized shear deformation occur across lath boundaries and inside of laths rather than along laths and lath boundaries. Consequently, fragmentation of the laths leads to an overall reduction in the lath aspect ratio.

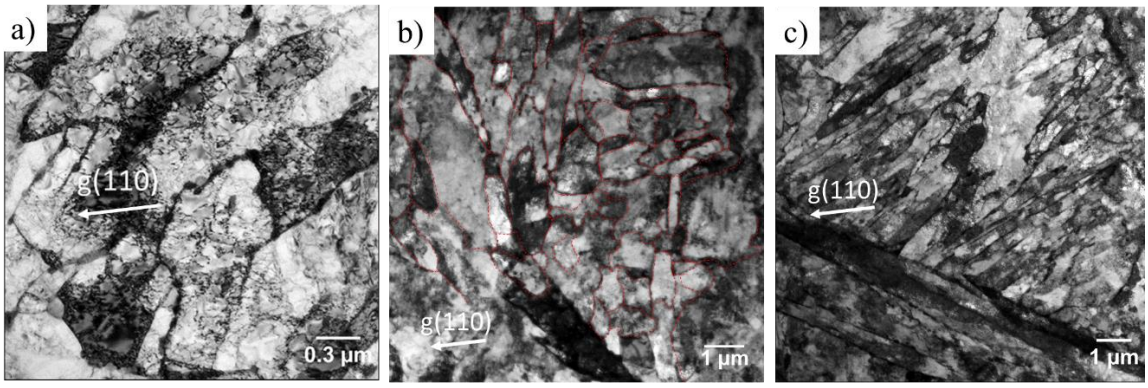

Figure 4.4 TEM bright field images of shock loaded HT-9 sample showing (a&b) the destruction of continuous parallel lath structure at different locations and magnifications (c) the large aspect ratio as a result of shock loading.

XRD was another method implemented to investigate the effect of shock loading on the microstructure of HT-9 steels. Dislocation densities were calculated by XRD line profile analyses. The diffraction angles and full width at half maximum (FWHM) values for the as-received and as-shocked samples before subtraction of instrumental broadening are given in Table 4.1. There are no clear changes in the diffraction angles as a result of the peak shift. On the other hand, the peak broadening as a result of shock loading is quite pronounced especially at high diffraction angles which is consistent with the significant increase in dislocation density.

Table 4.1 The XRD data of each reflection of the as-received and as-shocked HT-9 steels.

Bragg Reflection	2θ/deg (as-received)	FWHM (Δ2θ)/deg (as-received)	2θ/deg (as-shocked)	FWHM (Δ2θ)/deg (as-shocked)
(110)	44.7	0.3	44.7	0.4
(200)	64.9	0.4	64.9	0.6
(211)	82.2	0.5	82.2	0.6
(220)	98.7	0.6	98.7	0.7
(310)	116.0	0.8	116.0	1.1
(222)	136.5	1.0	136.5	1.5

Using the modified Williamson-Hall method [185-189], dislocation densities of the as-received and as-shocked HT-9 steel samples were calculated by using the

broadening values in Table 4.1 subtracted by the instrumental broadening as in the following equation.

$$\Delta K \cong \frac{0.9}{D} + \sqrt{\frac{\pi M^2 b^2}{2}} \rho^{1/2} K\bar{C}^{1/2} + O(K^2\bar{C}) \tag{4.3}$$

where $K = 2\sin\theta / \lambda$ and $\Delta K = \cos\theta[\Delta(2\theta)] / \lambda$. Here θ is diffraction angle, $\Delta(2\theta)$ is the full width at half maximum (in radians), and λ is the wavelength of the x-rays which is 1.54056 Å for Cu radiation. In equation 4.3, *D* is the average substructure size, *M* is a constant that depends on both the effective outer cut-off radius and the density of dislocations, *b* is Burger's vector and ρ is dislocation density. *O* represents the higher order terms in $K^2\bar{C}$ where $\bar{C}$ is the dislocation contrast factor and represented by equation 4.4.

$$\bar{C} = \bar{C}_{h00}(1 - qH^2) \tag{4.4}$$

$\bar{C}_{h00}$ is the average dislocation contrast factor on *(h00)* and is determined by crystal elasticity. It is calculated as 0.285 for pure iron [190]. Moreover, H^2 is a plane indices-dependent variable which can be represented as $H^2 = \frac{(h^2k^2 + h^2l^2 + k^2l^2)}{(h^2 + k^2 + l^2)^2}$. The *q* value is a parameter dependent on elastic constants of the crystal and edge or screw character of dislocations. Equation 4.3 can be converted to the linear relationship of $((\Delta K)^2 - \alpha) / K^2$ vs. H^2 as;

$$[(\Delta K)^2 - \alpha] / K^2 \cong \beta\bar{C}_{h00}(1 - qH^2) \tag{4.5}$$

where $\alpha = (0.9/D)^2$ and $\beta = \pi M^2 b^2 \rho / 2$. In order to be able to calculate α values, average lath sizes of 698±33 nm and 870±51 nm were measured by EBSD analyses for as-received

and as-shocked HT-9 samples, respectively. The slope of the $((\Delta K)^2 - \alpha)/K^2$ vs. H^2 plot shown in Fig. 4.5 gives $-\beta\bar{C}_{h00}q$. Moreover, the *q* values of 2.10±0.08 and 1.77±0.09 were obtained for the as-received and as-shocked samples, respectively from the intercept of linear fit to the x-axis.

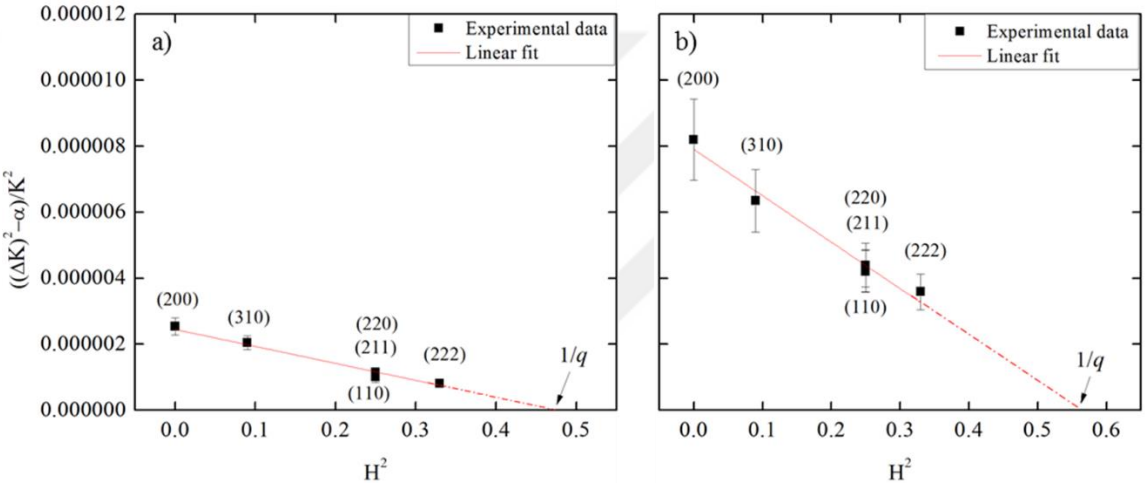

Figure 4.5 The modified Williamson–Hall plots of the FWHM for (a) as-received (b) as-shocked specimens. The Miller indices of the reflections are also indicated.

To calculate dislocation density from the slope of the plots, *M* is required. *M* is defined as $R_e\sqrt{\rho}$ where R_e is the effective outer cut-off radius of dislocations which is $R_e \approx 0.78R$. *R* is the radius of the circular sub-area and it is defined as $\frac{Gb}{2\tau}$ where *G* is shear modulus, *b* is Burger's vector and τ is shear stress. Consequently, R_e values for the as-received and as-shocked samples are calculated as 20.1 nm and 16.5 nm, respectively. By inserting the R_e values into the slope formula of $-\beta\bar{C}_{h00}q = -\frac{\pi R_e^{\,2} b^2 \rho^2}{2}\bar{C}_{h00}q$, the

dislocation densities of as-received and as-shocked specimens are calculated as $4.7\pm0.4\text{x}10^{14}$ m^{-2} and $10.3\pm0.6\text{x}10^{14}$ m^{-2}, respectively.

Theoretical values of q for edge and screw dislocations in pure iron are given as 1.28 and 2.67, respectively [191]. By using equation 4.6 the dislocation character can be determined as;

$$f^{edge} = \frac{q_{th}^{screw} - q_{\exp}}{q_{th}^{screw} - q_{th}^{edge}} = 1 - f^{screw} \tag{4.6}$$

where f^{edge} and f^{screw} are the fractions of edge and screw dislocations, respectively. By inserting the theoretical and experimental values of q into equation 4.6, the fractions of edge dislocations are determined to be 0.41±0.06 for the as-received sample; and 0.65±0.06 for the as-shocked sample showing an increase in fraction of edge dislocations from shock loading. Tang and Marian [192] studied the effect of high strain rate loading on single crystal iron by using dislocation dynamics simulations. At low temperatures, the mobility of edge dislocations is 2-3 times higher than that of screw dislocations resulting in plastic flow occurring mainly by screw dislocations. On the other hand, at higher temperatures and varying strain rates, it was discovered that edge dislocations move slower and plastic flow occurs mainly by entanglement of edge dislocations. They also reported that the fraction of the screw dislocations asymptotically converges to a rate-independent but temperature dependent value, f_{eq}. Consequently, f_{eq} values at 100, 300, and 600 K are calculated as 0.95, 0.73, and 0.55. These calculations show that with the increase in temperature, the mobility of screw dislocations increases. Therefore, the contribution of edge dislocations to the plastic deformation increases. Adiabatic heating

during shock loading leads to an increase in the temperature resulting in increased mobility of screw dislocations. Consequently, the density of screw dislocations decreases and the fraction of entangled edge dislocations rises.

4.4.1.2 Effect of shock loading on the mechanical properties

To understand the effect of shock loading on the mechanical properties, microhardness was measured. Hardness tests show that while the average hardness of the HT-9 sample is 246±3 HV before shock loading, it increases to 282±2 HV after shock loading.

The relationship between the Vickers hardness and the yield stress, which was originally described by Tabor [193] with a proportionality constant of ~3 has been investigated extensively. Busby et al. [194] showed that the proportionality constant between the hardness change (ΔH_v) and yield stress change ($\Delta\sigma_y$) is 3.03 for austenitic steels and 3.06 for ferritic steels. The yield stresses of as-received and as-shocked samples were measured in compression as 692±14 MPa and 842±17 MPa, respectively and reported in our previous study [159]. As a result, the proportionality constant between the hardness change and the yield stress change is derived as 2.35±0.81 which is close to the results previously documented in the literature within error.

According to the Taylor's formula [195], yield stress can be related to the square root of dislocation density using the following formula;

$$\sigma_y = \sigma_0 + M\alpha Gb\sqrt{\rho} \tag{4.7}$$

where σ_y is the yield stress, *M* is Taylor factor which is ~3 for polycrystalline metals [195,196], *G* is the shear stress (86.95 GPa for HT-9 steel), *b* is the length of the Burger's vector, 2.466 Å for the $\langle 111 \rangle \{110\}$ slip system, ρ is the dislocation density, and α is a factor describing the strength of the obstacles that a moving dislocation has to overcome during plastic deformation. Moreover, σ_0 is the stress required to move a dislocation in the absence of other dislocations that can arise as a result of solutes, Peierls-type stresses, grain-size strengthening, etc. The values of α being 0.22 and σ_0 being 386 MPa for HT-9 steel are obtained experimentally from the slope and y-intersection point of yield stress vs. dislocation density in Ref [197]. Hence, by using the above stated parameters, the dislocation densities of the as-received and as-shocked samples are calculated as $4.7 \pm 0.4 \times 10^{14}$ m^{-2} and $10.4 \pm 0.8 \times 10^{14}$ m^{-2}, respectively. This is a rudimentary calculation assuming that only dislocations contribute to the hardening without considering the effect of lath size and second phase particles; nevertheless, the results appear reasonable and consistent.

In summary, dislocation density measurements and calculations by TEM, XRD and hardness methods conclude the same result that dislocation density increases ~2-3 fold after shock loading. Table 4.2 shows the compiled dislocation densities obtained by the above stated methods. It should be noted that while dislocation densities calculated by XRD and hardness methods are almost the same, dislocation density measurements from TEM images give lower values. The reason can simply be attributed to the 2-D imaging of dislocations under TEM. Dislocations lying perpendicular to the image plane are not

accounted into the measurements. On the other hand, XRD and hardness methods provide 3-D information from larger sampling regions. However, the dislocation density increase as a result of shock loading is ~2-3 fold for all three cases.

Table 4.2 Dislocation densities of the as-received and as-shocked HT-9 samples obtained by different methods.

	Dislocation density (m^{-2}) TEM	Dislocation density (m^{-2}) XRD	Dislocation density (m^{-2}) Hardness
As-received	$3.3\pm0.7x10^{14}$	$4.7\pm0.4x10^{14}$	$4.7\pm0.4x10^{14}$
As-shocked	$7.8\pm1.6x10^{14}$	$10.3\pm0.6x10^{14}$	$10.4\pm0.8x10^{14}$

4.4.2 Effect of shock loading on the substructure boundaries: EBSD study

Grain boundaries are vulnerable sites for corrosion, cracking, segregation and precipitation. Since the composition and misorientation across the boundaries vary within a sample, grain boundary character can also play an important role during degradation processes [198]. In this study, the effect of shock loading on the characteristics and amount of the boundaries has been investigated using EBSD technique. Fig. 4.6 shows the distribution of phase boundary misorientations in the as-received and shock loaded HT-9 samples. Fig. 4.6b and Fig. 4.6e indicate that primary austenite grain boundaries have the misorientation angle between 15° and 50° which corresponds to random grain boundaries (RGBs). On the other hand, the misorientation angle between the laths, within and between the packets generally lies between 2°-15° (Fig. 4.6a and Fig. 4.6d) and 50°-65° (Fig. 4.6c

and Fig. 4.6f) corresponding to low angle boundaries (LABs) and special boundaries, respectively.

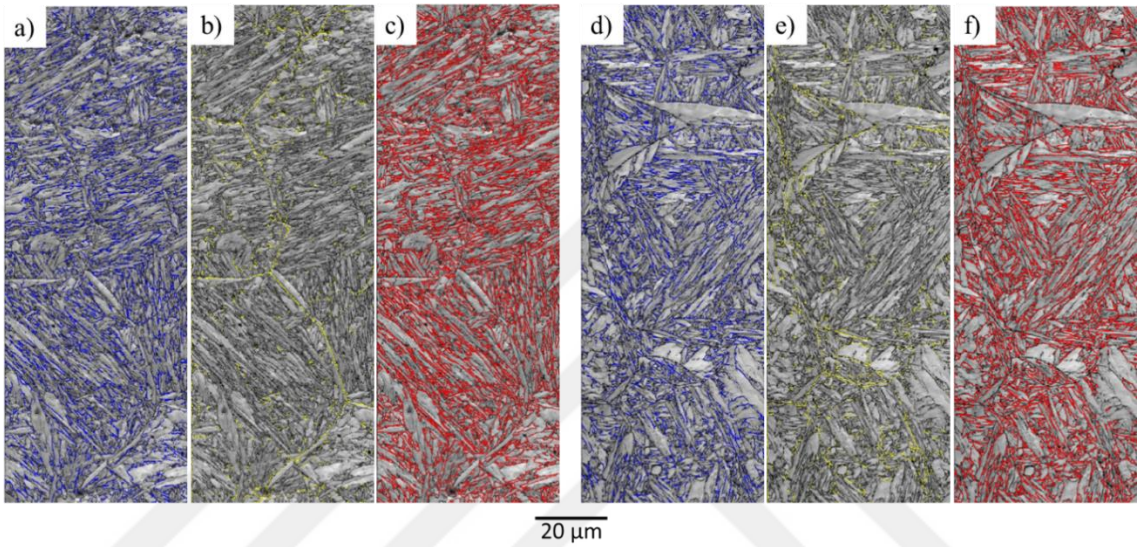

Figure 4.6 EBSD images of the as-received HT-9 steel showing the misorientation angles of (a) 2°-15° (LAB), (b) 15°-50° (RGB) and (c) 50°-65° (special boundaries); as-shocked HT-9 steel showing the misorientation angles of (d) 2°-15° (LAB), (e) 15°-50° (RGB) and (f) 50°-65° (special boundaries).

Fig. 4.7 shows the misorientation angle distribution of both the as-received and as-shocked HT-9 samples within single grains. For each condition, ~20 grains from at least three different regions were studied. The most obvious common feature of both conditions is that there is almost no boundary with a misorientation angle between 20° and 47° [199]. Although the fraction of the low angle grain boundaries ($2°<\theta<15°$) and high angle grain boundaries between 45° and 57° remain constant after shock loading, the type of the boundaries having the misorientation angle of ~60° decreases by ~5-10%. The postulated reason for this change is discussed in detail in the following section and can simply be

attributed to the atomic displacements as a result of a high dislocation density at the lath boundaries after shock loading.

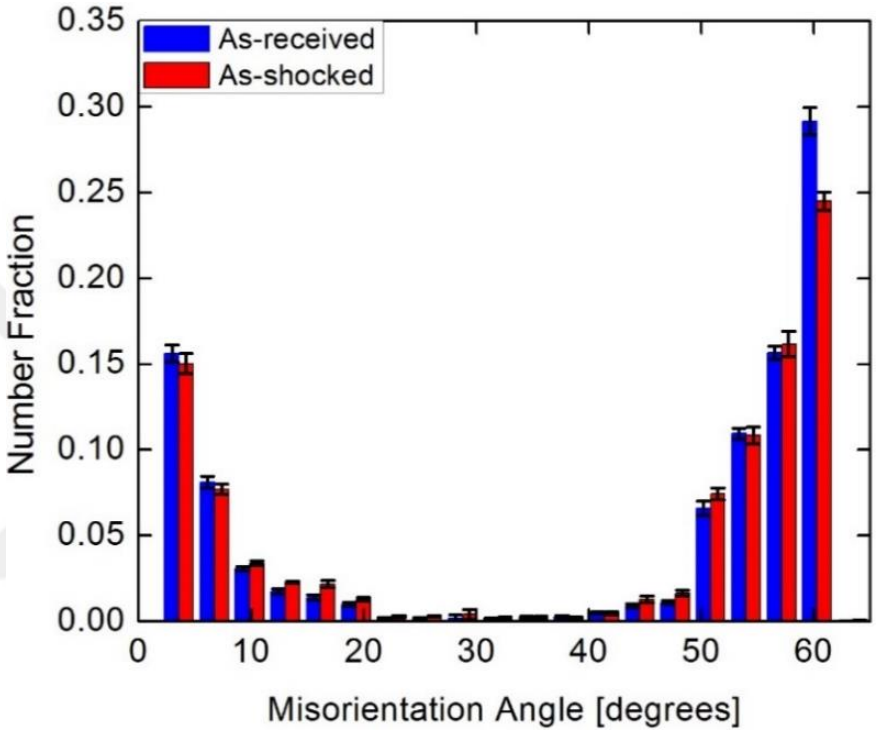

Figure 4.7 Histogram of misorientation fraction inside single primary austenite grains for the as-received and as-shocked HT-9 samples.

While the misorientation between the laths within the packets is primarily between 50° and 60°, the packet boundaries generally have misorientation angles of 10°-20° and 47°-50° as shown in Fig. 4.8.

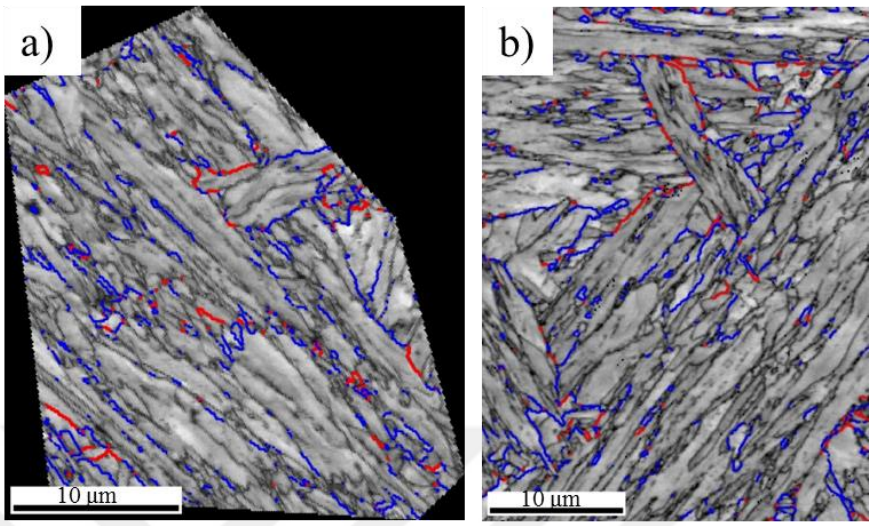

Figure 4.8 Misorientation angles between the packets of (a) as-received (b) as-shocked HT-9 samples (— 10°-20°; — 47°-50°).

EBSD analyses show that there are five different types of CSLBs in the investigated materials, namely Σ3, Σ11, Σ25b, Σ33c and Σ41c whose misorientation angles are tabulated in Table 4.3. The boundaries having Σ>29 are not special boundaries; however the deviation angle, $\Delta\theta$, from the ideal conditions should be taken into account while determining the special boundaries. $\Delta\theta$ for the Σ3 can be calculated using the Palumbo-Aust criterion which is much more restrictive than the widely used Brandon's criterion [200]. By using the Palumbo-Aust criterion that is given as $\Delta\theta \leq 15^{o}\Sigma^{-5/6}$, $\Delta\theta$ can be calculated as 6° for Σ3. According to this calculation, the misorientation angle for Σ3 is 60°±6 which includes the Σ33c and Σ41c.

Table 4.3 CSL boundaries existing in the HT-9 as-received and as-shocked samples and corresponding misorientation angles.

Σ	θ (degrees)	uvw
3	60.0	111
11	50.5	110
25b	51.7	331
33c	59.0	110
41c	55.9	110

Table 4.4 shows the fraction of special boundaries in the as-received and as-shocked conditions. It should be noted that the error introduced by the OIM (orientation imaging microscopy) analysis of EBSD results is less than 5%. In both conditions, the amount of Σ3 boundaries is higher compared to the other types of boundaries which is expected for the martensite structures. As a result of shock loading, the amount of the special boundaries decreases from 45.6±2.3% to 37.6±1.9%. This is attributed to the pile up of dislocations at the lath boundaries (Fig. 4.2), which is the main origin of increasing the average deviation degree and decreasing the fraction of low-Σ boundaries. Low-Σ boundaries, especially Σ3 boundaries have the lowest grain boundary energy. During plastic deformation in one direction, the generated dislocations pile up at the boundaries and the grain boundary energy increases. In order to reduce the energy, atoms near the lath boundaries should move to lower energy sites [201]. Besides these displacements, a number of atoms at the boundaries are removed in order to reduce the grain boundary energy. After the displacements and removals, the deviation degrees are beyond the

maximal deviation; therefore, CSL structures are lost. This is postulated to be the reason why especially the fraction of Σ3 boundaries decreases with shock deformation. It was also found that even though shock loading to 11 GPa results in a decrease in the amount of special boundaries, it does not affect the crystallographic orientation relationship between austenite and martensite.

Table 4.4 CSL boundary fractions before and after shock loading.

	As-received	As-shocked
CSL (Σ3) (%)	40.1±2.0	32.8±1.6
CSL (Σ11) (%)	4.4±0.2	3.6±0.2
CSL (Σ25b) (%)	1.1±0.1	1.2±0.1
Total # of CSL boundaries (%)	45.6±2.3	37.6±1.9

4.5 Conclusions

The microstructural changes and the mechanical response of an HT-9 steel shock loaded to a peak pressure of 11 GPa in the normalized and tempered condition have been investigated by TEM, XRD, microhardness and EBSD techniques. Results from TEM, XRD and microhardness methods are shown to be quite consistent and lead to the conclusion that a ~2-3 fold increase in dislocation density occurs as a result of shock loading. TEM analyses indicate that after shock loading the dislocations become entangled and concentrated mostly near or at the lath boundaries. Shock loading also causes local plastic deformation of the continuous parallel lath structure in some regions as well as an

overall decrease in the aspect ratio of laths due to local plastic deformation and lath fragmentation. XRD analyses show that the amount of edge dislocations increases from 0.41±0.06 to 0.65±0.06 after shock loading. Moreover, the hardness is seen to increase by ~40 HV after shock loading compared to the as-received condition. In addition, EBSD analyses indicate that shock loading causes a reduction in the fraction of CSL boundaries from 45.6±2.3% to 37.6±1.9%.

5. INVESTIGATION ON EFFECTS OF SHOCK LOADING ON THE IRRADIATION RESPONSE OF HT-9 STEEL

5.1 Overview

In this chapter, the effect of shock loading on the irradiation response of HT-9 steels has been investigated after 600 dpa ion irradiations at 450 °C. It has been found that the amount of the special boundaries decreases by 7.5% in both as-received and as-shocked samples while the as-received sample has finer and denser dislocation loops after irradiation. Even though the overall swelling is very low and occurs at the shallow regions for both samples, shock loaded sample shows slightly higher swelling. HAADF imaging together with EDS composition analysis shows the formation of M_2X and G-phase precipitates. In order to understand the effect of dislocations, boundaries and precipitates on the irradiation response of the materials, their sink strength was calculated. The sink stregth of M_2X precipitates is found to be very high compared to the dislocation and boundary sink strengths and the total sink strength is slightly lower in as-shocked sample. There is a high fraction of edge dislocations in the as-shocked sample which has a higher bias to SIAs compared to vacancies and might be another reason for slightly higher swelling. However, once the steady-state regime is reached, the swelling resistance of the samples might change depending on the sink strengths.

5.2 Introduction

Next generation advanced reactors are expected to operate at extreme conditions such as high temperatures and neutron damages as well as corrosive environments [202]. HT-9 ferritic/martensitic steels are one of the best candidates for structural materials in nuclear applications such as first wall and blanket for fusion reactors, and the fuel cladding and fuel ducts for fast reactors [47,203]. Radiation induced swelling in candidate materials is a serious problem and therefore considerable effort has been spent to understand and reduce swelling under irradiation. There is a general perception that cold working or an increase in the dislocation density suppresses the radiation induced swelling [204,205]. However, it has been found that cold working might either reduce [206-208] or increase swelling [209,210], besides having no effect on it [211,212]. For instance, cold worked austenitic stainless steels irradiated at 400 °C in high flux isotope reactor exhibited 4-27 times reduced swelling [213]. In contrast, Garner et al. showed that swelling increases in cold worked Fe-Cr-Ni solute free alloys at high temperatures [214]. Similarly, Dvoriashin et al. reported that cold worked pure iron neutron irradiated at 400 °C shows considerably higher swelling probably due to the shortening of transient regime [215]. On the other hand, increase in the dislocation density has no effect on the swelling of the He pre-injected Fe-Cr-Ni alloys [205].

Dislocation density and irradiation parameters have considerable impact on the radiation induced swelling behavior of the deformed materials. It has been shown that while swelling is quite high at low deformation strains, it starts to decrease with the increase in the plastic strain from deformation [216]. Similar to the amount of deformation

strain, temperature has a profound effect on void swelling. Garner et al. proposed that there is a critical temperature for Fe-Cr-Ni alloys beyond which cold-working has an opposite role on the swelling [214]. Moreover, while at low fluences swelling increases in cold worked high purity aluminum, high fluence neutron irradiation reduces the swelling at low temperatures [217].

Shock loading is a one-dimensional plane strain deformation similar to the uniaxial loading if the loading is enough and the sample is thin enough [90] It creates defects, basically edge dislocations, and those defects move in the direction of shock wave propagation in the case of a planar shock wave. Moreover, the density of defects increases with the increase in the peak shock pressure [95]. In the previous chapter, we have shown that the shock loading of ~11 GPa resulted in ~2-3 fold increase in the dislocation density of HT-9 steels. Besides that, lath size increased slightly and the amount of special boundaries decreased by 5-10%. Even though previous studies investigated the effect of deformation on swelling based on the dislocation density, we propose that other effects either resulted from deformation or irradiation itself, such as boundary types and second phase particles, might have prominent effect on the irradiation response of the materials. Thus, the following study compares the irradiation effects on as-received and shock deformed HT-9 materials considering sink strength and bias of the pre- and post-irradiation microstructures.

5.3 Experimental procedure

HT-9 samples in both as-received and as-shocked (shocked to 11 GPa) conditions were irradiated by using 3.5 MeV Fe^{2+} ions to 600 peak dpa at 450 °C. To investigate the effect of irradiation on the grain boundary characteristics and orientation relationships, EBSD studies were conducted using an FEI Inspect FEG SEM equipped with TSL EBSD equipment. During scans, an acceleration voltage of 20 kV and aperture size of 50 μm were used. The scan rate was kept as 140 nm for all scans. TEM studies were performed using FEI Tecnai F30 Analytical TEM/STEM operating at 300 kV. For dislocation studies, two beam studies were conducted with BF TEM and STEM. Moreover, precipitates were visualized with HAADF imaging mode and composition mapping was obtained using EDS. BFTEM and HAADF imaging at an under-focus condition of ~1 μm were used for the swelling studies. The specimens for cross-sectional TEM were prepared by using a FIB lift-out technique. Prior to FIB cutting, a thin Pt layer was deposited on the sample surface to protect the features beneath the surface. The FIB specimen thicknesses were determined by using EFTEM.

5.4 Results

5.4.1 Effect of irradiation on the substructure boundaries

EBSD technique has been utilized to investigate the effect of irradiation on the characteristics and amount of the boundaries in as-received and as-shocked HT-9 samples. Fig. 5.1 shows the distribution of boundary misorientations in the as-received and shock loaded samples after 600 dpa irradiation. Similar to the unirradiated conditions in Chapter

4, Fig. 5.1b and Fig. 5.1e indicate that primary austenite grain boundaries have the misorientation angle between 15° and 50° (RGBs). On the other hand, the misorientation angle between the laths, within and between the packets lies between 2°-15° (Fig. 5.1a and Fig. 5.1d) and 50°-65° (Fig. 5.1c and Fig. 5.1f) corresponding to LABs and special boundaries, respectively.

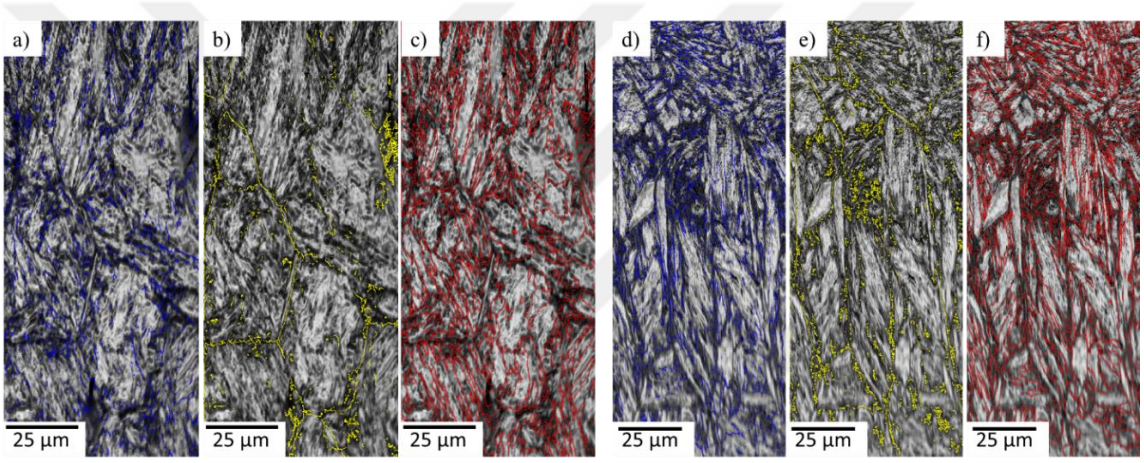

Figure 5.1 EBSD images of the as-received HT-9 steel showing the misorientation angles of (a) 2°-15° (LAB), (b) 15°-50° (RGB) and (c) 50°-65° (special boundaries); as-shocked HT-9 steel showing the misorientation angles of (d) 2°-15° (LAB), (e) 15°-50° (RGB) and (f) 50°-65° (special boundaries) after irradiation to 600 dpa.

Fig. 5.2 compares the misorientation angle distribution within single grains of both as-received and as-shocked HT-9 samples before and after irradiation. Even though there is almost no boundary having misorientation angle of 20°-47° before irradiation, the number of boundaries at this interval increases after 600 dpa irradiations. This can be attributed to the sink efficiency of the grain boundaries and misorientation angle changes as a result of defect pile-up at the boundaries. After irradiations, while total amount of the

low angle and high angle boundaries remains the same for both as-received and as-shocked samples, amount of the boundaries with misorientation angle of ~60º decreases by ~5% in the case of as-received sample.

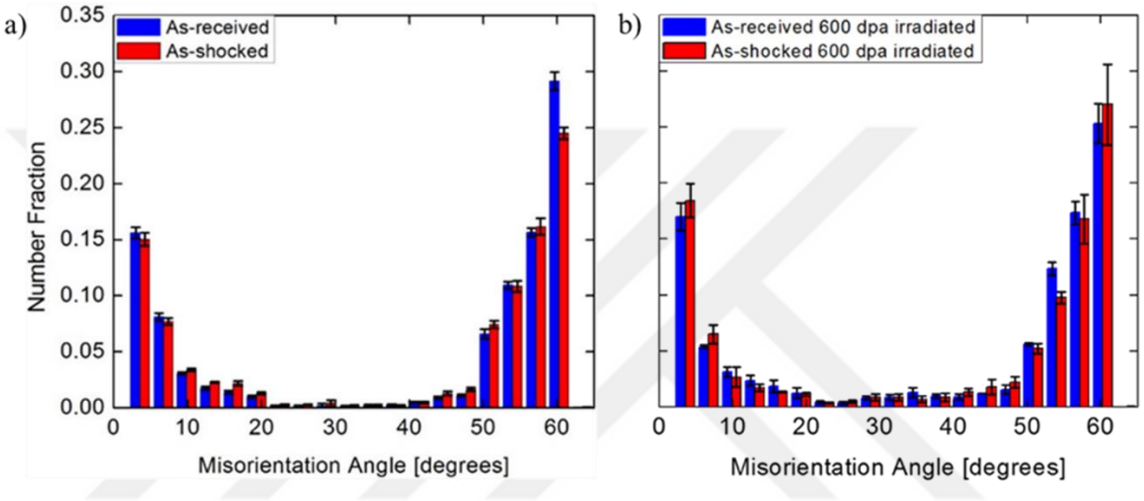

Figure 5.2 Misorientation angle distribution of as-received and as-shocked samples (a) before irradiation (b) after 600 dpa irradiation.

Table 5.1 shows the fraction of CSL boundaries in the as-received and as-shocked conditions before and after irradiation. It is obvious that the amount of special boundaries decreased by ~7.5% for both cases, with still higher amount in as-received sample. Moreover, after irradiation of shock loaded sample, special boundary of Σ13b having a misorintation angle of 27.8° appeared. It was also found that after irradiation, the crystallographic orientation relationship between austenite and martensite does not change.

Table 5.1 CSL boundary fractions of as-received and as-shocked samples before and after irradiation.

	Before irradiation		After irradiation	
	As-received	As-shocked	As-received	As-shocked
CSL (Σ3) (%)	40.1±2.0	32.8±1.6	32.8±1.6	25.3±1.3
CSL (Σ11) (%)	4.4±0.2	3.6±0.2	4.0±0.2	3.0±0.2
CSL (Σ13b) (%)	---	---	---	1.0±0.1
CSL (Σ25b) (%)	1.1±0.1	1.2±0.1	1.3±0.1	0.8±0.1
Total # of CSL boundaries (%)	45.6±2.3	37.6±1.9	38.1±2.0	30.1±1.5

5.4.2 Effect of irradiation on microstructure

Two beam studies were performed under the same kinematic conditions (g=(110)) using BF STEM as shown in Fig. 5.3. The continuous dislocations before irradiations in as-received condition is kept while the dislocations are mostly entangled in as-shocked sample. Moreover, even though a quantitative analysis was not conducted, knowing that the thickness of the foils are almost the same, dislocation loop size is finer while the density is higher in as-received samples.

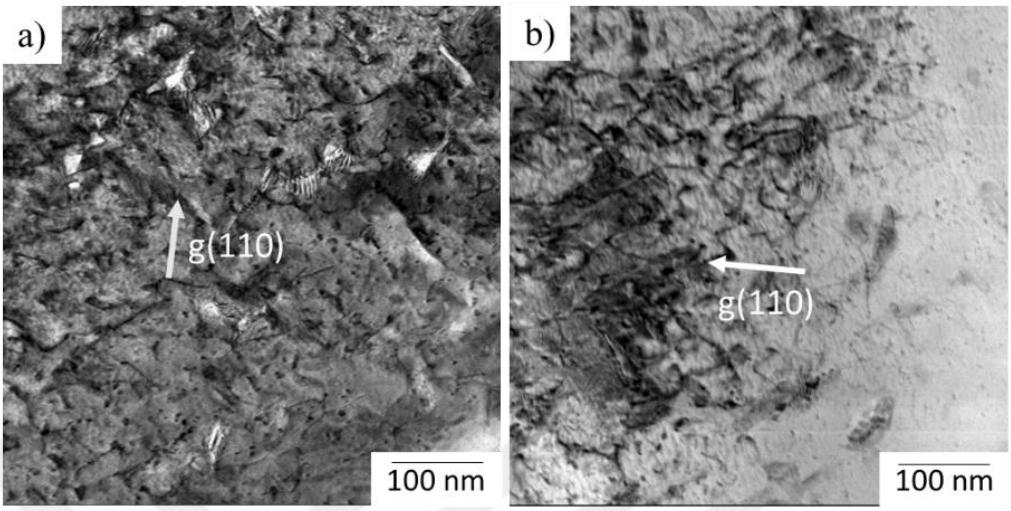

Figure 5.3 Bright field STEM images of (a) as-received (b) as-shocked conditions after 600 dpa irradiation along g=(110) direction.

Fig. 5.4 shows the microstructure of the as-received and as-shocked samples after 600 dpa irradiation. The distribution of voids is quite inhomogenous and the voids form generally at the shallow depths.

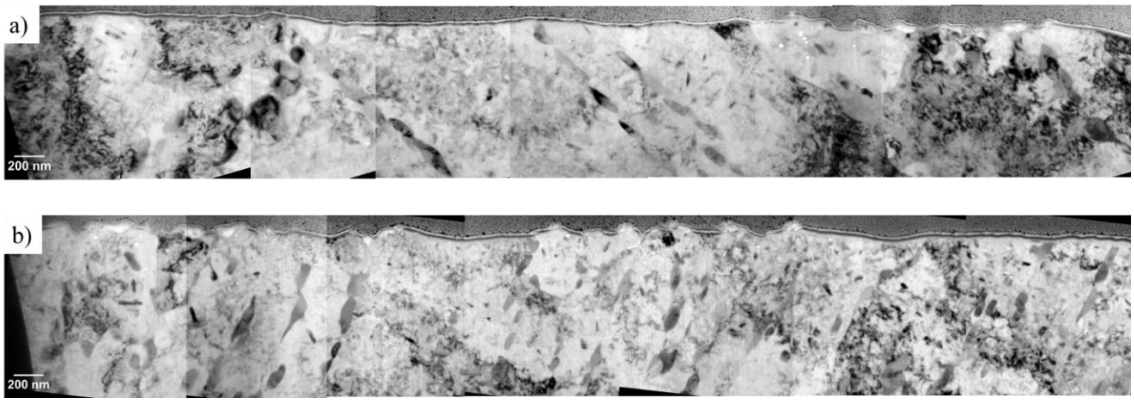

Figure 5.4 Stitched BFTEM images of (a) as-received (b) as-shocked samples irradiated to 600 dpa. Images were taken at ~1 µm under-focus condition.

Fig. 5.5 shows the depth-dependent swelling curves for as-received and as-shocked samples, superimposed on the SRIM-calculated dpa and injected Fe ion profiles. As seen in the micrographs as well, the swelling at the shallow regions is quite high compared to the deeper depths. This can be attributed to either defect imbalance at the shallow depths as reported by Shao et al., or surface effects [147].

If the deeper regions are magnified as shown in the inset in Fig. 5.5, it can be seen that the swelling in the case of as-shocked HT-9 is slightly higher than that of as-received HT-9 sample. It should also be noted that void formation at the regions beyond 500-600 nm was inhibited by injected interstitials [150].

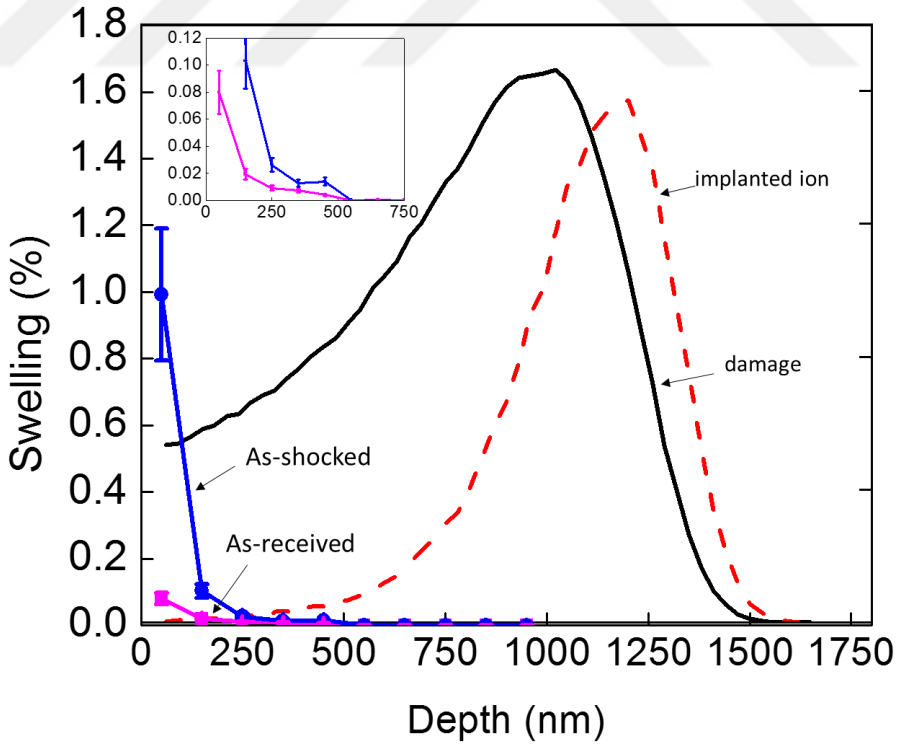

Figure 5.5 Swelling vs. depth profiles of the as-received and as-shocked HT-9 steels after 600 dpa irradiations. Swelling curves were superimposed on the SRIM-calculated dpa and injected Fe ion profiles.

5.5 Discussion

It has been shown that the swelling is closely related with the formation of needle-like precipitates which were reported to be M_2X (M: Fe or Cr; X: C or N) type precipitates having hexagonal crystal structure. They have coherent interfaces along {110} planes which act as efficient sinks for the recombination of vacancies and interstitials, similar to the ODS alloys having large density of coherent precipitates [218]. It has been reported by many authors that irradiation induces the precipitation of M_2X type precipitates especially in the alloys containing high amount of Cr and C [218,219]. In this study, we also observed the formation of needle-like precipitates as shown by arrows in Fig. 5.6.

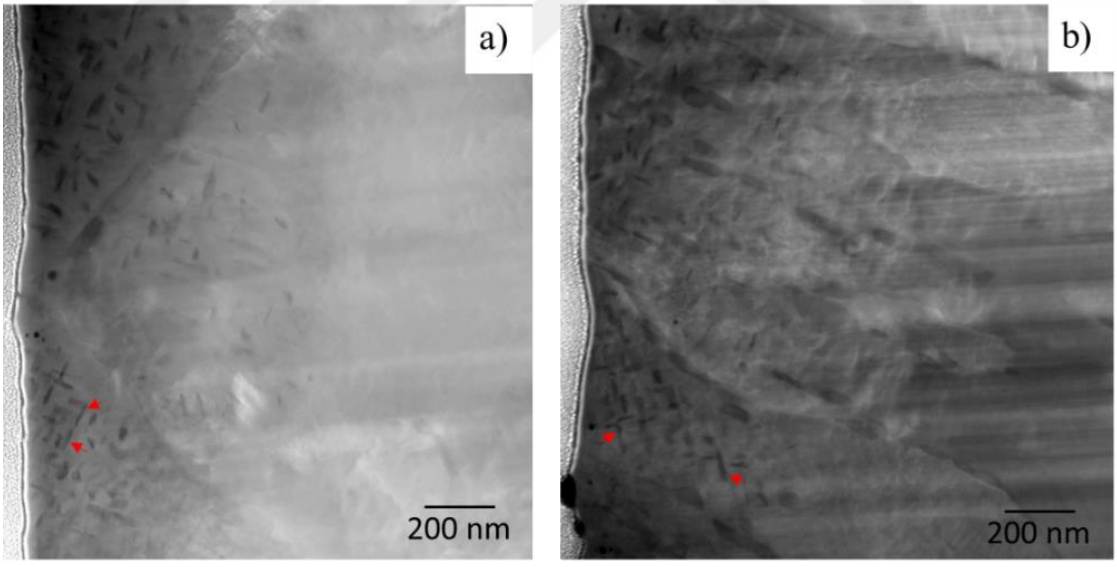

Figure 5.6 HAADF images of (a) as-received (b) as-shocked samples after 600 dpa irradiation. Arrows show the needle-like precipitate formation as a result of irradiation.

To investigate their composition, EDS mapping was performed on both samples as in Fig. 5.7. Large precipitates at the grain boundaries are rich in Cr, Mo, V and C which can be identified as $M_{23}C_6$ type carbides. Moreover, needle-like precipitates are rich in Cr, Fe and C which is consistent with the composition of $(Fe,Cr)_2C$ precipitates. The number densities of those precipitates were measured as $1.4\pm0.6 \times 10^{21}$ m^{-3} and $1.1\pm0.7 \times 10^{21}$ m^{-3} for as-received and as-shocked samples, respectively. Together with M_2X type precipitates, irradiations resulted in the formation of Si-W-Ni rich precipitates which are small in size and distributed mostly inside the (sub)grains. Those are either G-phase or M_6C precipitates. G-phase has the ideal composition of $M_6Ni_{16}Si_7$ and M can be a transition element such as Ti, Mn, Cr, Zr, V, W, Ta, Hf, or Hb [220]. Moreover, M_6C is a carbide where M is Si, Mo, Ti, Cr, Mn, Fe, Ni, V, Co and W depending on the composition of the alloys [220,221]. It is quite difficult to determine if those particles are G-phase or M_6C as EDS is not accurate on detection of low-z atoms and contamination on the sample might result in inaccurate signal detection. Moreover, it is not quite possible to distinguish them using diffraction methods as their lattice constants are very close (1.12 nm for G-phase and 1.08 nm for M_6C) [23]. Therefore, as Anderoglu et al. speculated [23], we will assume that those particles are almost the same except their carbon content. Therefore, we will name those precipitates as G-phase throughout this chapter. The densities of those precipitates were determined as $2.5\pm0.2 \times 10^{21}$ m^{-3} and $2.3\pm0.8 \times 10^{21}$ m^{-3} for as-received and as-shocked samples, respectively.

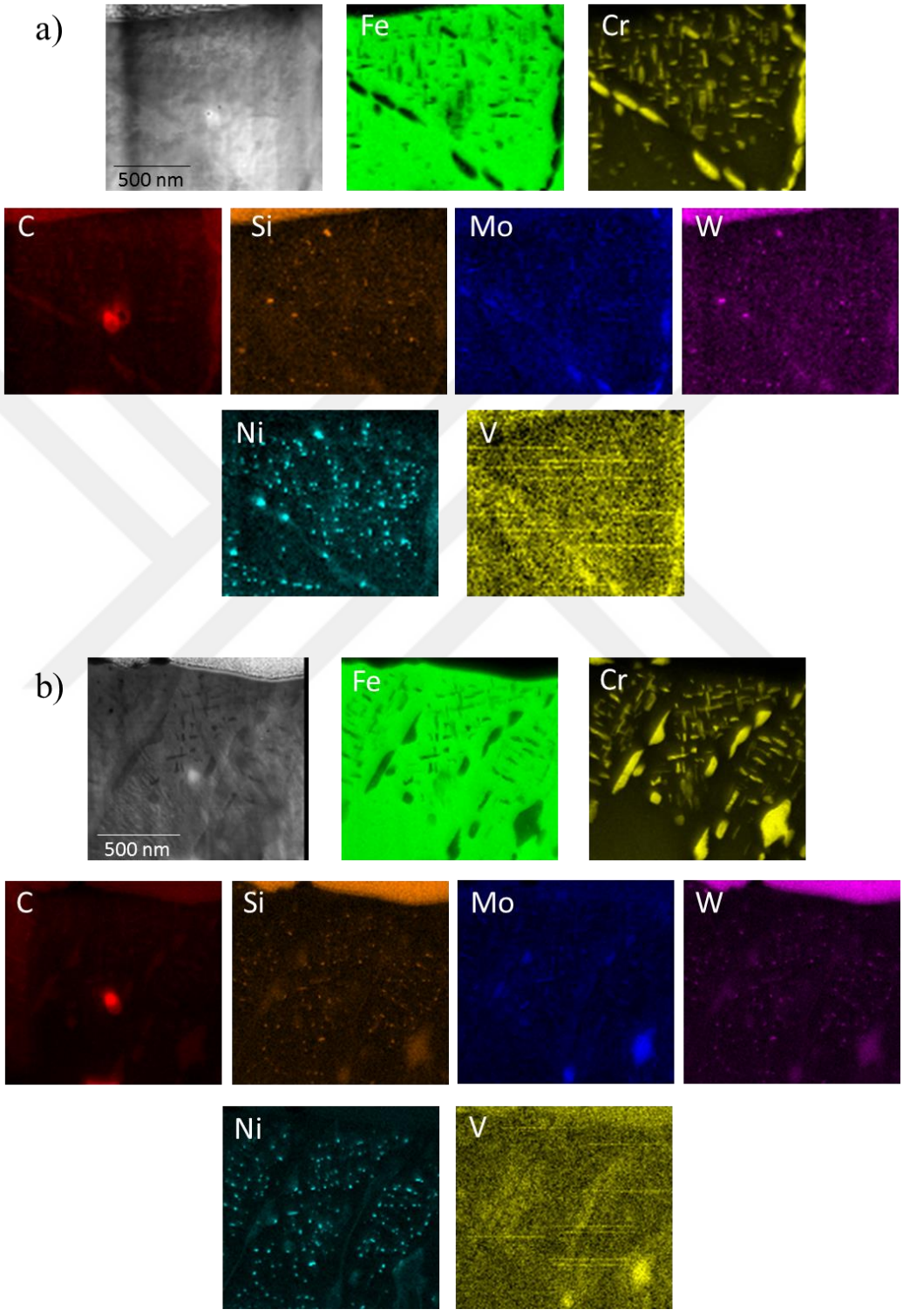

Figure 5.7 STEM EDS mapping of (a) as-received (b) as-shocked HT-9 samples irradiated to 600 dpa.

Even though before irradiation the dislocation density of as-shocked sample is ~2-3 fold higher compared to the as-received condition, swelling of the as-shocked sample seems to be slightly higher than that of as-received condition. Therefore, dislocation density is not the only factor effecting the swelling resistance. In order to understand the effect of dislocations together with irradiation induced precipitates and substructure boundaries, their sink strengths have been calculated assuming all the boundary types and dislocation types have the same sink efficiency. The sink strength, k^2, of the spherical-shaped G-phase particles is denoted as $k^2_{p,G-ph} = 4\pi R_p N_p$ where R_p and N_p are the average size and number fraction of the precipitates, respectively. For needle-like M_2X precipitates, sink strength is defined as $k^2_{p,M_2X} = 4\pi N_p (0.3A^{1/2})$ where A is the surface area of the precipitates and it is defined as $A = \sum_{i=1}^{n} \pi d_i l_i$ (n is the number of precipitates, d_i and l_i are the width and length of the precipitates, respectively). Moreover, sink strength for dislocations is defined as $k_d^2 = Z\rho_d$ where ρ_d is dislocation density and Z is the constant showing the efficiency of the interaction of dislocations with point defects and is determined to be ~1.02 [222]. Sink strength of the boundaries is represented as $k_b^2 = \frac{3\pi^2}{d^2}$ where d is the average (sub)grain (lath) size. The calculated sink strengths for both samples were tabulated in Table 5.2. It is obvious that the sink strength of the M_2X type precipitates is much higher compared to the others. Therefore, even though the dislocation density is higher in shock loaded sample, overall sink strength in the as-received sample is larger.

Table 5.2 Calculated sink strengths of G-phase, M_2X, dislocations and boundaries together with total sink strength in as-received and as-shocked HT-9 samples.

	$k^2_{p,G-ph}$ (m^{-2})	k^2_{p,M_2X} (m^{-2})	k^2_d (m^{-2})	k^2_b (m^{-2})	k^2_{total} (m^{-2})
As-received	$7.0x10^{14}$	$38.5x10^{14}$	$4.8x10^{14}$	$0.6x10^{14}$	$50.9x10^{14}$
As-shocked	$5.5x10^{14}$	$30.3x10^{14}$	$10.6x10^{14}$	$0.4x10^{14}$	$46.8x10^{14}$

Above stated discussion on boundaries assumes that all the boundaries have the same sink strength efficiency or bias. However, different boundaries have different characteristics. For instance, special boundaries are more ordered and have less energy. King et al. has shown that the very low angle boundaries between 0° and 3° have higher sink efficiency and larger denuded zones compared to Σ3 boundaries. Similarly, Demkowicz et al. reported that the existence of high fraction Σ3 twin boundaries does not improve the swelling resistance in Cu which was He implanted at room temperature [223]. Thus, above stated assumption that all the lath boundaries have the same sink strength is legitimate. Even though the amount of special boundaries does not affect the swelling resistance, they affect the radiation induced segregation/depletion (RIS/RID) behavior of the materials. It has been reported that the RID of Cr increases with increase in misorientation angle while low sigma special boundaries suppress this behavior [224].

Edge and screw dislocations have different sink efficiencies in contrast to the above stated assumption while calculating the sink strengths. Sivak et al. has shown that the sink strength efficiency of edge dislocations is higher than that of screw dislocations for SIAs [225]. On the other hand, both type of dislocations have equal efficiencies for

vacancies. As reported in the previous chapter, the fractions of edge dislocations are 0.41±0.06 for the as-received sample; and 0.65±0.06 for the as-shocked sample. Since the fraction of edge dislocations is higher in shock loaded sample, the fraction of SIAs annihilated at the dislocations will be higher compared to the vacancies. This might lead to the easy clustering of vacancies and formation of voids. Thus, together with slightly lower sink strength, high fraction of edge dislocations might be the reason for slightly higher swelling in shock loaded samples.

It should be noted that swelling is still in transient regime even at 600 peak dpa irradiations. At their steady state swelling regime, swelling resistance of as-received and as-shocked samples might change as their sink strength will change due to a possible change in the size and density of irradiation induced precipitates and an additional sink by high density voids.

5.6 Conclusions

In this study, the effect of shock loading on the irradiation response of the HT-9 steels has been investigated. It has been found that while total amount of the low angle and high angle boundaries remains the same for both as-received and as-shocked samples, the amount of boundaries with the misorientation angle of ~60° decreases by ~5% in the case of as-received sample. Moreover, the amount of special boundaries decreased by ~7.5% for both cases and as-received sample has still higher amount of special boundaries. Two beam studies infer that dislocation loop size is finer while the density is higher in as-received samples. Moreover, swelling studies indicates that the distribution of voids is

quite nonhomogenous and the voids form generally at the shallow depths. There is no voids observed at the deeper regions beyond 500-600 nm and the swelling at the depth of 300-600 nm is very low indicating that the swelling is still in the transition regime. At this depth, swelling of as-shocked sample is slightly higher. It has been found that irradiation results in the formation of M_2X and G-phase precipitates. The sink stregth of M_2X precipitates is very high compared to the dislocation and boundary sink strengths and the total sink strength is slightly lower in as-shocked sample. High fraction edge dislocations in as-shocked sample which has higher bias to SIAs compared to vacancies might be another reason for slightly higher swelling. However, once the steady-state regime is reached, the swelling resistance of the samples might change depending on the sink strengths.

6. EFFECT OF TUBE PROCESSING METHODS ON THE TEXTURE AND GRAIN BOUNDARY CHARACTERISTICS OF 14YWT NANOSTRUCTURED FERRITIC ALLOYS[‡]

6.1 Overview

Texture and microstructure of tubes and plates fabricated from a nanostructured ferritic alloy (14YWT), produced either by spray forming followed by hydrostatic extrusion (Process I) or hot extrusion and cross-rolling a plate followed by hydrostatic tube extrusion (Process II) have been characterized in terms of their effects on texture and grain boundary character. Hydrostatic extrusion results in a combination of plane strain and shear deformations which generate low intensity α- and γ-fiber components of {001}<110> and {111}<110> together with a weak ζ-fiber component of {011}<211> and {011}<011>. In contrast, multi-step plane strain deformation by hot extrusion and cross-rolling of the plate leads to a strong texture component of {001}<110> together with a weaker {111}<112> component. Although the total strains are similar, shear dominated deformation leads to much lower texture indexes compared to plane strain deformations. Further, the texture intensity decreases after hydrostatic extrusion of the alloy plate formed by plane strain deformation, due to a lower number of activated slip systems during shear dominated deformation. Notably, hot extruded and cross-rolled plane strain plate

[‡] Reprinted with permission from "Effect of tube processing methods on the texture and grain boundary characteristics of 14YWT nanostructured ferritic alloys" by E. Aydogan, S. Pal, O. Anderoglu, S.A. Maloy, S.C. Vogel, et al., 2016, Materials Science and Engineering A, 661, 222-232, Copyright 2016 by Elsevier.

deformation to ~50% engineering strain creates only a modest population of low angle grain boundaries (LABs), compared to the much larger population observed following the combination of plane strain and shear deformation of ~44% engineering strain resulting from subsequent hydrostatic extrusion.

6.2 Introduction

NFAs are leading candidates for structural components in nuclear reactors due to their exceptional irradiation tolerance, high strength and resistance to oxidation/corrosion under extreme conditions of temperature and stress [19,49,226-229]. There has been substantial progress on optimizing the production of larger heats of NFAs consolidated by hot extrusion (HE), and in some cases, hot isostatic pressing (HIP) [230]. Recently, an NFA with an approximately uniformly distributed population, ~$7x10^{23}/m^3$, of ~2.5 nm Y-Ti-O rich nano-oxides has been developed by Los Alamos National Laboratory (LANL), Oak Ridge National Laboratory (ORNL) and University of California Santa Barbara (UCSB) in collaboration [231]. The presence of coarsening resistant of nano-oxides along with predominantly fine grain size (<1 μm) and high dislocation densities imbue NFAs with higher strength and remarkable thermal stability compared to conventional ODS alloys. Moreover, the nano-oxides help to recombine displacement damage and trap neutron irradiation transmutation product, He, in extremely small bubbles, thereby supressing void swelling and grain boundary embrittlement [19,49-51].

Although significant progress has been made, some major issues associated with HE of NFAs include: severe texturing (the distribution of grain orientations) as well as

anisotropic microstructures and properties; and, bimodal grain size distributions [232-240]. The primary detrimental consequences of these characteristics include low fracture toughness and low creep strength in directions parallel to, and transverse to the HE axis, respectively [227,230,233,240-243]. Additional deformation processing steps to improve properties and/or fabricate shapes are also severely impacted by these characteristics of the HE condition. For example, HE cross-rolled plates develop microcracks [244] and deformation processed tubes experience radial through-wall cracks [245]. Extensive research in Japan and France have identified semi-optimized processing paths for tubing that differ in detail, but in both cases involve a series of cold-pilgering steps to reduce the wall thickness, with intermediate and final heat treatment softening schedules [228,246,247]. This general processing path has been most successful with lower 9 Cr transformable (γ -> α/martensite) steels [230], but 14YWT ferritic stainless nano-oxide strengthened alloys remain difficult to process into thin-walled tubing.

Recent studies have suggested that material with low ductility can effectively be processed to a near net shape using hydrostatic extrusion. It can also produce the final product with enhanced and more isotropic mechanical properties, as well as high powder consolidation densities [248-250]. For example, a recent review [251], and related research on hydrostatically extruded NiAl [252], revealed improved properties and beneficial changes in texture [253] due to the shear dominated stress state generated in hydrostatic extrusion. One hydrostatic extrusion path uses a high-pressure fluid in a die chamber to impose compressive stresses that lower ram pressures and temperatures, resulting in better formability and surface finishes [251-254].

In this chapter, the effects of different processing routes on texture and grain boundary characteristics of as processed 14YWT NFA tubes have been investigated using neutron and electron diffraction techniques.

6.3 Experimental procedure

In order to understand the effects of different processing methods on the resulting texture and grain boundary characteristics, 14YWT tubes were produced by two different initial routes followed by a novel hydrostatic extrusion process to produce tubes that were processed to full density. Process I utilizes the initial processing method of thermal spraying while Process II uses a conventional mechanical alloying method followed by hot extrusion. Fig. 6.1 shows that Process I is the combination of gas atomization reaction synthesis of Fe-based NFA precursor powders, deposited by high velocity oxy-fuel (HVOF) thermal spray methods on tubular pre-forms, followed by hydrostatic extrusion to process the tube to final dimensions. A "mother tube" was manufactured through HVOF deposition on an Al mandrel with Fe-based NFA precursor powders (20-53μm dia.). The fugitive Al mandrel was removed from the deposit section with a phosphoric acid etching treatment and initial machining was performed to remove the interior (~250μm) layer of intermetallic phase (FeAl or Fe_3Al) that appeared to form during the deposition process. The samples were then heat treated at 1000 °C for 5hr under vacuum following thermal spray deposition to promote the oxygen exchange reaction and Y-Ti-O dispersoid formation within the coating. Finally, hydrostatic extrusion was applied two times with a

4:1 area reduction (~44% engineering strain) at 815 °C by using a solid support mandrel plus external can to create a beneficial stress state for extrusion.

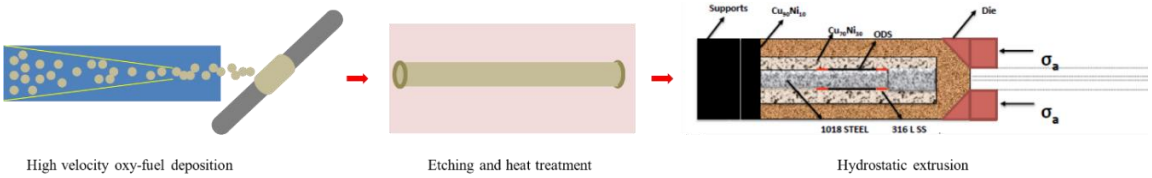

Figure 6.1 Processing steps of Process I

The schematic for Process II is shown in Fig. 6.2. Powders were first produced by gas atomization method by ATI Powder Metals Laboratory (Pittsburgh, PA). After atomization, the Y phase separates and requires ball milling to create a more homogenous chemistry. So, the nominal 14wt%Cr-3W-0.35Ti-0.25Y iron alloy powder was ball milled by Zoz, GmbH (Wenden, Germany) with the addition of FeO powder for 40 h in a CM100b attritor mill. The powders were sealed in cans backfilled with Ar to remove any atmosphere contamination and degassed at 400 °C. The canned powders were then hot extruded at 850 °C to create a solid billet. After extrusion, the alloy was annealed for 1 h at 1000 ºC and then hot cross-rolled at 1000 °C to a ~50% of thickness reduction (50 % engineering strain) resulting in a final thickness of ~10 mm. The solid billet was then electro-discharge machined in the direction perpendicular to hot cross-rolling direction to produce a tube. This tube was then hydrostatically extruded at 815 °C using the same process described for the thermally sprayed tube. Fig. 6.3 shows the tubes with a final wall

thickness of 0.5 mm and outer diameters of ~8 mm and ~3.5 mm for Process I and Process II, respectively.

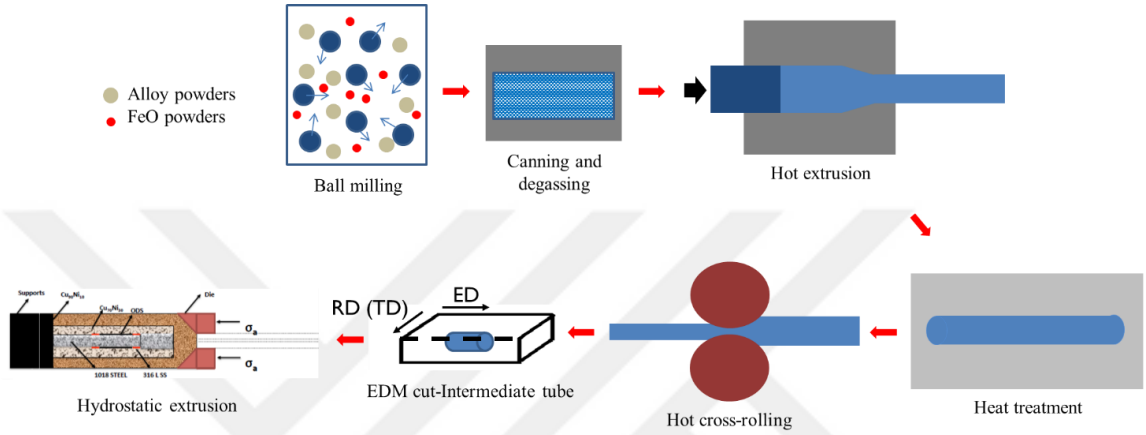

Figure 6.2 Processing steps of Process II (RD: rolling direction, TD: transverse direction, ED: extrusion direction)

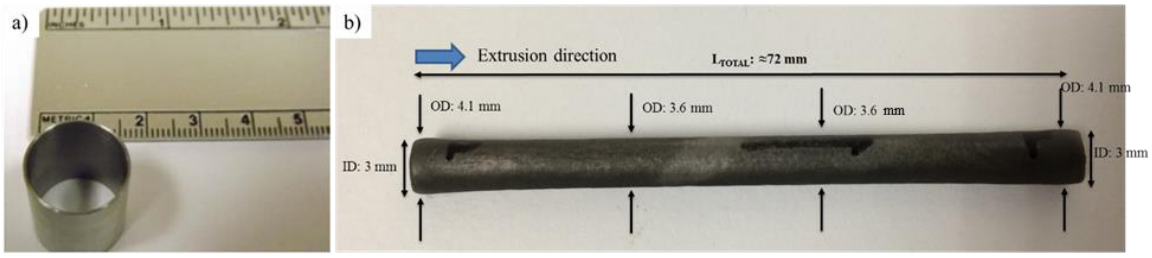

Figure 6.3 Photos showing the final dimensions of the tubes produced by (a) Process I, and (b) Process II.

Grain boundary characteristics were investigated by orientation imaging microscopy (OIM) while texture analysis was implemented using both OIM and neutron diffraction methods. OIM by EBSD using an SEM was used to examine the grain

boundary characteristics and texture of the plate and tubes. It should be noted that EBSD is limited to the grain size studies down to 60 nm [100,101]. Here, EBSD was carried out in an FEI Inspect FEG SEM equipped with TSL EBSD detector. All the experiments were performed by tilting the sample at 70° from the horizontal, at an acceleration voltage of 20 kV and aperture size of 50 µm. The sizes of the scanned regions was either 60µmx90µm or 240µmx320µm, where the step size for the data collection was chosen based on the grain and substructure dimensions. Samples for the EBSD scans were obtained from the tube and plate faces that were prepared to achieve very smooth surfaces by standard metallographic techniques followed by jet electropolishing using a solution of perchloric acid (5%) and methanol at -40 °C with an applied voltage of 20 V.

Bulk texture measurements probing the grain orientation distribution function over the complete volume of each sample were collected on the HIPPO instrument at the pulsed neutron spallation source at LANSCE [103]. The samples were located ~9 m from the neutron moderator and diffracted neutrons were detected by 1240 ^{3}He tubes arranged on panels distributed over five conical rings with scattering angles ranging from $2\theta = 40°$ to 150°. Samples were glued on standard HIPPO holders, with their tube axis parallel to the holder axis, and then loaded into the robotic sample-changer. The entire ~10 mm long tubes were centered in a 10 mm diameter beam, thus capturing the entire sample volume. Diffraction patterns were collected over ~20 minutes for samples rotated around the vertical axis at 0, 67.5 and 90 degrees. The diffraction data was analyzed by simultaneous Rietveld analysis of 135 diffraction patterns using the E-WIMV texture algorithm with a 10 degree resolution of the orientation distribution function.

Orientation distribution function (ODF) analysis and pole figure plotting for both electron and neutron texture measurements was performed using the MTEX package [255]. The EBSD data was analyzed using the TSL OIM Analysis 7 software.

6.4 Results

6.4.1 Tube processing by Process I

The only deformation that occurs in consolidation by Process I is by hydrostatic extrusion and the corresponding microstructures isolate the unique effects of this processing path. Fig. 6.4a shows the orientation distribution of the grains obtained by the OIM analysis of the 14YWT sample produced by Process I. Even though the physical extrusion direction is shown in a diagonal direction in the map, the coordinates of the map have been rotated in such a way that the extrusion direction is into the page in order to determine the grain orientations in the extrusion direction. Consequently, predominantly existing green color infers that most of the grains are oriented with a (101) plane normal that is parallel to the extrusion direction. The band contrast map in Fig. 6.4b together with Fig. 6.4c show that Process I results in wide grain area fraction distribution as a function of size. However, there are many more small grains that yield a corresponding average diameter of ~2μm. Fig. 6.4d shows that hydrostatic extrusion results in a large fraction (~53%) of low angle boundaries (LABs) with misorientation angles between $2° < \theta < 15°$.

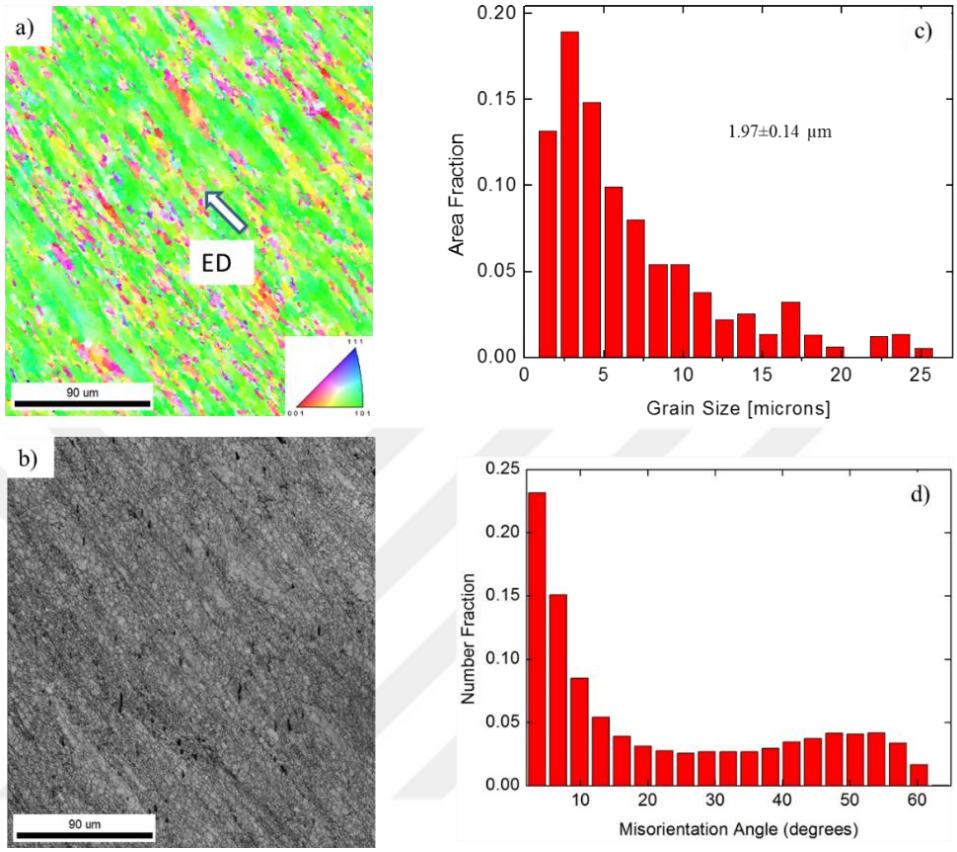

Figure 6.4 An OIM showing (a) the crystallographic orientation of the grains; (b) the corresponding band contrast gray scale map of the grain structure; (c) the grain area distribution as a function of the grain size; and, (d) the grain boundary misorientation angle distribution in 14YWT samples produced by Process I.

Fig. 6.5 shows the pole figures of the sample produced by Process I as determined by both neutron diffraction (Fig. 6.5a) and EBSD (Fig. 6.5b). Even though data processing functions and probed sample volumes are greatly different for neutron diffraction and EBSD, both produce similar pole figures with only a slight difference in the texture intensity. From the pole figures it is obvious that the hydrostatic extrusion to 44% strain produces a typical α-fiber texture <110>∥ED, generally common to deformation processed ferritic alloys [48,256].

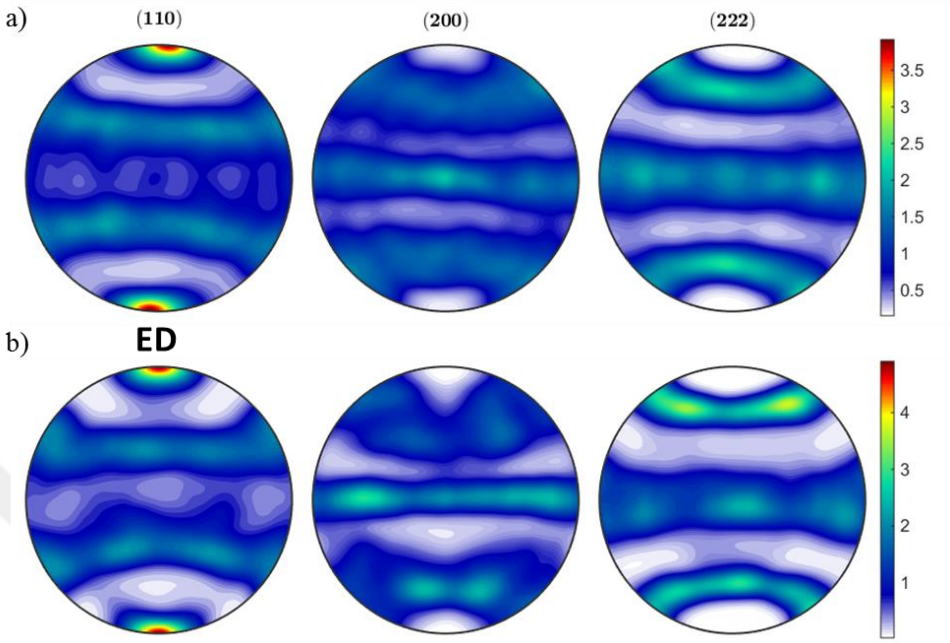

Figure 6.5 Pole figures of 14YWT samples produced by Process I and obtained by (a) Neutron diffraction and (b) EBSD techniques. (ED: extrusion direction)

The ideal orientations of texture components in bcc materials are shown schematically for φ_2 = 0° and 45° ODF sections in Fig. 6.6 and Table 6.1 [257]. As noted previously, for bcc steels the important fiber textures are the α-fiber (<110>∥RD), ε-fiber (<011>∥TD), γ-fiber (<111>∥ND), η-fiber (<100>∥RD), θ-fiber (<001>∥ND), and ζ-fiber (<011>∥ND) [258,259] where RD, TD and ND stand for rolling direction, transverse direction and normal direction, respectively. It should be noted that 'RD' will be replaced by 'ED' throughout the paper.

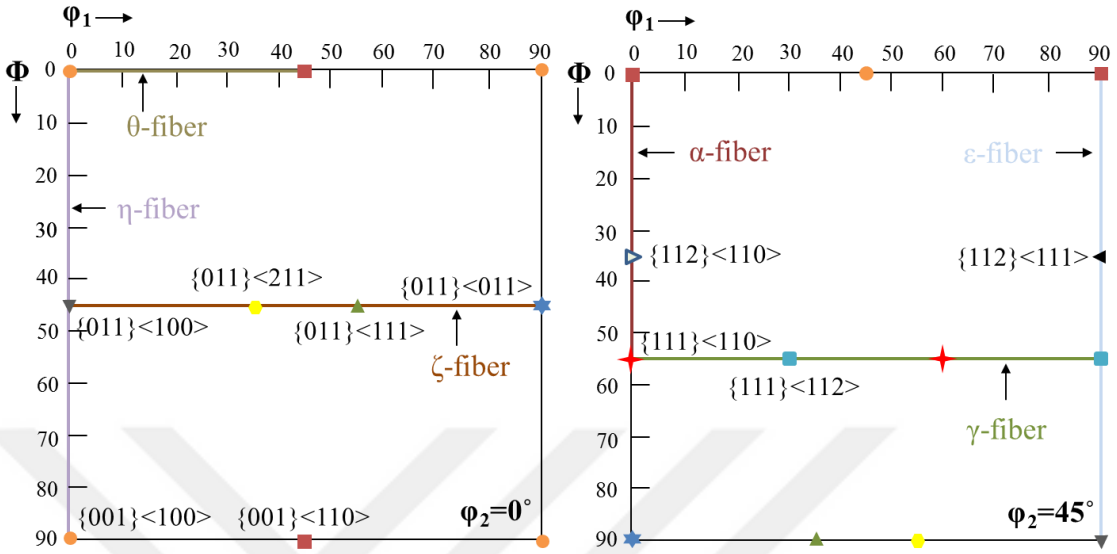

Figure 6.6 Schematic illustration of the important texture components in bcc materials (Reproduced from Ref [257]).

Table 6.1 Important fiber textures and orientations for bcc materials [257].

Fiber name	Fiber axis	Components
α	<110>∥RD	{001}<110>,{112}<110>, {111}<110>
ε	<011>∥TD	{001}<110>,{112}<111>, {111}<112>,{011}<100>
γ	<111>∥ND	{111}<110>,{111}<112>
η	<100>∥RD	{001}<100>,{011}<100>
θ	<001>∥ND	{001}<100>,{001}<110>
ζ	<011>∥ND	{011}<100>,{011}<211>, {011}<111>,{011}<011>

Although EBSD might not give fully representative results because of its limited probed volume, Fig. 6.5 confirms that the probed area on the tube surface using OIM analysis represents the bulk texture obtained by neutron diffraction well. However, there might be a texture gradient through the thickness of the tube wall. In order to further examine and represent the bulk texture, detailed analyses of ODF plots and inverse pole figures were obtained using the neutron diffraction method. It is worthwhile to point out that while neutron diffraction probes a much larger volume than OIM, all spatial information is lost. Hence, while the detailed texture analyses were employed using neutron diffraction, only OIM can provide grain misorientation angles and orientation maps.

Fig. 6.7 shows the neutron diffraction resulted ODF maps for the 14YWT sample produced by Process I at constant φ_2=0° and φ_2=45°. Comparing these maps with Fig. 6.6 shows that the dominant texture is α-fiber at <110> having the strongest intensity on {001}<110>. Furthermore, weaker γ-fiber component of {111}<110> and ζ-fiber on {011}<211> and {011}<011> can be observed. The overall texture index was calculated as 2.6 using ODF neutron diffraction data indicating a moderate texture strength relative to a texture index of 1 for a perfectly random texture and infinity for a single crystal.

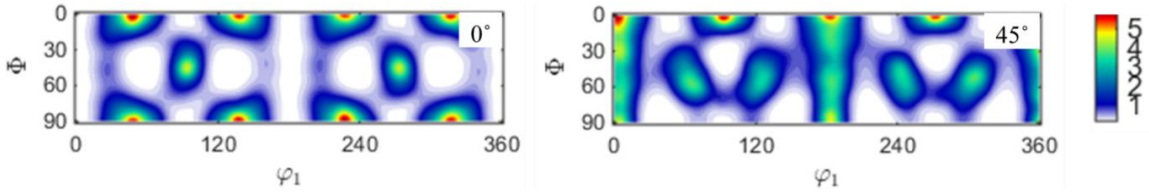

Figure 6.7 The neutron diffraction produced ODF, represented as sections in Euler space, for the 14YWT tube produced by process I at φ_2 values of 0° and 45°.

6.4.2 Tube processing by Process II

Fig. 6.8 shows EBSD measurements on the 14YWT intermediate tube, EDM-cut from the hot extruded and cross-rolled plate, with information analogous to that shown in Fig. 6.4 for the tube, only hydrostatically extruded in Process I. Note the tube is microstructurally identical to the cross-rolled plate, differing only in its geometric reference orientation. Since this alloy condition was characterized before the final hydrostatic extrusion step, as illustrated in Fig. 6.2, it is designated as being "intermediate". Fig. 6.8a is an orientation distribution map. The arrows indicate the initial hot extrusion (ED) and the transverse cross-rolling directions (RD). The predominantly red color infers that most of the grains are oriented with (100) plane normal parallel to the tube wall thickness. Fig. 6.8b, Fig. 6.8c and Fig. 6.8d show that the intermediate tube has a tri-modal grain size distribution and fewer LABs (~32%) compared to the tube produced by Process I (53%).

Since the intermediate tube was cut from the cross-rolled plate, coordinates of the plate were transformed into the tube coordinates as shown in Fig. 6.9. There is a common extrusion direction (ED) for the plate and tube. Radial wall thickness directions of the tube are designated ThD and directions corresponding to the normal and rolling directions are designated as ThND and ThRD, respectively. However, the tube surface ED is only parallel to that for the plate surface at 0° and 180° around the circumference, while it is parallel to the plate sides at 90° and 270°.

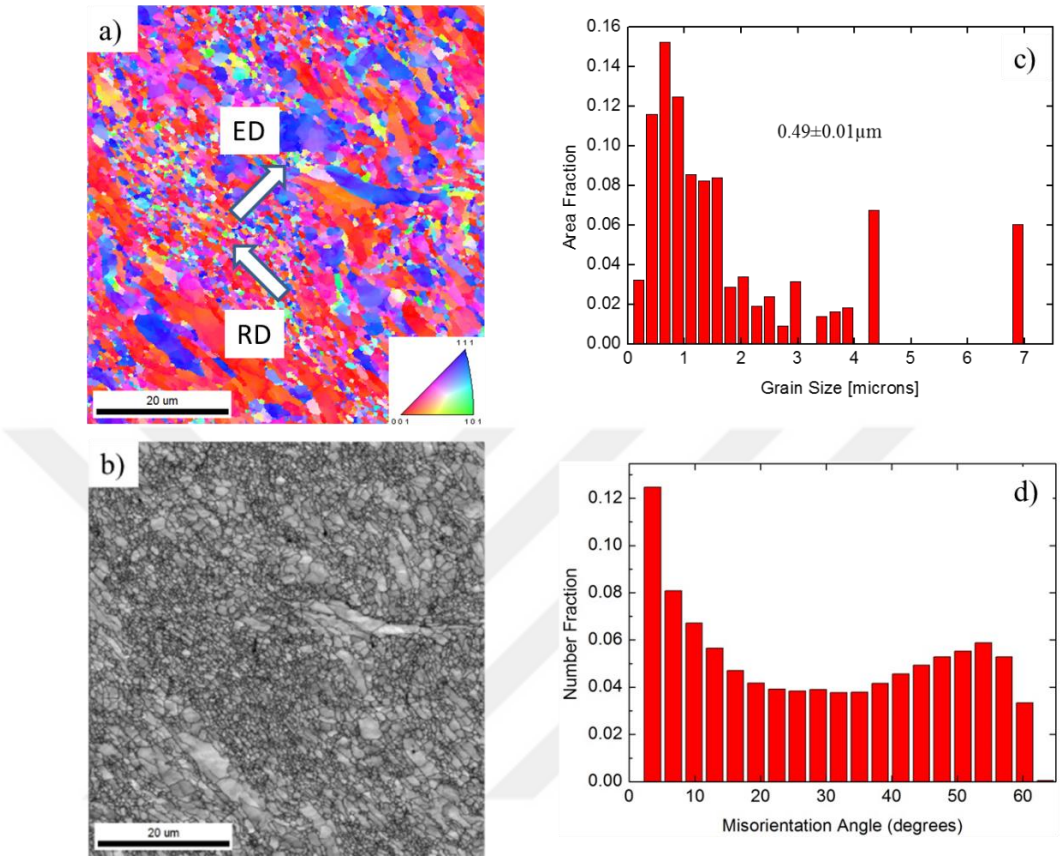

Figure 6.8 EBSD characterization of the intermediate tube alloy condition showing (a) an orientation map of the crystallographic distribution of the grains; (b) a band contrast map of the grain structure in gray scale; (c) the grain area distribution as a function of size; and, (d) the grain boundary misorientation angle distribution.

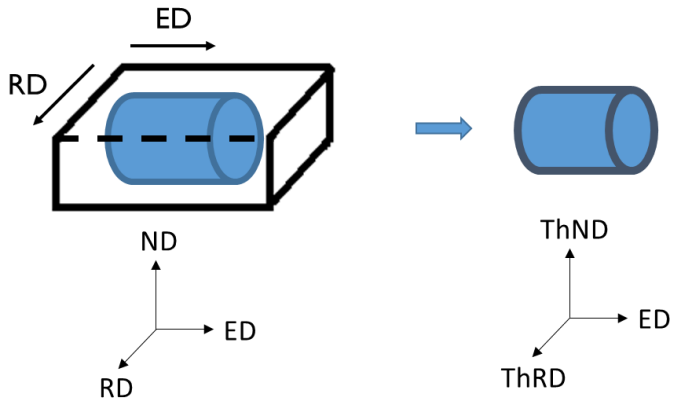

Figure 6.9 Coordinate system of the intermediate tube transformed from the plate form.

Fig. 6.10 shows the pole figures of the intermediate tube determined by both neutron diffraction (Fig. 6.10a) and EBSD (Fig. 6.10b) at 0° (or 180°). The pole figures calculated by both methods are again similar, with slight intensity differences is observed. Based on the coordinate system defined above, pole figures indicate that the intermediate tube has texture of both <110>∥ThRD and <200>∥ThND. Moreover, as it must, the intermediate tube RD shares the <110> α-fiber texture with the cross-rolled plate. As discussed elsewhere [245], (100)-type planes lie parallel to the plate faces as well as to the tube surface at 0° and 180°, while they are normal to the tube surface at 90° and 270° as illustrated in Fig. 6.9. The {001}<110> system is oriented for brittle cleavage fracture leading to microcracking in the plate [245] and radial tubing cracks, especially at 90° and 270°. The intermediate tube has a strong neutron diffraction texture index of 10.1.

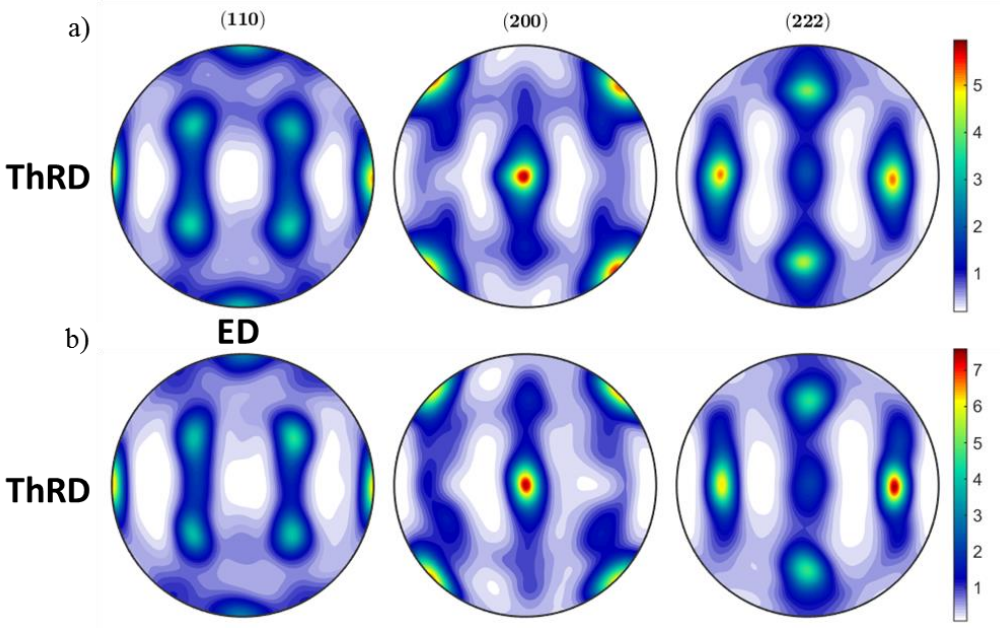

Figure 6.10 Pole figures of intermediate 14YWT tube obtained by (a) Neutron diffraction, and (b) EBSD techniques.

Fig. 6.11 shows the sections of the neutron diffraction resulted ODF maps in Euler space for the intermediate 14YWT tube at constant φ_2=0° and φ_2=45°. When compared with Fig. 6.6, it can be seen that intermediate tube has strong θ- and ε-fiber on {001}<110> together with a weak γ-fiber on {111}<112>. It should be noted that the main deformation axis is considered as the axis for all tubes, which is the extrusion direction. However, as shown in Fig. 6.10, intermediate tube has a stronger texture in rolling direction through the wall thickness (at 90° and 270°), which is transverse to the extrusion direction. Since the rolling direction was taken as the transverse direction during ODF calculations, the corresponding plots of the intermediate tube by reference frame definition exhibit θ- and ε-fiber texture (<110>∥TD) rather than α fiber (<110>∥RD) which is a typical texture for ferritic steels, as found in the plate. Again, the actual microstructures are identical in both cases.

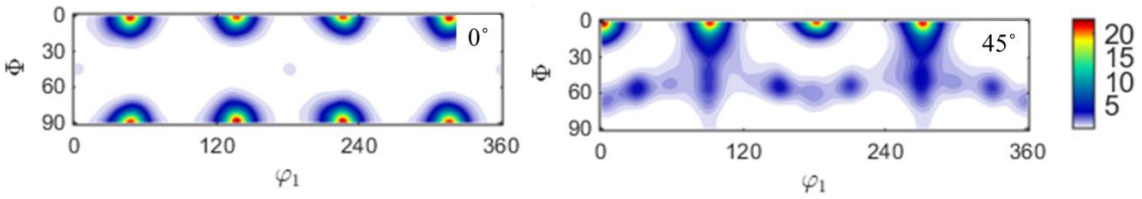

Figure 6.11 ODF, represented as sections through Euler space, of the intermediate 14YWT tube at constant φ_2 values of 0° and 45°.

Fig. 6.12a shows the orientation map of the grains in the extracted tube after final hydrostatic extrusion as described in Fig. 6.2. The coordinates of the map have been rotated in such a way that the radial direction of the tube (normal direction-ND) points

through the page. Consequently, the predominantly existing red color infers that most of the grains are oriented with (100) plane normal parallel to the sample normal direction. The band contrast map in Fig. 6.12b and grain size plot in Fig. 6.12c show that very small and very large grains exist, suggesting a bimodal grain size distribution with an average grain size of ~0.5 μm. Fig. 6.12d shows that fraction of LABs increases from 32% to 46% after hydrostatic extrusion.

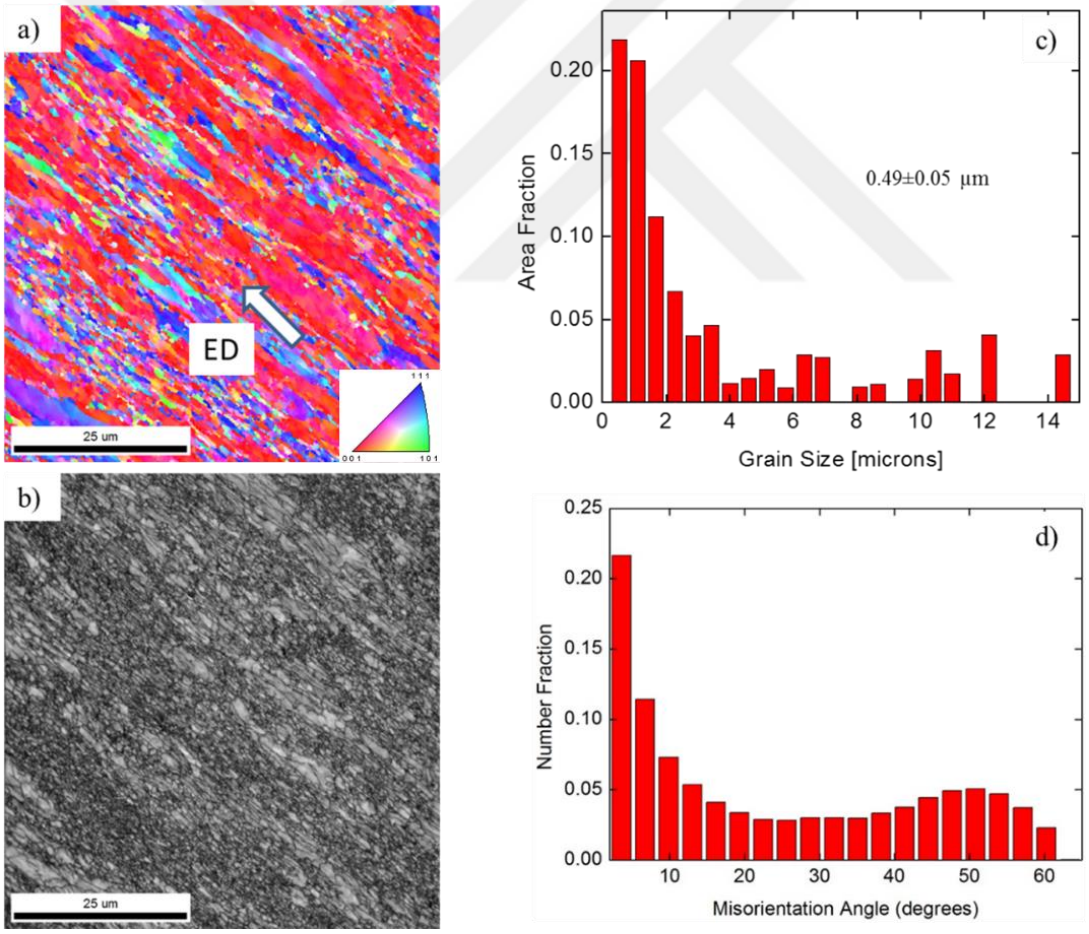

Figure 6.12 (a) Orientation map showing the crystallographic distribution of the grains; (b) band contrast map showing the microstructure in gray scale; (c) grain size distribution plot; and, (d) grain boundary misorientation angle distribution in 14YWT final tube produced by Process II.

Fig. 6.13 shows the pole figures of the tube after hydrostatic extrusion derived by both neutron diffraction (Fig. 6.13a) and EBSD (Fig. 6.13b), yielding different results in this case. While the neutron diffraction indicates a broken fiber texture of <110>∥ED, both the EBSD orientation map and pole figures show a maximum texture index in <200>∥ND. However, the difference between the bulk texture obtained by neutron diffraction and surface texture determined by EBSD is the result of the position of the EBSD sample on the SEM stage. Since the data shows the maximum texture on <200> rather than <110>, the EBSD reflects a region that is aligned 45° to the extrusion direction. Since the samples are tubes, their orientation reference frame determines the nominal texture that must be considered in reaching any conclusions or in making comparisons.

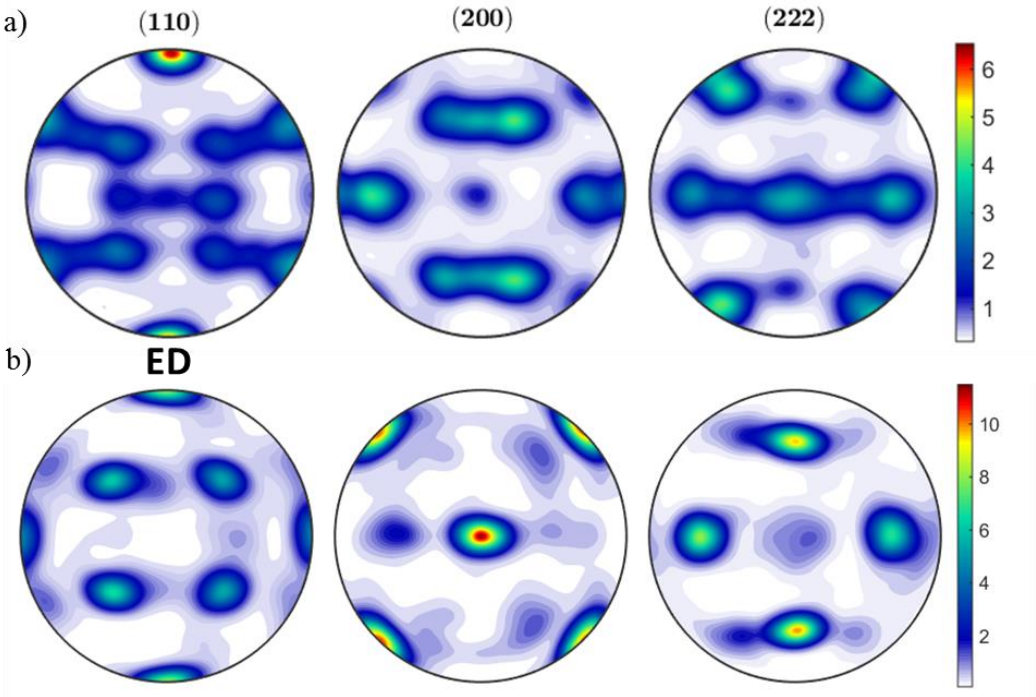

Figure 6.13 Pole figures of 14YWT final tube after hydrostatic extrusion obtained by (a) Neutron diffraction, and (b) EBSD techniques.

The neutron diffraction data shows that the initial processing steps of hot extrusion, annealing and hot cross-rolling, leads to discontinuity in the fiber texture as shown in Fig. 6.13a. The overall texture index was calculated as 8.6 using neutron diffraction. The texture index decreased from 10.1 to 8.6 after hydrostatic extrusion with 25% strain in the intermediate tube, since the principal deformation direction is in the opposite to that for the hot cross-rolling. These results in combination with those observed for Process I, indicate that hydrostatic extrusion produces relatively weak textures.

Fig. 6.14 shows the neutron diffraction resulted ODF maps of the 14YWT final tube produced by Process II at constant φ_2=0° and φ_2=45°. If they are compared with Fig. 6.6, it can be seen that α-fiber has the maximum intensity on {111}<110> along with a weak discontinuous γ-fiber on {001}<110>. For φ_2=0° there is a very weak ζ-fiber texture on {011}<211> and {011}<011>.

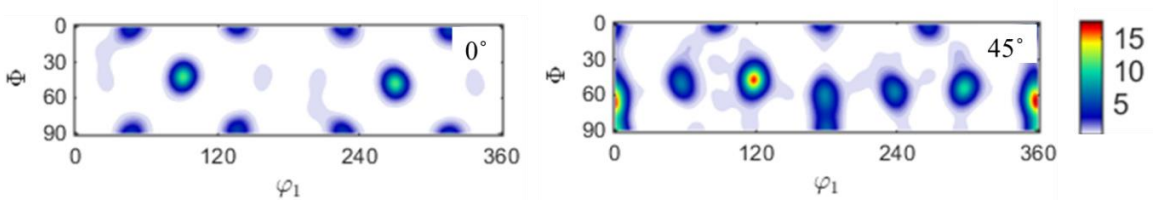

Figure 6.14 ODF, represented as sections through Euler space, of the 14YWT final tube after hydrostatic extrusion at constant φ_2 values of 0° and 45°.

6.5 Discussion

Large-scale deformation behavior of polycrystalline Fe is quite complex since it activates a number of different slip planes like {110}, {112} and {123}, and unlike fcc

materials, is not confined to only closed packed planes. Depending upon various factors like mode of deformation, processing history (strain path), composition, initial microstructure and orientation of the grains, deformation involves different combinations of these slip systems. These multiple factors also affect the dislocation substructure and local misorientations between sub-grains. The result is the production of a wide range of possible textures in the final microstructure [260]. In the present study two different large deformation processing methods were used to fabricate tubes. Both Process I and II create microstructures with a strong <110>∥RD texture with various grain sizes.

Rolling and extrusion are usually regarded as plane strain deformations. However, a gradient in the stress state exists in the through thickness of a rolled or extruded plate. Deformation in the near surface region, in contact with the die, is dominated by a shear component. The center of the plate experiences compressive stresses and deformation occurs under plane strain conditions [261]. In contrast, during hydrostatic extrusion of a thin-walled tube the outer layer is dominated by a state of compressive stress, while the central layer is deformed by a dominant shear stress component [262].

It is observed that both hydrostatic extrusion and conventional hot extrusion processes produce a strong texture on {001}<110>; however, there are remarkable differences in the texture intensities. The tube produced through hydrostatic extrusion in Process I shows maximum texture index of 2.6, whereas the tube produced at the intermediate step in Process II which experienced a similar amount of deformation shows a much stronger texture index of 10.1. Pal et al. [245] has investigated the inverse pole figures of the process II produced intermediate plate before EDM cutting tubes from it as

well as after hydrostatically extruding the intermediate tube. The texturing found here is generally consistent with their study; while the textures in the plate and the hydrostatically extruded tube are similar in the extrusion direction, the maximum texture intensity changes from <100> to <111> in the tube thickness normal direction as a result of the hydrostatic extrusion. This rationalizes the observation that while the intermediate plate exhibits an extensive amount of microcracking, the hydrostatically extruded final tube with a texture on <111>∥ND resists such cracking in Process II [245]. Similarly, comparing the inverse pole figures of the hydrostatically extruded final and intermediate tubes shown in Fig. 6.15 reveals that while hydrostatic extrusion develops a texture of a mixture of <111> and <100> along the ND, <100> is more profound along the ND of the intermediate tube. Hot working of the bcc steels results in cold rolling textures if the material does not undergo any kind of ferrite to austenite transformation or complete recrystallization [261,263]. Since 14YWT steels are fully ferritic and do not recrystallize during the present hot-working conditions, the observed texture differences can be explained in terms of cold rolling textures. Raphanel et al. [264] predicated the cold rolling texture of bcc steel based on a relaxed constant modification of Taylor theory. Simulations by reducing ε_{13} and ε_{23} shear strain components increases the intensity of {001}<110> texture and produces an elongated pan-cake shaped grains, as was observed in the cross-rolled plate and intermediate tube. Consequently, formation of high volume fraction of {001}<110> texture components in the intermediate tube orients the {001} plane normal along the tube thickness normal direction (shown in Fig. 6.15b).

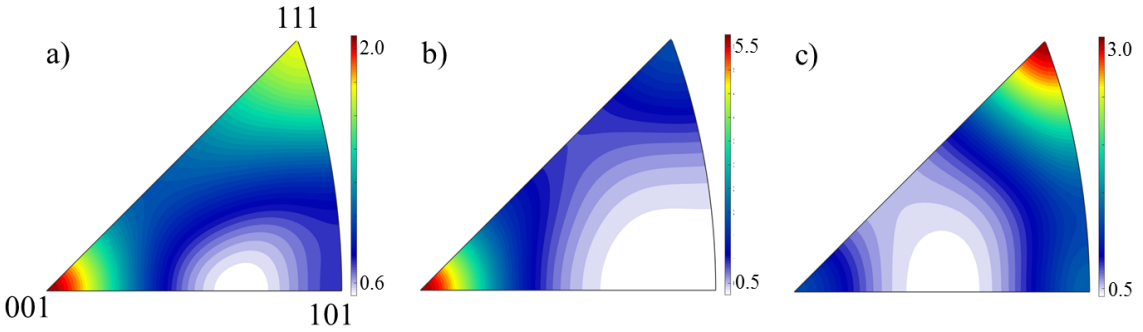

Figure 6.15 Neutron diffraction produced inverse pole figures of (a) hydrostatically extruded final tube in Process I, (b) intermediate tube in Process II and (c) hydrostatically extruded final tube in Process II.

Our results show that after hydrostatic extrusion of the intermediate tube in Process II, the texture index is weakened from 10.1 to 8.6. Raabe et al. [265] also reported that the shear stress weakens the texture relative to the pre-deformed condition. This is simply attributed to a lower number of activated slip systems during pure shear deformation. The major texture component originating under simple shear deformation of a bcc steel is the 'Goss' texture component {110}<001>. However, the 'Goss' texture component is not very stable, and can easily transform to the stable components of {001}<110> of α-fiber or {111}<110> of γ-fiber depending upon the relative strength of each fiber [265]. This is responsible for the origin of weak shear texture components of {111}<110> and {001}<110> producing a partial <111>∥ND texture.

The compressive part of the stress in hydrostatically extruded tubes introduces the common α-fiber. The nature of the deformation process is further corroborated using the number fraction vs. misorientation angle plots in Fig. 6.16. The hydrostatically extruded tubes contain large fraction of LABs indicating the association of shear deformation and

high amount of local reorientation [260], which in turn produces a continuous spread of orientation along α-fibers rather than developing a sharp texture. The effect of hydrostatic extrusion is more drastic when the starting material possesses a pre-existing texture (due to hot cross-rolling and extrusion), completely changing the texture. In this case, the maximum texture intensity is observed on the {111}<110> component of γ fiber due to the restriction of activated slip system and activation of high Taylor factor shear planes. Development of strong γ fiber has been reported to be good for the deep drawing ability of high chrome-ferritic steels [265]. It also supports the finding that the hydrostatically extruded final tube in Process II can be produced without cracking as reported by Pal et al. [245].

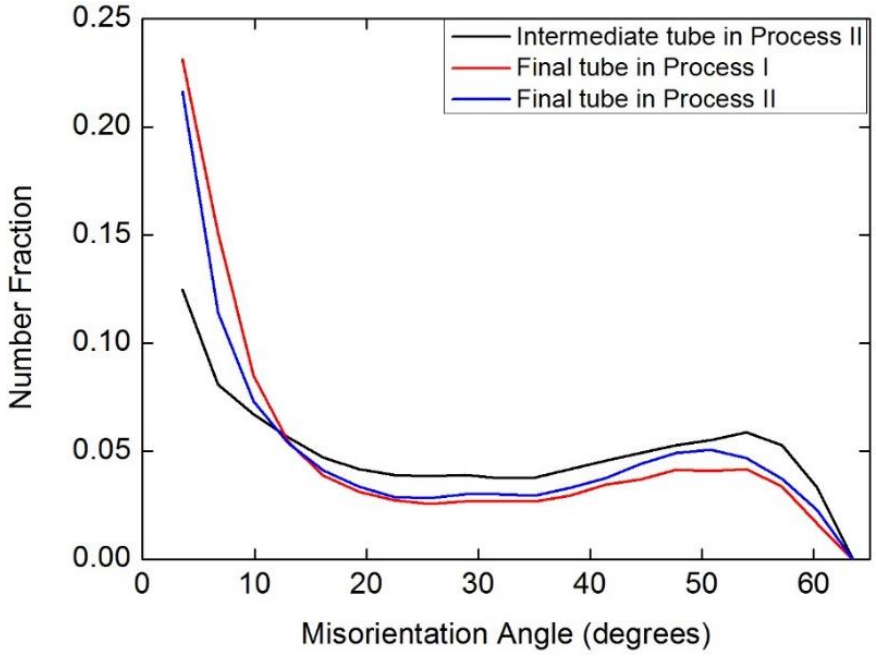

Figure 6.16 Grain boundary misorientation angle distribution of three different tubes produced by Process I and II.

6.6 Conclusions

In this study, the effect of different processing routes on texture and grain boundary characteristics for 14YWT NFA tubes have been investigated. Hydrostatic extrusion which introduces a combination of plane strain and shear deformations results in α- and γ-fibers on {001}<110> and {111}<110> as well as weak textures of ζ-fiber on {011}<211> and {011}<011>. On the other hand, hot extrusion and cross-rolling processes result in plane strain deformations in the case of intermediate plate and tube in Process II, leading to a strong texture on {001}<110> together with weak texture on {111}<112>. While both conventional hot extrusion and innovative hydrostatic extrusion produce a pronounced texture on {001}<110>, shear deformation introduced during hydrostatic deformation produces <111>∥ND texture component. Furthermore, hydrostatic extrusion results in weaker textures compared to the hot extrusion and rolling textures. Even though the final tube produced by Process I and the intermediate tube in Process II are exposed to similar amounts of deformation, the former has a texture index of 2.6 while the latter has a texture index of 10.1. Similarly, when the intermediate tube is hydrostatically extruded, its texture index decreases to 8.6. Together with a decrease in the texture index, α-fiber on {001}<110> weakens and γ-fiber on higher Taylor factor planes, {111}<110>, strengthens as a result of a reduced number of activated slip systems during shear deformation. Moreover, the effect of hydrostatic extrusion on the grain boundary characteristics is quite strong. Local reorientation during shear deformation results in high fractions of LABs compared to the intermediate tube produced by plane strain deformation.

7. EFFECT OF TUBE PROCESSING METHODS ON MICROSTRUCTURE, MECHANICAL PROPERTIES AND IRRADIATION RESPONSE OF 14YWT NANOSTRUCTURED FERRITIC ALLOYS

7.1 Overview

In this chapter, innovative thermal spray deposition (Process I) and conventional hot extrusion processing (Process II) methods have been used to produce thin walled tubing (~0.5 mm wall thickness) out of 14YWT (nanostructured ferritic alloy). The effects of processing methods on the microstructure, mechanical properties and irradiation response have been investigated by using SEM, TEM, micro- and nano-hardness techniques. Even though both processing methods yield the formation of various size Y-Ti-O particles, the conventional hot extrusion method results in a microstructure with smaller NFs (Y-Ti-O particles < 5nm) with higher density. Therefore, Process II tubes have twice the hardness of Process I tubes. Dislocation-dislocation interactions are calculated to be the main hardening mechanism compared to dispersion and grain size strengthening mechanisms in both type of tubes. Different initial microstructures result in different irradiation response in these tubes. The Process II tubes have a finer, denser and more homogenous distribution of NFs which presumably results in at least two orders of magnitude less swelling. Swelling and irradiation induced hardening varies within the Process I tubes due to the inhomogeneity in the initial microstructure. On the other hand, irradiation hardening saturated at ~0.8 GPa for Process II tubes for all irradiation doses.

7.2 Introduction

Next generation fission or fusion reactors will require materials that can withstand radiation doses of several hundreds of dpa over years or decades of service, at temperatures of several hundred degrees Celsius, while exposed to corrosive coolants such as supercritical water or liquid metal [266]. NFAs are considered to be one of the best candidates for structural components in advanced nuclear reactors due to their excellent irradiation resistance, high strength and resistance to oxidation/corrosion under extreme conditions of temperature and pressure [8,226,230,267-269]. The presence of the high density NFs having the size < 5 nm provide higher strength, better thermal stability and creep resistance to NFAs in comparison to conventional ODS alloys [8,232]. NFs hinder the recovery and creep by pinning the dislocations and grain boundaries. This results in fine microstructures with high density dislocations which create high sink densities and enhanced radiation damage resistance in NFAs [67]. Moreover, NFs are reported to serve as sinks for He gas, effectively trapping it in extremely small bubbles during neutron irradiation [9,19,49-51]. On the other hand, all the studies in the literature are limited to irradiations below ~150 dpa and understanding the response of microstructures to the high levels of radiation damage (>200 dpa) is necessary for the verification of the radiation tolerance of NFAs.

Composition as well as processing methods affect the microstructure and mechanical properties of NFAs. Since the solubility of Y is very small in the iron matrix, high energy ball milling is required to force yttrium into solution. Then, during hot consolidation, Y-Ti-O containing NFs form [19]. To obtain the optimal size and density

of the NFs, the bulk concentration of oxygen must be closely controlled [231]. Ukai and Fujiwara [230] studied numerous processing methods and parameters in order to understand microstructure development. It is suggested that improved high temperature properties can be obtained by using the consolidation methods of hot extrusion, hot rolling or hot isostatic pressing combined with hot forging after mechanical alloying of powders [230]. Recently, Hoelzer et al. [8] achieved sub-micrometer grain size and homogeneous microstructure by using a processing method consisting of hot extrusion and annealing. The resulting 14YWT steels have stable microstructure up to 1300 ˚C with outstanding mechanical properties such as high temperature tensile and creep strength up to 800˚C [8,232]. However, these processing methods are quite time intensive and therefore expensive. Therefore, alternative techniques are also being investigated.

The purpose of this study is to explore the effect of an innovative method of thermal spraying followed by hydrostatic extrusion on the microstructure and mechanical properties of 14YWT alloys compared to the conventional pre-alloying and hot extrusion methods. Moreover, effect of initial microstructure on the irradiation response of these tubes has been studied through extremely high dose ion irradiations up to 1100 dpa.

7.3 Experimental procedure

14YWT tubes were produced by two different processing routes, namely novel thermal spraying method of Process I and conventional hot extrusion method of Process II. Process I tubes were irradiated to 500 and 900 peak dpa while Process II tubes were irradiated to 500, 700, 900 and 1100 peak dpa at 450 °C.

Samples were characterized using both SEM and TEM techniques. They were prepared using standard metallographic techniques for characterization. Pre-irradiation TEM foils were prepared by mechanical polishing and jet electropolishing. A perchloric acid (5%) and methanol solution was used at -40 °C with an applied voltage of 20 V. The foils for the irradiations were jet electropolished from only one side for ~30 sec in order to clean the surface without having a deep dimple. After irradiation, TEM samples were prepared using standard FIB lift-out technique with a final cleaning step at 1 kV in an FEI Helios Nanolab 600 dual beam FIB instrument. The microstructure was characterized using an FEI Tecnai F30 TEM operating at 300kV. Average grain sizes of the tubes were determined using electron backscatter diffraction (EBSD) technique utilizing an FEI Inspect FEG SEM equipped with TSL EBSD equipment with an acceleration voltage of 20 kV and aperture size of 50 μm. Energy-dispersive X-ray spectroscopy (EDS) was used to measure the composition of the precipitates in both SEM and the scanning transmission (STEM) modes. Data collection times for each precipitate were at least 60 s in order to be able to get high peak-to-background ratios. Qualitative elemental analyses were achieved using the FEI software TIA. Scanning transmission electron microscopy (STEM) and bright field (BF) imaging at an under-focus condition of 1-3 μm were used for the swelling studies. Energy filtered TEM (EFTEM) was performed for both the electron energy loss mapping and thickness measurements based on the number of electron mean free paths [270] with a Gatan imaging filter. Fe and Ti electron loss images were obtained using K-peaks.

The effect of processing routes on the mechanical properties was investigated using a Struers DuraScan-70 microhardness tester with a 1 kg load. Moreover, the effect of irradiation-induced defects on the mechanical properties was studied by nanoindentation hardness measurements using a MTS Nano Indenter XP™. Tests were conducted in continuous stiffness mode at a constant strain rate of 0.05 s^{-1}. Fifty indentations were made on the irradiated surface of each sample using a Berkovich indenter tip.

7.4 Results and discussion

7.4.1 Microstructural investigation and mechanical properties before irradiation

7.4.1.1 Microstructural investigation

Fig. 7.1a and Fig. 7.1b show the band contrast maps exhibiting a bimodal grain size distribution with the average sizes of 1.97±0.14 μm and 0.49±0.05μm for Process I and Process II tubes, respectively as reported in the previous chapter [271].

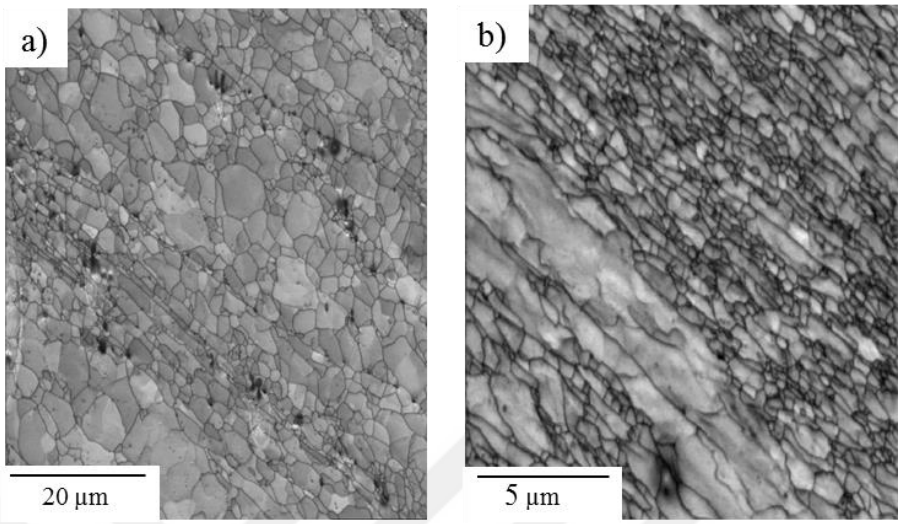

Figure 7.1 Band contrast maps showing the grain distribution for 14YWT tubes produced by (a) Process I and (b) Process II.

Fig. 7.2 shows the second phase particle shape, size and distribution in the 14YWT tubes produced by Process I and Process II. The particle size can be divided into four main groups: large particles (>250 nm), medium size particles (50-250 nm), small size particles (10-50 nm) and NFs (<10 nm). Both of the tubes have large irregular shaped particles at the grain boundaries. In Fig. 7.2a, the tube produced by Process I has variety of different shaped medium and small size particles either at the grain boundaries (GBs) or inside the grain. In general particles at GBs are typically circular while those inside the grains have either rectangular or polygonal (close to circular) shapes. On the other hand, determination of the shape of NFs shown by arrows is not possible at this magnification. Similar to the Process I, Process II results in the formation of variety shaped particles either at the grain boundaries or inside the grains (Fig. 7.2b). While the ones at the grain boundaries are close

to circular or ellipsoidal, the particles inside the grains are either circular or truncated rectangular. The NFs shown by arrows are close to being circular shaped.

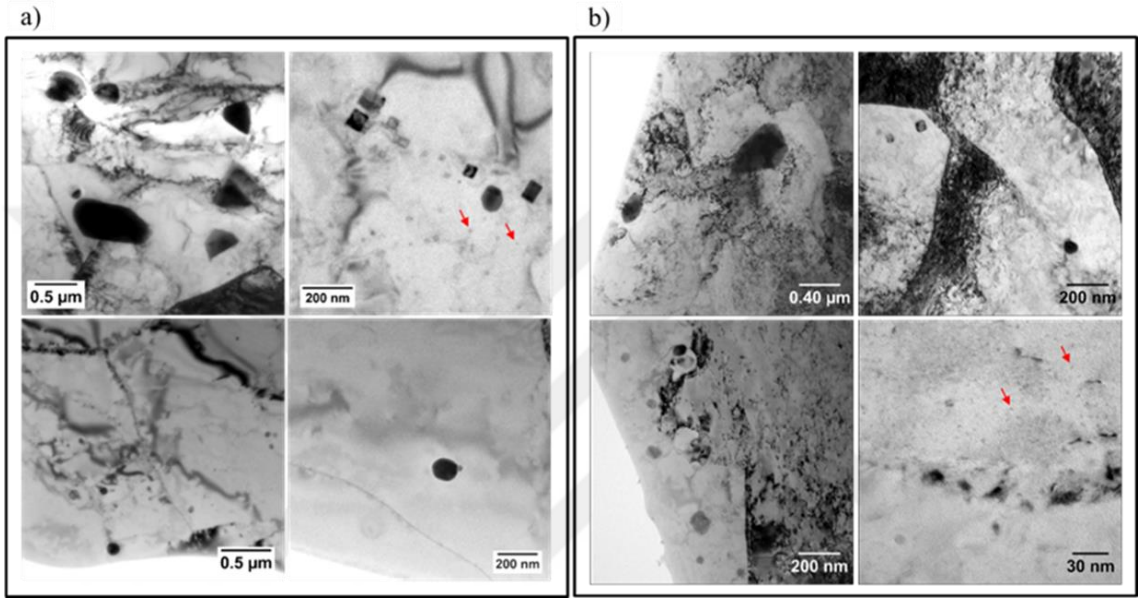

Figure 7.2 Bright field TEM images showing the second phase particle size and distribution in 14YWT tubes produced by (a) Process I and (b) Process II.

High-angle annular dark field (HAADF) scanning transmission electron microscopy (STEM), or z-contrast imaging, shows that there are second phase particles having different contrast inferring that they have different compositions for both Process I and Process II tubes shown in Fig. 7.3. The particles having bright contrast have larger atomic weights compared to the matrix composition while the ones in dark contrast have a lower atomic weight compared to the matrix. In Fig. 7.3a, it is shown that Process I results in bright and dark contrasted rectangular shaped particles together with polygonal

shaped particles. On the other hand, Process II results in either polygonal or irregular shaped bright and dark contrasted particles (Fig. 7.3b).

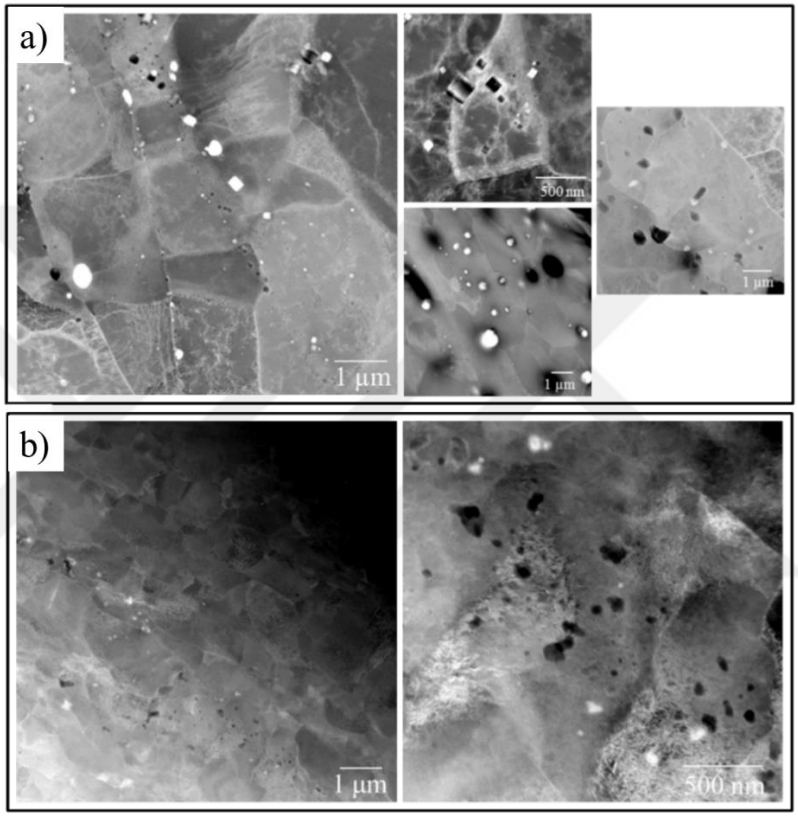

Figure 7.3 High-angle annular dark field (HAADF) scanning transmission electron microscopy (STEM) image showing large, medium and small size particles in 14YWT tubes produced by (a) Process I and (b) Process II.

Detailed composition analysis was done by SEM and STEM EDS methods. In order to investigate the composition of large particles having the size larger than 250 nm, EDS mapping was obtained using SEM. Fig. 7.4a and Fig. 7.4b show that coarse white particles along the grain boundaries are Ti-Al-O particles in both tubes. They are elongated in the direction of extrusion. Although it is not intended to have, Al contamination is

resulted from thermal spraying processing steps on Al mandrel and initial powder mixing processes for Process I and Process II, respectively.

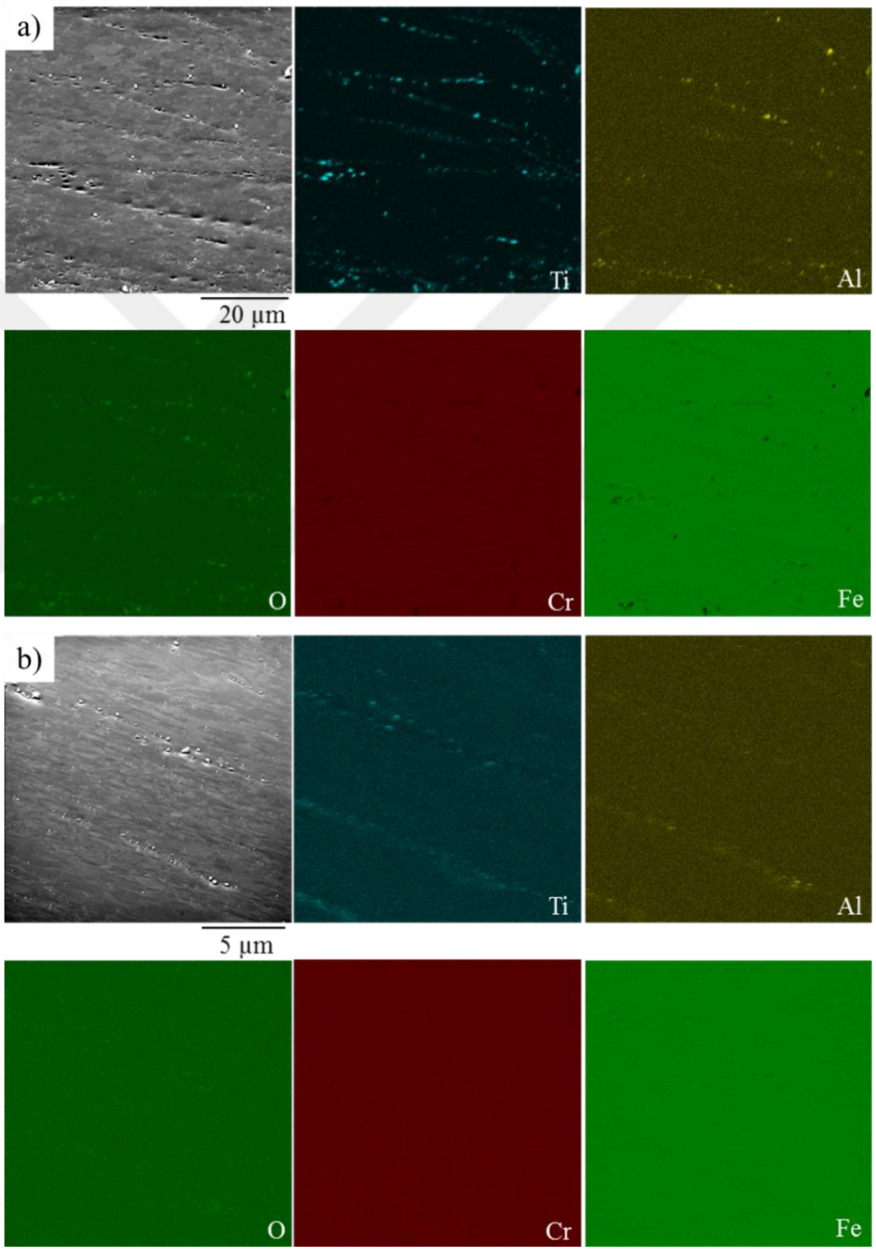

Figure 7.4 SEM-EDS mapping of various elements in 14YWT tubes produced by (a) Process I and (b) Process II. Large oxide particles are located at the grain boundaries and elongated in extrusion direction.

Compositions of the medium and small particles were determined using EDS analysis under TEM. In the Process I produced microstructures, dark rectangular particles ranging from 250 nm to 10 nm are Y-Ti-O particles having trace amount of Al as shown in Fig. 7.5. The amount of Al decreases with the decrease in size of the particles. On the other hand, their Y/Ti ratio does not change relative to the particle size as reported by Bhattacharyya et al. [2]; it rather fluctuates between 1.2 and 1.5. Fig. 7.6 shows that composition and shape of some of the dark particles in Process I tube are different. These are small to large size ellipsoidal or polygonal particles with compositions of Ti-Al-O. It should also be noted that the tables show considerable amount of C. They do not represent the exact amount of C as C quantification by EDS is not accurate. It rather shows the existence of carbon qualitatively.

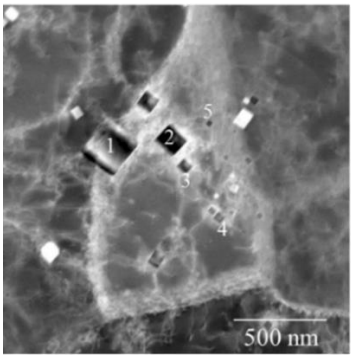

at%	C	O	Al	Si	Ti	Cr	Fe	Y	W
Matrix	29.6	0	0	0.8	0	11.5	57.0	0	1.1
Particle 1	31.9	13.5	1.0	0	15.4	2.7	14.6	20.6	0.4
Particle 2	47.5	12.3	0.4	0	7.0	3.6	19.4	9.7	0
Particle 3	39.4	7.5	0.5	0	5.2	6.0	34.5	6.2	0.7
Particle 4	37.5	10.4	0	0	2.8	7.9	36.8	4.2	0.4
Particle 5	35.5	10.7	0	0.4	2.2	8.1	40.1	2.6	0.4

Figure 7.5 Composition analysis of 5 different dark rectangular particles having size ranging between 10-250 nm in Process I tube.

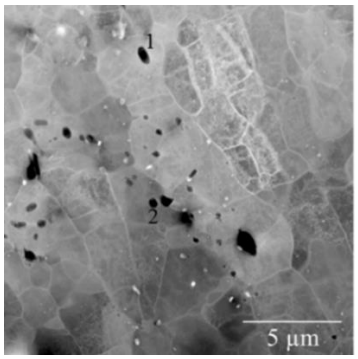

at%	C	O	Al	Si	Ti	Cr	Fe	Y	W
Matrix	29.6	0	0	0.8	0	11.5	57.0	0	1.1
Particle 1	25.0	12.7	0.3	0.1	59.2	0.5	2.2	0	0
Particle 2	28.7	27.3	4.3	0.3	28.3	2.2	8.8	0	0.1

Figure 7.6 Composition analysis of ellipsoidal or polygonal dark particles having sizes between 10 nm and up to 1 µm in Process I tube.

Fig. 7.7 shows that bright rectangular particles ranging from 250 nm to 10 nm are Y-Ti-O particles having trace amount of Al. Similar to the dark rectangular particles, their Y/Ti ratio does not change relative to the particle size. Their Y/Ti ratio fluctuates randomly between 0.6 and 1.4.

HAADF images in Fig. 7.5 and Fig. 7.7 show the rectangular particles in Process I microstructure. Even though they have different contrasts, they are Y-Ti-O rich particles having maximum Y/Ti ratio of 1.5. Similarly, Wen et al. [272] reported the different contrast particles and it was attributed to the remnant diffraction contrast since different contrast particles had same composition.

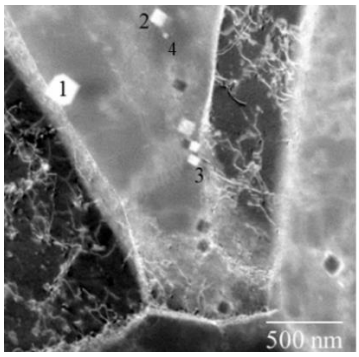

at%	C	O	Al	Si	Ti	Cr	Fe	Y	W
Matrix	29.6	0	0	0.8	0	11.5	57.0	0	1.1
Particle 1	0	18.9	0.5	0	5.9	10.3	55.6	8.2	0.6
Particle 2	26.7	4.3	0	0.7	3.4	10.6	50.6	3.0	0.7
Particle 3	22.0	11.4	0	0	2.1	9.9	51.0	3.0	0.5
Particle 4	35.7	5.3	0	0.9	1.8	8.7	45.3	1.1	1.3

Figure 7.7 Composition analysis of rectangular bright particles having a size between 10-250 nm in Process I tube.

Bright polygonal particles are composed of Y-Ti-Al-O (Fig. 7.8). Initial high amount of Al decreases with decrease in the size of particles, similar to the other particles. On the other hand, large and medium size particles have trace amount of Zr while small size particles do not have neither Al nor Zr. The Y/Ti ratios seem to be constant ~1.2 for all size of particles except for the very large particles having the size as particle 1 in Fig. 7.8.

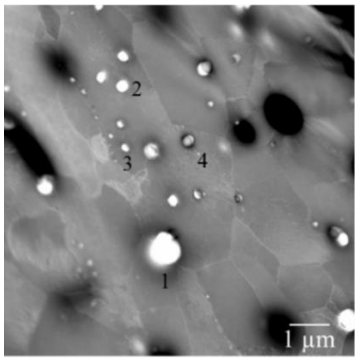

at%	C	O	Al	Si	Ti	Cr	Fe	Y	W	Zr
Matrix	29.6	0	0	0.8	0	11.5	57.0	0	1.1	0
Particle 1	0	32.9	8.8	0	30.8	3.3	16.9	6.3	0	0.9
Particle 2	0	16.8	1.7	0	16.6	7.1	36.1	20.0	0.6	1.1
Particle 3	0	16.8	1.7	0	16.6	7.1	36.1	20.0	0.6	1.1
Particle 4	27.6	10.0	0	0	3.8	8.9	43.8	4.5	0.3	0

Figure 7.8 Composition analysis of polygonal shaped bright particles having a size ranging between 10 nm and up to 1 µm in Process I tube.

Process II tubes have particles with various compositions and sizes ranging 1-2 nm to 500 nm. Fig. 7.9 indicates that dark particles numbered through 1 to 5 in decreasing size are composed of Ti-Si-O-N. Moreover, some of them contain trace amount of Al and Y. Even though the particles numbered through four are deficient in Cr and rich in Si, Particle 5 has no Si with Cr amount larger than the matrix. It was also observed that there are other similar shaped dark large oxide/nitride particles having a large Si/Ti ratio.

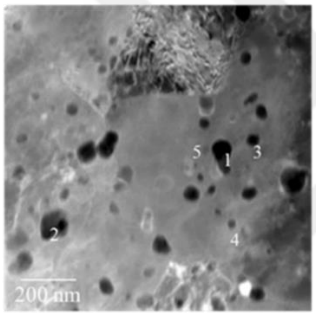

at%	C	N	O	Al	Si	Ti	Cr	Fe	Y	W
Matrix	15.63	0	0	0	0	0	12.0	71.1	0	1.2
Particle 1	0	28.5	15.8	0	1.6	28.2	4.4	21.1	0	0.4
Particle 2	0	31.9	11.9	0.3	1.1	29.7	4.0	20.2	0.2	0.7
Particle 3	0	22.3	17.7	0.4	1.0	19.7	6.0	31.9	0	1.0
Particle 4	0	22.1	14.4	0.2	1.3	12.7	7.7	40.4	0	1.2
Particle 5	0	0	0.1	0	0	7.5	15.2	76.3	0	0.9

Figure 7.9 Composition analysis of polygonal shaped dark particles having a size ranging between 10-250 nm in Process II tube.

The composition of bright particles is different than the dark particles. Fig. 7.10 shows the composition of three different particles having a bright contrast. Particles 1 and 2 having the size of 50-250 nm are aluminum oxide particles having trace amount of Ti. On the other hand, particle 3 having size < 50 nm is yttrium oxide with trace amount of Al and Ti.

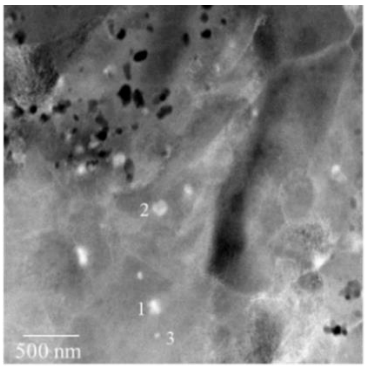

at%	C	O	Al	Ti	Cr	Fe	Y	W
Matrix	15.63	0	0	0	12.0	71.1	0	1.2
Particle 1	0	15.6	10.3	0.2	11.2	62.4	0	0.3
Particle 2	0	28.1	15.2	0.6	7.1	48.7	0	0.3
Particle 3	39.5	11.1	0.1	0.6	5.7	37.8	5.0	0.3

Figure 7.10 Composition analysis of polygonal shaped bright particles having a size ranging between 10-250 nm in Process II tube.

Composition analysis on NFs having the size less than 10 nm is quite difficult using EDS. Instead, energy filtered TEM (EFTEM) allows composition mapping as seen in Fig. 7.11. Besides giving information on the composition of the NFs, EFTEM is utilized to determine the size and distribution of the NFs. Figure 7.11 shows the Ti and Fe jump ratio maps of the microstructures produced by Process I and Process II. It indicates that the NFs are rich in Ti and deficient in Fe. Even though Y and O jump ratio maps are not shown here, NFs are determined to be Y-Ti-O containing particles. Fig. 7.11a shows that Process I results in Y-Ti-O NFs having relatively larger size compared to Process II in Fig. 7.11b. Furthermore, the Y-Ti-O particles in the resultant microstructures of Process I are not distributed homogenously whereas conventional mechanical alloying method in Process II results in relatively homogenous distribution of NFs.

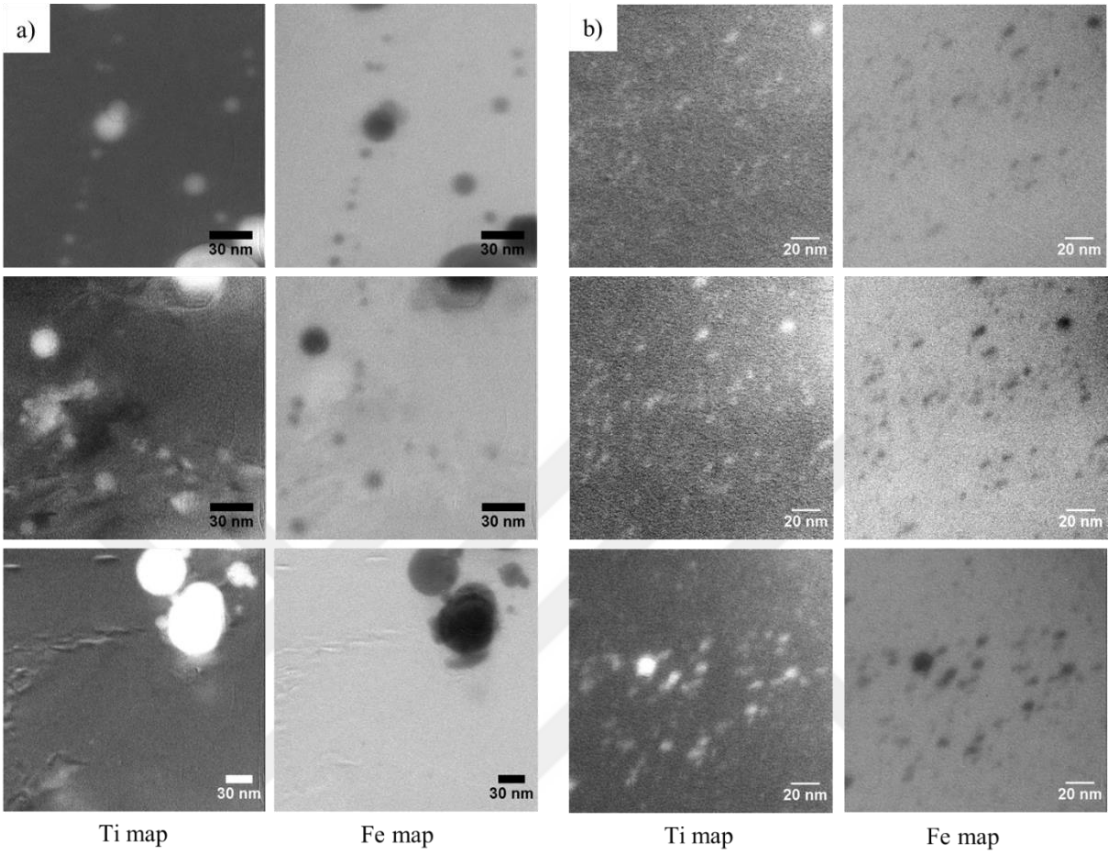

Figure 7.11 EFTEM Ti and Fe elemental maps obtained from the tubes produced by (a) Process I and (b) Process II.

The size of the NFs having the size less than 10 nm was measured using the EFTEM images. The measurements were taken from fifteen different regions and a total of 100 to 270 particles were included to the calculations. Fig. 7.12 shows the size distribution of NFs in both Process I and Process II tubes. While the number fraction of the particles peaks ~4 nm in the case of Process II tube, there is no particle observed below 4.5 nm in Process I tube. The average size and density of the NFs in the Process I tube is measured as 7.2±1.5 nm and 2.3×10^{21} m^{-3}, respectively. Moreover, the average size and concentration of the NFs in the Process II tube is measured as 4.2±1.5 nm and 2.0×10^{23} m^{-}

^{3}, respectively. Table 7.1 summarizes the measured grain size, NF size, volume fraction and density for Process I and Process II tubes.

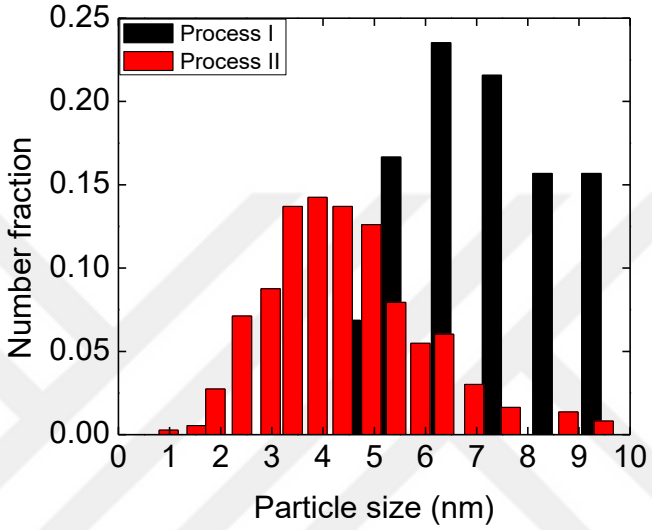

Figure 7.12 NF size (<10 nm) distribution of (a) Process I and (b) Process II alloys.

Table 7.1 Summary of measured grain and NF sizes, as well as volume fraction and number density in 14YWT tubes produced by different processes.

Processing method	Measured grain size (μm)	Average particle diameter (nm)	Volume fraction of particles (%)	Number density of particles (m^{-3})
Process I	1.97±0.14	7.2±1.5	0.05±0.01	$2.3x10^{21}$
Process II	0.49±0.05	4.2±1.5	1.13±0.13	$1.5x10^{23}$

Process I, consisting of cold spraying followed by hydrostatic extrusion, results in the formation of Y-Ti-O NFs even though it does not contain the ball milling step for the

dissolution of Y. However, the average size of the NFs is much larger and the density of NFs is extremely low compared to the NFs formed by Process II. Cunningham et al. [231] reported that the bulk oxygen content of the alloy is quite important for the size and density of the NFs. They showed that low oxygen content leads to few and coarse NFs. In this study, even though the oxygen amount in the initial powders was aimed to be the same for both processes, either it actually is lower in Process I or entropy of the system is not high enough to create high density NFs in Process I.

7.4.1.2 Mechanical properties

Effect of processing routes on the mechanical properties was investigated by microhardness measurements at room temperature. While the average hardness of the Process I tube is 190.9±5.7 HV, Process II tube has twice the hardness of former, 387.6±12.1 HV. The proportionality constant between Vickers hardness and the yield stress change has been found to be 3.06 for ferritic steels [194]. Therefore, the yield stresses were calculated simply by dividing the hardness to 3.06 as shown in Table 7.2.

Table 7.2 Microhardness and yield stress values of the 14YWT tubes.

Processing Method	Microhardness (HV)	Microhardness (MPa)	Yield Stress (H/3.06) (MPa)
Process I	190.9±5.7	1872±56	612±18
Process II	387.6±12.1	3801±119	1242±39

There are basically four strengthening components determining the yield strength of the 14YWT tubes, namely direct strengthening due to NFs, indirect or Hall-Petch strengthening due to grain size, dislocation forest strengthening and matrix strengthening.

Dispersed barrier hardening (DBH) model is used for the hardening calculations as in equation 7.1. DBH model was introduced by Seeger [31] and is based on only geometrical considerations between dislocations and obstacles [32].

$$\Delta\sigma_d = 0.8M\alpha(r)Gb/\lambda \tag{7.1}$$

M is Taylor factor which is 3.06 for NFAs [273], *α(r)* is a barrier strength coefficient, *G* is the shear modulus (81.07 GPa for 14YWT), *b* is the length of the Burgers vector, 2.48 Å for the $\langle 111 \rangle \{110\}$ slip system [274], and λ is the mean planar center to center distance between NFs which is defined as in equation 7.2.

$$\lambda = 2\sqrt{\frac{2}{3}}r\left[\left(\frac{\pi}{4f}\right)^{1/2} - 1\right] \tag{7.2}$$

where *r* is the average radius and *f* is the volume fraction of NFs. λ can be calculated as ~226 nm and ~26 nm for the Process I and Process II tubes, respectively. The barrier strength coefficient, *α(r)*, can be defined as cos(φ/2) (φ is the critical angle between dislocation lines where the pinned dislocation is about to detach from the obstacle) [275]. Odette et al. [19] found that there is a linear correlation between *α(r)* and *log(r/2b)* when r>2b:

$$\alpha(r) \approx 0.27\log(r/2b) \tag{7.3}$$

When the barriers are impenetrable as in the case of Orowan by-pass mechanism, then α(r)=1. In the present work, *α(r)* is calculated as 0.23 and 0.17 for Process I and Process

II tubes, respectively. It has been reported that particles are soft obstacles when $\alpha(r)$ is in the range of 0.05 and 0.3 meaning that dislocation bowing produces φ larger than 0º. This argument is plausible for the NFs having 2-3 nm size (with mostly coherent interfaces). The reason of 'softness' is either easy shearing of the particles or dipole interactions between bowed dislocations [19]. Consequently, DBH method results in the direct strengthening of 50.4±26.2 MPa and 315.6±99.2 MPa for the tubes produced by Process I and Process II, respectively.

Hall-Petch strengthening is crucial for fine grained materials and it can be represented by the following equation:

$$\sigma_i = k_{HP} d^{-1/2} \tag{7.4}$$

where k_{HP} is Hall-Petch parameter and it can be obtained by the slope of yield stress vs. grain size plots by analysing the 14YWT samples having different grain sizes. Although Schneibel et al. [276] used k_{HP} value of 0.6 MPa√m, Kim et al. [277] obtained room temperature k_{HP} value of 0.338 MPa√m from the yield stress vs grain size plots of 14YWT samples having different grain size reported in Ref [276]. Hall-Petch coefficient of 0.338 MPa√m and grain sizes of 1.97±0.14 μm and 0.49±0.05 μm for Process I and Process II, respectively were used to calculate the indirect strengthening. As a result, indirect strengthening of 240.8±8.6 MPa and 482.9±24.6 MPa were obtained for the tubes produced by Process I and Process II, respectively.

Dislocation forest strengthening might be another important component since especially the Process II tube is produced by mechanical alloying which introduces severe deformation to the powders. It has been reported that the dislocation density of the samples

can still remain high after high temperature processing because of the NFs [277]. Consequently, it is necessary to investigate the strengthening effect of dislocations. Dislocation densities were measured from TEM images taken at the same kinematic conditions as shown in Fig. 7.13. A line-intercept method defined in Ref [180,278] was used to calculate dislocation densities. The dislocation density ρ is calculated by dividing the total number of intercept points, N, by the total line length of the random lines L_t and foil thickness t [189]:

$$\rho = \frac{N}{L_t t} \tag{7.5}$$

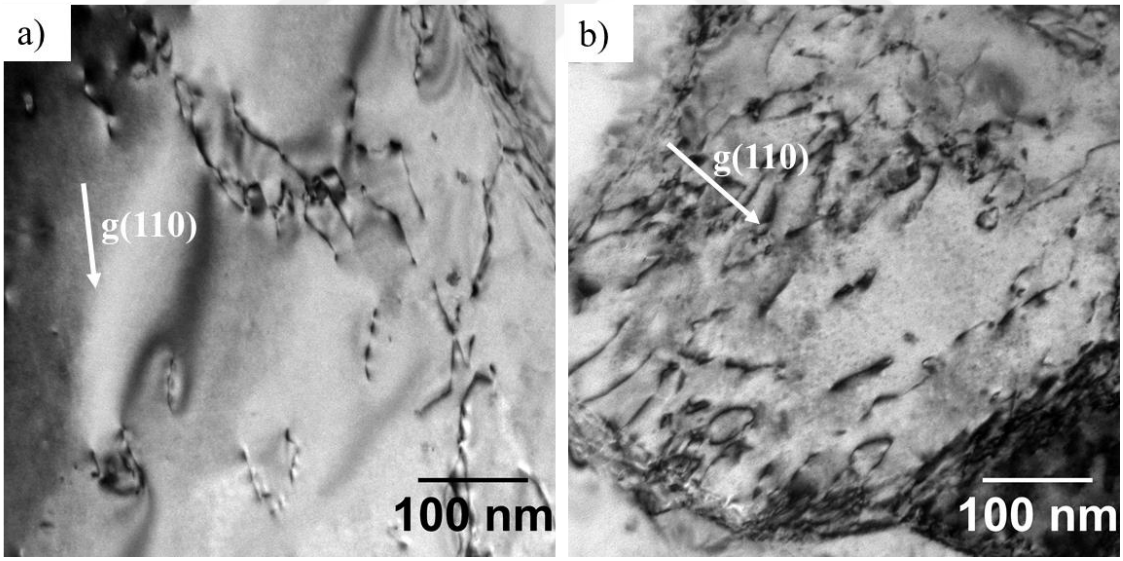

Figure 7.13 TEM bright field images of (a) Process I and (b) Process II tubes along g(110) direction showing the distribution of dislocations.

Dislocation densities for Process I and Process II tubes were calculated as $2.5\pm0.5x10^{14}$ m^{-2} and $8.2\pm1.6x10^{14}$ m^{-2}, respectively. Dislocation densities were inserted into the formula of;

$$\sigma_{\rho} = M\alpha Gb\sqrt{\rho} \tag{7.6}$$

where α is a material dependent constant reported as 0.38 for polycrystalline iron [279,280]. As a result, the dislocation strengthening values of 369.6±37.0 MPa and 669.5±66.9 MPa were obtained for the tubes produced by Process I and Process II, respectively.

The matrix hardening (σ_m) occurs by solid solution hardening and intrinsic lattice resistance to slip [277]. In order to investigate the matrix hardening of 14YWT, Kim et al. [277] prepared a mixture of pre-alloyed Fe–14Cr–3W–0.4Ti powder without mechanical alloying, HIPed and annealed at 1100 ˚C for 4 h. A microstructure having a grain size of ~0.5 mm without any NFs has been obtained. Consequently, the room temperature matrix strength was measured as ~255 MPa by tensile testing.

Linear superposition method is based on the assumption that hardening mechanisms act independently. Even though linear superposition method is used extensively in the literature, it may not always be correct that the hardening mechanisms are correlated linearly and there is some influence among the mechanisms [277]. Besides, it has been reported that individual hardening mechanisms can be linearly added only when hardening mechanisms are completely independent [281,282]. Thus, combination of mechanisms might be a better approach to consider their correlation [283]. Kocks introduced an approach called as root mean-square (RMS) method [281,284]. This method

suggests that the hardening caused by individual obstacles is proportional to the square root of the obstacle density. Statistical calculations by Hanson and Morris have confirmed that RMS method works well over different density of obstacles [285]. Moreover, the studies in Ref [286-288] has applied RMS method successfully and it is proposed that this method is suitable for NFAs as they have many correlated hardening mechanisms [285,289]. Formulas of linear superposition and RMS approaches are given in equation 7.7 and 7.8.

$$\sigma_{y,ls} = \sigma_d + \sigma_i + \sigma_\rho + \sigma_m \tag{7.7}$$

$$\sigma_{y,rms} = \sqrt{\sigma_\rho{}^2 + (\sigma_d + \sigma_i + \sigma_m)^2} \tag{7.8}$$

Table 7.3 summarizes the individual contributions of direct, indirect, dislocation forest and matrix strengthening and compares the calculated yield strength values with the measured ones by using both linear superposition and RMS approaches. Obviously, the linear superposition method over estimates the experimentally determined yield stress values, while RMS approach gives almost the same results with the experimentally determined yield stress values. It should also be noted that the maximum strengthening occurs due to dislocation interactions for both types of tubes.

Table 7.3 Summary of direct, indirect, dislocation forest and matrix strengthening as well as a comparison between measured and calculated yield stresses by both linear superposition and RMS approaches.

Processing method	Direct strengthening (MPa)	Indirect strengthening (MPa)	Dislocation forest strengthening (MPa)	Matrix strengthening (MPa)
Process I	50.4±26.2	240.8±8.6	369.6±37.0	255
Process II	315.6±99.2	482.9±24.6	669.5±66.9	255
	Calculated yield stress by linear superposition approach (MPa)	Calculated yield stress by RMS approach (MPa)	Yield stress calculated from hardness measurements (MPa)	
Process I	915.8±95.2	659.5±49.6	612±18	
Process II	1723.0±190.7	1248±111.4	1242±39	

7.4.2 Microstructural investigation and mechanical properties after irradiation

7.4.2.1 Microstructural investigation

Fig. 7.14 shows TEM micrographs of Process I and Process II tubes after self-ion irradiation up to 1100 dpa at 450 °C. It is clear that Process I tube shows much higher swelling compared to the Process II tubes. Fig. 7.14a shows void distribution within ~700 nm depth below the surface. Their distribution is quite inhomogeneous which is attributed

to inhomogeneous distribution of NFs. Fig. 7.14b shows stitched micrographs of Process II tubes after 500 to 1100 dpa irradiations to show the depth distribution of voids. Compared to the Process I tubes, there is almost no voids visible at this magnification.

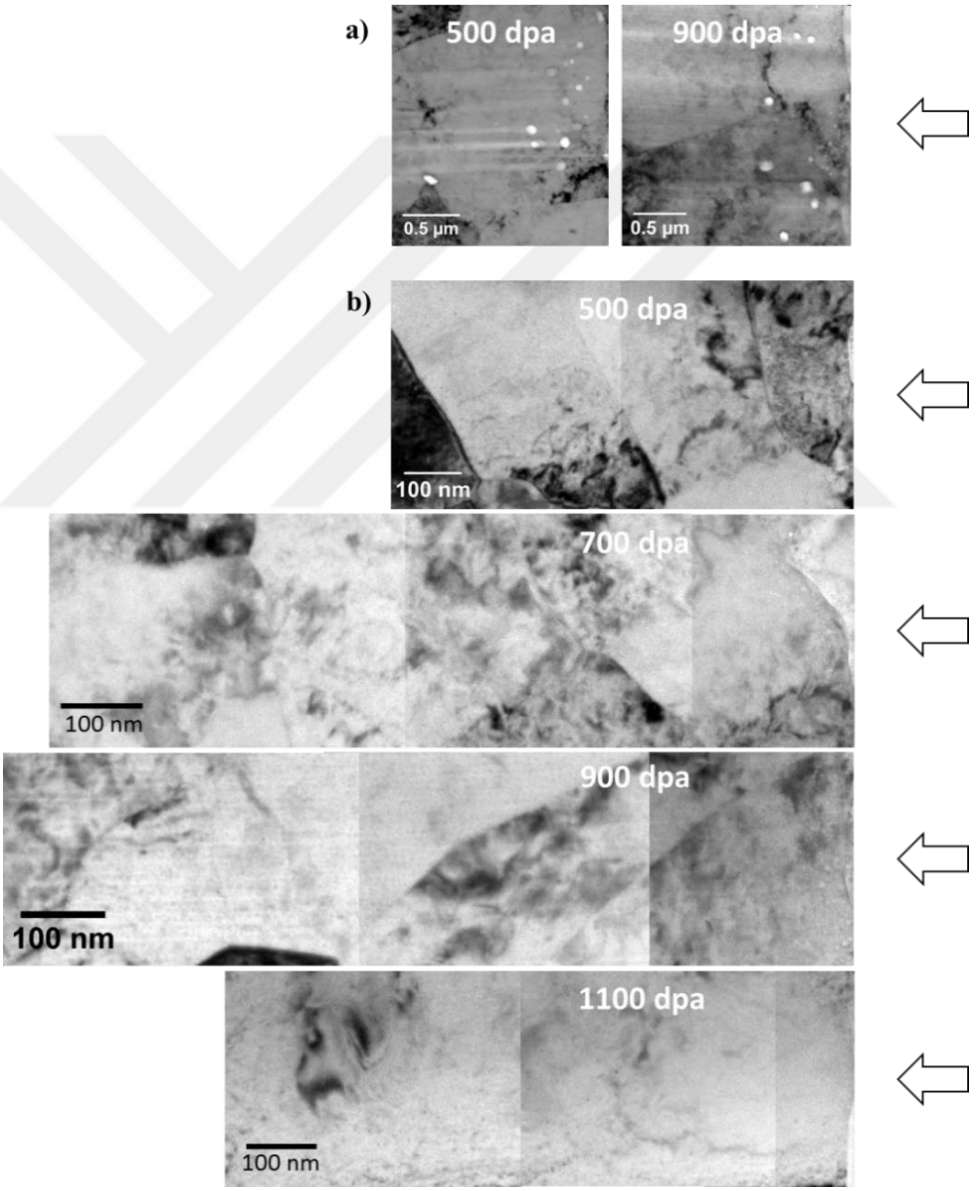

Figure 7.14 Microstructures of (a) Process I tube after 500 and 900 dpa (b) Process II tube after 500, 700, 900 and 1100 dpa irradiations with Fe^{2+} at 450 °C. Arrows indicate the direction of ion beam. Images were taken at 1 µm under focus condition.

Higher magnification micrographs of irradiated Process II tubes in Fig. 7.15 shows that small bubbles mostly form at very shallow regions within ~100 nm below the surface. Even at 1100 peak dpa irradiation condition, the depth of the bubbles is limited to this shallow depths.

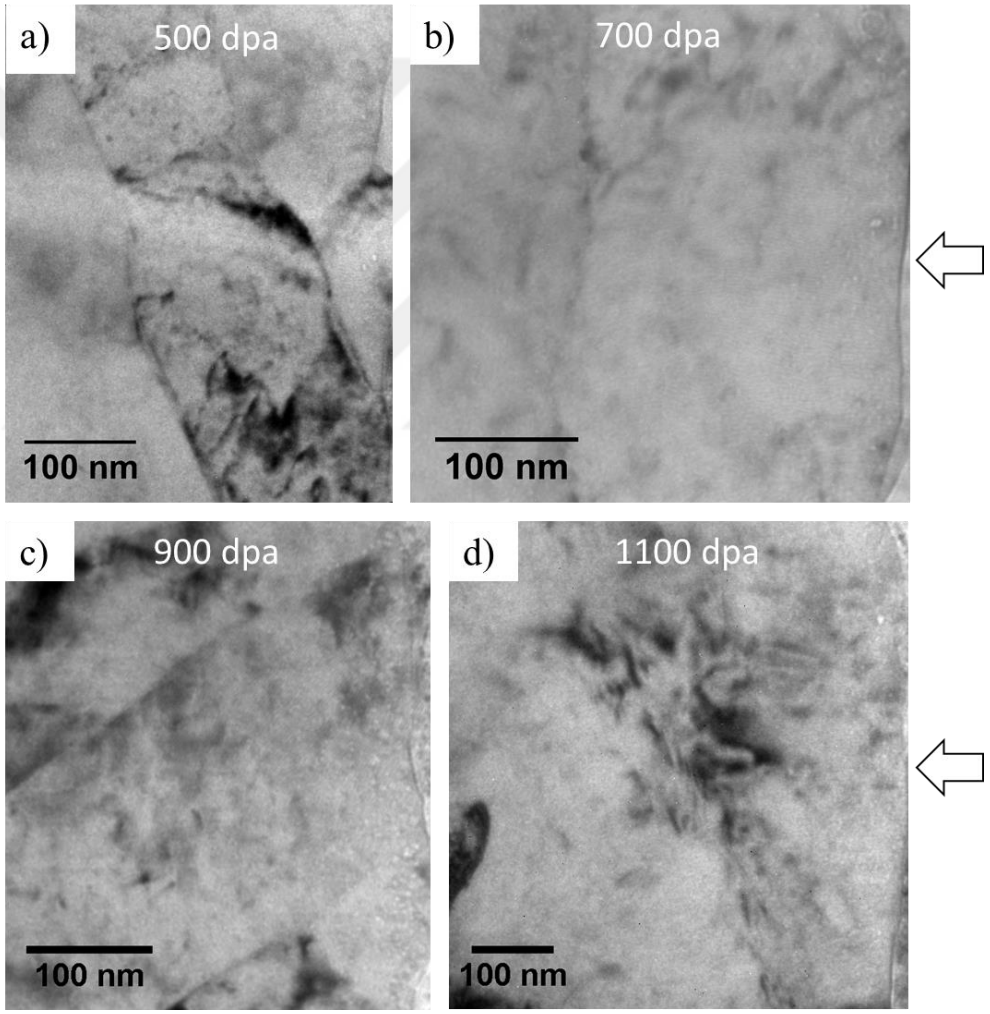

Figure 7.15 BFTEM images of Process II tube after (a) 500 dpa (b) 700 dpa (c) 900 dpa and (d) 1100 dpa irradiations. Arrows indicate the direction of ion beam. Images were taken at ~3 μm under focus condition.

Fig. 7.16 shows the depth-dependent swelling curves for Process I and Process II tubes irradiated to 500 and 900 dpa and 500, 700, 900 and 1100 dpa, respectively, superimposed on the SRIM-calculated dpa and injected Fe ion profiles. It is obvious that the swelling in the Process I tube is at least two orders of magnitude higher than in Process II tube. In Fig. 7.16a, swelling shows large variation presumably due to the initial inhomogenity in the microstructure. Furthermore, the injected intestitial effect becomes considerable at the deeper regions especially for the high dose levels. Especially after 400 nm depth, swelling starts to be lower in 900 peak dpa irradiated sample due to the high amount of injected interstitials. In Fig. 7.16b, maximum swelling occurs at the shallow regions and decreases to very low amounts. It should be noted that strong injected insterstitial effect suppresses the swelling at te deeper depths for all dpa levels. This suppression is a well-known phenomenon where void nucleation is strongly suppressed by orders of magnitude, and the post-transient swelling rate is often suppressed by a factor of 3 to 5 [150].

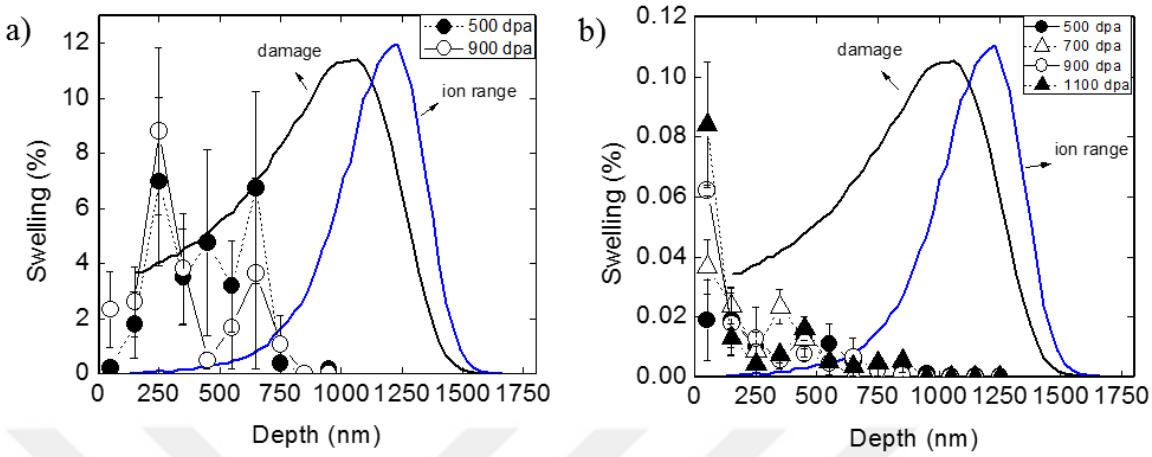

Figure 7.16 Swelling vs. depth profiles of the (a) Process I tube after 500 and 900 dpa (b) Process II tube after 500, 700, 900 and 1100 dpa irradiations with Fe^{2+} at 450 °C. Note the difference in the scale of swelling (%).

7.4.2.2 Mechanical properties

Fig. 7.17 shows the depth dependent nanohardness for the Process I and Process II tubes in irradiated and unirradiated conditions. As the range of the ions is ~1.5 μm, the depth of investigation was limited to the shallow depths since the probed information comes from much deeper regions. Moreover, hardness profiles at the depth of 300-400 nm were considered in order to reduce the effects of surface and unirradiated regions. At the deeper regions, hardness of the irradiated samples decreases to the values close to the unirradiated condition. Nanohardness of the unirradiated Process I tube is measured as 3.3±0.1 GPa. After irradiation, the hardness of 500 dpa and 900 dpa irradiated samples increased to 4.0±0.1 GPa and 4.5±0.2 GPa, respectively, shown in Fig. 7.17a. In Fig. 7.17b, hardness of unirradiated Process II tube is measured as 5.6±0.1 GPa while the hardness of irradiated samples is measured as 6.4±0.1 GPa. Irradiation caused hardness

saturation with ~0.8 GPa of hardening in Process II tubes. Initial inhomogenous microstructure in Process I tube, on the other hand, resulted in hardness variations after irradiations.

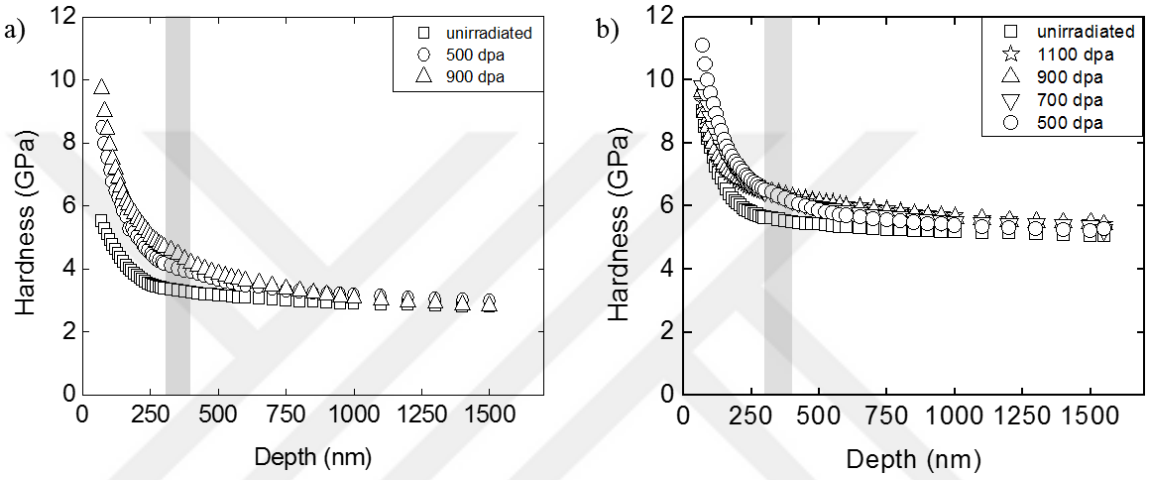

Figure 7.17 Hardness as a function of penetration depth for (a) Process I tube after 500 and 900 dpa (b) Process II tube after 500, 700, 900 and 1100 dpa irradiations with Fe^{2+} at 450 °C. Shaded regions between 300-400 nm depth shows the region of investigation.

The irradiation damage observed in the microstructure of 14YWT alloys are also reflected in their hardness. A radiation induced hardening model which considers the interactions between mobile dislocations and irradiation induced defects can be used to calculate the change in hardness as shown in equation 7.9 [290]. Radiation-induced defects are basically the dislocation loops and voids or bubbles. As will be discussed in Chapter 8, irradiations to various doses resulted in a slight decrease in the NF size together with a slight increase in their densities. Since changes are subtle, their contribution to the radiation hardening is neglected and hardening can be represented as;

$$\Delta\sigma = \Delta\sigma_{disl} + \Delta\sigma_{void} \tag{7.9}$$

$\Delta\sigma_{disl}$ is the strengthening coming from irradiation-induced dislocation loops and can be defined based on the dispersed hardening model as [291]:

$$\Delta\sigma_{disl} = M\alpha Gb\sqrt{dN} \tag{7.10}$$

where *N* and *d* are the density and size of the loops, respectively.

Second term in equation 7.9 is the strengthening resulted from the dislocation interactions with voids (or bubbles) and it can be described as in equation 7.10 where *d* and *N* represent the density and size of the voids, respectively. However, bubbles are relatively weak barriers and their strengthening was defined by Friedel-Kroupa-Hirsch model [292,293] as in equation 7.11.

$$\Delta\sigma_{bubble} = \frac{1}{8} MGbdN^{2/3} \tag{7.11}$$

Fig. 7.18 shows the BF-STEM images of Process I and Process II tubes irradiated to various damage levels in the two beam conditions. Images were taken at the same kinematic conditions for all samples (g=(110)). Table 7.4 summarizes the void (bubble) and dislocation loop size and densities. In Process I tubes, while both loop size and density increase with increasing dose levels, void size increases slightly and void density decreases. On the other hand, in Process II tube, the trend of dislocation and bubbles are the reverse of Process I tube. The calculated hardening using equation 7.9 is found to be slightly lower than the measured values. There might be two reasons: (1) TEM visualizes in 2D and if the loops lie in the direction perpendicular to the surface, it might have been missed during measurements; (2) linear dislocation network density might have increased

which we are not taking into account. It should also be noted that contribution of void (bubble) hardening is quite small due to either low density of voids or small size of the bubbles.

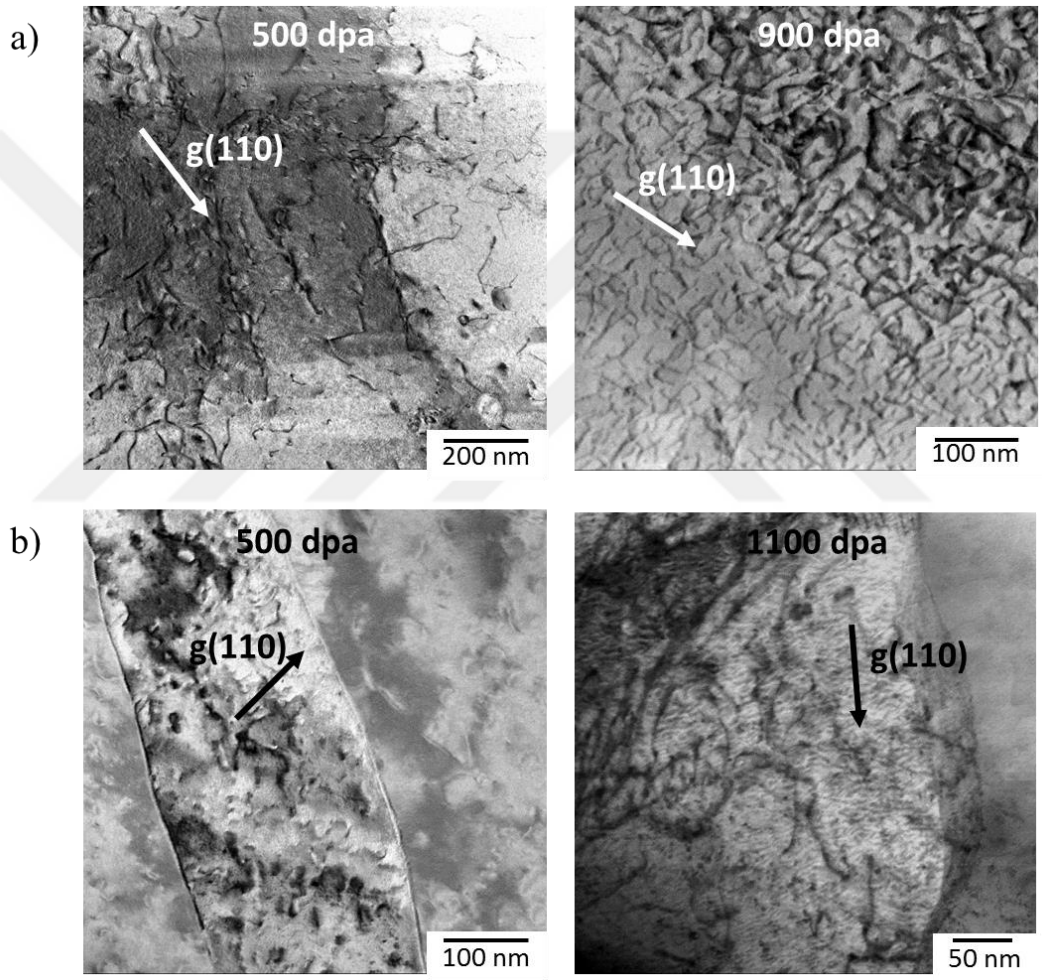

Figure 7.18 BF-STEM images showing dislocation loop distribution in two-beam condition (g=(110)) for (a) Process I tube irradiated up to 500 and 900 peak dpa doses (b) Process II tubes irradiated up to 500 and 1100 peak dpa dose.

Table 7.4 Summary of dislocation and void size and densities as well as hardening for the irradiated samples at various dose levels.

	Dose	Void (bubble) size (nm)	void density (m^{-3})	dislocation loop size (nm)	dislocation loop density (m^{-3})	Calculated hardening (GPa)
Process I	500 peak dpa	63	$2.5x10^{20}$	9.0	$1.2x10^{21}$	0.51±0.13
	900 peak dpa	76	$5.2x10^{19}$	10.6	$3.7x10^{21}$	0.58±0.15
Process II	500 peak dpa	2.9	$3.7x10^{21}$	8.2	$5.9x10^{21}$	0.54±0.14
	1100 peak dpa	2.1	$9.0x10^{21}$	4.8	$1.7\ x10^{22}$	0.65±0.16

7.5 Conclusions

14YWT tubes produced by two different processing methods, namely novel cold spraying and conventional hot extrusion methods, were investigated in terms of their microstructure and mechanical properties before and after high dose self-ion irradiations. Both methods lead to the formation of broad range of Y-Ti-(Al)-O particle size together with Ti-O, Al-O, Y-O and Ti-Si-O-N particles. Process I results in larger grain size and Y-Ti-O particles while Process II produces smaller grain size with NFs having the size of <5 nm. Furthermore, the density of the NFs is higher in the Process II tube. The yield

strength of the Process II tube is two times higher due to its smaller and denser NF content, smaller grain size and higher dislocation density. Contribution of dislocation-dislocation interactions to the strength is much higher compared to especially the NF strengthening.

Irradiation response of the two tubes produced by two different methods is different. Process II tube shows at least two orders of magnitude less swelling compared to the Process I tube because of the finer, denser and more homogenous distribution of NFs in Process II tubes. Due to the inhomogeneity in the initial microstructure as a result of Process I, there is a large deviation in the depth distribution of swelling and irradiation hardening. On the other hand, irradiation hardening was saturated by ~0.8 GPa for Process II tubes for all radiation damages. Proportion of hardening resulted from dislocation void (or bubble) interactions is less than that of dislocations. Hardening calculations match well with the measured values.

8. STABILITY OF NANOSIZED OXIDES IN FERRITE UNDER EXTREMELY HIGH DOSE SELF ION IRRADIATIONS

8.1 Overview

14YWT NFAs, produced in thin-walled tubular form using conventional ball-milling followed by hot extrusion, hot cross rolling and hydrostatic extrusion methods, were ion irradiated with 3.5 MeV Fe^{2+} up to 1100 peak dpa at 450 °C. TEM and APT results show that the average size of the NFs decreases slightly while their density increases after irradiation. This can be explained by an 'inverse coarsening' behavior which is a result of overwhelming radiation driven dissolution compared to thermal diffusion driven growth. On the other hand, irradiation enhanced diffusion effects make the reformation of the NFs possible, leading to a higher density of NFs with smaller size. There is no significant change in the composition of the matrix and NFs after irradiation. Moreover, HRTEM shows the existence of a high density coherent and semicoherent $Y_2Ti_2O_7$ and Y_2TiO_5 NFs before irradiation. After irradiation, $Y_2Ti_2O_7$ NFs retain their crystal structure but there is a slight increase in their lattice parameters.

8.2 Introduction

Advanced nuclear energy systems can improve energy creation efficiency, safety and reliability, but these designs require improved radiation tolerance up to 400 dpa and operation temperatures up to 1000 °C [2,294]. NFAs are attractive materials for Generation IV reactors because of their excellent high temperature strength, stability, and

creep resistance thanks to the high density of Y-Ti-O NFs having the size < 5 nm [8,229,295]. Even though APT indicates that NFs are nonstoichiometric phases with low O/(Y+Ti) ratio, TEM and XRD studies have shown that most of them have pyrochlore $Y_2Ti_2O_7$ structure having Y/Ti≈1 [296-298].

NFs can pin grain boundaries and immobilize dislocations, leading to high strength and superior structural stability [2,229,294,295]. Moreover, they may act as sinks for both point defects created from neutron damage and helium atoms created from transmutation [2,229,294]. Overall, NFAs are expected to have remarkable radiation tolerance, but their behaviors under extreme radiation conditions need to be systematically tested.

The stability of NFs has been studied extensively under both neutron and heavy ion irradiations, but the majority of these previous studies were limited to relatively low dpa damage levels (dpa<200). As a brief summary, Yamashita et al. reported that small oxides disappear under neutron irradiation in 11Cr and 13Cr alloys irradiated in the experimental fast reactor JOYO at 20 dpa and 450-561 °C [299]. They also found that nano-oxide density decreases in MA957 after neutron irradiation at 500 °C up to 100 dpa [300]. However, Mathon et al. reported that NFs are stable at 325 °C up to 5.5 dpa of neutron irradiation in MA957 [301]. Similarly, Gelles found no significant changes in nano-oxide distribution in MA957 irradiated in the FFTF/MOTA at 420 °C to 200 dpa [302]. Ribis et al. showed that the size of the nano-oxides are almost the same after neutron irradiation up to 75 dpa at 430 °C in the same alloy [303-305]. 9Cr and 12Cr ODS alloys were also reported to be stable under neutron irradiations at 330-500 °C up to 15 dpa [306]. Similar to the neutron irradiations, nano-oxides were found to be stable after ion

irradiation up to 10 dpa at 300 and 500 °C in MA957 [307,308]. At higher ion damage levels, the same trends were observed for 20 dpa at 200, 500 and 700 °C, for 60 dpa at 650 °C, and for 150 dpa at 670 °C [309-311]. On the other hand, Allen et al. has shown that the size of the NFs decreases while their density increases at the temperatures 500-700 °C up to 150 dpa irradiation by Ni ions [294]. Parish et al. [312] and Certain et al. [313] reported that at low temperatures the NFs dissolve under heavy ion irradiations as a result of ballistic effects while at high temperatures either stable or slightly increased NF size is resulted similar to the recent findings by Lescoat et al. [314].

In summary, the NF stability studies cited above are not fully consistent, especially at high temperatures and they are limited by dpa values. The maximum ion irradiation damage level reported is ~150 dpa. Different from previous research, the present chapter is targeted to study radiation response of NFA 14YWT under extreme radiation damage levels up to 1100 dpa. Furthermore, the materials are extruded in tube form, in a way closer to their actual application as fuel cladding materials.

8.3 Experimental procedure

14YWT tubes were produced by conventional ball-milling followed by hot extrusion, hot cross rolling and hydrostatic extrusion methods as explained in the previous chapters. Samples were irradiated at Ions and Materials Facility at Texas A&M University using 3.5 MeV Fe^{2+} ions to reach damage levels of 500, 700, 900 and 1100 peak dpa at 450 °C. The vacuum during ion irradiations was better than 1×10^{-6} Torr and a 6mm×6mm defocused ion beam was used with 200 nA current.

Fig. 8.1 shows the calculated damage profile and Fe distribution profile for 1100 peak dpa irradiation, obtained from SRIM code [97]. The calculations used the Kinchin-Pease mode with Fe displacement energy of 40 eV. For 3.5 MeV Fe ions, the projected Fe range is ~1.2 μm and dpa peaks at ~1.0 μm. For 1100 peak dpa irradiation, the amount of injected Fe atoms exceeds 10 at% at depths beyond 700 nm. Therefore, in order to avoid the effects from injected interstitials, structural characterization focuses on the depth regions from 400 to 600 nm, as shown by the shaded region in Fig. 8.1. At this depth interval, the concentration of injected atoms, even for 1100 peak dpa irradiations, is below 3 at%. For this depth region, the averaged local dpa for 500, 700, 900 and 1100 dpa peak values are about 270, 375, 480 and 585 dpa, respectively.

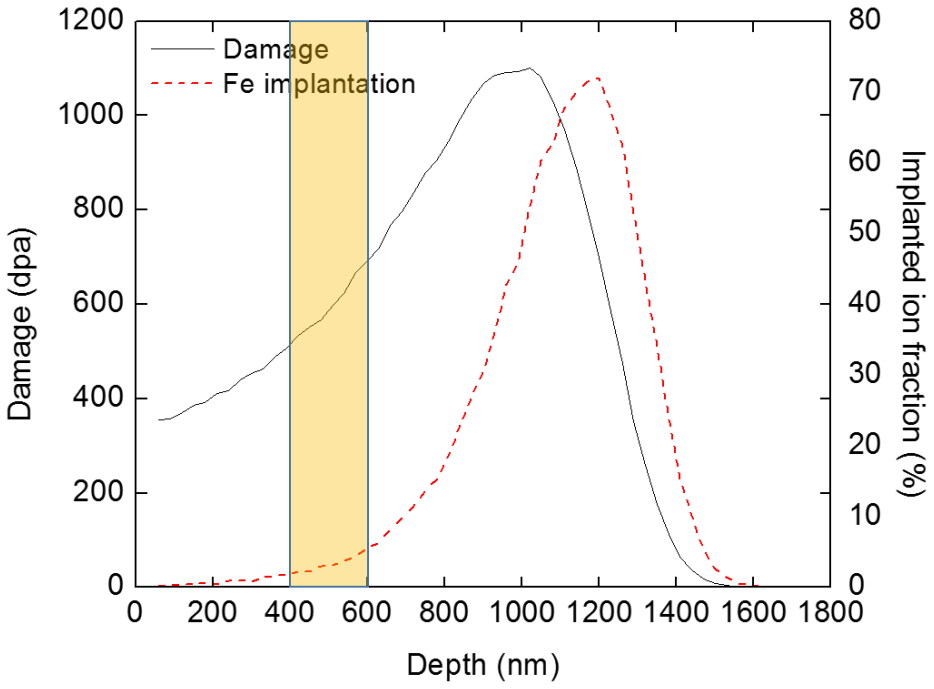

Figure 8.1 SRIM-calculated depth profiles of damage and implanted Fe atoms for 1100 peak dpa irradiation in pure Fe.

The microstructures prior to and after irradiations were characterized by TEM and APT. The samples were prepared for TEM studies as described in the previous section. APT specimens were prepared from the electropolished foils using the FIB technique. Atom probe needles pre-mounted on Si stubs were sharpened via annular milling using decreasing voltage and beam current with final 2 kV voltage and 28 pA beam current. The APT experiments were conducted on a Cameca Local Electrode Atom Probe (LEAP) 3000x HR at 50 K, using 200 kHz voltage pulse modes with a 20% voltage pulse fraction. 3D reconstructions were performed using commercial Cameca Integrated Visualization and Analysis Software (IVAS) package. Maximum separation distance methods for Y, Ti, O, TiO and YO were used in order to identify the NFs and analyze their composition [315]. Mass to charge ranges were established on the time of flight spectrum to determine the number of individual ion types. Radius of gyration and volume of the clusters (l_g) can be determined by using all the ranged ions. However, size calculations based on atom spatial measurements have large errors introduced by trajectory aberrations and oxygen atom diffusion on the tip. Therefore, an alternative method defined by Cunningham et al. [316] was used to calculate the NF size. Further, in this method, Fe and excess Cr were removed from the NFs as they are reported to be an APT artefact associated with trajectory aberrations [317-321]. This procedure may underestimate the Cr content of the features, but this is not expected to have a significant effect on the results. The NF size and composition were calculated by using the adjusted solute counts. It should be noted that APT reconstructions observe lower Y/Ti and O/(Ti+Y) ratios in the embedded NF oxides and bulk pyrochlore $Y_2Ti_2O_7$, which may be partially an APT artefact or partially due to

a Ti-rich NO shell [317]. On the other hand, recent TEM studies have shown that those NFs are $Y_2Ti_2O_7$ particles with Y/Ti≈1 [296,298].

8.4 Results

8.4.1 Microstructure before irradiation

The micrograph presented in Fig. 8.2a shows a bright-field (BF) TEM image of the typical microstructure of 14YWT samples containing finely distributed NFs together with larger particles reported to be Ti-Si-O-N rich together with trace amount of Y in the previous chapter. As shown in Fig. 8.2a, the density of large particles is quite low compared to the density of NFs. Fig. 8.2b presents the higher magnification BF TEM image of nanoparticles. The size and density of the NFs were determined as 2.8±0.7 nm and 4.3×10^{23} m^{-3}, respectively.

It has been reported by many authors that there is a relationship between NF size and their corresponding coherency with the matrix. Small NFs are often reported to be coherent, as expected, while transitioning to semicoherent or incoherent interfaces as the size increases [322-325]. Examples of coherent and semicoherent NFs are shown in the HRTEM micrographs in Fig. 8.3. While the small ~1.5 nm NF in Fig. 8.3a appears to be coherent, the larger ~5 nm NF in Fig. 8.3b has misfit Moiré fringes indicating semicoherency.

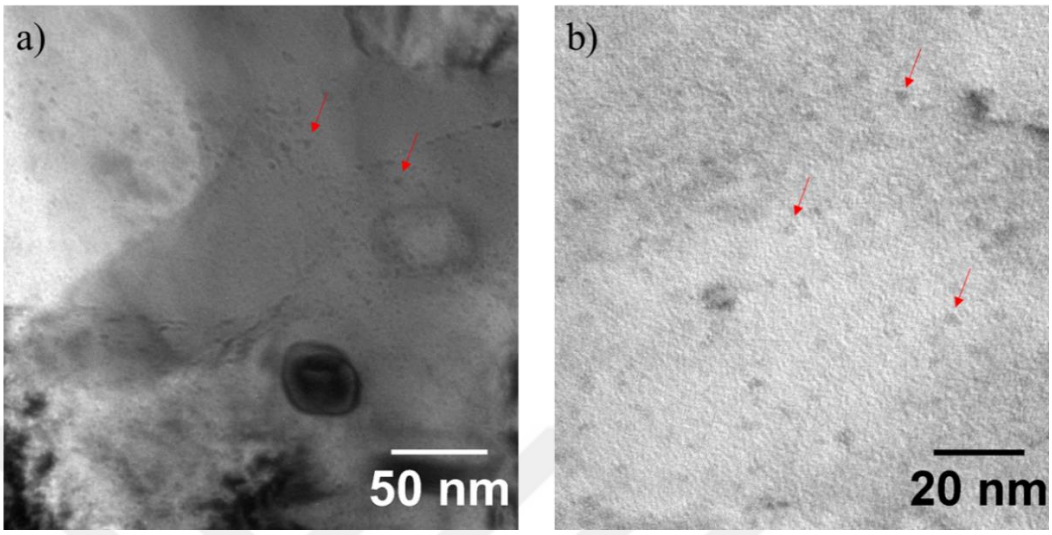

Figure 8.2 Distribution of particles before irradiation. (a) Low magnification BF TEM image showing both larger particles together with NFs (b) high magnification image showing the NF distribution.

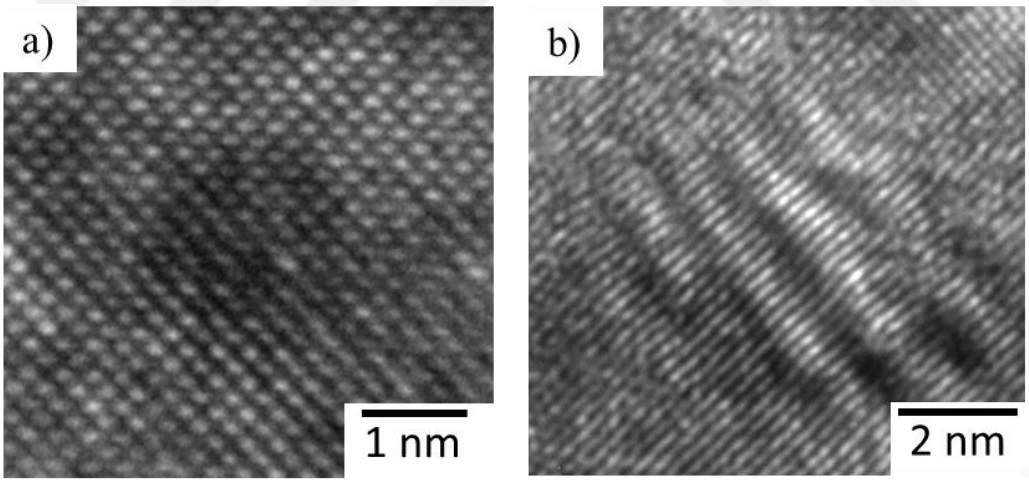

Figure 8.3 HRTEM images of (a) coherent small NF having the size ~1.5 nm (b) semicoherent larger ~5 nm NF showing misfit Moiré fringes.

NFs having 2-3 nm have been investigated along both [100] and [110] zone axis of α-iron matrix. Fig. 8.4a and Fig 8.4b show the HR images of 2-3 nm size particles and

their corresponding FFTs along $[100]_{\alpha}$. Since the particles are very small, it is quite difficult to detect any diffraction from them. The faint diffractions, shown by red arrows, well match with {044} and {004} planes of $Y_2Ti_2O_7$. Apparently, those two particles have different orientation relationships (ORs) with the matrix in such a way that $(00\bar{2})\alpha \,||\, (04\bar{4})Y_2Ti_2O_7$ for the particle in Fig. 8.4a while it is $(00\bar{2})\alpha \,||\, (00\bar{4})Y_2Ti_2O_7$ for the particle in Fig. 8.4b. Since any other diffraction cannot be detected from the particles, the zone axis of the particles yet remains unknown.

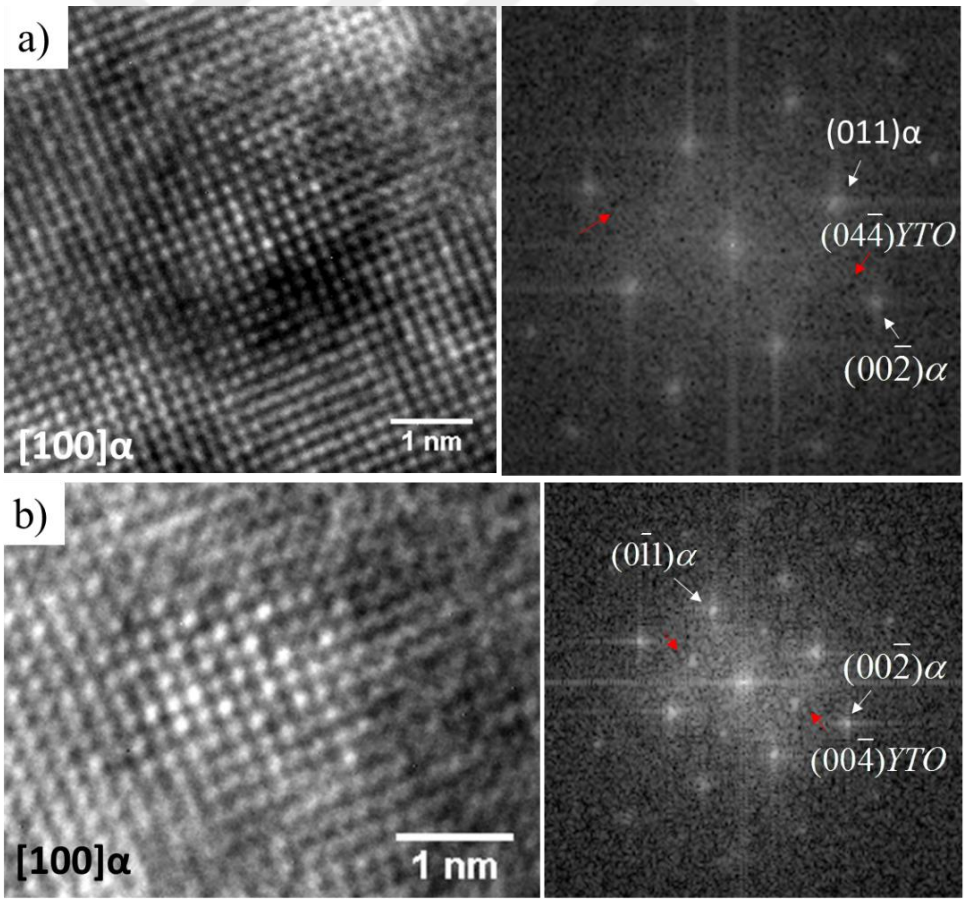

Figure 8.4 HRTEM micrographs and their corresponding FFTs along [100]α in particles having the OR of (a) $(00\bar{2})\alpha \,||\, (04\bar{4})Y_2Ti_2O_7$ and (b) $(00\bar{2})\alpha \,||\, (00\bar{4})Y_2Ti_2O_7$.

Fig. 8.5 also shows the existence of NFs having different orientations along [110]α. Fig. 8.5a shows an overview HRTEM image and corresponding FFT diagram containing extra diffractions other than the matrix diffractions. To be able to understand the features contributing to the formation of this diffractogram, investigations were done at different regions as labelled 1 to 3 in Fig 8.5a. Fig. 8.5b to Fig. 8.5d show the images and corresponding FFT diagrams from different regions in Fig. 8.5a. As shown in Fig. 8.5b, there are some regions where there is no particles. FFT from the region in Fig. 8.5b lacks the extra diffraction spots. On the other hand, Fig. 8.5c and Fig. 8.5d show two different regions having different particle orientations. It should be noted that the double diffractions in Fig. 8.5d might be resulted from the diffraction from overlapping particles as the thickness of the foils is at least 10 times larger than the particles. When the FFT diagrams from matrix and those particles are summed, the overall diffractogram in Fig. 8.5a can be obtained.

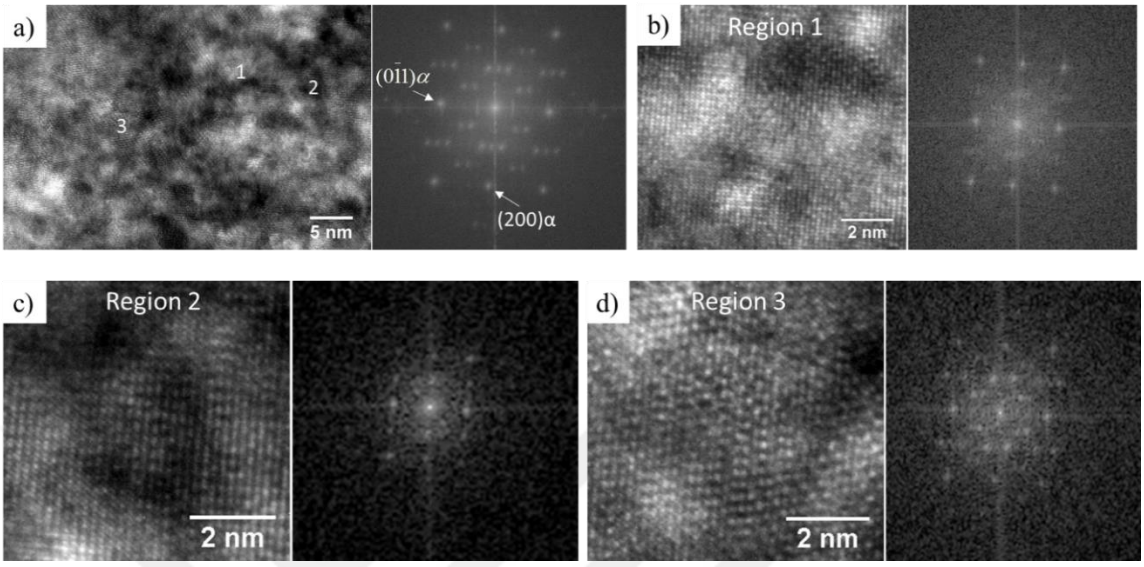

Figure 8.5 (a) HRTEM micrograph of a region and its corresponding FFT diagram along [110]α; HRTEM images and corresponding FFTs from (b) region 1, (c) region 2, (d) region 3 as labelled in (a).

At least ~20 particles were investigated and Fig. 8.6 shows the indexing of representative particles and their ORs with the matrix. Lattice spacings and parameters of particles in Fig. 8.6a and Fig 8.6b match with pyrochlore $Y_2Ti_2O_7$. Fig. 8.6a shows a particle having an OR of $(\bar{4}00)\alpha \,||\, (200)Y_2Ti_2O_7$ and $[011]\alpha \,||\, [0\bar{1}\bar{1}]Y_2Ti_2O_7$ while Fig. 8.6b shows a particle having an OR of $(01\bar{1})\alpha \,||\, (\bar{2}22)Y_2Ti_2O_7$ and $[011]\alpha \,||\, [110]Y_2Ti_2O_7$. On the other hand, the particle in Fig. 8.6c is consistent with the orthorhombic crystal structure of Y_2TiO_5. The relationship is found as $(002)\alpha \,||\, (\bar{2}\bar{1}0)Y_2TiO_5$ and $[110]\alpha \,||\, [001]Y_2TiO_5$. Furthermore, there are some particles that do not show any extra diffraction other than matrix as shown in Fig. 8.6d. Thus, their crystal structures remain unknown.

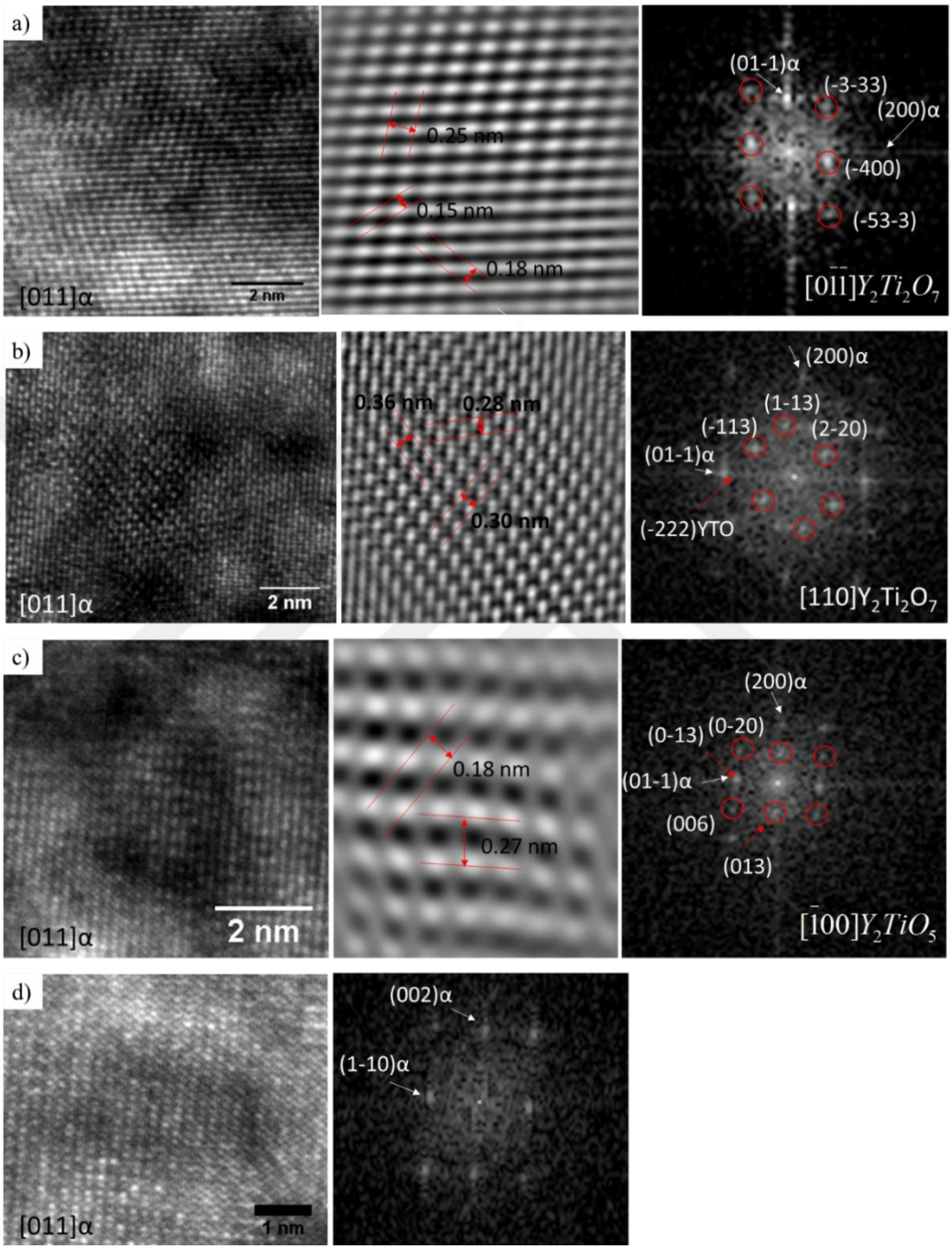

Figure 8.6 (a) HRTEM micrographs and corresponding FFT diagrams of (a) $Y_2Ti_2O_7$ particle having OR of $(\bar{4}00)\alpha \,||\, (200)Y_2Ti_2O_7$ and $[011]\alpha \,||\, [0\bar{1}\bar{1}]Y_2Ti_2O_7$; (b) $Y_2Ti_2O_7$ particle having OR of $(01\bar{1})\alpha \,||\, (\bar{2}22)Y_2Ti_2O_7$ and $[011]\alpha \,||\, [110]Y_2Ti_2O_7$; (c) Y_2TiO_5 particle having OR of $(002)\alpha \,||\, (\bar{2}\bar{1}0)Y_2TiO_5$ and $[110]\alpha \,||\, [001]Y_2TiO_5$; (d) an unknown particle with no extra diffractions.

In the literature, NFs are reported to be mostly $Y_2Ti_2O_7$ and their OR is generally $\{110\}\alpha \,||\, \{440\}Y_2Ti_2O_7$, indicating that pyrochlore-type particles are coherent at the entire interface with a cube-on-cube OR [326]. However, present study reports the existence of variety of OR other than cube-on-cube OR. While cube-on-edge OR between $Y_2Ti_2O_7$ and the matrix has been reported before [327,328], ORs of $(01\bar{1})\alpha \,||\, (\bar{2}22)Y_2Ti_2O_7$ along $[011]\alpha \,||\, [110]Y_2Ti_2O_7$ and $(002)\alpha \,||\, (\bar{2}\bar{1}0)Y_2TiO_5$ along $[110]\alpha \,||\, [001]Y_2TiO_5$ have not been reported. It should be noted that indexing was conducted based on the reported lattice parameters of the stoichiometric $Y_2Ti_2O_7$ and Y_2TiO_5 particles. However, Hirata et al. has shown that those particles are quite disordered with high volume of vacancies [329]. Therefore, the lattice parameters of the non-stoichiometric particles might be different. This might have introduced some uncertainty on the indexing of some non-stoichiometric Y-Ti-O particles.

Detailed NF sizes, number densities and compositions were obtained by 3D APT studies. For each condition 3 to 10 tips were investigated depending on the variability of the microstructure. For instance, the distribution of the NFs in unirradiated condition is less homogenous which required to investigate 10 tips. On the other hand, the samples irradiated at various damage levels does not show large variation, therefore, 3-4 tips were investigated. Each condition has average atom counts of ~4 millions. Fig. 8.7 is a representative APT reconstruction for the unirradiated 14YWT condition, showing a 3D spatial distribution of Y, Ti, O, YO and TiO ions, including the NF clusters. Note the oxygen distribution associated with the NFs is relatively scattered, which is an APT

artefact [318]. The APT reconstructions show that the NF distribution is somewhat nonhomogenous in the grains, but, except for a few cases, they do not appear to preferentially form at grain boundaries. In contrast to Y and O, Ti and W segregation occurs at all types of grain boundaries. The 3D grain boundary character is partially defined by the boundary plane and the misorientation angle between two adjacent grains. It is generally believed that constituent segregation and depletion are related to the grain boundary character [62]. The average sizes and densities of NFs are measured to be 2.1±0.5 nm and 6.2±1.5 x10^{23} m^{-3}, respectively, from APT analysis.

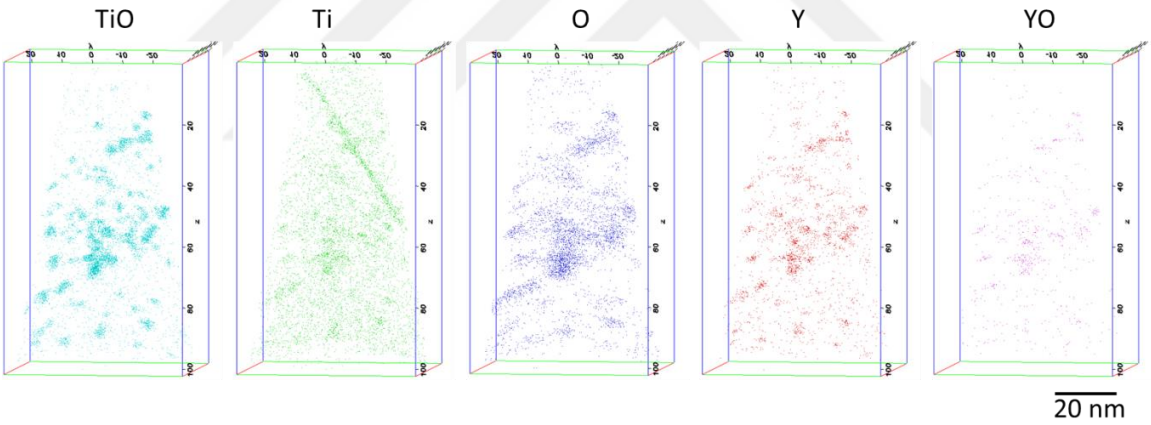

Figure 8.7 APT 3D reconstruction of unirradiated 14YWT samples showing distribution of various elements and ions.

The APT compositions of the matrix and NFs are given in Table 8.1. Even though the composition of NFs was corrected for excess Fe and Cr, they still contain a considerable amount of Cr. It is not possible to reliably determine if the Cr is in the NF or segregated in the matrix at its interface, as widely reported [330,331]. Although TEM

characterization shows that the small NFs are mostly $Y_2Ti_2O_7$, APT characterization measures Y/Ti/O ratio as 13/45/42. Composition deficiency of Y and O have been reported by many authors and attributed to the trajectory errors of elements [316]. It should also be noted that the composition of the matrix is quite consistent for different tips while the composition of NFs show large variations from cluster to cluster.

Table 8.1 Compositions (at%) of the matrix and NFs in unirradiated condition as determined by APT analyses.

Element (at%)	Matrix composition	NF composition
Fe	83.92±0.15	0
O	0.13±0.01	29.86±9.43
Cr	14.72±0.13	18.00±8.82
Ti	0.12±0.01	38.13±6.97
Y	0.02	11.74±4.74
Si	0.06	0.40±0.59
W	0.92±0.01	0.82±1.57
Mn	0.02	0.11±0.29
C	0.04±0.01	0.43±0.69
Al	0.01	0.45±0.63
Y/Ti/O	-	13/45/42

8.4.2 Microstructures after irradiation

BF TEM micrographs of irradiated samples at various dpa levels are shown in Fig. 8.8. While irradiations up to 480 dpa result in almost the same oxide size and distribution, as shown in Fig. 8.8a to Fig. 8.8c, 585 dpa irradiation visually produces much smaller NFs with denser distribution, as shown in Fig. 8.8d. Both sizes and densities of NFs, obtained from TEM characterization are summarized in Table 8.2. TEM measurements show that size of the NFs decreases while their density increases, with accumulating dose at 450˚C. Specifically, the NF size decreases from ~2.8 nm to ~2.1 nm after the irradiations at 270, 375 and 480 dpa irradiations and further decreases to ~1.7 nm after 585 dpa irradiations. The corresponding NF density increases considerably from ~4.3×10^{23} m^{-3} in the unirradiated condition to ~8.3×10^{23} m^{-3} in the case of 585 dpa irradiation condition.

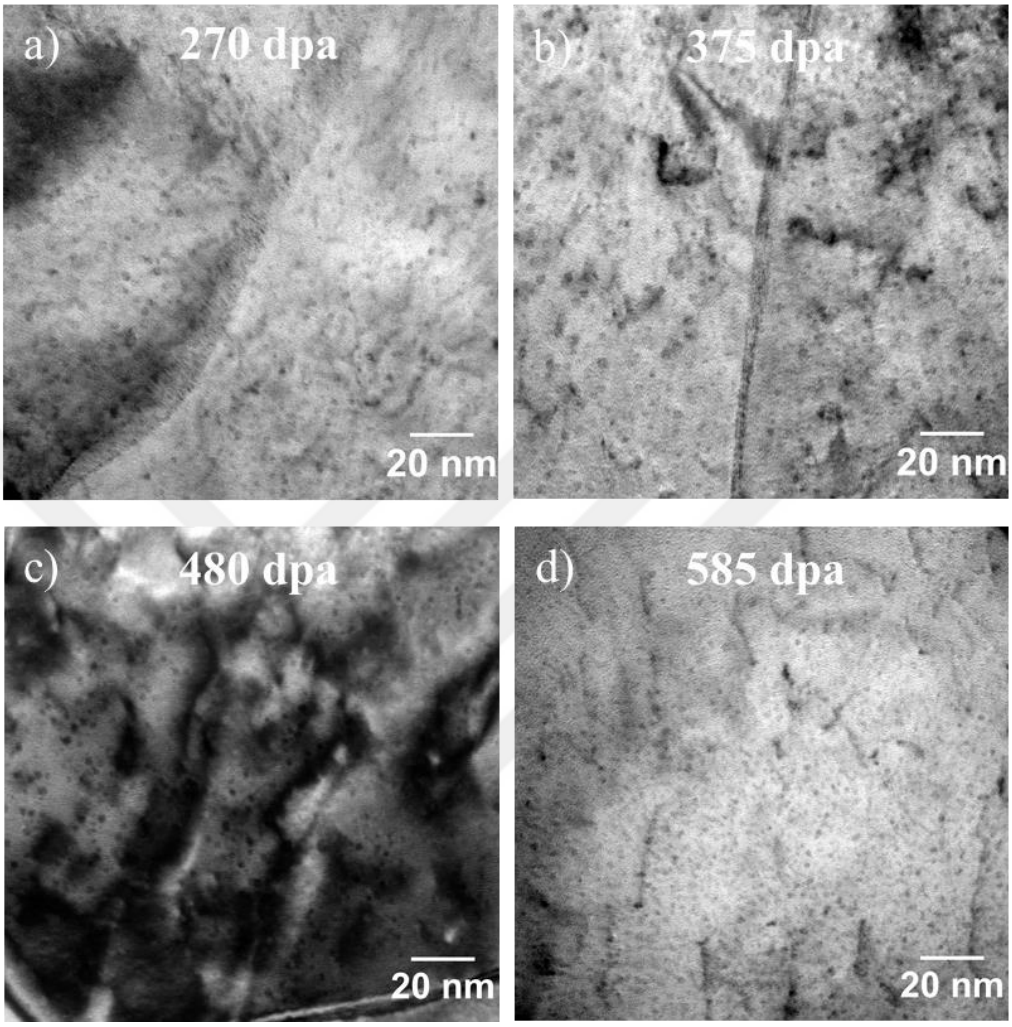

Figure 8.8 TEM images of samples collected from the depth region of 400 nm to 600 nm, after irradiation to (a) 270 dpa (b) 375 dpa (c) 480 dpa and (d) 585 dpa at 450 °C.

Table 8.2 Summary of NF size and density obtained from TEM and APT characterizations.

	unirradiated	270 dpa irradiated	375 dpa irradiated	480 dpa irradiated	585 dpa irradiated
Average size (TEM)	2.8±0.7	2.1±0.6	2.1±0.6	2.1±0.7	1.7±0.40
Average size (APT)	2.1±0.5	1.8±0.4	-	1.7±0.3	1.7±0.30
Number density (TEM)	$4.3\pm0.7\times10^{23}$	$6.3\pm1.2\times10^{23}$	$6.7\pm1.1\times10^{23}$	$7.3\pm2.4\times10^{23}$	$8.3\pm1.6\times10^{23}$
Number density (APT)	$6.2\pm1.5\times10^{23}$	$9.3\pm1.6\times10^{23}$	-	$7.1\pm0.7\times10^{23}$	$9.0\pm0.3\times10^{23}$

Fig. 8.9 shows HRTEM image of NFs after 480 dpa irradiation along [110] zone axis of the matrix. The size of the NFs is less than 5 nm and misfit Moiré fringes are not visible to infer the semicoherency contrary to the unirradiated case.

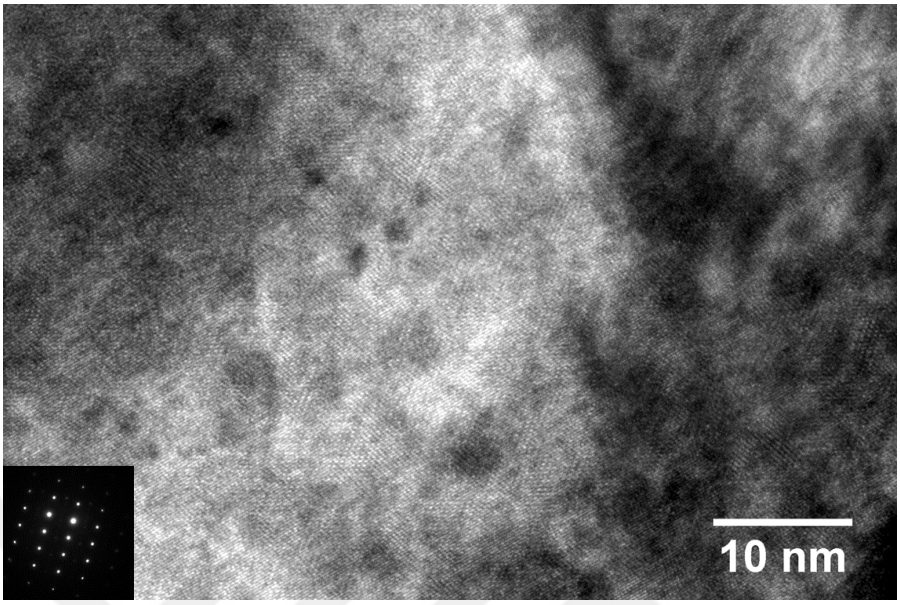

Figure 8.9 HRTEM image showing the NF distribution along [110] zone axis of the matrix after 480 dpa irradiation.

HRTEM studies were performed along both [100] and [110] zone axis of α-iron matrix after 480 dpa irradiation. Fig. 8.10a and Fig. 8.10b show the HRTEM images of 2-3 nm size particles and their corresponding FFTs along $[100]_{\alpha}$. Similar to the unirradiated case, FFT diagrams from small particles result in either no extra diffraction spots as in Fig. 8.10a or very weak diffractions as in Fig 8.10b. While the particle crystal structure cannot be determined in Fig. 8.10a, the lattice spacings and angles obtained from the FFT diagram in Fig. 8.10b suggests the $Y_2Ti_2O_7$ particles having pyrochlore crystal structure. Moreover, the OR is determined as cube-on-cube in such a way that $(002)\alpha \,||\, (440)Y_2Ti_2O_7$, $(110)\alpha \,||\, (400)Y_2Ti_2O_7$ along $[001]\alpha \,||\, [001]Y_2Ti_2O_7$.

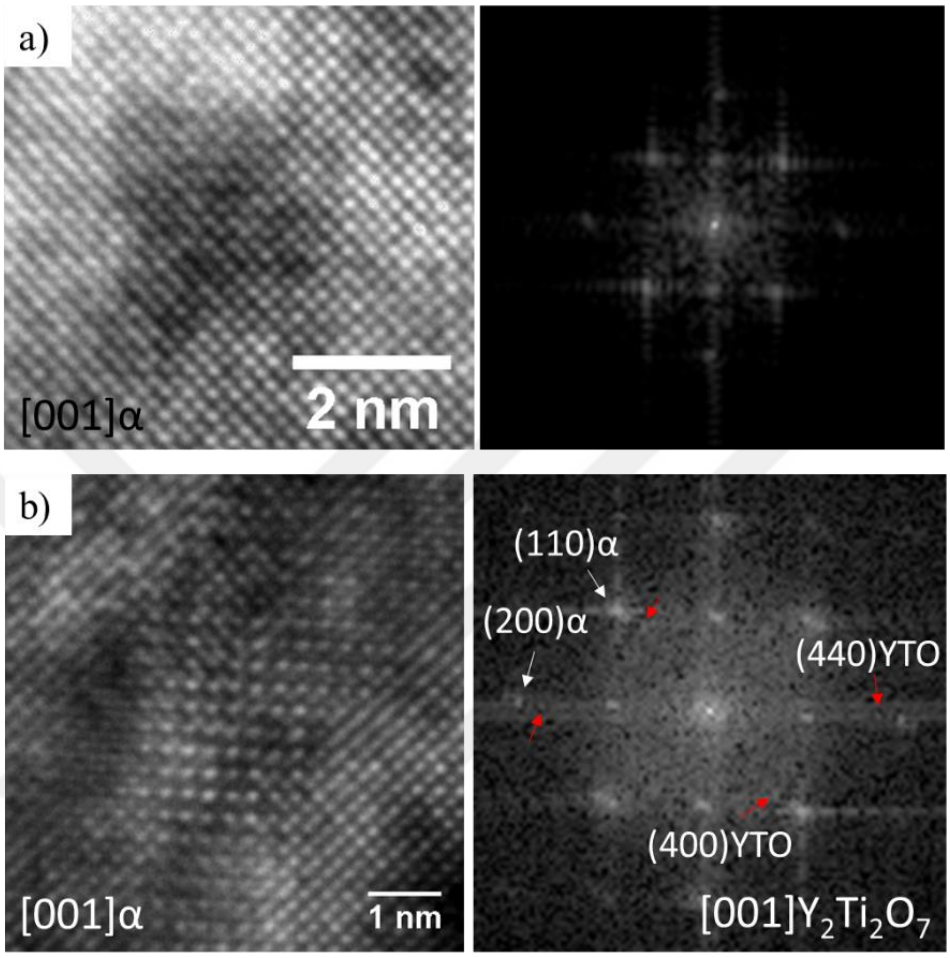

Figure 8.10 HRTEM micrographs and their corresponding FFTs along [100]α in particles (a) with unknown OR as it lacks extra diffraction spots in FFT diagram (b) having the OR of $(002)\alpha \,||\, (440)Y_2Ti_2O_7$, $(110)\alpha \,||\, (400)Y_2Ti_2O_7$ along $[001]\alpha \,||\, [001]Y_2Ti_2O_7$.

Fig. 8.11 shows the indexing of representative particles and their ORs with the matrix. Similar to the unirradiated condition, lattice parameters and angles of particles in Fig. 8.11a and Fig. 8.11b match with pyrochlore $Y_2Ti_2O_7$. Fig. 8.11a shows a particle having an OR of $(00\bar{4})\alpha \,||\, (002)Y_2Ti_2O_7$ along $[1\bar{1}0]\alpha \,||\, [110]Y_2Ti_2O_7$ while Fig. 8.11b shows a particle having an OR of $(110)\alpha \,||\, (\bar{2}22)Y_2Ti_2O_7$ along $[1\bar{1}0]\alpha \,||\, [110]Y_2Ti_2O_7$. Their OR

before and after irradiation is the same; however, the lattice parameters of both particles are slightly larger compared to the unirradiated conditions. Ribis et al. suggested lattice parameter changes as a result of the interaction between damage cascades and nano-particles if the particles are not at the thermodynamic equilibrium [304]. It should also be noted that Y_2TiO_5 particles were not detected among ~20 investigated particles. The reason might simply be attributed the low density of Y_2TiO_5 particles compared to $Y_2Ti_2O_7$ particles.

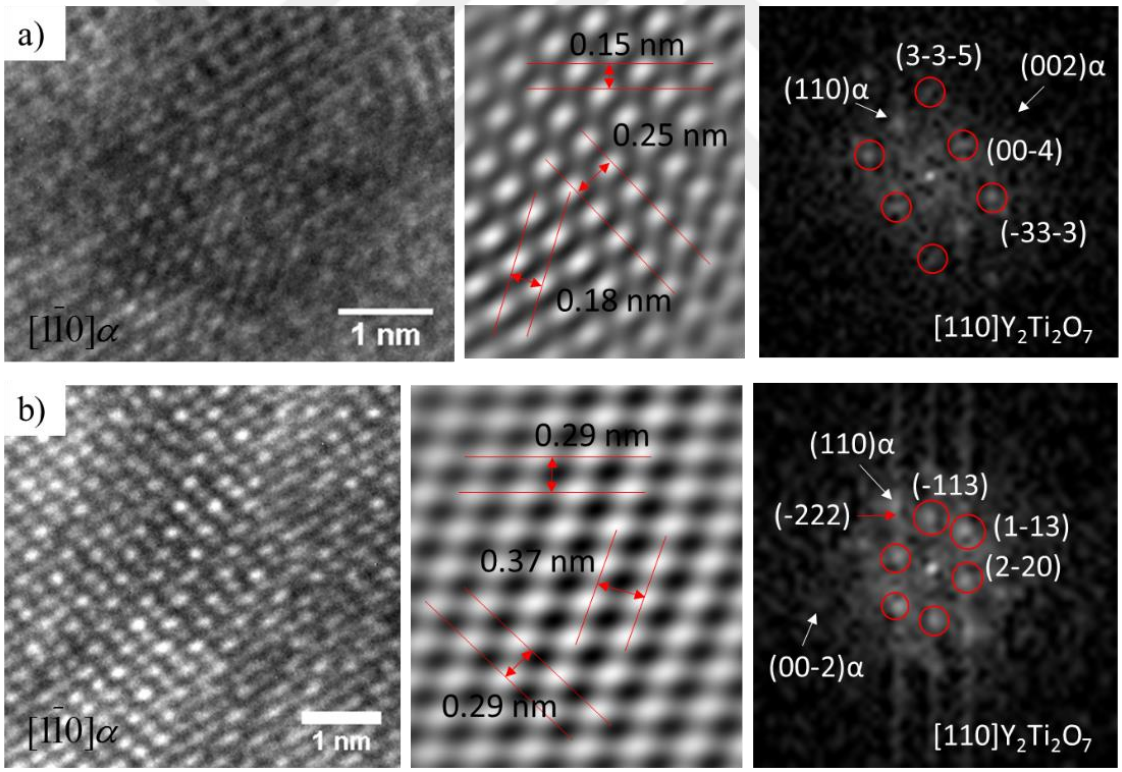

Figure 8.11 (a) HRTEM micrographs and corresponding FFT diagrams of $Y_2Ti_2O_7$ particles having OR of (a) $(\bar{4}00)\alpha \,||\, (200)Y_2Ti_2O_7$ and $[011]\alpha \,||\, [0\bar{1}\bar{1}]Y_2Ti_2O_7$; (b) $(01\bar{1})\alpha \,||\, (\bar{2}22)Y_2Ti_2O_7$ and $[011]\alpha \,||\, [110]Y_2Ti_2O_7$.

Fig. 8.12a to Fig. 8.12c show the representative APT reconstructions of 270, 480 and 585 dpa irradiated 14YWT conditions. In contrast to the particle distribution in the unirradiated condition, after irradiation, NFs are distributed more homogenously. The NF size and density tabulated in Table 8.2 are broadly similar to the TEM results in that the APT analyses indicate that size of the NFs decreases slightly after irradiation, while the density increases. While there are moderated differences at lower dpa the TEM and APT data are remarkably consistent following the 585 dpa irradiations. Note others also have reported that even if initially they are slightly refined, the oxides are stable above a certain damage level [294,322,332,333].

Fig. 8.13 compares the NF size plots obtained by APT and BF TEM analyses. Before irradiation, NFs show a broad size distribution up to 6 nm; in contrast, the size distribution of NFs after irradiation becomes narrower and is limited to the sizes below 5 nm. That is, the concentration of smaller NFs increase, while the larger NFs disappear. It should be noted that in general TEM gives slightly larger size and lower density compared to APT, likely due to a lower resolution limit. Thus it is notable that TEM studies observe the same size and even a higher number density in the case of the 585 dpa irradiated 14YWT samples, but the differences are well within the estimated errors.

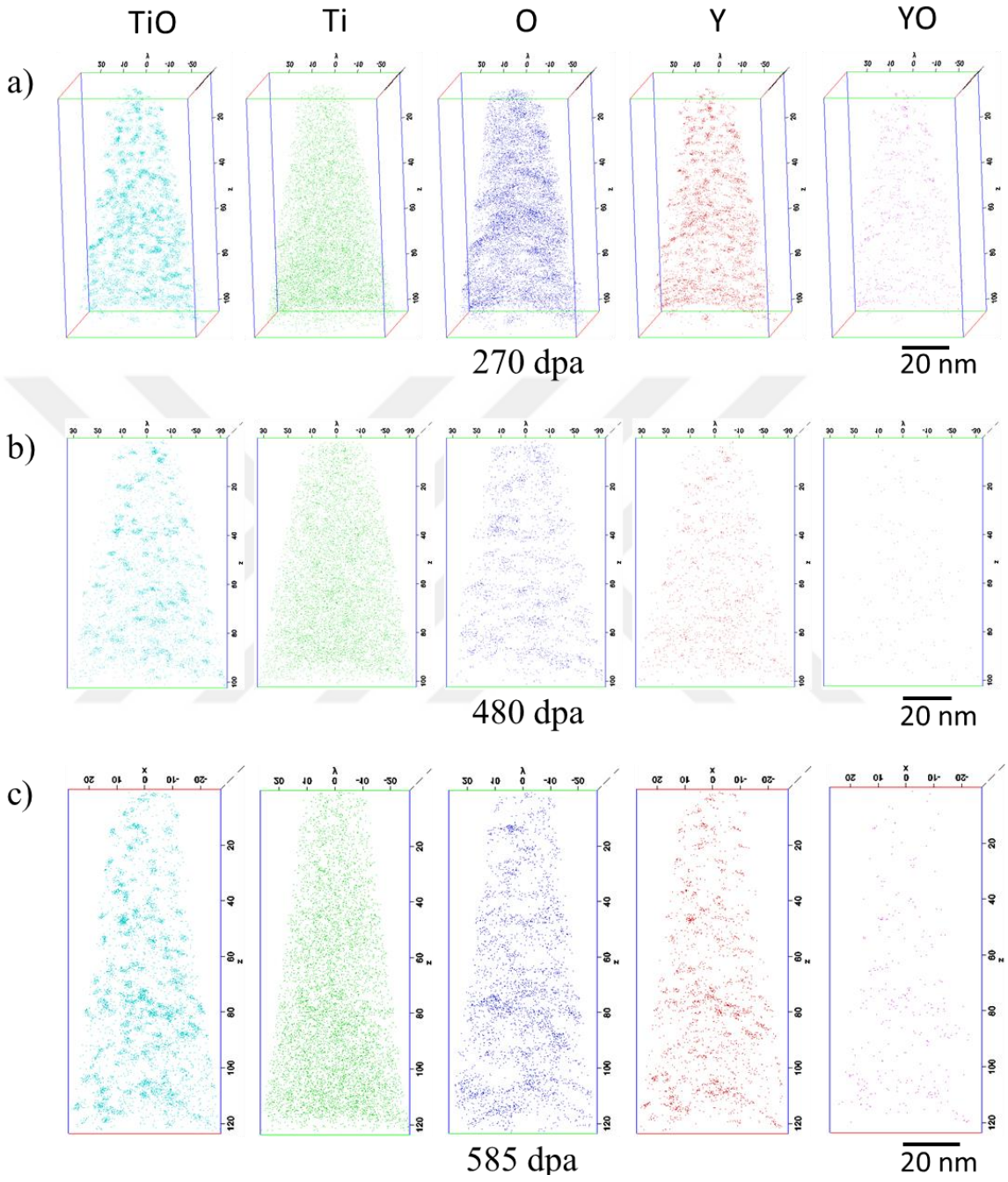

Figure 8.12 APT 3D reconstructions showing the distribution of various elements and ions in 14YWT samples irradiated to (a) 270 dpa (b) 480 dpa and (c) 585 dpa at 450 °C.

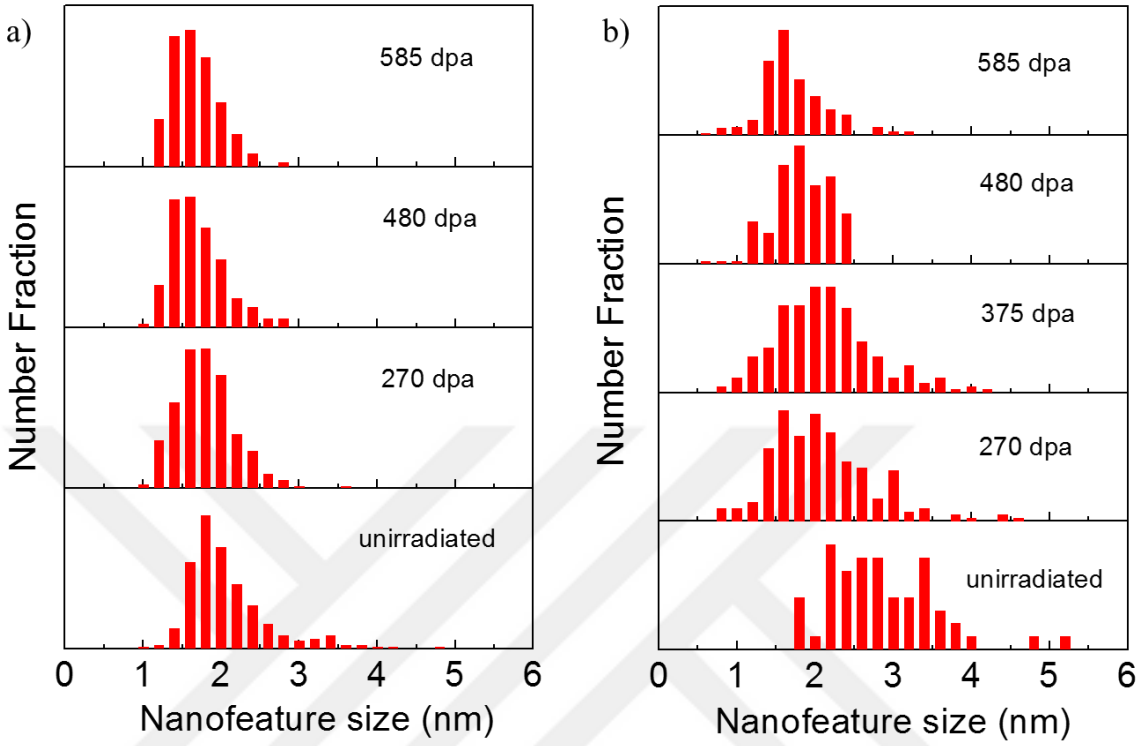

Figure 8.13 NF size distribution in unirradiated and various dose irradiated samples obtained by (a) APT and (b) TEM analyses.

The compositions of matrix and NFs after irradiation are summarized in Table 8.3. Following irradiation, the Cr content of both the matrix and NFs decrease slightly, possibly due to segregation at the grain boundaries. The matrix Fe fraction increases due to the effect of injected interstitials which can reach up to ~3 at% at the depth of 400-600 nm for 585 local dpa irradiation. Moreover, O increases slightly in NFs. However, all those changes are within the estimated error and there is no second phase precipitation in the microstructure to explain significant variations in the bulk composition. Table 8.1 shows that NF Y/Ti/O ratio of the unirradiated sample is 13/45/42 compared to an average of 13/44/43 following irradiation, with Ti approximately constant while, Y and O slightly

change. Thus the most important conclusion is that there is no large change in the NF compositions following irradiation. It should be noted that the low Y/Ti ratio might be an APT artefact, that can be even observed in bulk stoichiometric $Y_2Ti_2O_7$. Thus the APT results are not inconsistent with the TEM analysis showing that the crystal structure of small NFs below 5 nm are cubic pyrochlore $Y_2Ti_2O_7$ complex oxides before and after irradiation.

Table 8.3 Compositions (at%) of the matrix and NFs in irradiated 14YWT samples at 450 °C up to 270, 480 and 585 local dpa doses at the depth of 400-600 nm.

	270 dpa		480 dpa		585 dpa	
Element (at%)	Matrix composition	NF composition	Matrix composition	NF composition	Matrix composition	NF composition
Fe	84.52±1.91	0	86.67±4.14	0	88.32±2.07	0
O	0.19±0.08	35.63±4.84	0.10±0.03	36.76±5.36	0.14±0.05	35.04±4.87
Cr	13.98±1.96	7.23±8.20	11.93±4.36	11.52±9.46	10.31±2.24	12.11±9.94
Ti	0.20±0.02	37.93±6.40	0.15±0.05	40.69±7.08	0.19±0.06	39.30±6.30
Y	0.03±0.01	16.52±9.02	0.01	8.84±6.04	0.02	11.54±5.63
Si	0.05±0.01	0.48±0.78	0.02±0.02	0.47±1.04	0.03±0.01	0.59±1.08
W	0.91±0.06	0.15±0.88	1.03±0.20	0.16±0.76	0.88±0.08	0.09±0.35
Mn	0.02	0.08±0.33	0.01±0.01	0.13±0.47	0.01	0.08±0.33
C	0.05	0.37±0.67	0.03±0.01	0.86±2.08	0.07±0.03	1.13±1.96
Al	0.02±0.01	0.43±0.71	0.03±0.02	0.83±1.22	0.02	0.38±0.91
Y/Ti/O	-	15/44/42	-	11/44/45	-	13/45/42

8.5 Discussion: Stability of NFs under irradiation

Stability of dispersoids can be predicted from Russel's precipitation model, which considers both decay and growth, due to ballistic-collision-induced dissolution and thermal-diffusion-induced recovery of dispersoids [294,334]. In consistent with the model, many previous studies have shown that large dispersoids shrink and small ones grow under irradiation, reaching an equilibrium size which depends on various irradiation parameters. The model, however, might be oversimplified for not considering the effects of interface coherency, as pointed in the recent study by Chen et al. [322]. For small dispersoids, they are dominated by coherent and semi-coherent interfaces, while for large dispersoids they are incoherent. Since dispersoids in the present study are relatively small (less than 5 nm as shown in Fig. 8.13), the complexity in interface energy changes due to transition from incoherency to coherency can be ignored. Hence the decay and growth competition can be described by [335,336];

$$\frac{dr}{dt} = -K\Psi + \frac{3D'c}{4\pi rp} \tag{8.1}$$

where r is the dispersoid radius, K is defect production rate, Ψ is dissolution parameter, D' is irradiation enhanced diffusion coefficient, c is the atomic concentration of solute in solution, and p is the solute atom fraction in NFs. The first term on the right side of the equation describes the dissolution and the second term describes the recovery. Both dissolution and growth are believed to be largely limited by Y diffusion due to its low diffusivity as a large solute atom. Furthermore, oversize substitutional atoms diffuse primarily through vacancy diffusion mechanism. Hence Y diffusivity is proportional to

the level of vacancy supersaturation. O atoms are fast diffuser and can quickly migrate to accommodate dispersoid composition change needs, and their contribution in limiting dispersoid recovery can be ignored. Therefore, D' can be approximated by the diffusivity of Y atoms, described by [314];

$$D' = \frac{C_v'}{C_v^{eq}} D^{th} \tag{8.2}$$

where C_v' is non-equilibrium concentration of vacancies; C_v^{eq} is equilibrium concentration of vacancies; D^{th} is the Y thermal diffusivity under equilibrium condition.

Determination of C_v' needs to solve defect reaction equation which considers defect generation, interstitial-vacancy recombination and defect trapping by sinks. At high temperature and in the presence high density defect sink, numerical solution leads to a quasi-steady state of vacancy supersaturation with $C_v' = K/(K_{vs}C_s)$, where K is defect creation rate, K_{vs} is vacancy-sink reaction rate, C_s is vacancy sink concentration. Details on numerical calculation to obtain C_v' can be found in Ref. 13. Assuming the only vacancy trapping sites are dispersoids (since TEM does not observe significant voids), C_s represents the dispersoid density. The vacancy-sink reaction rate can be calculated by $K_{vs} = 4\pi r D_V$, where r is dispersoid size and D_v is vacancy diffusivity. Based on these approximation, equation 8.2 can be rewritten as;

$$D' = K(4\pi r D_V N C_V^{eq})^{-1} D^{th} \tag{8.3}$$

From APT characterization, we can obtain average dispersoid radius *r* and average dispersoid density *N*. The defect creation rate is 9.7×10^{-4} dpa/s. The vacancy diffusivity D_V is calculated by using Debye frequency of 10^{13} s^{-1} and vacancy migration energy of 0.7 eV [314,337]. The equilibrium vacancy concentration C_V^{eq} is calculated by using vacancy formation energy of 2.2 eV in bcc Fe. The thermal diffusivity of Y is calculated by $D^{th} = 0.1\exp\left(-3.25eV/k_BT\right)$ cm^2/s [338].

Under a quasi-steady state of dispersoid growth, the growth and dissolution reaches a balance with *dr/dt*=0 in equation 8.1. The present experimental study shows that after the radiation damage of 270 dpa and beyond, the mean size of dispersoids is saturated to about 1.7 nm and the average dispersoid density is saturated to about $8.5x10^{17}cm^{-3}$ Substituting these two values into above stated equations for *T*=450 °C, we calculate the dissolution parameter Ψ to be 1.5×10^{-10} cm.

Fig. 8.14 plots Nr^2 vs. T, with the solid line representing the equilibrium condition when growth and dissolution reaching the balance. The curve is obtained by using Ψ value determined from the above discussion. For the region above the curve, dissolution dominates and dispersoids will shrink until the dispersoid morphology evolve into the condition specified by the line. For the region beneath the curve, dispersoids will grow under ion irradiation. In Fig. 8.14, Nr^2 values of the as-received samples and irradiated samples up to 270 dpa are also plotted and arrow in the inlet shows the trajectory of dispersoid changes.

Figure 8.14 is in agreement with previous experimental studies that dispersoids will shrink under ion irradiations and, as a function of ion irradiation temperature, the final equilibrium sizes will increase with increasing temperatures, as shown by Chen et al. recently on 12Cr ODS alloys [322]. The irradiation parameters Ψ and K depend on specific experimental conditions. Hence the equilibrium curve will shift under different irradiation conditions. On the other hand, if parameter difference and their conversions under different conditions, such as accelerator ion irradiation vs. reactor neutron irradiation, are known, in principle the prediction on stability of dispersoids is possible from accelerator testing. In addition to the fact that the current model does not consider the role of interface coherency, the effects from void swelling is ignored since even for the highest dpa, we barely see small bubble formation. For other ODS systems which have much more void swelling, such as MA956, the discussion on sink strength must consider vacancy-void interactions. Therefore, the current model presents a simplified approach to predict dispersoid stability.

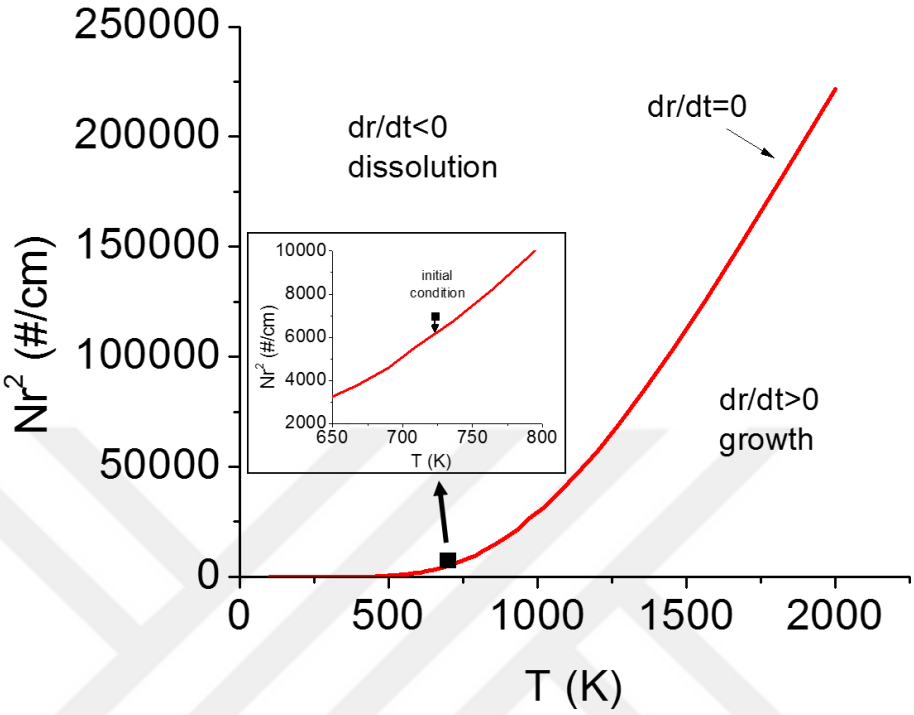

Figure 8.14 Nr^2 vs. T plot showing the behaviour of the dispersoids in the present study.

Slight increase in the density of the NFs after irradiation might indicate that the dissolved atoms forms new NFs instead of growing the previously existing ones. Similar 'inverse coarsening' behaviour was first observed by Frost and Russell [339]. It was attributed to the solute atom ejection to the matrix as a result of irradiation and subsequent diffusion of those solute atoms either to the original precipitate or another place to form new precipitates. Li et al. [340] reported that in thermally-aged CF8 steels irradiated with 1 MeV Kr ions, the size of the G-phase precipitates decreased while their density increased. Moreover, Tan et al. [341] found that the ejected atoms from original TaC nanoprecipitates during radiation-induced displacement cascade led to reduced size of the

original particles and helped nucleating new particles, consequently increasing particle density.

8.6 Conclusions

14YWT NFA tubes were irradiated at very high doses up to 1100 peak dpa at 450 °C and the structure, composition and size of NFs have been investigated via TEM and APT techniques. It has been determined that the NFs are mostly $Y_2Ti_2O_7$ having pyrochlore structure. On the other hand, there are some Y_2TiO_5 particles having orthorhombic crystal structure. HRTEM images suggest that NFs are either coherent or semicoherent with the matrix. After irradiation, NFs having pyrochlore structure kept their crystal structure with slight increase in their lattice parameter. No Y_2TiO_5 particles were observed presumably due to their low density compared to $Y_2Ti_2O_7$ particles. Furthermore, self-ion irradiations results in a slight decrease in the NF size together with an increase in their density. This has been explained by the 'inverse coarsening' phenomena due to the disruption of balance between irradiation induced dissolution of the NFs and thermal back diffusion of solute atoms to the particle. The experimental results were confirmed by the theoretical calculations. The net change in the NF size calculations indicated the dissolution of the particles.

9. SUMMARY AND CONCLUSIONS

(1) Self-ion irradiations up to 400 peak dpa were conducted on ferritic EK-181 alloy produced in severely plastically deformed and annealed conditions in order to understand the effect of grain boundaries on the radiation resistance. It was found that severe plastic deformation (SPD) changes the depth distribution of swelling. Furthermore, SPD accelerates the onset of swelling in a shallow depth region rather than improving swelling resistance of EK-181 alloys. This result is attributed to the instability of nano-grains in the severely deformed material arising from the combined effects of thermal annealing and ion irradiation. Both variants swell with the rate of 0.2%/dpa at their steady state regime. However, the incubation period preceding this steady state rate is dependent on the dpa rate associated with the depth range where the data were extracted. While higher dpa rates increase the incubation period of annealed samples, variation of incubation periods in the severely deformed samples is much less because swelling occurs in a relatively narrower and shallower region indicating lower dpa rate effect and weaker injected interstitial effect.

(2) Effect of shock deformation on microstructure and mechanical properties was investigated on tempered HT-9 shock loaded to a peak pressure of 11 GPa. It was found that shock deformation leads to a ~2-3 fold increase in dislocation density resulting in an increase in hardness. Dislocation pile-up at the lath boundaries as a result of shock deformation increases the misorientation angle leading to a reduction in the fraction of coincidence site lattice boundaries (CSLBs) by 5-10%. Moreover, shock loading causes

local plastic deformation of the continuous parallel lath structure in some regions as well as an overall decrease in the aspect ratio of laths due to local plastic deformation and lath fragmentation.

(3) The effect of shock loading on the radiation response of HT-9 steels was investigated under 600 dpa ion irradiations at 450 °C. It was found that irradiations cause a further decrease (by ~7.5%) in the fraction of CSLBs while it is still higher in as-received undeformed material. Both as-received and shock deformed samples exhibit a very low amount of swelling limited to shallow depths of 500-600 nm. At this transient regime, shock deformed material shows slightly higher swelling compared to the as-received undeformed sample. It was found that irradiation induces the formation of M_2X and G-phase precipitates. The sink stregth of M_2X precipitates is very high compared to the dislocation and boundary sink strengths, and the total sink strength is slightly lower in the as-shocked material. A high fraction edge dislocations in as-shocked material which has a higher bias to self interstitial atoms (SIAs) compared to vacancies might be another reason for slightly higher swelling. However, once the steady-state regime is reached, the swelling resistance of the materials might change depending on the sink strengths.

(4) In this study, the effect of different processing routes on texture and grain boundary characteristics for 14YWT NFA cladding tubes was investigated. The tubes were produced either by spray forming followed by hydrostatic extrusion (Process I) or by hot extrusion and cross-rolling a plate followed by hydrostatic tube extrusion (Process II). Hydrostatic extrusion which introduces a combination of plane strain and shear deformations results in α- and γ-fibers on {001}<110> and {111}<110> as well as weak

textures of ζ-fiber on {011}<211> and {011}<011>. On the other hand, hot extrusion and cross-rolling processes result in plane strain deformations leading to a strong texture on {001}<110> together with weak texture on {111}<112>. While both conventional hot extrusion and innovative hydrostatic extrusion produce a pronounced texture on {001}<110>, shear deformation introduced during hydrostatic deformation produces the <111>∥ND texture component. Furthermore, hydrostatic extrusion results in weaker textures compared to the hot extrusion and rolling textures. Together with a decrease in the texture index, α-fiber on {001}<110> weakens and γ-fiber on higher Taylor factor planes, {111}<110>, strengthens as a result of a reduced number of activated slip systems during shear deformation. The beneficial stress state and texture created by hydrostatic extrusion results in the production of crack-free cladding tubes. In addition, local reorientation during shear deformation results in high fractions of low angle boundaries (LABs) compared to the intermediate tube produced by plane strain deformation.

(5) 14YWT tubes produced by the above stated methods (Process I and Process II) were investigated in terms of their microstructure and mechanical properties before and after high dose self-ion irradiations. It was found that different microstructures result in considerably different irradiation responses. Pre-irradiation microstructures have shown that Process II results in finer grain size together with high density Y-Ti-O nanofeatures (NFs) compared to Process I. Moreover, the yield strength of the Process II tube is two times higher due to its finer and denser NF content, smaller grain size and higher dislocation density. Microstructural analysis after irradiations demonstrated that Process II tube shows at least two orders of magnitude less swelling compared to the Process I

tube because of the finer, denser and more homogenous distribution of NFs in Process II tubes. Due to the inhomogeneity in the initial microstructure as a result of Process I, there is a large deviation in the depth distribution of swelling and irradiation hardening. On the other hand, irradiation hardening was saturated by ~0.8 GPa due to defect saturation for Process II tubes for all radiation damages.

(6) The stability of NFs in 14YWT NFA tubes irradiated at very high doses of up to 1100 peak dpa was investigated via transmission electron microscopy (TEM) and atom probe tomography (APT) techniques. It was found that the NFs are mostly $Y_2Ti_2O_7$ and Y_2TiO_5 particles which are either coherent or semicoherent with the matrix. After irradiation, NFs having the pyrochlore structure retain their crystal structure with a slight increase in their lattice parameter. Furthermore, self-ion irradiations result in a slight decrease in the NF size together with an increase in their density. This is explained by the 'inverse coarsening' phenomena due to the disruption of balance between irradiation induced dissolution of the NFs and thermal back diffusion of solute atoms to the particle. A theoretical model was established to explain the NF stability. The model has shown that present irradiation parameters lead to a slight dissolution of the NFs.

REFERENCES

[1] R. Goldston, M. Abdou, C. Baker, M. Campbell, V. Chan, et al., J. Fus. Energy 21 (2002) 61-111.

[2] D. Bhattacharyya, P. Dickerson, G. R. Odette, S. A. Maloy, A. Misra, et al., Philos. Mag., 92 (2012) 2089–2107.

[3] K. Ehrlich, Philos. Trans. R. Soc. London Ser. A 357 (1999) 595–623.

[4] H. Bolt, V. Barabash, W. Krauss, J. Linke, R. Neu, et al., J. Nucl. Mater. 329–333 (2004) 66–73.

[5] T. R. Allen, J. T. Busby, R. L. Klueh, S. A. Maloy, M. B. Toloczko, JOM 60 (2008) 15–23.

[6] D. S. Gelles, J. Nucl. Mater. 239 (1996) 99-106.

[7] F. A. Garner, M. B. Toloczko, B. H. Sencer, J. Nucl. Mater. 276 (2000) 123– 142.

[8] D. T. Hoelzer, J. Bentley, M. A. Sokolov, M. K. Miller, G. R. Odette, et al., J. Nucl. Mater. 367–370 (2007) 166-172.

[9] T. Hayashi, P. M. Sarosi, J. H. Schneibel, M. J. Mills, Acta Mater. 56 (2008) 1407–1416.

[10] J. H. Schneibel, C. T. Liu, D. T. Hoelzer, M.J. Mills, P. Sarosi, et al., Script. Mater. 57 (2007) 1040–1043.

[11] S. J. Zinkle, N. M. Ghoniem, Fus. Eng. Des. 51–52 (2000) 55–71.

[12] M. Nastasi, J. W. Mayer, Ion Implantation and Synthesis of Materials, Springer, Berlin, 2006.

[13] G. Was, Fundamentals of Radiation Materials Science: Metals and Alloys, Springer, Berlin, 2007.

[14] G. H. Kinchin and R. S. Pease, Rep. Prog. Phys. 18 (1) (1955) 1-51.

[15] W. E. King, K. L. Merkle, M. Meshii, J. Nucl. Mater. 117 (1983) 12-25.

[16] ASTM Standards (E521), Standard Practice for Neutron Radiation Damage Simulation by Charged-Particle Irradiation, ASTM International, Philadelphia, PA, 1996.

[17] D. R. Olander, Fundamental Aspects of Nuclear Reactor Fuel Elements, Report No.TID-26711-P1, California University, Berkeley, Department of Nuclear Enginerring, 1976.

[18] C. K. Gupta, Nuclear reactor materials: irradiation effects, in: K. H. J. Buschow, R. W. Cahn, M. C. Flemings, B. Ilschner, E. J. Kramer, et al. (Eds.), Encyclopedia of Materials - Science and Technology, Volumes 1-11, Elsevier, Oxford, 2001, pp. 6349-6360.

[19] G. R. Odette, M. J. Alinger, B. D. Wirth, Ann. Rev. Mater. Res. 38 (2008) 471-503.

[20] G. S. Was, P. L. Andresen, Radiation damage to structural alloys in nuclear power plants: mechanisms and remediation, in: A. Shirzadi, S. Jackson (Eds.), Structural Alloys for Power Plants - Operational Challenges and High-Temperature Materials, Elsevier, Oxford, 2014, pp. 355-420.

[21] A. G. Certain, Radiation Stability of Nanoclusters in Nanofeatured Oxide Dispersion Strengthened (ODS) Steel, PhD Thesis, University of Wisconson-Madison, 2012.

[22] S. M. Bruemmer, E. P. Simonen, P. M. Scott, P. L. Andresen, G. S. Was, L. J. Nelson, J. Nucl. Mater. 274 (1999) 299–314.

[23] O. Anderoglu, J. Van den Bosch, P. Hosemann, E. Stergar, B. H. Sencer, et al., J. Nucl. Mater. 430 (2012) 194–204.

[24] S. I. Golubov, A. M. Ovcharenko, A. V. Barashev, B. N. Singh, Phil. Mag. A, 81(3) (2001) 643–658.

[25] D. J. Edwards, E. P. Simonen, S. M. Bruemmer, J. Nucl. Mater. 317 (2003) 13-31.

[26] B. H. Sencer, J. R. Kennedy, J. I. Cole, S. A. Maloy, F. A. Garner, J. Nucl. Mater. 414 (2011) 237–242.

[27] T. R. Allen, J. I. Cole, C. L. Trybus, D. L. Porter, H. Tsai, et al., J. Nucl. Mater. 348, (2006) 148-164.

[28] L. K. Mansur, J. Nucl. Mater. 216, (1994) 97-123.

[29] R. L. Klueh, Effect of neutron irradiation on properties of steels, in: ASM International Handbook Committee (Eds.), ASM Handbook: Properties and Selection: Irons, Steels, and High-Performance Alloys, Volume 1, ASM International, Materials Park, OH, 1990, pp. 653-661.

[30] J. L. Brimhall, H. E. Kissinger, G. L. Kulcinski, in: Proceedings of International Conference on Radiation Induced Voids in Metals, J. W. Corbett and L. C. Ianello, (Eds.), CONF-710601, National Technical Information Service, U. S. Department of Commerce, 1972, pp. 338-375.

[31] A.K. Seeger, in: Proceedings of the Second United Nations International Conference on the Peaceful Uses of Atomic Energy, Volume 6, United Nations, New York, 1958, p. 250.

[32] S. J. Zinkle, Y. Matsukawa, J. Nucl. Mater. 329–333, (2004) 88-96.

[33] F. A. Garner, Irradiation performance of cladding and structural steels in liquid metal reactors, in: B. R. T. Frost (Ed.), Materials Science and Technology: A Comprehensive Treatment, Volume 10A, VCH Publishers, New York, 1994, pp. 419-543.

[34] F. A. Garner, Radiation damage in austenitic steels, in: R.J.M. Konings, (Ed.) Comprehensive Nuclear Materials, Volume 4, Elsevier, Amsterdam, 2012, pp. 33-95.

[35] E. H. Lee and L. K. Mansur, Philos. Mag. A 61 (1990) 733-749.

[36] P. J. Maziasz, J. Nucl. Mater. 205 (1993) 118-145.

[37] S. Ukai, T. Uwaba, J. Nucl. Mater. 317 (2003) 93-101.

[38] F. A. Garner, J. Nucl. Mater. 122 (1-3) (1984) 459-471.

[39] F. A. Garner, H. R. Brager, in: F. A. Garner, J. S. Perrrin (Eds.), Proceedings of Twelfth International Symposium on Effects of Radiation on Materials, Volume 1, ASTM, Philadelphia, PA, 1985, pp. 187-201.

[40] F. A. Garner, A. S. Kumar, in: F. A. Garner, N. H. Packan, A. S. Kumar (Eds.), Proceedings of Thirteenth International Symposium on Effects of Radiation on Materials, Part 1: Radiation-Induced Changes in Microstructure, ASTM, Philadelphia, PA, 1987, pp. 289-314.

[41] M. L. Hamilton, F. H. Huang, W. J. S. Yang, F. A. Garner, in: F. A. Garner, C. H. Henager Jr., N. Igata (Eds.), Proceedings of International Thirteenth Symposium on Effects of Radiation on Materials, Part II: Influence of Radiation on Material Properties, ASTM Philadelphia, PA, 1987, pp. 245-270.

[42] V. S. Neustroev, F. A. Garner, J. Nucl. Mater., 378 (2008) 327-332.

[43] S. I. Porollo, A. N. Vorobjev, Y. V. Konobeev, A. M. Dvoriashin, V. M. Krigan, et al., J. Nucl. Mater. 258-263 (1998) 1613-1617.

[44] R. L. Klueh, D. L. Harries, High Chromium Ferritic and Martensitic Steels for Nuclear Applications, ASTM, West Conshohocken, PA, 2001.

[45] G. R. Odette, J. Nucl. Mater. 155-157 (1988) 921-927.

[46] A. Kimura, R. Kasada, K. Morishita, R. Sugano, A. Hasegawa, et al., J. Nucl. Mater. 307 (2002) 521-526.

[47] R. L. Klueh, A. T. Nelson, J. Nucl. Mater. 371 (2007) 37–52.

[48] Z. Oksiuta, P. Hosemann, S. C. Vogel, N. Baluc, J. of Nucl. Mater. 451 (2014) 320–327.

[49] G. R. Odette, D.T. Hoelzer, JOM 62 (9) (2010) 84-92.

[50] T. Yamamoto, G. R. Odette, P. Miao, D. J. Edwards, R. J. Kurtz, J. Nucl. Mater. 386–388, (2009) 338-341.

[51] G. R. Odette, P. Miao, D. J. Edwards, T. Yamamoto, R.J. Kurtz, et al., J. Nucl. Mater. 417, (2011) 1001-1004.

[52] L. K. Mansur, Mechanisms and kinetics of radiation effects in metals and alloys, in: G.R. Freeman (Ed.), Kinetics of Nonhomogenous Processes, Wiley-Intersci, New York, 1987, pp. 377-463.

[53] R. E. Stoller, G. R. Odette, in: Proceedings of Eleventh International Symposium on Effects of Radiation on Materials, Volume 782, ASTM, Philadelphia, 1982, pp. 275-294.

[54] R. E. Stoller, G. R. Odette, in: Proceedings of Thirteenth International Symposium on Effects of Radiation on Materials, Volume 955, ASTM, Philadelphia, 1987, pp. 371-392.

[55] G. R. Odette, P. J. Maziasz, J. A. Spitzbagel, J. Nucl. Mater. 103, (1981) 1289-1303.

[56] B. N. Singh, Philos. Mag. 29, (1974) 25-42.

[57] B. N. Singh, A. J. E. Foreman, Philos. Mag. 29, (1974) 847-857.

[58] B. N. Singh, S. I. Golubov, H. Trinkaus, D. J. Edwards, M. Eldrup, J. Nucl. Mater. 328 (2004) 77-87.

[59] X. M. Bai, A. F. Voter, R. G. Hoagland, M. Nastasi, B. P. Uberuaga, Science 327 (2010) 1631-1634.

[60] D. Chen, J. Wang, T. Chen, L. Shao, Sci. Rep. 3 (2013) 1450.

[61] C. Sun, M. Song, K. Y. Yu, Y. Chen, M. Kirk, et al., Metall. and Mat. Trans. A 44 (2013) 1966-1974.

[62] L. Yao, S. P. Ringer, J. M. Cairney, M. K. Miller, Script. Mater. 69 (2013) 622-625.

[63] Y. Sekio, S. Yamashita, N. Sakaguchi, H. Takahashi, J. Nucl. Mater. 458 (2015) 355-360.

[64] T. Yamamoto, Y. Wu, G. R. Odette, K. Yabuuchi, S. Kondo, et al., J. Nucl. Mater. 449 (2014) 190–199.

[65] J. J. Sniegowski, W. G. Wolfer, in: Proceedings of Topical Conference on Ferritic Alloys Use in Nuclear Energy Technologies, Metallurgical Society of AIME, New York, 1984, pp. 579–586.

[66] J. Henry, X. Avery, Y. Dia, J. P. Pizzanelli, J. J. Espinas, J. Nucl. Mater. 386-388 (2009) 345-348.

[67] J. Roberto, T. D. de la Rubia (co-chairs), Basic research needs for advanced nuclear energy systems. Rep. Basic Energy Sci. Workshop Basic Res. Needs Adv. Nucl. Energy Sys., Rockville, MD, July 31–Aug. 3, 2006.

[68] ASM International Handbook Committee, Steel melt processing, in: ASM Handbook: Casting, Volume 15, ASM International, Materials Park, OH, 2008, pp. 206-229.

[69] B. Mishra, Steel making practices and their influence on properties, in: J. R. Davis (Ed.), Metals Handbook, Desk Edition (2nd Ed.), ASM International, Materials Park, OH, 1998, p. 188.

[70] J. S. Benjamin, Metall. Trans. 1 (1970) 2943-2951.

[71] M. K. West, Processing and Characterization of Oxide Dispersion Strengthened 14YWT Ferritic Alloys, PhD Dissertation, University of Tennessee, 2006.

[72] J. R. Davis, Mechanical Alloying, in: Alloying - Understanding the Basics, ASM International, Materials Park, OH, 2001, pp. 303-305.

[73] J. J. Lewandowski, P. Lowhaphandu, Int. Mater. Rev. 43 (4) (1998) 145-187.

[74] B. Avitzur, J. Eng. Ind. Trans. ASME Ser. B 87 (1965) 487-494.

[75] H. L. D. Pugh, J. Mech. Eng. Sci. 6 (1964) 362-370.

[76] B. I. Beresnev, L. F. Vereshchagin, Y.N. Ryabinin, Izv. Akad. Nauk SSSR Mekh. Mashin. 7 (1959) 128-132.

[77] S. N. Patankar, A. L. Grow, R. W. Margevicius, J. J. Lewandowski, in: V. A. Ravi, T. S. Srivatsan, J. J. Moore (Ed.), Proceedings of Processing and Fabrication of Advanced Materials III, TMS, Warrendale PA, 1994, pp. 733-745.

[78] A. L. Grow, J. J. Lewandowski, SAE Trans., Paper No. 950260, (1993) 1-5.

[79] A. R. Austen, W. L. Hutchinson, Adv. Cryogen. Eng. Mater. 36 (1990) 741-748.

[80] T. Z. Blazynski, Metal forming, in: E. H. Smith, Mechanical Engineer's Reference Book (12th Ed.), Elsevier, Oxford, 1998, pp. 16/12-16/32.

[81] O. D. Neikov, Advanced aluminum alloy powders, in: O. D. Neikov, S. S. Naboychenko, I. V. Murashova, V. G. Gopienko, I. V.Frishberg, et al. (Eds.), Handbook of Non-Ferrous Metal Powders - Technologies and Applications, Elsevier, Oxford, 2009, pp. 284-313.

[82] W. F. Gale, T. C. Totemeier, Smithells Metals Reference Book (8th Ed.), Elsevier, Netherlands, 2004, pp. 23/1-23/37.

[83] A. Lawley, R. D. Doherty, Spray forming, in: P. W. Lee, Y. Trudel, R. Iacocca, R. M. German, B. L. Ferguson, et al. (Eds.), ASM Handbook, Volume 7: Powder Metal Technologies and Applications, ASM International, Materials Park, OH, 1998, pp. 396-407.

[84] P. C. Mathur, D. Apelian, A. Lawley, Acta Metall. 37 (2) (1989) 429-443.

[85] S. Annavarapu, R. D. Doherty, Int. J. Powder Metall. 29 (4) (1993) 331-343.

[86] M. Rose, A. G. Balogh, H. Hahn, Mater. Sci. Forum 248-249 (1997) 213-216.

[87] N. A. Smirnova, V. I. Levit, V. P. Pilyugin, R. I. Kuznezov, L.S. Davidova, et al., Phys. Met. Metallogr. 61(6) (1986) 127-134.

[88] V. M. Segal, V. I. Reznikov, F. E. Drobishevski, V. I. Kopilov, Izv. SSSR Metall. 1 (1981) 115-123.

[89] J. R. Groza, Nanocrystalline powder consolidation methods, in: C. C. Koch (Ed.), Nanostructured Materials: Processing, Properties, and Applications, Noyes Publications, New York, 2002, pp. 119–172.

[90] G. R. Gray III, Shock wave testing of ductile materials, in: H. Kuhn, D. Medlin (Eds.), ASM Handbook: Mechanical Testing and Evaluation, Volume 8, ASM International, Materials Park, OH, 2000, pp. 530-538.

[91] M. H. Rice, R. G. McQueen, J. M. Walsh, Solid State Phys. 6 (1958) 1-63.

[92] R. G. McQueen, Laboratory techniques for very high pressures and the behavior of metals under dynamic loading, in: K. A. Gschneider, Jr., M. T. Hepworth, N. A. D. Parlee, (Eds.), Metallurgy at High Pressures and High Temperatures, Gordon and Breach, New York, 1964, pp. 44– 132.

[93] R. G. McQueen, S. P. Marsh, J. W. Taylor, J. N. Fritz, W. J. Carter, The equation of state of solids from shock wave studies, in: R. Kinslow (Ed.), High Velocity Impact Phenomena, Academic Press, New York, 1970, pp. 293– 417.

[94] L. E. Murr, Metallurgical effects of shock and high-strain-rate loading, in: T. Z. Blazynski (Ed.), Materials at High Strain Rates, Elsevier Science Publishers, London & New York, 1987, pp. 1-46.

[95] L. E. Murr, K. P. Staudhammer, Shock-induced microstructures and mechanical property changes in metals and alloys, in: L. E. Murr, Shock Waves for Industrial Applications, Noyes Publications, New Jersey, 1988, pp. 22-38.

[96] M. T. Myers, Toward Understanding Dynamic Annealing Processes in Irradiated Ceramics, PhD Dissertation, Texas A&M University, 2013.

[97] J. F. Ziegler, J. P. Biersack, "SRIM2006: The Stopping and Range of Ions in Matter: Version 2006", available at http://www.srim.org.

[98] L. R. Greenwood, R. K. Smither, SPECTER: Neutron Damage Calculations for Materials Irradiations, ANL/FPP/TM-197, Argonne National Laboratory, Argonne, IL, January 1985, available at http://www.osti.gov.

[99] R. E. Stoller, M. B. Toloczko, G. S. Was, A. G. Certain, S. Dwaraknath, et al., Nucl. Instrum. Meth. B, 310 (2013) 75–80.

[100] B. L. Adams, Ultramicroscopy 67 (1997) 11-17.

[101] V. Kumar, IEEE Trans. Image Process. 22 (7) (2013) 2637-2645.

[102] S. C. Vogel, ISRN Mater. Sci. 2013 (2013) 1-24.

[103] P. W. Lisowski, K. F. Schoenberg, Nucl. Instr. Meth. Phys. Res. A 562 (2) (2006) 910–914.

[104] H. R. Wenk, L. Lutterotti, S. C. Vogel, Nucl. Instr. Meth. Phys. Res. A 515 (2003) 575–588.

[105] A. S. Losko, S. C. Vogel, H. M. Reiche, H. Nakotte, J. Appl. Cryst. 47 (2014) 2109–2112.

[106] D. B. Williams, C. B. Carter, Transmission Electron Microscopy: a textbook for materials science, Springer, New York, 2009.

[107] R. E. Smallman, A. H. W. Ngan, Physical Metallurgy and Advanced Materials (7th Ed.), Elsevier, Oxford, 2007, pp. 161-238.

[108] A. Cerezo, P. H. Clifton, M. J. Galtrey, C. J. Humphreys, T. F. Kelly, et al., Mater. Today, 10 (12) (2007) 36-42.

[109] G. Sha, A. Cerezo, G. D. W. Smith, Appl. Phys. Lett. 92 (4) (2008) 043503 (1-3).

[110] F. C. Campbell, Inspection of Metals - Understanding the Basics, ASM International, Materials Park, OH, 2013, pp. 100-102.

[111] W. C. Oliver, G. M. Pharr, J. Mater. Res. 7 (1992) 1564-1583.

[112] M. F. Doerner, W. D. Nix, J. Mater. Res. 1 (1986) 601-609.

[113] C. Sun, Mechanical Properties and Radiation Tolerance of Ultrafine Grained and Nanocrystalline Metals, PhD Dissertation, Texas A&M University, 2013.

[114] S. V. Rogozhkin, V. S. Ageev, A. A. Aleev, A. G. Zaluzhnyi, M. V. Leont'eva-Smirnova, et al., Phys. Met. Metallogr. 108 (6) (2009) 579-585.

[115] A. Kohyama, A. Hishinuma, Y. Kohno, K. Shiba, A. Sagara, Sci. Rep. RITU, 45 (1) (1997) 137-141.

[116] A. G. Ioltukhovskiy, A. I. Blokhin, N. I. Budylkin, V. M. Chernov, M. V. Leont'eva-Smirnova, et al., J. Nucl. Mater. 283–287 (2000) 652-656.

[117] R. L. Klueh, Proceedings of the IEA Workshop/Working Group Meeting on Ferritic/Martensitic Steels, ECN Nuclear, Petten, Netherlands, 1-2 October 1998.

[118] A. V. Vatulin, Vopr. At. Nauki Tekh., Ser. Materialoved. Nov. Mater., 1 (62), (2004) 26-41.

[119] V. V. Sumin, V. G. Simkin, S. G. Sheverev, M. V. Leont'eva-Smirnova, V. M. Chernov, Phys. MET. Metal., 108 (6) (2009) 600-605.

[120] B. K. Kardasheva, V. M. Chernov, Mat. Sci. Eng. A 521–522 (2009) 329-334.

[121] V. M. Chernov, M. V. Leont'eva-Smirnova, M. M. Potapenko, N. I. Budylkin, Yu. N. Devyatko, et al., Nucl. Fusion 47 (2007) 839-848.

[122] I. A. Evstyukhina, N. V. Boiko, O. N. Izmaylov, S. G. Rudakov, Yu. N. Devyatko et al., Inorg. Mater.: Appl. Res. 3 (2) (2012) 102-106.

[123] V. M. Chernov, G. N. Ermolaev, M. V. Leont'eva-Smirnova, Tech. Phys. 55 (7) (2010) 985-990.

[124] A. V. Golubeva, N. P. Bobyr, D. I. Cherkez, A. V. Spitsyn, M. Mayer, et al., J. Nucl. Mater. 438 (2013) S983-S987.

[125] A. V. Panin, V. A. Romanova, R. R. Balokhonov, O. B. Perevalova, E. A. Sinyakova, et al., Phys. Mesomech., 15 (1-2) (2012) 94-103.

[126] A. V. Panin, V. M. Chernov, M. V. Leont'eva-Smirnova, E. A. Melnikovaa, J. Nucl. Mater. 386–388 (2009) 466-470.

[127] O. V. Emelyanova, P. S. Dzhumaev, V. L. Yakushin, B. A. Kalin, M. G. Ganchenkova et al., Nucl. Instrum. Meth. B 365 (2015) 218-221.

[128] A. R. Kilmametov, D. V. Gunderov, R. Z. Valiev, A. G. Balogh, H. Hahn, Script. Mater. 59 (2008) 1027-1030.

[129] B. Radiguet, A. Etienne, P. Pareige, X. Sauvage, R. Valiev, J. Mater. Sci. 43 (23-24) (2008) 7338–7343.

[130] P. B. R. Rajan, I. Monnet, E. Hug, A. Etienne, N. Enikeev, et al., IOP Conf. Ser.: Mater. Sci. Eng. 63 (2014) 012121 (1-5).

[131] N. Nita, R. Schaeublin, M. Victoria, J. Nucl. Mater. 329–333 (2004) 953–957.

[132] R. Z. Valiev, M. J. Zehetbauer, Y. Estrin, H. W. Hoppel, Y. Ivanisenko, et al., Adv. Eng. Mater. 9 (2007) 527–533.

[133] Y. T. Zhu, T .C. Lowe, T. G. Langdon, Script. Mater. 51 (2004) 825–830.

[134] C. Sun, K. Y. Yu, J. H. Lee, Y. Liu, H. Wang, et al., J. Nucl. Mater. 420 (2012) 235–240.

[135] C. Sun, Y. Yang, Y. Liu, K. T. Hartwig, H. Wang, et al., Mater. Sci. Eng. A 542 (2012) 64–70.

[136] D. C. Foley, K. T. Hartwig, S. A. Maloy, P. Hosemann, X. Zhang, J. Nucl. Mater. 389 (2009) 221–224.

[137] M. Song, R. Zhu, D. C. Foley, C. Sun, Y. Chen, et al., J. Mater. Sci. 48 (2013) 7360–7373.

[138] M. Song, C. Sun, J. Jang, C. H. Han, T. K. Kim, et al., J. Alloys Compd. 577 (2013) 247–256.

[139] S. V. Rogozhkin, T. V. Kulevoy, N. A. Iskandarov, N. N. Orlov, B. B. Chalykh, et al., At. Energ. 114 (1) (2013) 14-20.

[140] A. Alsabbagh, R. Z. Valiev, K. L Murty, J. Nucl. Mater. 443 (2013) 302-310.

[141] A. Alsabbagh, A. Sarkar, B. Miller, J. Burns, L. Squires, et al., Mater. Sci. Eng. A 615 (2014) 128–138.

[142] V. K. Shamardin, Y. D. Goncharenko, T. M. Bulanova, A. A. Karsakov, I. V. Alexandrov, et al., Rev. Adv. Mater. Sci. 31 (2012) 167-173.

[143] R. Z. Valiev, R. K. Islamgaliev, I. V. Alexandrov, Progr. Mater. Sci 45 (2000) 103–189.

[144] J. A. Sprague, F. A. Smidt, Jr., Naval Research Laboratory Semiannual Progress Report, April 1973, NRL Memorandum Report 2629, 1973, pp. 27-36.

[145] E. Getto, Z. Jiao, A. M. Monterrosa, K. Sun, G. S. Was, J. Nucl. Mater. 465 (2015) 116-126.

[146] J. G. Gigax, E. Aydogan, T. Chen, D. Chen, L. Shao, et al., J. Nucl. Mater. 465 (2015) 343-348.

[147] L. Shao, C-C. Wei, J. G. Gigax, A. Aitkaliyeva, D. Chen, et al., J. Nucl. Mater. 453 (2014) 176–181.

[148] F. A. Smidt, P. R. Malmberg, J. A. Sprague, J. E. Westmoreland, Swelling behavior of commercial ferritic alloys, EM-12 and HT-9, as assessed by heavy ion bombardment, in: J. B. Wheeler, H. M. Hoersch, E. J. McGlinchey (Eds.), Irradiation Effects on the Microstructure and Properties of Metals, ASTM STP-611, American Society for Testing and Materials, Philadelphia, 1976, pp. 227-241.

[149] V. Bryk, O. Borodin, A. Kalchenko, V. Voyevodin, V. Ageev, et al. in: Proceedings of Accelerator Applications, Bruges, Belgium, 2013, pp. 1-6.

[150] F. A. Garner, J. Nucl. Mater. 117 (1983) 177-197.

[151] F. A. Garner, G. L. Guthrie, in: Proceedings of International Conference on Radiation Effects and Tritium Technology for Fusion Reactors, Gatlinburg, TN, 1975, pp. 491-518.

[152] F. A. Garner, R. W. Powell, D. W. Keefer, A. G. Pard, K. R. Garr, et al., in: Proceedings of Workshop on Correlation of Neutron and Charged Particle Damage, Oak Ridge, TN, 1976, pp. 147-175.

[153] D. Kaoumi, A. T. Motta, R. C. Birtcher, J. Appl. Phys. 104 (2008) 073525 (1-13).

[154] W. Voegeli, K. Albe, H. Hahn, Nucl. Instrum. Meth. B 202 (2003) 230-235.

[155] N. T. Park, personal communication, Atomic Weapons Establishment, UK, November 5, 2008.

[156] M. A. Shehadeh, E. M. Bringa, H. M. Zbib, J. M. McNaney, B. A. Remington, Appl. Phys. Lett. 89 (2006) 171918 (1-3).

[157] D. H. Kalantar, J. F. Belak, G. W. Collins, J. D. Colvin, H. M. Davies, et al., Phys. Rev. Lett. 95 (2005) 075502 (1-4).

[158] N. K. Bourne, G. T. Gray III, J. C. F. Millett, J. Appl. Phys. 106 (2009) 091301 (1-14).

[159] S. Perez-Bergquist, G. T. Gray III, S. A. Maloy, E. K. Cerreta, O. Anderoglu, AIP Conf. Proc. 1426 (2012) 1355-1358.

160] K. Wongiwat, L. E. Murr, Mater. Sci. Eng. 35 (1978) 273–285.

[161] F. Greulich, L. E. Murr, Mater. Sci. Eng. 39 (1979) 81–93.

[162] R. L. Nolder, G. Thomas, Acta Metall. 12 (1964) 227–240.

[163] L. E. Murr, K. P. Staudhammer, Mater. Sci. Eng. 20 (1975) 35–46.

[164] D. Bancroft, E. L. Peterson, S. Minshall, J. Appl. Phys. 17 (1956) 291-298.

[165] P. C. Johnson, B. A. Stein, R. S. Davis, J. Appl. Phys. 33 (1962) 557-561.

[166] J. C. Jamieson, A. W. Lawson, J. Appl. Phys. 33 (1962) 776-780.

[167] T. Takahashi, W. A. Bassett, Science 145 (1964) 483-486.

[168] L. M. Dougherty, G. T. Gray III, E. K. Cerreta, R. J. McCabe, R .D. Field, et al., Script. Mater. 60 (2009) 772–775.

[169] V. Livescu, J. F. Bingert, T. A. Mason, Mater. Sci. Eng. A 556 (2012) 155–163.

[170] L. E. Murr, M. A. Meyers, Acta Mater. 45 (1) (1997) 157–175.

[171] W. Visser, Y. Sun, O. Gregory, G. Plume, C-E. Rousseau, et al., Mater. Sci. Eng. A 528 (2011) 7857–7866.

[172] J. A. Yan, C. Y. Wang, S. Y. Wang, Phys. Rev. B, 70 (2004) 174105 (1-5).

[173] S. Taketomi, R. Matsumoto, N. Miyazaki, Int. J. Mech. Sci. 52 (2010) 334–338.

[174] O. Gregory, J. Oxley, J. Smith, M. Platek, H. Ghonem, et al., Mater. Charact. 61 (3) (2010) 347–354.

[175] T. De Resseguier, M. Hallouin, J. Appl. Phys. 84 (4) (1998) 1932–1938.

[176] J. N. Johnson, R. W. Rohde, J. Appl. Phys. 42 (11) (1971) 4171–4182.

[177] G. T. Gray III, Influence of Shock-Wave Deformation on the Structure/Property Behavior of Materials, in: J. R. Asay, M. Shahinpoor (Eds.), High Pressure Shock Compression of Solids, Springer-Verlag, New York, 1993, pp. 187-215.

[178] G. T. Gray III, K .S. Vecchio, Metall. Mater. Trans. A 26A (1995) 2555-2563.

[179] D. M. Norfleet, D. M. Dimiduk, S. J. Polasik, M. D. Uchic, M. J. Mills, Acta Mater. 56 (2008) 2988–3001.

[180] U. Matrin, U. Muhle, O. Heinrich, Prakt. Metallogr. 32 (1995) 207-209.

[181] T. Kruml, V. Paidar, J. L. Martin, Intermetallics 8 (2000) 729-736.

[182] K. Yasunaga, M. Iseki, M. Kiritani, Mater. Sci. Eng. A 350 (2003) 76-80.

[183] V. I. Zel'dovich, A. E. Kheifets, N. Y. Frolova, B. V. Litvinov, Doklady Phys. 51 (10) (2006) 547-550.

[184] M. A. Meyers, H. Jarmakani, E. M. Bringa, B. A. Remington, Dislocations in shock compression and release, in: J. P. Hirth (Ed.), Dislocations in Solids, Volume 15, Elsevier, The Netherlands, 2009, pp. 95-196.

[185] W. Woo, T. Ungar, Z. Feng, E. Kenik, B. Clausen, X-ray and Neutron Diffraction Measurements of Dislocation Density and Subgrain Size in a Friction-Stir Welded Aluminum Alloy, TMS and ASM International, 41 (2009) 1210-1216.

[186] Z. Cong, Y. Murata, Mater. Trans. 52 (12) (2011) 2151-2154.

[187] T. Ungar, JCPDS-International Centre for Diffraction Data ISSN 1097-0002, 2008.

[188] T. Ungar, J. Gubicza, P. Hanak, I. Alexandrov, Mater. Sci. Eng. A319–321 (2001) 274–278.

[189] R. K. Khatirkar, B. S. Murty, Mater. Chem. Phys. 123 (2010) 247–253.

[190] F. Yin, T. Hanamura, O. Umezawa K. Nagai, Mater. Sci. Eng. A 354 (2003) 31–39.

[191] T. Ungar, I. Dragomir, A. Revesz, A. Borbely, J. Appl. Cryst. 32 (1999) 992-1002.

[192] M. Tang, J. Marian, Acta Mater. 70 (2014) 123–129.

[193] D. Tabor, Br. J. Appl. Phys. 7 (1956) 159-166.

[194] J. T. Busby, M. C. Hash, G. S. Was, J. Nucl. Mat. 336 (2005) 267–278.

[195] G. I. Taylor, J. Inst. Mat. 62 (1938) 307-324.

[196] R. E. Stoller, S. J. Zinkle, J. Nucl. Mat. 283-287 (2000) 349–352.

[197] P. L. Mosbrucker, D. W. Brown, O. Anderoglu, L. Balogh, S. A. Maloy, et al., J. Nucl. Mat. 443 (2013) 522–530.

[198] S. J. Fensin, E. K. Cerreta, G. T. Gray III, S. M. Valone, Sci. Rep., 4 (2014) 5461 (1-6).

[199] F. Barcelo, Y. de Carlan, J. L. Bechade, B. Fournier, Phase Transitions, 82 (11) (2009) 808–820.

[200] G. Palumbo, K. T. Aust, E. M. Lehockey, U. Erb, P. Lin, Script. Mater., 38 (11) (1998) 1685–1690.

[201] J. Hou, J. Q. Wang, W. Ke, E. H. Han, Mater. Sci. Eng. A, 518 (2009) 19–26.

[202] E. Getto, Z. Jiao, A. M. Monterrosa, K. Sun, G. S. Was, J. Nucl. Mat. 462 (2015) 458–469.

[203] E. E. Bloom, J. Nucl. Mater. 258–263 (1998) 7–17.

[204] H. R. Brager, F. A. Garner, Dependence of void formation on phase stability in neutron irradiated type 316 stainless steel, in: J. A. Sprague, D. Kramer (Eds.), Effects of Radiation on Structural Materials, ASTM-STP 683, ASTM, Philadelphia, 1979, pp. 207-232.

[205] Y. Murase, J. Nagakawa, N. Yamamoto, H. Shiraishi, J. Nucl. Mat. 258-263 (1998) 1639-1643.

[206] K. Uematsu, T. Kodama, Y. Ishida, K. Suzuki and M. Koyama, in: M. L. Bleiberg, J. W. Bennett (Eds.), Proceedings of International Conference on Radiation Effects in Breeder Reactor Structural Materials, AIME, New York, 1977, pp. 571-589.

[207] W. K. Appleby, E. E. Bloom, J. E. Flinn, F. A. Garner, in: M.L. Bleiberg, J. W. Bennett (Eds.), Proceedings of International Conference on Radiation Effects in Breeder Reactor Structural Materials, AIME, New York, 1977, pp. 509-527.

[208] W. van Witzenburg, A. Mastenbroek, J. D. Elen, J. Nucl. Mater. 103 (1981) 1187-1191.

[209] A. Risbet, V. Levy, J. Nucl. Mater. 46 (3) (1973) 341-352.

[210] W. van Witzenburg, P. J. van Tilborg, A. Mastenbroek and J. D. Elen, ASTM STP 782 (1982) 251-259.

[211] V. Levy, J. Mathie, A. Risbet, R. Levy , J. P. Poirier, in: S. H. Pugh, M. H. Loretto, D. I. R. Norris (Eds.), Voids Formed by Irradiation of Reactor Materials, British Nuclear Society, Reading, United Kingdom, 1971, pp. 63-69.

[212] H. R. Brager and F. A. Garner, ASTM STP 782 (1982) 152-165.

[213] E. Wakai, N. Hashimoto, J. P. Robertson, T. Sawai, A. Hishinuma, J. Nucl. Mat. 307–311 (2002) 352–356.

[214] F. A. Garner, K. Miyahara, J. W. Newkirk, H. Kinoshita, J. Nucl. Mat. 199 (1993) 132-142.

[215] A. M. Dvoriashin, S. I. Porollo, Yu. V. Konobeev, F. A. Garner, J. Nucl. Mat. 283-287 (2000) 157-160.

[216] T. Leffers, B. N. Singh, S. N. Buckley, S. A. Manthorpe, J. Nucl. Mat. 118 (1983) 60-67.

[217] W. van Witzenburg, A. Mastenbroek, J. Nucl. Mat. 133-134 (1985) 553-557.

[218] X. Wang, Q. Yan, G. S. Was, L. Wang, Script. Mater. 112 (2016) 9–14.

[219] A. M. Dvoriashin, S. I. Porollo, Yu. V. Konobeev, F. A. Garner, J. Nucl. Mat. 329–333 (2004) 319–323.

[220] R. L. Klueh, N. Hashimoto, M. A. Sokolov, K. Shiba, S. Jitsukawa, J. Nucl. Mat. 357 (2006) 156–168.

[221] G. S. Upadhyaya, Cemented Tungsten Carbides - Production, Properties, and Testing, Noyes Publications, New Jersey, 1998, pp. 166-192.

[222] S. E. Danilov, V. L. Arbuzov, N. L. Pecherkina, V. V. Sagaradze, Phys. Met. Metallogr. 116 (7) (2015) 711-717.

[223] M. J. Demkowicz, O. Anderoglu, X. Zhang, A. Misra, J. Mater. Res. 26 (14) (2011) 1666-1675.

[224] R. Hu, G. D. W. Smith, E. A. Marquis, Acta Mater. 61 (2013) 3490–3498.

[225] A. B. Sivak, P. A. Sivak, V. A. Romanov, V. M. Chernov, Inorg. Mater.: Appl. Res. 6 (2) (2015) 105-113.

[226] R. L. Klueh, D. J. Alexander, J. Nucl. Mater. 233–237 (1996) 336–341.

[227] S. Ukai, S. Ohtsuka, Energy Mater. 2 (2007) 26–35.

[228] S. Ukai, Oxide dispersion strengthened steels, in: R. J. M. Connings (Ed.), Comprehensive Nuclear Materials, Volume 4, Elsevier, Germany, 2012, pp. 241-271.

[229] G. R. Odette, JOM 66 (12) (2014) 2427-2441.

[230] S. M. Ukai, M. Fujiwara, J. Nucl. Mater. 307–311 (2002) 749–757.

[231] N. J. Cunningham, Y. Wu, A. Etienne, E. M. Haney, G. R. Odette, et al., J. Nucl. Mater. 444 (2014) 35–38.

[232] M. K. Miller, D. T. Hoelzer, E. A. Kenik, K. F. Russell, Intermetallics 13 (3-4) (2005) 387–392.

[233] M. L. Hamilton, D. S. Gelles, R. J. Lobsinger, G. D. Johnson, W. F. Brown, et al., Fabrication technological development of the oxide dispersion strengthened alloy MA957 for fast reactor applications, PNL-13168, Richland, WA: Pac. Northwest Lab, 2000.

[234] T. S. Chou, H. K. D. H. Bhadeshia., Metall. Trans. A 24A (1993) 773–779.

[235] A. Alamo, V. Lambard, X. Averty, M. H. Mathon, J. Nucl. Mater. 329-333 (2004) 333–337.

[236] I. S. Kim, B. Y. Choi, C. Y. Kang, T. Okuda, P. J. Maziasz, et al., ISIJ Int. 43 (2003) 1640–1646.

[237] M. J. Alinger, On the Formation and Stability of Nanometer Scale Precipitates in Ferritic Alloys During Processing and High Temperature Service, PhD Thesis, University of California, Santa Barbara, 2004.

[238] P. Miao, G. R. Odette, T. Yamamoto, M. J. Alinger, D. Hoelzer, et al., J. Nucl. Mater. 367–370 (2007) 208–212.

[239] P. Miao, G. R. Odette, T. Yamamoto, M. J. Alinger, D. Klingensmith, J. Nucl. Mater. 377 (1) (2008) 59–64.

[240] W. J. Yang, G. R. Odette, T. Yamamoto, P. Miao, M. J. Alinger, et al., J. Nucl. Mater. 367–370 (2007) 616–620.

[241] S. Ukai, T. Okuda, M. Fujiwara, T. Kobayashi, S. Mizuta, et al., J. Nucl. Sci. Technol. 39 (2002) 872–79.

[242] S. Ukai, S. Mizuta, M. Fujiwara, T. Okuda, T. Kobayashi, J. Nucl. Sci. Technol. 39 (2002) 778–788.

[243] M. J. Alinger, G. R. Odette, G. E. Lucas, J. Nucl. Mater. 307–311 (2002) 484–489.

[244] M. E. Alam, K. Fields, G. R. Odette, D. T. Hoelzer, S. A. Maloy, Tensile Property Characterization of 14YWT Nanostructured Ferritic Alloy NFA1, Fusion Materials Semiannual Progress Report December 31, 2014, DOE/ER-313/57, 2015, pp. 39–48.

[245] S. Pal, M. E. Alam, G. R. Odette, J. J. Lewandowski, D. T. Hoelzer and S. A. Maloy, Characterization of the Microstructures and Textures of NFA-1 for Two Deformation Processing Routes, Fusion Materials Semiannual Progress Report June 30, 2015, DOE/ER-313/58, 2015, pp. 29–41.

[246] L. Toualbi, C. Cayron, P. Olier, J. Malaplate, M. Praud, et al., J. Nucl. Mater. 428 (2012) 47–53.

[247] L. Toualbi, C. Cayron, P. Olier, R. Loge, Y. de Carlan, J. Nucl. Mater. 442 (2013) 410–416.

[248] S. Zherebtsov, A. Mazur, G. Salishchev, W. Lojkowski, Mater. Sci. Eng. A 485 (2008) 39–45.

[249] S. Zherebtsov, G. Salishchev, W. Lojkowski, Mater. Sci. Eng. A 515 (2009) 43–48.

[250] M. Lewandowska, A. T. Krawczynska, M. Kulczyk, K. J. Kurzydłowski, J. Nucl. Mater. 389–388 (2009) 499–502.

[251] J. J. Lewandowski, B. Berger, J. D. Rigney, S. N. Patankar, Phil. Mag. A 78 (3) (1998) 643–656.

[252] R. W. Margevicius, J. J. Lewandowski, I. E. Locci, Script. Metall. Mater. 29 (1992) 1733–1736.

[253] R. W. Margevicius, J. J. Lewandowski, Script. Metall. Mater. 25 (9) (1991) 2017-2022.

[254] R. W. Margevicius, J. J. Lewandowski, I. E. Locci, R. D. Noebe, Script. Metall. Mater. 29 (1993) 1309–1312.

[255] R. Hielscher, H. Schaeben, J. Appl. Cryst. 41 (2008) 1024–1037.

[256] D. Orlov, P. P. Bhattacharjee, Y. Todaka, M. Umemoto, N. Tsuji, Script. Mater. 60 (10) (2009) 893-896.

[257] R. Jamaati, M. R. Toroghinejad, M. A. Mohtadi-Bonab, H. Edris, J. A. Szpunar, M. R Salmani, J. Mater. Eng. Perform. 23 (2014) 4436–4445.

[258] F. J. Humphreys, M. Hatherly, Recrystallization and Related Annealing Phenomena (2nd ed.), Elsevier, Oxford, 2004.

[259] O. Engler, V. Randle, Introduction to Texture Analysis - Macrotexture, Microtexture, and Orientation Mapping (2nd ed.), Taylor & Francis Group, New York, 2010.

[260] J-Y. Kang, B. Bacroix, H. Regle, K. H. Oh, H-C. Lee, Acta Mater. 55 (2007) 4935–4946.

[261] M. Holscher, D. Raabe and K. Lucke, Mater. Technol. 62(12) (1991) 567-575.

[262] O. A. Bauchau, J. I. Craig, Structural Analysis with Applications to Aerospace Structures, Springer, New York, 2009.

[263] W. B. Hutchinson, Phil. Trans. R. Soc. Lond. A 357 (1999) 1471–1485.

[264] J. L. Raphanel, P. Van Houtte, Acta Metall., 33 (8) (1985) 1481–1488.

[265] D. Raabe, K. Lucke, Mater. Sci. Tech., 9 (4) (1993) 302–312.

[266] S. J. Zinkle, J. T. Busby, Mater. Today 12 (11) (2009) 12–19.

[267] D. A. McClintock, D. T. Hoelzer, M. A. Sokolov, R. K. Nanstad, J. Nucl. Mater. 386–388 (2009) 307–311.

[268] R. Lindau, A. Moslang, M. Rieth, M. Klimiankou, E. Materna-Morris, et al., Fusion Eng. Des. 75–79 (2005) 989–996.

[269] M. E. Abd El-Azim, Mech. Mater. 25 (1997) 255-261.

[270] T. Malis, S. C. Cheng, R. F. Egerton, J. Electron. Micr. Tech. 8 (1988) 193–200.

[271] E. Aydogan, S. Pal, O. Anderoglu, S. A. Maloy, S. C. Vogel, et al., Mater. Sci. Eng. A 661 (2016) 222–232.

[272] Y. Wen, Y. Liu, A. Hirata, F. Liu, T. Fujita, et al., Mater. Sci. Eng. A 544 (2012) 59– 69.

[273] W. Blum, X. H. Zeng, Acta Mater. 57 (2009) 1966-1974.

[274] C. E. Carlton, P. J. Ferreira, Acta Mater. 55 (2007) 3749–3756.

[275] P. M. Kelly, Int. Metall. Rev. 18 (1973) 31–36.

[276] J. H. Schneibel, M. Heilmaier, W. Blum, G. Hasemann and T. Shanmugasundaram, Acta Mater. 59 (2011) 1300–1308.

[277] J. H. Kim, T. S. Byun, D. T. Hoelzer, C. H. Park, J. T. Yeom, et al., Mater. Sci. Eng. A 559 (2013) 111–118.

[278] E. Aydogan, O. Anderoglu, S. A. Maloy, V. Livescu, G. T. Gray III, et al., Mater. Sci. Eng. A 651 (2016) 75–82.

[279] A. J. Lapointe, Microstructure and Strength of Continuously Cooled Low Alloy Vanadium and Niobium Steels, PhD Dissertation, University of Strathclyde, 1975.

[280] A. S. Keh, in: J. B. Newkirk, J. H. Wernick (Eds.), Proceedings of Direct observations of Imperfections in Crystals, J. Wiley, London, 1962, pp. 213–233.

[281] U. F. Kocks, in: P. Haasen, V. Gerold, G. Kostorz (Eds.), Proceedings of the Fifth International Conference on Strength of Metals and Alloys, Volume 3, Pergamon Press, Oxford, 1979, pp. 1661–1680.

[282] S. Maropoulos, J. D. H. Paul, N. Ridley, Mater. Sci. Technol. 9 (11) (1993) 1014-1019.

[283] Q. Li, Mater. Sci. Eng. 361 (2003) 385–391.

[284] U. F. Kocks, A. S. Argon, M. F. Ashby, Prog. Mater. Sci. 19 (1975) 1-281.

[285] S. Maropoulos, J. D. H. Paul, N. Ridley, Mater. Sci. Technol. 9 (11) (1993) 1014-1019.

[286] T. J. Koppenaal, D. Kuhlmann-Wilsdorf, Appl. Phys. Lett. 4 (3) (1964) 59-61.

[287] J. Irvine, T. N. Baker, Mater. Sci. Eng. 64 (1) (1984) 123-134.

[288] T. J. Koppenaal, J. Appl. Phys. 35 (9) (1964) 2750-2753.

[289] R. Labusch, Verh. Deut. Phys. Ges. 1 (1979) 222-223.

[290] K. G. Field, X. Hu, K. C. Littrell, Y. Yamamoto, L. L. Snead, J. Nucl. Mater. 465 (2015) 746-755.

[291] G. E. Lucas, J. Nucl. Mater. 206 (1993) 287-305.

[292] J. Friedel, Dislocations, Pergamon Press, Oxford, etc., 1964.

[293] F. Kroupa, P. B. Hirsch, Disc. Faraday Soc. 38 (1964) 49-55.

[294] T. R. Allen, J. Gan, J. I. Cole, M. K. Miller, J. T. Busby, et al., J. Nucl. Mater. 375 (2008) 26–37.

[295] H. W. Hoppel, Private communication, University of Erlangen-Nurnberg, Germany, August 23, 2009.

[296] Y. Wu, E. M. Haney, N. J. Cunningham, G.R. Odette, Acta Mater. 60 (8) (2012) 3456-3468.

[297] M. K. Miller, E. A. Kenik, K. F. Russell, L. Heatherly, D. T. Hoelzer, et al., Mater. Sci. Eng. A 353 (2003) 140-145.

[298] R. Kasada, N. Toda, K. Yutani, H. S. Cho, H. Kishimoto, et al., J. Nucl. Mater. 367–370 A, (2007) 222-228.

[299] S. Yamashita, K. Oka, S. Ohnuki, N. Akasaka, S. Ukai, J. Nucl. Mater. 307–311 (2002) 283-288.

[300] S. Yamashita, N. Akasak, S. Ukai, S. Ohnuki, J. Nucl. Mater. 367–370 (2007) 202-207.

[301] M-H. Mathon, Y. de Carlan, X. Averty, A. Alamo, C-H. de Novion, J. ASTM Int. 2 (9) (2005) 213-227.

[302] D. S. Gelles, Microstructural Examination of Commercial Ferritic Alloys at 200 dpa, Fusion reactor materials semiannual progress report for the period ending March 31, DOE/ER-0313/16, 1994, pp. 146-160.

[303] J. Ribis, J. Nucl. Mater. 434 (2013) 178-188.

[304] J. Ribis, S. Lozano-Perez, J. Nucl. Mater. 444 (2014) 314-322.

[305] J. Ribis, S. Lozano-Perez, Mater. Lett. 74 (2012) 143-146.

[306] N. Akasaka, S. Yamashita, T. Yoshitake, S. Ukai, A. Kimura, J. Nucl. Mater. 329–333 (2004) 1053-1056.

[307] P. Pareige, M. K. Miller, R. E. Stoller, D. T. Hoelzer, E. Cadel, et al., J. Nucl. Mater. 360 (2007) 136-142.

[308] K. Yutani, R. Kasada, H. Kishimoto, A. Kimura, J. ASTM Int. 4 (7) (2007) 1-9.

[309] A. Kimura, H. S. Cho, N. Toda, R. Kasada, K. Yutani, et al., J. Nucl. Sci. Technol. 44 (2007) 323-328.

[310] H. Kishimoto, R. Kasada, O. Hashitomi, A. Kimura, J. Nucl. Mater. 386–388 (2009) 533-536.

[311] H. Kishimoto, K. Yutani, R. Kasada, O. Hashitomi, A. Kimura, J. Nucl. Mater. 367–370 (2007) 179-184.

[312] C. M. Parish, R. M. White, J. M. LeBeau, M. K. Miller, J. Nucl. Mater. 445 (2014) 251–260.

[313] A. Certain, K. Kuchibhatla, V. Shutthanandan, D. T. Hoelzer, T. R. Allen, J. Nucl. Mater. 434 (2013) 311-321.

[314] M. -L. Lescoat, J. Ribis, Y. Chen, E. A. Marquis, E. Bordas, et al., Acta Mater. 78 (2014) 328–340.

[315] D. Vaumousse, A. Cerezo, P. J. Warren, Ultramicroscopy 95 (2003) 215-221.

[316] N. Cunningham, Y. Wu, D. Klingensmith, G. R. Odette, Mater. Sci. Eng. A 613 (2014) 296–305.

[317] N. J. Cunningham, Study of Structure, Composition, and stability of Y–Ti–O nm-scale features in nano-structured ferritic alloys, PhD Dissertation, University of California, Santa Barbara, 2012.

[318] C. A. Williams, E. A. Marquis, A. Cerezo, G. D. W. Smith, J. Nucl. Mater. 400 (2010) 37–45.

[319] P. Wells, N. Cunningham, G. R. Odette, Recent progress on understanding and quantifying atom probe tomography artifacts for high evaporation rate nm-scale phases in

Fe based alloys, Fusion Materials Semiannual Progress Report for the Period Ending December 31, 2011, DOE-ER-0313/51, 2012, pp. 9-21.

[320] C. Oberdorfer, G. Schmitz, Microsc. Microanal. 17 (2011) 15–25.

[321] E. A. Marquis, Appl. Phys. Lett. 93 (2008) 181904 (1-3).

[322] T. Chen, E. Aydogan, J. G. Gigax, D. Chen, J. Wang, et al., J. Nucl. Mater. 467 (2015) 42–49.

[323] Y. Miao, K. Mo, B. Cui, W. Y. Chen, M. K. Miller, et al., Mater. Charact. 101 (2015) 136–143.

[324] P. Dou, A. Kimura, T. Okuda, M. Inoue, S. Ukai, et al., J. Nucl. Mater. 417 (2011) 166–170.

[325] X. Mao, K. H. Oh, S. H. Kang, T. K. Kim, J. Jang, Acta Mater. 89 (2015) 141-152.

[326] J. Ribis, Y. de Carlan, Acta Mater. 60 (2012) 238-252.

[327] K. Dawson, G. J. Tatlock, J. Nuc. Mat. 444 (2014) 252-260.

[328] J. Ciston, Y. Wu, G. R. Odette, P. Hosemann, The Structure of Nanoscale Precipitates and Precipitate Interfaces in an Oxide Dispersion Strengthened Steel, Fusion Materials Semiannual Progress Report for the Period Ending December 31, 2011, DOE-ER-0313/51, 2012, pp. 6-8.

[329] A. Hirata, T. Fujita, Y. R. Wen, J. H. Schneibel, C. T. Liu et al., Nature Materials 10 (2011) 922-926.

[330] A. J. London, S. Lozano-Perez, M. P. Moody, S. Amirthapandian, B. K. Panigrahi et al., Ultramicroscopy 159 (2015) 360–367.

[331] V. Badjeck, M. G. Walls, L. Chaffron, J. Malaplate, K. March, J. Nucl. Mater. 456 (2015) 292–301.

[332] K. Mo, Z. Zhou, Y. Miao, D. Yun, H-M. Tung, et al., J. Nucl. Mater. 455 (2014) 376-381.

[333] Y. Miao, K. Mo, Z. Zhou, X. Liu, K-C. Lan, et al., Mater. Sci. Eng. A 625 (2015) 146-152.

[334] K. C. Russell, J. Nucl. Mater. 206 (1993) 129-138.

[335] R. S. Nelson, J. A. Hudson, D. J. Mazey, J. Nucl. Mater. 44 (1972) 318-330.

[336] F. S. Ham, J. Phys. Chem. Solids 6 (1958) 335-351.

[337] F. Soisson, C. C. Fu, Phys. Rev. B 76 (2007) 214102 (1-12).

[338] C. Hin and B. D. Wirth, J. Nucl. Mater. 402 (2010) 30–37.

[339] H. J. Frost, K. C. Russell, J. Nucl. Mater. 103-104 (1981) 1427-1432.

[340] M. Li, M. K. Miller, W-Y. Chen, J. Nucl. Mater. 462 (2015) 214–220.

[341] L. Tan, T. S. Byun, Y. Katoh, L. L. Snead, Acta Mater. 71 (2014) 11–19.